University of Glasgow

Puthenvila, George John (2026) *Incorporating nitinol shape memory alloy in class IV flextensional transducers for future ultrasonic surgical devices.* PhD thesis.

https://theses.gla.ac.uk/86384/

Copyright and moral rights for this work are retained by the author

A copy can be downloaded for personal non-commercial research or study, without prior permission or charge

This work cannot be reproduced or quoted extensively from without first obtaining permission in writing from the author

The content must not be changed in any way or sold commercially in any format or medium without the formal permission of the author

When referring to this work, full bibliographic details including the author, title, awarding institution and date of the thesis must be given

Enlighten: Theses
https://theses.gla.ac.uk/
research-enlighten@glasgow.ac.uk

INCORPORATING NITINOL SHAPE MEMORY ALLOY IN CLASS IV FLEXTENSIONAL TRANSDUCERS FOR FUTURE ULTRASONIC SURGICAL DEVICES

GEORGE JOHN PUTHENVILA

Submitted to the School of Engineering,

College of Science and Engineering,

University of Glasgow,



October 2026

© Copyright 2026 by George John Puthenvila. All Rights Reserved

Abstract

This research investigates the design, fabrication, material characterisation, and performance of class IV flextensional ultrasonic transducers incorporating Nitinol (Ni–Ti), a shape memory alloy (SMA) capable of reversibly transforming between martensitic and austenitic phases under the influence of temperature and applied stress. Previous studies have demonstrated the potential of Nitinol for resonance frequency tuning in class V cymbal transducers and enhanced thermal stability in Langevin ultrasonic transducers. The aim of this work was to evaluate the suitability of Nitinol for class IV flextensional ultrasonic transducers and to determine how its thermomechanical behaviour influences transducer performance under varying electrical, thermal, and mechanical operating conditions.

Material characterisation was first performed on the Nitinol components used throughout the study. Differential scanning calorimetry (DSC) was employed to determine transformation temperatures for Nitinol end-caps produced from materials with austenite finish temperatures (A_F) of 35 °C and 45 °C, together with Nitinol wire possessing an A_F of 30 °C. Energy-dispersive X-ray spectroscopy (EDXS) was used to evaluate elemental composition, while dynamic mechanical analysis (DMA) and tensile testing were conducted to investigate temperature-dependent mechanical behaviour, damping characteristics, and static mechanical performance. The results demonstrated that the thermomechanical response of Nitinol is influenced by both transformation behaviour and material processing history, highlighting the importance of material characterisation when integrating shape memory alloys into ultrasonic devices.

Class IV flextensional transducers incorporating Nitinol, aluminium (1050A), titanium (Ti-6Al-4V), and stainless steel (grade 316) end-caps were designed, fabricated, and characterised. Finite element analysis (FEA), electrical impedance analysis (EIA), resonance frequency tracking, displacement amplitude measurements, mechanical quality factor evaluation, and temperature-dependent testing were performed to assess transducer performance. While the conventional metallic transducers generally exhibited reductions in resonance frequency and mechanical quality factor with increasing temperature, the Nitinol transducer demonstrated greater resonance stability and reduced sensitivity to thermal variations. Although distinctive temperature-dependent behaviour was observed, the thermally

induced resonance frequency tuning previously reported for Nitinol-based cymbal transducers was not observed within the flextensional transducer configurations investigated in this study.

To further investigate the influence of shape memory alloy integration, Nitinol wires were incorporated into the flextensional transducers and evaluated using impedance-matching circuitry. The wire-integrated transducers were characterised under varying voltage and temperature conditions to assess changes in resonance frequency, electrical impedance, mechanical quality factor, and power transfer characteristics. The results indicated that wire attachment influenced the electromechanical response of the transducers, while stable operation was maintained.

Ultrasonic surgical cutting was then conducted using the wire-integrated transducers. Cutting experiments were performed on bone-mimicking Sawbones® material while simultaneously monitoring resonance frequency, electrical impedance, phase, and load power. Among the investigated configurations, the Nitinol transducer with wire achieved the greatest measured cutting depth of 627.9 μm and exhibited one of the most stable electromechanical responses during prolonged operation. The titanium and stainless steel transducers with wires produced comparable cutting depths, while the aluminium transducer with wire exhibited the lowest cutting performance. Although the cutting depths achieved were low, the results demonstrated the feasibility of wire-integrated flextensional transducers for ultrasonic cutting applications and provided insight into the relationship between resonance stability and material removal.

Overall, this work demonstrates that Nitinol can be successfully integrated into class IV flextensional ultrasonic transducers and can influence their thermal response, dynamic behaviour, and cutting performance. While controllable frequency tuning was not demonstrated using the investigated configurations, the enhanced resonance stability exhibited by the Nitinol transducers suggests that shape memory alloys remain promising materials for future adaptive ultrasonic devices. The findings provide a foundation for the continued development of smart-material-integrated ultrasonic transducers for surgical and industrial applications.

Acknowledgements

20 *Daniel said, "Let the name of God be blessed forever and ever, for wisdom and power belong to Him.* ***21*** *"It is He who changes the times and the epochs; He removes kings and establishes kings; He gives wisdom to wise men and knowledge to men of understanding.****22*** *"It is He who reveals the profound and hidden things; He knows what is in the darkness, and the light dwells with Him.* ***23*** *"To You, O God of my fathers, I give thanks and praise, for You have given me wisdom and power; even now You have made known to me what we requested of You, for You have made known to us the king's matter." – Daniel 2:20-23.*

First and foremost, all honour, praise, and glory go to the God and Father of my Lord Jesus Christ. I am deeply grateful for His unfailing mercy, and the grace of the Lord Jesus Christ, and the power of the Holy Spirit, which have sustained me through every step of my PhD journey at the University of Glasgow.

I extend my heartfelt gratitude to my wonderful and loving parents (Daddy and Mummy) and my dear sister, Helen Mole, for their unwavering support, encouragement, and prayers. Your love has been my anchor, and your belief in me has given me strength through every challenge. I could not have done this without you.

I would like to express my sincere appreciation to my incredible supervisors, Professor Margaret Lucas and Dr. Andrew Feeney, for their invaluable guidance, support, patience and mentorship. Your expertise, encouragement, and patience have been instrumental in shaping my research and helping me grow into a confident and independent researcher. Margaret, I am especially grateful for the kindness and warmth you showed me when I first arrived in Glasgow. Spending my first Christmas with you, Jess, and Isla, and watching *It's a Wonderful Life* was such a special moment—one that I will always hold dear. It was my first Christmas movie, and thanks to you, it is now a tradition I cherish.

I am deeply grateful to Dr. Martin Hofmann and Professor Jürgen Burger for giving me the opportunity to work with the School of Biomedical and Precision Engineering (SBPE) as a Scientific Associate at the University of Bern. Their trust and support have been invaluable to my professional growth and research journey.

I am also immensely grateful to Dr. Xuan Li for sharing his knowledge, wisdom, and time with me. Xuan, your patience and insights in Lab 391 were invaluable in helping me understand transducer design and characterisation, and your friendship made the lab a place filled with laughter and learning. You have been like an older brother to me, and I wish you every success in your lectureship at the University of Southampton.

To my dear Bunmi, thank you for being a constant source of positivity and kindness. Your smile could brighten any day, and our long walks and deep conversations brought me so much joy.

May God bless you abundantly in all that you do. And Lyne, it has been such a pleasure getting to know you (and, of course, competing for Bunmi's affection). I think we both know who the favourite is now! Wishing you every success and happiness in life.

I would like to express my heartfelt gratitude to the Centre for Medical and Industrial Ultrasonics (C-MIU) for the unwavering support and guidance they provided throughout my PhD journey.

Additionally, I am grateful to Andrew Monaghan from the School of Chemistry for his assistance with DSC, and to Bill Brynes from the Spark Erosion Centre for his support with wire-EDM machining. A special thank you to Wilson Macdougall and Alistair Bell from the mechanical workshop for always being there to help with machining Nitinol parts. Alistair, our conversations in the workshop were always enjoyable, and I greatly appreciated them. I also extend my thanks to Liene Spruzeniece from the School of Geographical and Earth Sciences for her help with EDXS tests.

I would like to express my deep gratitude to Gerwyn Miles and Pastor Chris Collins from Cardiff for their prayers, encouragement, and wisdom. Gerwyn, our monthly conversations were filled with laughter and inspiration, and I always looked forward to them. Your support has meant the world to me.

Finally, a very special thank you to Leejo, Sidharth, and Sanjana, my Glasgow family. The friendships we have built are truly priceless. Thank you for all the laughter, late-night discussions, shared experiences, and the countless movies and series we watched together. You have helped shape me into the person I am today, and you will always hold a special place in my heart. The three of you will forever be my cherished family, no matter where life takes us.

Nomenclature

Symbol	Definition	Base Unit
AAA	Abdominal aortic aneurisms	-
A_F	Austenite finish temperature	°C
ANOVA	Analysis of variance	-
A_P	Austenite peak temperature	°C
A_S	Austenite start temperature	°C
BLT	Bolted Langevin transducer	-
BVD	Butterworth-Van Dyke	-
C_O	Clamping capacitance	F
CAD	Computer aided design	
C_{SE}	Motion capacitance	F
CUSA	Cavitron Ultrasonic Surgical Aspirator	-
d_{31}	Piezoelectric radial charge coefficient	C/N
d_{33}	Piezoelectric longitudinal charge coefficient	C/N

DMA	Dynamic mechanical analysis	-
DSC	Differential scanning calorimetry	-
ε	Engineering strain	-
E	Young's modulus	Pa
E'	Storage modulus	MPa
E''	Loss modulus	MPa
EDXS	Energy dispersive X-ray spectroscopy	-
EDM	Electrical discharge machining	-
EIA	Electrical impedance analysis	-
EMA	Experimental modal analysis	-
f	frequency	Hz
f_a	Anti-resonance frequency	Hz
f_r	Resonance frequency	Hz
F	Applied force	N
FEA	Finite element analysis	-
FFT	Fast Fourier transform	-
HAZ	Heat affected zone	-

hMSC	Human mesenchymal stem cells	-
I	Light intensity	Candela
k_{eff}	Effective electromechanical coupling effect	-
LDV	Laser Doppler vibrometer	-
L_{SE}	Motion inductance	H
M^d	Detwinned martensite	-
M_P	Martensite peak temperature	°C
M_S	Martensite start temperature	°C
M^t	Detwinned martensite	-
NOL	Naval Ordnance Laboratory	-
PAM	Plasma arc melting	-
PZT	Lead zirconate titanate	-
Q_m	Mechanical quality factor	-
R_P	R-phase peak temperature	°C
R_S	R-phase start temperature	°C
s	Displacement	m

SMA	Shape memory alloy	-
SLM	Selective laser melting	-
SME	Shape memory effect	-
Tan (δ)	Damping factor	-
TWSME	Two-way shape memory effect	-
VAM	Vacuum arc melting	-
VIM	Vacuum induction melting	-
V_{p-p}	Peak-to-peak voltage	V
$V_{(rms)}$	Root mean square voltage	V
λ	Wavelength	m
σ	Engineering stress	Pa
σ_F	Detwinning finish stress	Pa
σ_s	Detwinning start stress	Pa
ω_s	Series angular frequency	Rad/s
ω_p	Parallel angular frequency	Rad/s

Contents

Abstract ..... **i**

Acknowledgements ..... **iii**

Nomenclature ..... **v**

List of tables ..... **xii**

List of figures ..... **xiii**

1 Introduction **1**

1.1 Nitinol, its characteristics and applications 2

1.2 Nitinol in power ultrasonics and its challenges 8

1.3 Contributions to knowledge 13

1.4 Brief overview of thesis 15

2 Literature Review **16**

2.1 History of ultrasound 16

2.2 History of ultrasonic surgical devices for bone surgeries 17

2.3 State of the art in ultrasonic surgical devices 21

2.4 Ultrasonic surgical devices: Design 27

2.5 Ultrasonic surgical devices: miniaturisation and its challenges 32

2.6 Evolution of flextensional transducers 33

2.7 The history of SMAs and further applications 44

2.8 Challenges of Nitinol 47

2.9 Machining of Nitinol 51

2.10 Additive manufacturing of Nitinol 53

2.11 Summary of literature and research gaps 55

3 Material characterisation of Nitinol end-caps and wires **57**

3.1 Methodology 57

3.1.1 DSC 57

3.1.2 EDXS of Nitinol end-caps and Nitinol wire specimens 61

3.1.3 Static mechanical characterisation 62
3.1.4 Dynamic mechanical characterisation 65
3.2 Results from experimental characterisations 67
3.2.1 Results from DSC 67
3.2.2 Results from EDXS 75
3.2.3 Results from static tests 84
3.2.4 Results from dynamic tests 89
3.3 Summary 91
4 Design, fabrication and characterisation of a class IV transducer 93
4.1 Methodology 93
4.1.1 Design of class IV transducers 93
4.1.2 Fabrication and assembly of transducers 102
4.1.3 Resonance frequency characterisation 104
4.1.4 Experimental modal analysis 105
4.1.5 Harmonic response analysis 108
4.1.6 Temperature studies 110
4.2 Results from experimental characterisations 111
4.2.1 Results from EIA 111
4.2.2 Results from EMA 117
4.2.3 Results from harmonic response analysis 121
4.2.4 Results from temperature studies 139
4.2.5 Results of Nitinol transducers with A_F of 35 ˚C and 45 ˚C 149
4.3 Summary 157
5 Design, fabrication and characterisation of class IV transducers with wires 159
5.1 Incorporating Nitinol wires to the class IV flextensional transducers 160
5.2 Results from EIA 161
5.3 Results from EMA 165

5.4 Results from harmonic response analysis 167
5.5 Results from temperature studies 179
5.6 Summary 188
6 Performance evaluation of transducers with wires 192
6.1 Impedance matching 192
6.2 Displacement amplitude measurements 196
6.3 Cutting tests using the Nitinol wire 206
6.4 Assessment of cutting penetration in Sawbones material 212
6.5 Summary 215
7 Conclusion and future work 216
7.1 Conclusions 216
7.2 Future work 218
8 References 220

List of Tables

Table 3.1. Wt% compositions of wire face, length and end-cap regions.....82

Table 3.2. Tan delta, storage and loss moduli of Nitinol samples at three different temperatures.....90

Table 4.1. Mechanical properties of end-cap materials and epoxy resin.....98

Table 4.2. Pz26 specimen dimensions and material properties 98

Table 4.3. Electromechanical characteristics of class IV flextensional transducers with different end-cap materials as identified by EIA 112

Table 4.4. Electromechanical characteristics of class IV flextensional transducers with different end-cap materials as identified by FEA 113

Table 4.5. Resonance frequencies of additional vibration modes in the transducers with different end-cap materials as identified by EIA and FEA.....117

Table 5.1. Electromechanical characteristics of class IV flextensional transducers with Nitinol wires from EIA and FEA 165

Table 6.1. Matching network parameters for flextensional transducers.....195

List of Figures

Figure 1.1. The superelastic effect....4
Figure 1.2. The shape memory effect....5
Figure 1.3. The two-way shape memory effect....6
Figure 1.4. Cymbal (class V) transducer....9
Figure 1.5. Langevin transducer....10
Figure 1.6. Evolution of class IV transducer....12
Figure 2.1. Schematic representation of vibration modes in cylindrical rods....18
Figure 2.2. Schematic representation of a torsional vibration mode in a cylindrical rod....21
Figure 2.3. Stryker Sonopet® ultrasonic aspirator....24
Figure 2.4. Misonix BoneScalpel....25
Figure 2.5. Structural layout of bolted Langevin transducer (BLT)....28
Figure 2.6. Non-longitudinal vibration mode in a rod....31
Figure 2.7. The Harmonic scalpel....32
Figure 2.8. Comparison of flextensional architectures....35
Figure 2.9. Mode shapes of the class III flextensional transducer....36
Figure 2.10. Comparison of class V flextensional architectures....38
Figure 2.11. Schematic illustration of symmetric effects in cymbal transducers....40
Figure 2.12. Modified cymbal transducer with commercial cutting insert....41
Figure 2.13. Concept of class IV flextensional transducer with biopsy needle....43
Figure 2.14. Multiple phases of superelastic Nitinol....49
Figure 3.1. Simplified diagram of the DSC setup....58
Figure 3.2. Regions of the Nitinol end-cap from where the 31 cubic samples were taken....59
Figure 3.3. Nitinol dogbone....64
Figure 3.4. Tensile test setup....64
Figure 3.5. Nitinol sample mounted on load cell of DMA 8000....66
Figure 3.6. DSC thermogram of sample #9 (edge region)....68

Figure 3.7. DSC thermogram of samples with additional peaks before/after the A_P 68

Figure 3.8. DSC thermogram of wire sample #1 69

Figure 3.9. DSC thermogram of end-cap sample #1 (Edge region) 70

Figure 3.10. Box and whiskers plots of end-cap regions and wire 71

Figure 3.11. BSE images of end-cap and wire sections.....76

Figure 3.12. Elemental composition of (a-d) wire face spectra 1-4 and (e-h) wire length spectra 7-10. 77

Figure 3.13. Elemental composition of (a-f) end-cap edge spectra 16-21. 78

Figure 3.14. Elemental composition of (a-f) end-cap apex spectra 28-33.. 79

Figure 3.15. Elemental composition of (a-f) end-cap protrusion spectra 46-51.. 80

Figure 3.16. Elemental composition of (a-f) end-cap slanted region spectra 34-39.. 81

Figure 3.17. Stress-Strain relationship for three dogbone samples 85

Figure 3.18. BSE images of dogbone specimens.....87

Figure 3.19. DMA analysis of Nitinol specimen with A_F of 55 ˚C 89

Figure 4.1. Schematic of piezoceramic plate showing generation of longitudinal vibration ..94

Figure 4.2. Schematic representation of the fundamental plate-mode resonances of a rectangular piezoelectric element 95

Figure 4.3. End-cap dimensions for class IV flextensional transducers, dimensions in mm ..96

Figure 4.4. FEA model of the transducer in its symmetric vibration mode.....100

Figure 4.5. Mesh convergence study 100

Figure 4.6. Finite element modal analysis 102

Figure 4.7. A Nitinol class IV transducer 103

Figure 4.8. Schematic of LDV setup 106

Figure 4.9. EMA experimental setup 107

Figure 4.10. Harmonic response analysis experimental setup 108

Figure 4.11. Duffing like behaviour 109

Figure 4.12. Experimental setup for free boundary condition 110

Figure 4.13. Measured impedance magnitude and phase spectra of the flextensional transducers 112

Figure 4.14. FEA predictions of additional vibration modes in the flextensional transducer116

Figure 4.15. EMA, FEA and EIA results of the extensional mode of the piezoceramic plate 118

Figure 4.16. Modal response and frequency of symmetric mode from LDV scans 120

Figure 4.17. Vibrational response of end-cap of flextensional transducer in its symmetric mode.....120

Figure 4.18. Harmonic response analysis results from the transducers 122

Figure 4.19. Maximum displacement amplitudes of the symmetric vibration modes for transducers at incrementally increasing voltage levels 123

Figure 4.20. EMA and EIA of neighbouring asymmetric mode of aluminium transducer ...126

Figure 4.21. Change in the mechanical quality factor as a function of excitation voltage 128

Figure 4.22. Power density of flextensional transducers as a function of excitation voltage 132

Figure 4.23. Electrical impedance measured across excitation voltages 134

Figure 4.24. Change in the resonance frequency as a function of temperature 139

Figure 4.25. Electrical impedance as a function of temperature.....142

Figure 4.26. Mechanical quality factor as a function of temperature 145

Figure 4.27. Resonance frequency of Nitinol transducers as a function of temperature 150

Figure 4.28. Electrical impedance of Nitinol transducers as a function of temperature.....153

Figure 4.29. Mechanical quality factor of Nitinol transducers as a function of temperature 155

Figure 5.1. Transducer and FEA model of a class IV flextensional transducer with a Nitinol wire 162

Figure 5.2. Impedance magnitude of the transducers with and without Nitinol wires 163

Figure 5.3. FEA model of class IV transducer with Nitinol wire at its asymmetric vibration mode.....164

Figure 5.4. Symmetric mode from LDV scans of transducers with and without wires.....167

Figure 5.5. Harmonic response analysis for transducers with and without wires.....169

Figure 5.6. Displacement amplitude as a function of voltage for transducers with wires 170

Figure 5.7. Measurements of the mechanical quality factors as a function of excitation voltage....172

Figure 5.8. Power density of flextensional transducers as a function of excitation voltage..175

Figure 5.9. Electrical impedance as a function of excitation voltage....177

Figure 5.10. Resonance frequency as a function of temperature....180

Figure 5.11. Electrical impedance as a function of temperature....183

Figure 5.12. Mechanical quality factor as a function of temperature....187

Figure 6.1. BVD model at resonance....194

Figure 6.2. Simplified equivalent circuit at resonance of a transducer matched to an electrical source....195

Figure 6.3. Displacement amplitude as a function of excitation voltage for the wire-integrated transducers during continuous excitation....198

Figure 6.4. Impedance magnitude as a function of excitation voltage for the wire-integrated transducers during continuous excitation. 201

Figure 6.5. Resonance frequency as a function of excitation voltage for the wire-integrated transducers during continuous excitation. 203

Figure 6.6. Load power as a function of excitation voltage for the wire-integrated transducers during continuous excitation. 205

Figure 6.7. Parameters varying with time....210

Figure 6.8. Sawbones samples prepared for SEM 214

Figure 6.9. SEM images showing cut depths created by flextensional transducers with wires 214

Chapter 1

Introduction

Ultrasound refers to acoustic waves with frequencies above the range of human hearing, typically greater than 20 kHz [1]. Power ultrasonics focuses on using ultrasonic waves in applications where the ultrasound has a direct and irreversible effect on the medium. Applications include ultrasonic welding, cleaning, drilling and surgical cutting [1-3].

Power ultrasonic devices operate by converting electrical energy into high-frequency mechanical vibrations, which are then coupled into a medium for cutting, drilling or welding [1-3]. In surgical contexts, ultrasonic energy can be delivered to tissues to achieve cutting, coagulation, or fragmentation with high precision and minimal lateral thermal damage [4-6].

There is increasing interest in developing ultrasonic transducers capable of demonstrating multiple tuneable resonance frequencies within power ultrasonics. For example, selectable frequency ultrasonic surgical cutting could be used for cutting through hard and soft tissues which require different cutting frequencies [4-6]. This is valuable in a surgical context because different surgical procedures and tissues respond optimally at different frequencies. For example, hard tissues such as bone typically require lower ultrasonic frequencies (20–35 kHz) for efficient cutting, whereas soft tissues and delicate dissection procedures may benefit from higher frequencies (>50 kHz), which can improve precision and reduce unintended lateral tissue effects. A single device that can adapt its resonance frequency during operation enables a surgeon to perform multiple procedures without changing instruments, ensuring stable and effective operation throughout the procedures [4-6].

One route to achieving tuneability is through the integration of shape memory alloys (SMAs), such as Nitinol, a nickel–titanium alloy. Nitinol exhibits two unique behaviours: the shape memory effect (SME), where the material returns to a pre-defined shape when heated above a transformation temperature, and superelasticity, where large strains can be recovered upon unloading at temperatures above this transformation range [7]. These properties are linked to a phase transformation between austenite (stiff phase) and martensite (comparatively compliant) phases [7].

In biomedical applications, the unique properties of Nitinol are exploited in devices such as vascular stents and thermally activated implants. For example, self-expanding stents are typically designed such that the austenite finish temperature (A_F) lies slightly below body temperature (37 °C), ensuring that the material remains in the austenitic phase in vivo and

exhibits superelastic behaviour, allowing large recoverable strains during deployment and operation [7]. SME based behaviour is utilised in shape-setting implants and orthodontic archwires [8]. In such cases, Nitinol components can be deformed in the martensitic phase at lower temperatures, for example, at room temperature, and subsequently recover their original shape when heated above A_F, which is slightly below body temperature.

In the context of ultrasonic devices, controlled changes in stiffness via thermomechanical stimuli could shift the resonance frequency of the transducer, allowing it to switch between operations, from hard tissue cutting to soft tissue cutting and cauterisation, or from a cutting function to a healing stimulus.

The incorporation of Nitinol into an ultrasonic transducer offers the potential for an adaptable surgical device. This approach could enable a single transducer to perform both low-frequency operations, such as bone cutting, and high-frequency tasks, such as soft tissue dissection or cauterisation.

This chapter discusses ultrasound and outlines its applications, with emphasis on its use in ultrasonic surgical devices and the motivation for developing systems with tuneable operational capability. It then presents the material science of Nitinol, and its key behaviours, including superelasticity and the SME, in relation to temperature- and stress-induced phase transformations. The chapter contextualises these properties through established biomedical applications, highlighting the functional advantages of Nitinol. Building on this foundation, the potential for integrating Nitinol into ultrasonic transducers is explored as a means of enabling controllable stiffness variation and resonance frequency tuning. The chapter briefly discusses the practical challenges associated with machining Nitinol components. Finally, the aims, objectives, and original contributions to knowledge are defined, establishing the scope and direction of the research presented in this thesis.

1.1. Nitinol, its characteristics and applications

Nitinol is widely used in biomedical devices such as vascular stents, orthodontic archwires, and endodontic instruments due to its unique mechanical adaptability, biocompatibility, and corrosion resistance [8-10]. Nitinol has a high level of strain recovery and demonstrates a good resistance to corrosion because of a passive-rich titanium oxide layer formed at the material's surface [9]. Another excellent quality of Nitinol is its ability to withstand high mechanical stress without permanent deformation, due to its superelastic behaviour in the austenite phase. This allows recovery of strains between 6-8% compared to around 0.2% in conventional metals such as stainless steel [7,9].

Precise control of the chemical composition of Nitinol is essential to achieve the desired material behaviour in response to changes in stress and temperature [11]. Nitinol was discovered in 1963 by William Buehler at the U.S. Government Naval Ordnance Laboratory [12]. Buehler observed that the material exhibited remarkable flexibility, allowing it to reopen multiple times without breaking after being folded. Additionally, when his team exposed the folded material to heat from a pipe lighter, it returned to its original shape. These properties intrigued the team, and Buehler named the alloy Nitinol, a blend of "Nickel Titanium Naval Ordnance Laboratory" [7,12]. Fredrick Wang, another member of the Naval Ordnance Laboratory, explained that the unique behaviour of Nitinol is due to atomic rearrangements and phase changes that occur at different temperatures [7,12], as discussed in Figures 1.1-1.3.

The mechanical properties of Nitinol are influenced by both stress and temperature [13-14]. Nitinol undergoes phase transformations between the highly symmetric, rigid austenite phase at high temperatures and the softer martensite phase at low temperatures [15]. The Young's modulus of martensite ranges between 28-41 GPa, while austenite has a Young's modulus of 60-90 GPa. Nitinol typically becomes stiffer as temperature increases [7]. A transformation from austenite to martensite is known as a forward transformation, while a transition from martensite to austenite is called a reverse transformation. These phase transitions occur through a diffusionless shear distortion of the crystal lattice, in which the atoms undergo coordinated shifts from their original positions rather than long-range atomic diffusion [12,15].

The R-phase, a pre-martensite phase, is a distortion of the parent austenite phase. This phase can appear in either twinned or detwinned forms and can be stress-induced [12,15]. The R-phase is commonly seen in nickel-rich Nitinol alloys, especially those cold-worked or subjected to specific heat treatments, typically in the temperature range of 350–500 °C [14]. The rhombohedral R-phase appears when austenite cools to martensite, sometimes during the transition from martensite to austenite.

A range of SMA systems have been developed, including Cu-based alloys, such as Cu–Al–Ni and Cu–Zn–Al, and Fe-based alloys, such as Fe–Mn–Si [7,12,17]. Although these materials exhibit useful shape-memory behaviour, Nitinol provides a particularly favourable combination of large recoverable strain, cyclic durability, corrosion resistance and established biomedical applicability [7–9]. Its biomedical suitability is further supported by the formation of a stable Ti-rich passive oxide layer, which improves corrosion resistance and limits the release of Ni ions from the underlying alloy into the surrounding biological environment [8–10]. At the crystallographic level, the diffusionless lattice rearrangement described above

corresponds to transformation between the ordered cubic B2 structure of austenite and the lower-symmetry monoclinic B19′ structure of martensite [7,12]. The associated change in crystal structure produces temperature-dependent changes in mechanical properties, including elastic modulus and damping, while the transformation temperatures can be tailored through composition and thermomechanical processing [11].

Nitinol exhibits two key properties: superelasticity (or pseudoelasticity) and the SME. Superelasticity is a stress-induced phenomenon that allows Nitinol to show much higher elasticity than typical metals, approximately ten times that of stainless steel [16]. The SME refers to Nitinol's ability to return to its original shape after being deformed, once exposed to a thermal stimulus [17]. These properties have been leveraged in various fields, including aerospace (for vibration damping and actuation components), automotive (for temperature-responsive actuators) and structural engineering (for energy dissipation and seismic dampers) [12,14-15].

The superelastic effect is illustrated in Figure 1.1 using a stress–strain curve for Nitinol at a temperature above A_F [18].

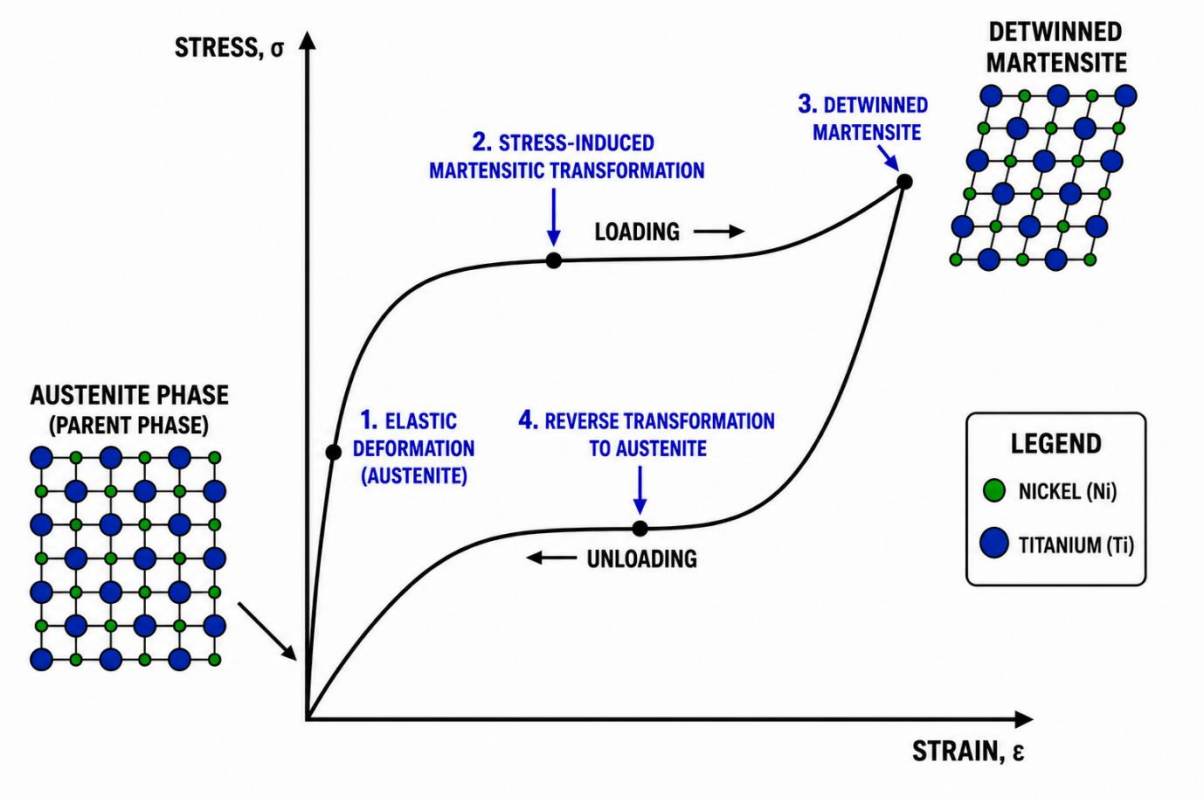


Figure 1.1 - The superelastic effect [18].

The superelastic behaviour of Nitinol begins with elastic deformation of the austenite phase (1), which is the high-temperature, stiff parent phase. With increasing applied stress, a stress-induced martensitic transformation occurs (2), leading to the formation of detwinned martensite (3), a comparatively compliant phase that accommodates large strains through lattice reorientation [19]. This transformed phase remains stable under continued loading. Upon unloading, the reverse transformation to austenite occurs (4) due to the instability of martensite at temperatures above A_F, i.e. in the superelastic regime. This reversible phase transformation enables Nitinol to undergo relatively large deformations, with strains of up to approximately 8% being fully recoverable [19–21].

The principle of the SME is illustrated in Figure 1.2.

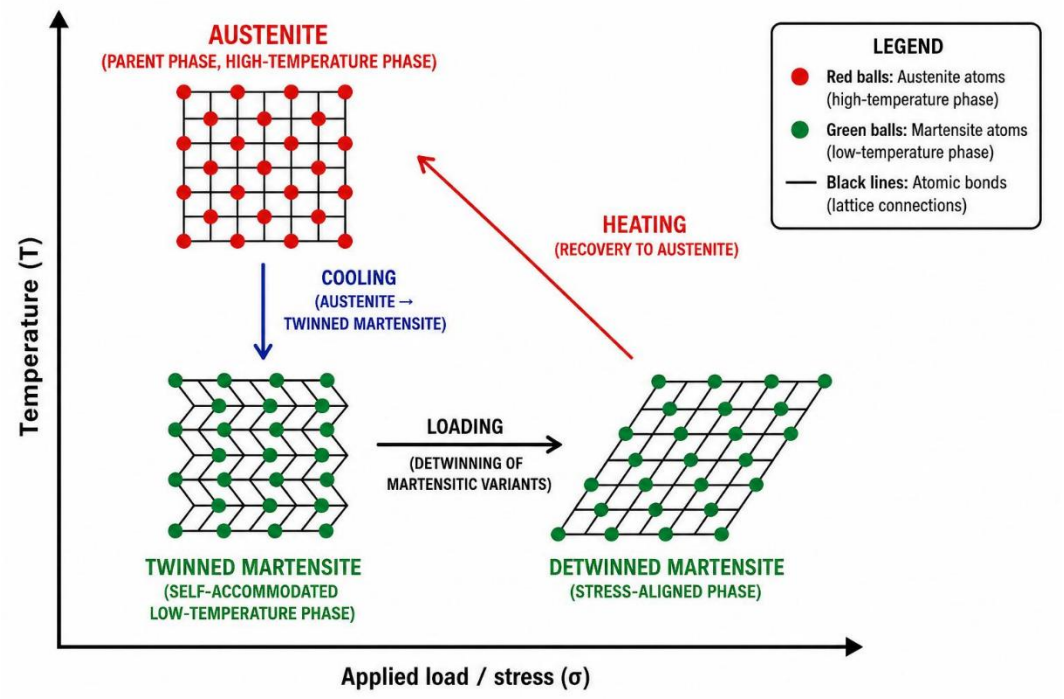


Figure 1.2 - The shape memory effect [19].

The SME in Nitinol begins with the high-temperature austenite phase. Upon cooling, the material transforms into twinned martensite, a low-temperature, self-accommodated phase composed of multiple martensitic variants that minimise macroscopic strain [17]. When an external load is applied, these variants reorient through a detwinning process, forming detwinned martensite and resulting in observable macroscopic deformation. This deformation is retained after unloading, as the material remains in the martensitic phase at low temperature. Upon subsequent heating above the A_F, the reverse transformation to austenite occurs, enabling

recovery of the original shape. This thermally driven phase transformation underpins the SME, allowing Nitinol to recover significant imposed strains through heating [17,19].

Sometimes an SMA can exhibit repeatable shape changes when subjected to a cyclic thermal load. This behaviour is called the two-way shape memory effect (TWSME). The TWSME, Figure 1.3, is usually found in SMAs that have undergone training, which involves repeated thermomechanical cycling (alternating heating and cooling under controlled loading conditions) to condition the material to memorise distinct shapes in both martensite and austenite phases [12].

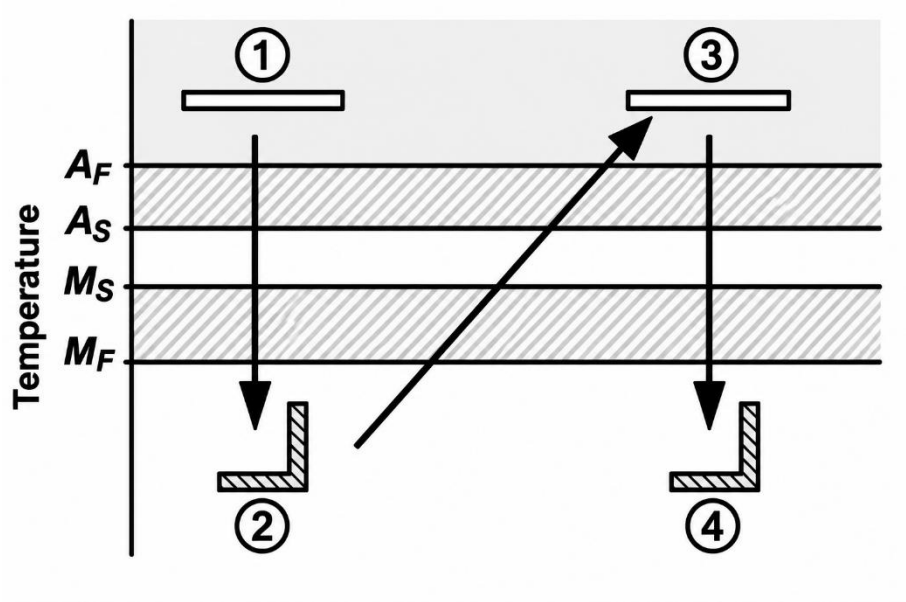


Figure 1.3 - The two-way shape memory effect [17].

At ①, the sample is above the A_F temperature. The sample is cooled and causes a phase change from austenite to martensite, leading to a shape change at ②. The temperature is increased above the A_F temperature from ② to ③. Cooling returns the sample to its low-temperature shape at ④.

Nitinol was first implemented in the biomedical field in 1975 by Dr. Andreasen in an implantation of an orthodontic device [8]. In orthodontics, Nitinol archwires exploit the superelastic effect to maintain an almost constant corrective force over a wide range of tooth displacement. This property allows gradual, controlled movement of teeth, such as in cases of overcrowding in the mandible region, without frequent re-tightening. Compared with stainless steel wires, Nitinol archwires reduce patient discomfort and improve treatment efficiency by sustaining optimal force levels for extended periods. Another example of a

Nitinol-based medical application is the Homer Mammalok ® which was introduced in the 1980s and was the first commercial Nitinol medical device used for breast tumour localisation. The Homer Mammalok ® breast lesion localisation device utilises a Nitinol wire formed into a pre-set hooked shape. During insertion through a fine needle, the Nitinol wire is temporarily straightened, taking advantage of its superelastic behaviour to withstand high strain without permanent deformation. Once deployed, it returns to its memorised hook shape, securely anchoring in the target tissue. This allows precise localisation of lesions prior to surgical excision, minimising patient discomfort and tissue trauma [8].

The first Nitinol-based implant was the Mitek ® bone anchor [8]. This implant is used in orthopaedic and sports medicine surgery to attach soft tissues like tendons or ligaments to bone. The Mitek ® bone anchor incorporates Nitinol elements that can be compressed for insertion through a small pilot hole and then expand to their memorised configuration within the bone. This deployment uses Nitinol's superelasticity for deformation during insertion and its SME for returning to the pre-set shape within the body. The result is secure soft-tissue-to-bone fixation with minimal bone removal and reduced risk of fracture compared to traditional screw-type anchors [8].

Within the orthopaedic field, Nitinol rods have been incorporated into corrective devices for scoliosis to enable gradual realignment of the vertebrae [22]. This recovery refers to the material's ability to return to its original shape following deformation. In physiotherapy applications, Nitinol-based actuators have been investigated to support partially atrophied muscles by acting as artificial contractile elements [17]. When heated above their transformation temperature, the rods undergo a shape recovery process, shortening along their length. This reduction in length generates a tensile force analogous to muscle contraction. Upon cooling, the material returns to its deformed configuration, allowing for repeated contraction -relaxation cycles during functional rehabilitation. Porous Nitinol foams have been used for the osteointegration process because of the properties that they possess: good mechanical stability within the host tissue, high strength (to prevent deformation or fracture), relatively low stiffness (to minimise stress shielding effects) and high toughness (essential to avoid brittle behaviour) [23].

In the vascular field, Nitinol has been used in self-expandable vascular stents. Stents have been used to open stenotic vessels (obstructed by atherosclerotic deposits) to provide blood supply to peripheral tissues. Stent-grafts have also been used to treat abdominal aortic aneurisms (AAA) [24]. The stent-graft can be crimped onto the catheter and is flexible during insertion. The graft returns to its original shape, anchoring to the aorta once appropriately placed [25].

Nitinol stents are also used for treating intracranial atherosclerotic disease. The stent recovers the original blood flow where there is a narrowed lumen. Nitinol coils have been used to treat cerebral aneurysms where the coils have been positioned into the aneurysms as a ball to induce clotting, which can remove the risk of rupture [26].

1.2. Nitinol in power ultrasonics and its challenges

In recent years, Nitinol has been integrated into flextensional transducer designs, such as the cymbal transducer (class V), as shown in Figure 1.4. The piezoceramic disk is the active element, generating mechanical strain in response to an applied electric field. The metallic end-caps and epoxy bonding layers are passive components that do not exhibit electromechanical coupling [27-28]. The end-caps act as mechanical amplifiers, converting radial deformation of the piezoceramic into flexural motion, while the epoxy layer facilitates efficient load transfer between components [27-28].

Previous studies have explored the incorporation of Nitinol into the end-caps of cymbal transducers to investigate their frequency tuneability in response to thermal stimuli [27-30].

A flextensional transducer can be viewed as a mechanical shell powered by an internal piezoelectric element, although some early variants also utilised magnetostrictive materials (Terfenol-D) for enhanced power handling and magnetic-to-mechanical energy conversion [31]. A cymbal transducer consists of two dome-shaped metal end-caps and a piezoceramic disk that is poled in the thickness direction. The end-caps are bonded to the disk using epoxy resin. Initially, cymbal transducers were employed as moderate- to high-power underwater projectors and later adapted for use as hydrophones in shallow water applications (less than 200 metres) [30-31]. These transducers were modified for high-pressure environments and have since been used in arrays for transdermal drug delivery through the sonophoretic effect [32] and in energy harvesting applications [33].

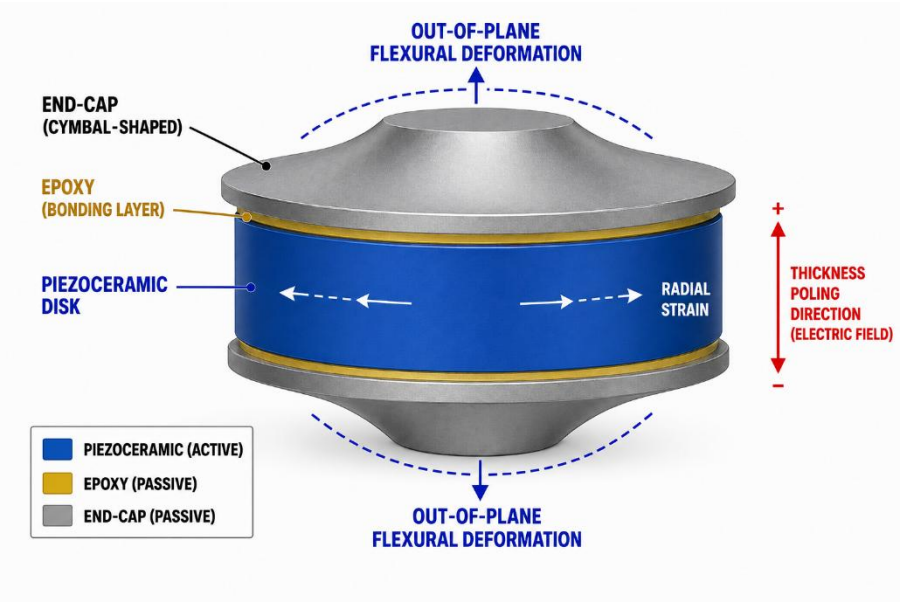
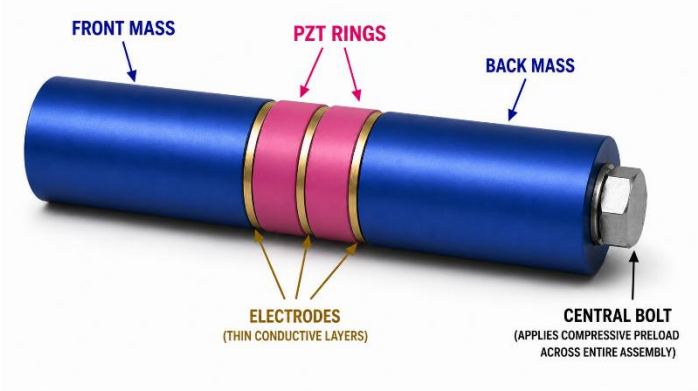
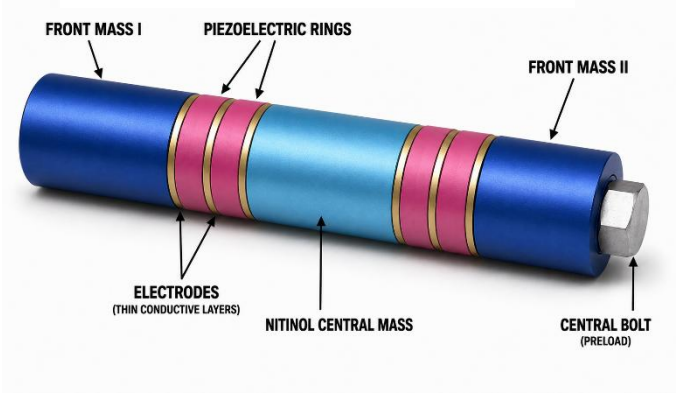


Figure 1.4 - Cymbal (class V) transducer.

In addition to flextensional transducer configurations, Nitinol has been incorporated in a version of the Langevin transducer configuration called the cascaded Langevin transducer, Figure 1.5b. [34-35]. The standard Langevin transducer is shown in Figure 1.5a. The standard bolted Langevin transducer comprises a stack of piezoelectric rings sandwiched between two metal masses under compression with a centrally aligned bolt. The cascaded Langevin transducer [34-35], Figure 1.5b, comprises four lead zirconate titanate (PZT) rings arranged as two stacks on either side of a central mass. In this case, a central Nitinol ring mass was used. The standard cascaded Langevin transducer has been used in semiconductor wire bonding and metal machining industrial applications. More recently, the introduction of Nitinol into the central mass of the transducer has been explored for thermal tuning [34-35]. These studies demonstrated minimal resonance frequency drift in the Nitinol transducer under varying thermal stimuli demonstrating its potential for use in hostile environments such as in cryogenics (space instrumentation or liquefied gas systems) or high-temperature welding [34].



(a) Standard Langevin transducer.



(b) Cascaded Langevin transducer incorporating Nitinol.

Figure 1.5 - Langevin transducer.

Within the field of power ultrasonics, flextensional transducers (Class V) have been investigated for high-power applications such as ultrasonic surgical cutting [36]. In ultrasonic transducers, a mode refers to a specific pattern of vibration (mode shape) that the structure exhibits at a particular resonant frequency. Each mode is characterised by a distinct displacement distribution and deformation behaviour across the transducer [27]. Conventional Langevin transducers, Figure 1.5, typically operate in a longitudinal (axial) mode, where displacement occurs along the axis of the device. Flextensional transducers like the cymbal transducer, Figure 1.4, utilise flexural (bending) deformation of the end-caps to generate displacement [27-28]. Integrating Nitinol enables mechanical tuning of the primary operating mode's resonance frequency through temperature-induced stiffness changes. This preserves the desired mode shape and displacement profile while shifting the frequency, allowing the same optimised surgical mode to be adapted for different tissues without altering the transducer structure or attachments [27-30].

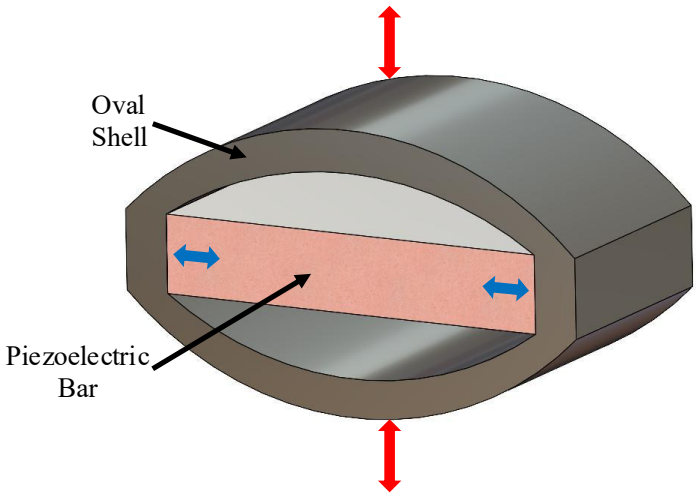
Although progress has been made with the class V cymbal, it has been reported that enhanced vibration performance can be achieved through the class IV, when compared per unit volume of piezoelectric material in the configuration [37].

Among the seven recognised flextensional transducer configurations, which will be discussed in detail in section 2.6 of the thesis, the class IV design (Figure 1.6a) is one of the most widely studied due to its ability to achieve significant displacement amplification [38-39]. In this configuration, a longitudinally driven piezoelectric actuator is coupled to an outer shell structure, which converts axial motion into flexural deformation. The piezoelectric element typically operates in a longitudinal mode, generating axial displacement that is transferred to the shell [38-39]. Due to the geometry of the structure, this axial input produces amplified flexural motion of the shell, resulting in increased output displacement. This mode conversion mechanism enables efficient vibration amplification while maintaining a compact design, making class IV transducers suitable for applications requiring high displacement at relatively low frequencies [38].

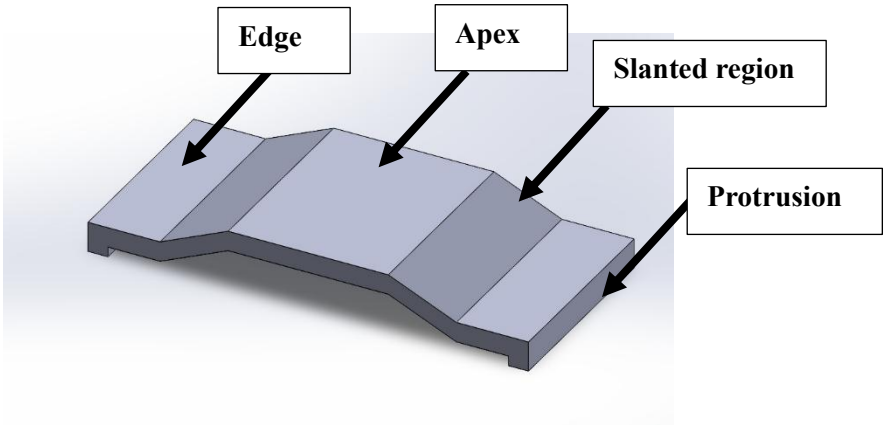
The class IV transducer has successfully been used in low-frequency underwater applications [38]. The first recorded occurrence of the class IV transducer was a patent filed termed 'Sound Generating and Directing Apparatus' by Hayes in 1936 [39-40]. The class VII transducer is visually similar to the class IV transducer except that the shell is inverted [39].

The traditional class IV transducer, Figure 1.6a, comprises a longitudinally driven piezoelectric bar which drives an oval-shaped shell. The small longitudinal vibration displacement of the driving element causes a much higher flexural displacement of the shell, which provides significant vibration amplification [39].

Materials that are used in the end-caps for underwater applications are usually high-strength aluminium, glass reinforced plastic (GRP) and steel. The piezoelectric material is usually Type I (PZT-4) or Type III (PZT-8) [37]. For this research, the oval shaped end-caps were modified to the end-caps shown in Figure 1.6b.



(a) Schematic of the traditional class IV flextensional transducer, showing an oval metallic shell (flexural motion, red arrows) enclosing a piezoelectric bar (extensional motion, blue arrows).



(b) Modified class IV end-cap.

Figure 1.6 - Evolution of the class IV transducer.

The inspiration, benefits and dimensions of the end-cap design is discussed in Chapter 4. The end-cap in Figure 1.6b is split into four sections (protrusions, edge, apex and slanted regions) for material thermal characterisation studies, which are discussed in Chapter 3. The modified end-cap design was previously used for developing an ultrasonic bone biopsy needle [41].

Nitinol presents significant challenges in machining, particularly for use in ultrasonic transducers. One of the main reasons is the titanium oxide layer that naturally forms on the surface of the material. This oxide layer, combined with the inherent hardness of Nitinol, requires high cutting forces to either remove or deform the material. As a result, machining Nitinol can wear cutting tools, leading to frequent tool replacements [42-44]. Another factor in

machining Nitinol is the thermal stress it generates. Being an SMA, Nitinol is highly sensitive to temperature, and thermal cutting methods like laser cutting introduce a heat-affected zone (HAZ), which can alter the microstructure through grain growth, residual stress formation, and changes in local composition [43-44]. Additionally, oxidation during thermal processing can degrade surface integrity. These effects can impair the material's ability to exhibit shape memory and superelastic behaviour, reducing its functional performance in applications. Waterjet cutting does not generate as much heat, reducing the risk of thermal damage. Producing small structures from thin Nitinol sheets with waterjet cutting is problematic, resulting in poor surface integrity and quality of Nitinol [43-44].

For the study of shape memory Nitinol cymbal transducers, the Nitinol end-caps were produced through cold-rolling, allowing for a precise austenitic transformation temperature of 60 ± 10 °C [18]. Superelastic cymbal end-caps were fabricated using shape-set annealing [18], a thermomechanical process in which the Nitinol is heated to a prescribed temperature while constrained in a die to define its final geometry. This process enables the material to retain its shape upon unloading and ensures that the A_F is below the operating temperature, allowing the end-caps to exhibit superelastic behaviour [18]. As a result, the caps can undergo repeated flexural deformation with large recoverable strains, which is advantageous for ultrasonic applications involving cyclic loading.

In this research, the Nitinol end-caps for the class IV flextensional transducer were machined using wire-electrical discharge machining (wire-EDM). Wire-EDM is a contactless manufacturing method that removes material through heat generated between the workpiece and the electrode [45-46]. Wire-EDM provided precise, accurate machining and a smooth surface finish. Minor inaccuracies in the machining of the end-caps can significantly affect transducer dynamics, hence tight tolerance is essential to ensure precise alignment of components and stable vibration performance in the transducer.

1.3. Contributions to knowledge

In this study, Nitinol is incorporated into the class IV transducer design for the first time [47]. The transducer's design and fabrication, and the resulting dynamic performance are explored. The original contributions to knowledge are:

1. Incorporating Nitinol into the class IV flextensional transducer for power ultrasonic applications such as ultrasonic surgery. Comparing the dynamic performance of a Nitinol class IV transducer against three geometrically identical class IV ultrasonic transducers with end-caps made from conventional metals: aluminium (1050A),

stainless steel (grade 316) and titanium (Ti-6Al-4V). The vibration characterisation methods involve electrical impedance analysis (EIA) measurements, experimental modal analysis (EMA) and harmonic response analysis. Finite element models of the four class IV transducers showed close correlation with the experimental results.

2. Analysing the challenges of fabricating a Nitinol class IV transducer using the wire-EDM method. Differential scanning calorimetry (DSC) shows the extent to which the thermal profiles of the Nitinol end-caps are affected by the wire-EDM method. Additionally, energy dispersive X-ray spectroscopy (EDXS) tests are conducted on Nitinol end-cap specimens to investigate how the elemental composition across different regions of the Nitinol end-cap influences the transformational characteristics at locations on the Nitinol end-cap.
3. Comparing the dynamic performance of a Nitinol class IV transducer with a Nitinol wire with three geometrically identical devices with end-caps made from conventional metals, which also incorporate Nitinol wires: aluminium (1050A), stainless steel (grade 316) and titanium alloy (Ti-6Al-4V). The vibration characterisation methods involve finite element models, electrical impedance analysis (EIA), experimental modal analysis (EMA) and harmonic response analysis.
4. Temperature and excitation voltage studies investigate how parameters like resonance frequency, electrical impedance and mechanical quality factor (Q_m) relate with temperature and voltage, for transducers with and without Nitinol wires. DSC of the wire specimens characterises the temperature-dependent phase transformation behaviour of the material, enabling its relationship with the ultrasonic transducers' vibration response to be investigated.
5. Surgical cutting tests using Sawbones bone mimic samples to analyse and compare the performance of the transducers with wires. Tests are conducted with continuous excitation and impedance matching. Resonance frequency, load power, electrical impedance and electrical phase are monitored. The cut depths of the Sawbones samples are measured using scanning electron microscopy (SEM).
6. Development of a complete material characterisation procedure for Nitinol, incorporating static and dynamic testing. Static tensile tests determine ultimate tensile strength, stress–strain behaviour, and fatigue-relevant deformation limits. Dynamic mechanical analysis (DMA) measures storage modulus, loss modulus, and damping across temperatures, directly linking these properties to ultrasonic device performance.

These tests clarify how Nitinol's thermomechanical response under cyclic loading affects its suitability for frequency-tuneable ultrasonic transducers [13-14,48].

1.4. Brief overview of thesis

This thesis investigates the design and development of class IV flextensional ultrasonic transducers for surgical applications, with a focus on integrating Nitinol to enable tuneable resonance behaviour. Chapter 2 reviews ultrasonic transducer technologies, including Langevin and flextensional designs, as well as surgical device architectures and the material behaviour of SMAs. Chapter 3 examines the material characterisation and mechanical response of Nitinol under relevant conditions. Chapter 4 presents the baseline design, modelling and fabrication of a class IV transducer. Chapter 5 explores the integration of Nitinol wire attachments for potential adaptive frequency tuning. Chapter 6 evaluates the performance of the developed transducers in surgical cutting applications. Chapter 7 summarises the key findings and outlines future work.

Chapter 2

Literature Review

2.1. History of ultrasound

Acoustics, the scientific study of sound, traces its origins back to ancient Greece. Thinkers like Pythagoras explored sound through mathematical principles, reportedly fascinated by the noise produced by blacksmiths working with hammers on anvils. Two centuries later, Aristotle proposed that sound propagates as waves [49-50].

Galileo explored the relationship between the pitch of a vibrating string and its length, connecting the frequency of vibrations to the pitch [51]. The English mathematician Brook Taylor later contributed a dynamic solution for understanding the frequency of a vibrating string based on its curve of the fundamental mode of vibration [52].

In the early 19th century, Laplace built upon Newton's work from 1687 to develop the first precise formula for calculating the speed of sound in air [53]. The first reasonably accurate measurement of sound speed in air (within 1% of current standards) was conducted at the Paris Academy in 1798. In 1808, Biot made the first accurate measurement of the speed of sound in an iron rod and in 1826 Swiss physicists Colladon and Sturm achieved a precise measurement of sound speed in water by using an underwater bell in Lake Geneva [54-55].

By the mid-1800s, studies on human and animal hearing thresholds were underway. In 1830, Savart used a toothed wheel to produce sounds with frequencies up to and exceeding 20 kHz to investigate the limits of human hearing and pitch perception [56]. Later, in 1899, Keonig conducted more comprehensive research on human hearing thresholds, developing tuning forks with frequencies ranging from 16 Hz to 90 kHz. Keonig also invented the wave siren in 1867, a device further developed in the 19th and 20th centuries to study acoustic phenomena such as beats and pitch discrimination [57-58].

The field of acoustics saw its most influential publication in 1877 when Lord Rayleigh's work explored both optics and acoustics, providing a mathematical foundation for understanding sound waves [59].

The birth of ultrasonics can be traced back to Galton’s whistle. Significant technological advancements followed with the discovery of the piezoelectric effect in Rochelle salt and quartz crystals by Pierre and Jacques Curie in 1880 [60]. The Curie brothers demonstrated that certain non-centrosymmetric crystals generate an electric charge when subjected to mechanical stress, a phenomenon known as the direct piezoelectric effect. Following Lippmann’s

theoretical prediction in 1881, the converse piezoelectric effect was subsequently demonstrated, whereby an applied electric field produces mechanical deformation within the material [61]. These coupled electromechanical effects form the fundamental operating principle of modern piezoelectric ultrasonic transducers, enabling the conversion of electrical energy into mechanical vibrations and vice versa. Magnetostriction, first observed by Joule in 1842, also contributed to the development of ultrasonic technology [62]. Magnetostriction is the property of certain ferromagnetic materials to undergo a change in dimensions when exposed to a magnetic field, allowing electrical energy to be converted into mechanical vibration. Prior to the widespread adoption of piezoelectric materials, magnetostrictive transducers were among the earliest devices used for the generation of ultrasonic waves [62].

The 20th century saw further advances in ultrasonics, driven by two pivotal events: the sinking of the Titanic and the onset of World War I [63]. These events highlighted the need for underwater detection and led to innovations such as Paul Langevin's hydrophone system. Langevin, a former PhD student of Pierre Curie, developed the first hydrophone using quartz crystals sandwiched between steel plates, with a resonance frequency of 150 kHz. However, this design required large volumes of quartz crystals and high voltage levels.

Langevin refined this work using quartz crystals and high voltage excitation, leading to the development of one of the first practical ultrasonic transducers for naval detection during World War I [64]. Modern bolted Langevin transducers (BLTs), described in Section 1.2, are a later development that build upon this principle using piezoceramic materials and a prestressed assembly.

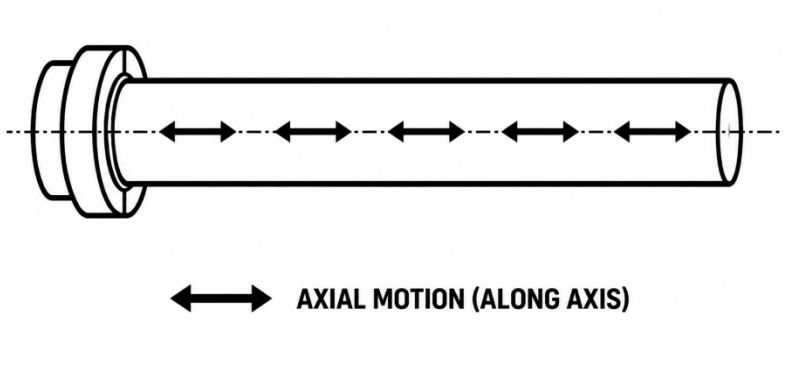
After World War I, Langevin and Chilowsky advanced echo-ranging technology using piezoelectric transducers in water for submarine detection. However, a significant downside was the large number of dead fish resulting from the ultrasonic waves, which led to the implementation of safety measures for ultrasonic technologies [64].

Sokolov contributed to the field using piezoelectric resonators for flaw detection in structures [53]. Wood and Loomis later advanced power ultrasonics by developing an ultrasonic oscillator tube for applications such as drilling, heating, and surface treatment [65].

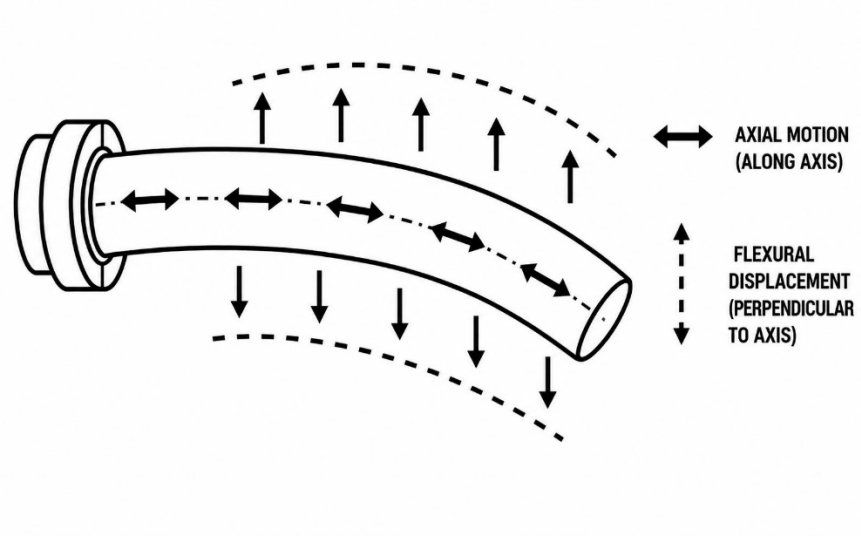
2.2. History of ultrasonic devices for bone surgery

Ultrasonic devices were first developed for bone surgery during the 1950s, particularly in dentistry. One early example was an ultrasonic industrial impact grinder, patented by Balamuth and used by Catuna to drill extracted teeth. A magnetostrictive Langevin transducer excited longitudinal vibrations in a straight cutting tip and longitudinal-flexural vibrations in a curved

cutting tip [66-67]. Figure 2.1 is a schematic representation of the longitudinal and longitudinal–flexural vibration modes in straight and curved tips.



(a) Longitudinal mode.



(b) Longitudinal-flexural mode.

Figure 2.1 - Schematic representation of vibration modes in cylindrical rods.

A longitudinal vibration mode (Figure 2.1a) refers to motion occurring parallel to the axis of the transducer, where the structure undergoes axial oscillation along its length. Longitudinal–flexural vibration (Figure 2.1b) involves a combination of axial motion and bending deformation, typically arising in curved or asymmetric structures where axial excitation induces flexural displacement.

These ultrasonic dental devices offered several advantages over traditional mechanical and pneumatically driven tools, such as reduced pressure on the operation site, enhanced patient comfort, and minimal tissue heating. However, their use was short-lived due to factors like

high device cost, the need for an abrasive paste that obscured the dentist's view of the cutting site, and the rise of high-speed turbine devices developed around the same time [68].

Despite the early setbacks, ultrasonic dental devices saw greater success with development of the dental descaler. The Dentsply-Cavitron descaler became a standard in dental practice, offering a highly effective method for treating dental calculus. Using ultrasonic vibrations with a small tip and adding an irrigation flow to cool the tip, improved patient outcomes by reducing bleeding, pain, and operator fatigue, eliminating the need for heavy scraping [69].

The 1950s also marked the introduction of ultrasonics in neurosurgery through the development of high-intensity focused ultrasound (FUS). FUS is a technique in which ultrasonic waves are concentrated at a focal point within tissue to generate thermal or mechanical effects, enabling precise ablation without the need for open incisions. In 1954, Lindstrom began experiments using FUS irradiation through a burr hole in the skull, achieving targeted lesions without scarring or permanent structural damage to surrounding tissue [70]. The Fry brothers expanded this work by demonstrating the use of high-intensity ultrasound for craniotomies in animal models, and Meyers later conducted the first human neurosurgical procedure using ultrasound [70–71]. While FUS operates through localised heating or cavitation effects rather than the large-amplitude mechanical vibrations employed by power ultrasonic surgical devices, its emergence illustrates the diversity of ultrasonic modalities in medicine and highlights the potential for ultrasound-based approaches to achieve surgical precision with minimal collateral damage [70].

The 1960s brought significant innovations in ultrasonic surgical devices, particularly for phacoemulsification, where a Cavitron unit was adapted for emulsifying the lens in cataract surgeries [72]. During the same period, ultrasonic saws were developed for cutting through bone without requiring abrasive paste. Animal studies by Mararow [67] and McFall [68] compared ultrasonic saws with electric and pneumatic saws, revealing that ultrasonic saws offered advantages such as greater precision and reduced soft tissue damage. However, drawbacks included slow material removal and slower post-operative healing rates. These issues were addressed using saline solutions to lower cutting temperatures and improve healing [73-74].

Throughout the 1970s and 1980s, ultrasonic devices were increasingly recognised for their high precision in cutting procedures. Research by Horton and Aro highlighted some limitations, such as overheating devices and the need to manually adjust the optimal operating frequency [75-77].

In 1974, Volkov documented the first use of an ultrasonic device in human osteotomies after 311 clinical procedures in 1969. The ultrasonic device operated in the 25–30 kHz frequency range, and featured an exponentially shaped horn and a chisel-like cutting tip. This allowed for small incisions, and reduced soft tissue damage compared to conventional bone-cutting tools. However, Volkov noted that the ultrasonic device did not improve the regeneration rate of surgical sites [78].

During the late 1970s, the Cavitron ultrasonic surgical aspirator (CUSA) was developed for soft tissue removal, particularly in open surgeries to dissect and remove diseased tissues [79–80]. CUSA operates by using high-frequency ultrasonic vibration to fragment soft tissue, which is simultaneously aspirated, allowing selective removal while preserving surrounding structures. In the late 1980s and early 1990s, ultrasonic technology was further adapted for soft tissue cutting and vessel sealing, with vibrating surgical tips used as controlled heating sources. Another application was in body contouring, where ultrasonic energy was used to break down subcutaneous fat deposits, facilitating extraction and reimplantation in other areas [80]. This became popular in liposuction procedures, reducing postoperative pain, bleeding, bruising, and operator fatigue [81–82].

Technological advancements in the 1980s and 1990s focused on improving ultrasonic device design, particularly through developments in driving electronics. These included automatic frequency tracking to maintain operation at resonance under varying loading conditions, where vibration amplitude is maximised. The tip velocity, v, is related to the excitation frequency, f, and displacement amplitude, A by equation 2.1 [58-59].

$$v = 2\pi fA \qquad (2.1)$$

Equation 2.1 highlights the importance of frequency control in achieving high vibration amplitudes. The acoustic power output, P is proportional to the square of the displacement amplitude, A, as expressed as:

$$P=kA^2 \qquad (2.2)$$

Where k is a proportionality constant. Equation 2.2 demonstrates that increases in displacement amplitude result in a corresponding quadratic increase in acoustic power output, meaning that even relatively small increases in amplitude can significantly enhance cutting efficiency [83]. Modulated pulse excitation techniques were also introduced to improve power delivery and enable greater control over vibration amplitude. These developments increased cutting efficiency and reduced the likelihood of tip stalling during surgery [81-83].

In the mid-1990s, piezoelectric transducers replaced magnetostrictive ones in most ultrasonic surgical devices, simplifying system design and improving operational efficiency. Earlier systems often required internal cooling mechanisms to prevent overheating and maintain stable operating temperatures. However, the improved electromechanical efficiency of piezoelectric transducers reduced heat generation, thereby minimising the need for such cooling systems and lowering the risk of cross-contamination between saline solutions and cooling fluids [83].

2.3. State of the art in ultrasonic surgical devices

Ultrasonic surgical devices have become integral tools in modern operating theatres due to their ability to deliver precise, energy-efficient cutting and coagulation while minimising thermal injury and mechanical trauma to surrounding tissues. These devices typically operate in the range of 20–60 kHz, which are transmitted through a surgical tip to interact with target tissue. Depending on the design, the mechanical motion at the tip can be longitudinal (Figure 2.1a), torsional (angular oscillation about the central axis as shown in Figure 2.2), or a composite mode (coupling of fundamental modes), each optimised for specific surgical applications such as tissue dissection, bone cutting, or vessel sealing.

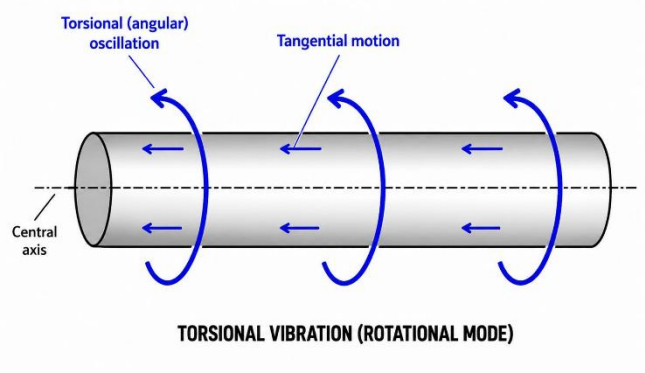


Figure 2.2 - Schematic representation of torsional vibration in a cylindrical rod where the structure undergoes angular oscillation about its central axis, resulting in rotational motion with no net axial displacement.

The development of advanced transducer configurations, improved coupling mechanisms, and optimised tip geometries has enabled ultrasonic surgical systems to achieve higher efficiency, broader versatility, and greater procedural safety [4].

Cavitron Ultrasonic Surgical Aspirator (CUSA®) – The CUSA, originally developed for neurosurgery, uses low-frequency ultrasonic vibrations to fragment soft tissue while simultaneously irrigating and aspirating the surgical field [79]. This combination allows for selective tissue removal, as softer pathological tissue emulsifies more readily than surrounding

healthy structures, reducing the risk of unintended damage. Modern CUSA systems have been adapted for liver resection, tumour debulking, and spinal procedures, with adjustable power settings enabling control over the extent of tissue fragmentation [79].

Harmonic Scalpel® (Ethicon) – Widely used in laparoscopic and open surgical procedures, the Harmonic Scalpel converts ultrasonic vibrations into rapid longitudinal motion at the blade tip, enabling simultaneous cutting and coagulation. The Harmonic Scalpel seals vessels via protein denaturation from mechanical energy and frictional heat, typically at lower peak temperatures. This results in reduced lateral thermal spread and minimal smoke generation, improving visibility within the surgical field [84]. The device has been reported to seal vessels up to 5 mm in diameter reliably, making it particularly valuable in gastrointestinal, gynaecological, and endocrine surgeries.

Piezosurgery® (Mectron S.p.A.) – Developed in 2001 by Dr. Tomaso Vercellotti in collaboration with Mectron S.p.A, the Piezosurgery device uses modulated ultrasonic microvibrations (typically in the range of 25–30 kHz) to selectively cut mineralised tissues while preserving adjacent soft tissues such as nerves and blood vessels [85]. The cutting action is based on the principle that bone, due to its higher density and stiffness, resonates efficiently at these frequencies, whereas soft tissue does not respond to the oscillations and is largely unaffected. The device operates with amplitude modulation between 60 and 210 μm, allowing precise control of cutting depth and speed depending on the bone density [86-87]. Continuous peristaltic irrigation cools the surgical site, maintaining tip temperatures below thresholds that could cause thermal necrosis (>47°C), while simultaneously clearing debris to improve visibility. Piezosurgery is widely used in dental implantology, periodontics, orthognathic surgery, maxillofacial reconstruction, and spinal procedures. Clinical advantages over rotary and oscillating instruments include improved intraoperative visibility, reduced intraoperative bleeding due to cavitation-induced haemostasis, and smoother postoperative healing with less inflammatory response. The combination of precision, tissue selectivity, and safety has made Piezosurgery a preferred choice in anatomical regions where critical neurovascular structures are in close proximity to bone-cutting sites [85-87].

Other Commercial Ultrasonic Devices – Other commercial ultrasonic devices, such as those developed by Söring GmbH, are employed in neurosurgery and liver surgery, offering modular platforms with interchangeable handpieces and tips optimised for different tissue types. The selection of an appropriate tip is governed by several factors, including tip geometry, size, and operating amplitude, which must be matched to the mechanical properties of the target tissue. For instance, smaller-diameter tips with lower vibration amplitudes are preferred for soft and

delicate tissues, such as in neurosurgical applications, where precise control and minimal mechanical trauma are required. Larger and more robust tips operating at higher amplitudes are used in hepatic surgery to enable efficient parenchymal transection of denser and more fibrous tissue [88-89]. Tip geometry also plays a role, with straight tips favouring predominantly longitudinal motion and curved tips introducing longitudinal–flexural vibration, improving accessibility and cutting efficiency in complex anatomical regions. This modularity allows surgeons to tailor the mechanical response of the device to specific surgical requirements without altering the core ultrasonic generator, thereby improving workflow efficiency and expanding clinical versatility [88–90].

The Sonopet® Ultrasonic Aspirator (Stryker), Figure 2.3, is designed for precision bone removal and soft tissue aspiration in neurosurgery, maxillofacial, and orthopaedic procedures. It operates at selectable frequencies of 25 kHz or 35 kHz, depending on the handpiece and application. At 25 kHz, the device produces higher amplitude, lower frequency vibrations suited to cutting dense cortical bone, while 35 kHz delivers finer, more rapid oscillations optimised for softer or more delicate tissues. The Sonopet employs a hybrid vibration profile combining longitudinal (Figure 2.1a) and torsional modes (Figure 2.2). The hybrid vibration profile arises from the superposition of longitudinal and torsional vibration modes [91-92]. The combination of these motions results in a coupled trajectory at the tip, often described as elliptical or helical, rather than purely linear. This hybrid motion enhances cutting performance by simultaneously generating normal and shear stresses at the tool–tissue interface, improving material removal efficiency while reducing the required axial force. This combination allows for controlled, efficient removal of mineralised tissue without excessive force, which is particularly important in confined anatomical spaces such as the skull base. It integrates irrigation, aspiration, and ultrasonic fragmentation in a modular handpiece system [91-92]. Its tips are engineered for both bone and soft tissue removal, allowing surgeons to transition between delicate neurovascular dissection and robust osseous resection without switching instruments. In cranial base surgery, for instance, fine, angled tips enable work in confined spaces near critical structures such as the optic nerve or carotid artery, while in spinal decompression, broader tips deliver higher cutting power for laminectomy or facetectomy. The ability to adapt tip geometry, length, and stiffness to the surgical site enhances precision and safety, while the integrated suction–irrigation function keeps the field clear of debris and heat [91-92].

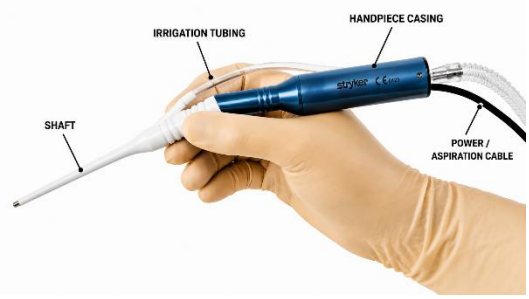
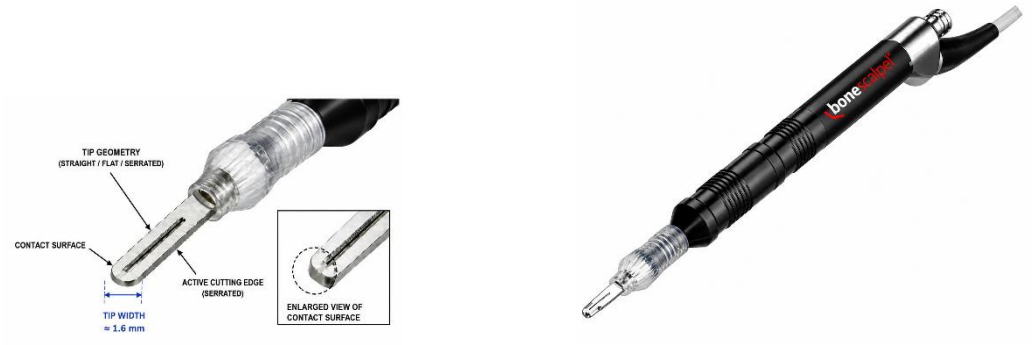


Figure 2.3- Stryker Sonopet® ultrasonic aspirator handpiece showing the handpiece casing, shaft, irrigation tubing and power/aspiration cable.

The Misonix BoneScalpel®, Figure 2.4, is engineered for selective bone cutting in orthopaedic, reconstructive, and spinal surgeries, operating at a frequency of 22.5 kHz with high-amplitude longitudinal motion. Its tissue selectivity arises from the mechanical impedance mismatch between bone and soft tissue: bone efficiently transmits ultrasonic energy at this frequency, while soft tissue dissipates it without significant cutting [93-94]. This allows the BoneScalpel to sharply incise bone while sparing adjacent soft tissue structures such as dura mater or blood vessels[93-95].

For hard tissue, a sharp-tip blade maximises cutting precision and reduces required force; for softer tissue applications, a blunt-tip blade minimises accidental penetration while still allowing surface sculpting. The device reduces cutting forces by up to 70% compared to manual saws, lowering heat generation and microfracture formation. Its telescopic waveguides (angled or straight, up to 145 mm in length) allow surgeons to access deep or narrow surgical corridors in minimally invasive procedures. In spinal surgery, the BoneScalpel enables controlled laminar removal adjacent to the dura and nerve roots, significantly lowering the risk of incidental durotomy or neural injury. This adaptability makes it an increasingly preferred tool in complex spine cases, craniofacial reconstruction, and other procedures requiring both power and precision [93-95].



(a) Cutting insert showing the blade-like geometry and active cutting region.

(b) Handpiece housing the ultrasonic transducer assembly.

Figure 2.4 - Misonix BoneScalpel [93].

The Misonix BoneScalpel comprises a cutting insert and an ultrasonic handpiece (Figure 2.4). The cutting insert exhibits a slender, blade-like geometry with a rectangular cross-section and a flat, rounded tip. A longitudinal groove is present along the centreline, while the active cutting edge is serrated to enhance interaction with bone tissue [93]. The blade has a thickness of approximately 0.5 mm and permits an insertion depth of up to 20 mm. The exposed metallic portion of the insert forms the active cutting region, which interacts directly with the target tissue during ultrasonic vibration [94-95].

The handpiece comprises a cylindrical housing (150-200 mm overall length and diameter between 20-30 mm) that accommodates the ultrasonic transducer assembly. The distal end tapers to accommodate the cutting insert, while the proximal end provides connection to the power supply via an electrical cable [93].

From the literature, it is evident that current ultrasonic surgical devices are typically optimised for specific clinical applications, often operating at fixed frequencies with limited adaptability to changing intraoperative conditions. While devices such as the Harmonic Scalpel and Piezosurgery systems have demonstrated strong clinical utility [84-87], their performance can be constrained by an inability to dynamically adjust to variations in loading conditions.

In practice, interaction with biological tissue introduces changes in mechanical loading, which alters the effective impedance seen by the transducer and can shift the resonance frequency. Since ultrasonic devices achieve maximum vibration amplitude when operating at resonance, even small deviations can result in reduced amplitude and decreased cutting efficiency. This

makes it challenging to maintain consistent vibration amplitude during surgical procedures, particularly when transitioning between tissues with different mechanical properties.

Moreover, the majority of commercial systems rely on conventional metallic components (e.g., titanium alloys and stainless steel), which provide mechanical strength and stability but do not exhibit any inherent functional response to changes in temperature or stress. As a result, these systems depend primarily on external electronic control (e.g., frequency tracking) to maintain performance, rather than intrinsic material adaptability.

This limitation presents an opportunity for innovation through the integration of functional materials such as Nitinol into ultrasonic transducer designs. Owing to its temperature-dependent phase transformation, as described in section 1.1, Nitinol exhibits changes in elastic modulus, which directly influence the effective stiffness of the system. The resonance frequency of an ultrasonic transducer can be approximated using a lumped parameter model, in which the system is represented as an equivalent mass-spring oscillator. In this framework, the natural frequency is given by [53,58]:

$$f \propto (k/m)^{0.5} \qquad (2.3)$$

In relation 2.3,k represents the effective stiffness and m, the effective mass. This relationship indicates that increases in stiffness raise the resonance frequency, while increases in mass reduce it. In addition, the resonance is governed by wave propagation, where the wave speed is given by [59,61]:

$$c = (E/\rho)^{0.5} \qquad (2.4)$$

Where E denotes Young's modulus and ρ the material density. Since wave speed, c, frequency, f, and wavelength, λ are related by $c=f\lambda$, the frequency can be expressed as:

$$f =(1/\lambda) \times (E/\rho)^{0.5} \quad (2.5)$$

For a fixed geometry and vibration mode, equation 2.5 demonstrates that changes in Young's modulus alter the wave speed and consequently the resonance frequency. Therefore, the change in elastic modulus associated with the phase transformation of Nitinol provides a mechanism for tuning the resonance behaviour of the transducer. This is consistent with the lumped-

parameter description in equation 2.3, in which changes in effective stiffness result in corresponding changes in resonance frequency [59,61].

In cymbal (class V) transducers, tuneability arises from the coupling between the piezoelectric element and deformable end-caps, where stiffness changes modify the flexural response and displacement amplification characteristics [27–30]. Similarly, in class IV flextensional transducers, variations in stiffness can influence the dynamic behaviour of the shell structure, enabling shifts in resonance frequency while preserving the desired amplification mechanism. Cascaded Langevin transducers incorporating Nitinol showed enhanced frequency stability under changing thermal conditions [34-35]. By combining this adaptive material behaviour with optimised transducer geometries, Nitinol-based designs offer a route to passive frequency tuning and enhanced operational stability, addressing key limitations associated with conventional ultrasonic surgical systems.

2.4. Ultrasonic surgical devices: Design

Despite significant advancements in the ultrasonic surgical devices, including innovations in drive electronics, various surgical tips for applications like endodontics and ultrasonic scaling, and different vibration modes for surgical tips, most ultrasonic surgical devices still rely on the BLT. The BLT shown in Figure 2.5, incorporates a tuned horn with a cutting insert and remains widely used for both hard and soft tissue surgical applications. The device is designed to operate in a longitudinal resonance mode, where its total length corresponds to a multiple of half-wavelength segments of the standing wave. In this configuration, the BLT itself typically forms a half-wavelength resonator, while the attached cutting tip also approximates a half-wavelength section. This arrangement ensures that displacement nodes and antinodes are positioned appropriately along the structure, allowing efficient transmission and amplification of vibration to the cutting insert [4-5,96]. The longitudinal vibration mode is designed such that a displacement node (minimal axial motion) is located at the piezoelectric stack, while an antinode (maximum displacement) occurs at the cutting insert, enabling efficient transmission and amplification of vibration for cutting.

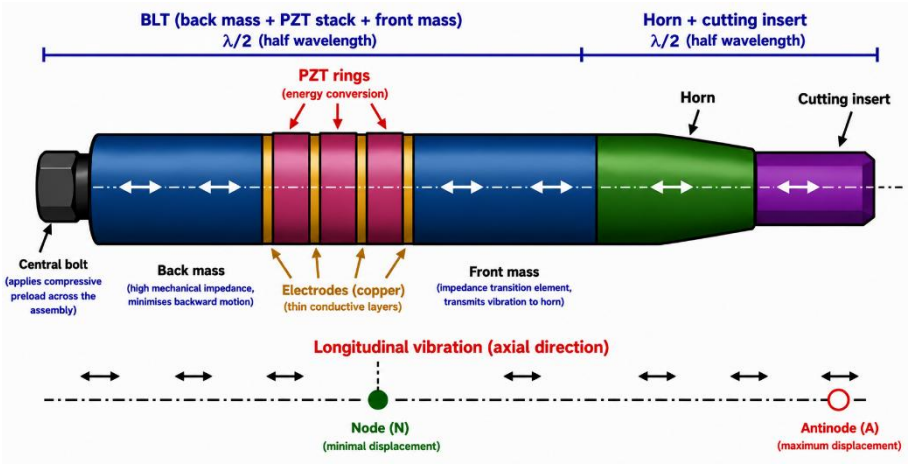


Figure 2.5 – Structural layout of a BLT.

The function of the key components of an ultrasonic surgical device is outlined as follows:

1. Transducer: Represented by a stack of piezoelectric rings, the transducer converts electrical energy from a generator into mechanical vibrations. It serves as the core of the system, with the piezoelectric rings sandwiched between the back and front masses. The back mass is designed with high mechanical impedance, which minimises its vibrational amplitude and reflects energy towards the front of the device, thereby improving energy transfer efficiency. The front mass acts as an impedance transition element, facilitating the transmission of vibrational energy from the piezoelectric stack into the horn and cutting insert. Together, the back and front masses influence the distribution of displacement along the transducer, determine the location of vibration nodes, and contribute to achieving efficient resonance and amplitude amplification. [97].
2. Pre-stress bolt: The pre-stress bolt is positioned through the centre of the piezoceramic stack and applies a controlled compressive force to the assembly. This constant pre-load ensures that the piezoceramic discs, which are inherently brittle under tensile stress, remain in compression throughout the ultrasonic cycle. By eliminating tensile stresses, the risk of cracking and failure during high-amplitude vibration is significantly reduced. Additionally, pre-stressing maintains intimate mechanical contact between the stack components, improving acoustic coupling between the piezoceramics and the end masses, thereby optimising energy transfer efficiency and preserving stable resonance performance under operational loads [84].
3. Coupler/Horn: The coupler, also referred to as the horn, is located between the piezoelectric stack and the tissue-contacting component. Its primary function is to

amplify mechanical vibration amplitude while efficiently transmitting energy to the cutting insert. This behaviour can be understood in terms of mechanical impedance, which describes the resistance of a structure to vibrational motion and governs how energy is transmitted or reflected within the system. The horn acts as an impedance transformation element, progressively modifying the mechanical impedance along its length to facilitate efficient energy transfer from the transducer to the load [83-84]. This is typically achieved through a gradual reduction in cross-sectional area, which lowers the local mechanical impedance and results in an increase in vibration amplitude towards the distal end. As a result, displacement is concentrated at the cutting tip, enabling effective material interaction. While horns are commonly designed for longitudinal motion, geometric modifications such as curvature, asymmetric features, or slotted designs can enable conversion of longitudinal input into flexural or torsional motion for specific surgical applications. In certain configurations, intermediate amplification elements, known as boosters, may also be incorporated to further modify vibration amplitude through controlled impedance transformation [83-84, 98-99].

4. Cutting Insert: The cutting insert is the tissue-interacting component of the ultrasonic surgical device, designed to transfer the amplified mechanical vibrations from the horn directly into the target material. Its geometry, length, and material are optimised for the intended surgical application, whether cutting, dissecting, or emulsifying tissue. Cutting inserts can be straight, angled, or feature specific tip geometries to improve access and precision in confined surgical fields. In addition, inserts are often designed to minimise heat generation at the cutting site, either through inherent geometry that reduces friction or by incorporating integrated irrigation channels to cool the tissue and flush debris away. By tailoring the insert's shape, size, and surface finish, manufacturers can optimise performance for different tissue types, ranging from delicate soft tissues to dense mineralised structures such as cortical bone [83-84,98]. Examples of such tips are:

   <u>Solid Surgical Tips</u>

   Solid tips are most often used for bone-related procedures such as osteotomy and spinal decompression. Fabricated from high-strength titanium alloys (e.g. Ti-6Al-4V), these tips offer high fatigue resistance, biocompatibility, and favourable acoustic impedance which promotes efficient coupling of ultrasonic energy into biological tissue by minimising impedance mismatch and reflection at the interface. The acoustic impedance, Z, of a material is given by:

$$Z=\rho c \qquad (2.6)$$

Where ρ is the material density and c is the acoustic wave speed. When an acoustic wave passes from one material to another, the proportion of incident intensity reflected at the interface can be expressed by the intensity reflection coefficient [93-95,98]:

$$R=[(Z_2-Z_1)/(Z_2+Z_1)]^2 \quad (2.7)$$

Where Z_1 and Z_2 represent the acoustic impedances of the two media. Equation 2.7 demonstrates that a large impedance mismatch increases the proportion of acoustic energy reflected at the interface, whereas closer impedance matching reduces reflection and promotes transmission of ultrasonic energy into the adjoining medium.

The geometries of solid tips vary according to application:

- Flat-faced tips are suited for general bone removal where controlled material removal is needed.
- Serrated or fluted tips concentrate stress at discrete points, enhancing cutting efficiency in dense cortical bone.

Such tips are typically driven in longitudinal vibration mode at operational frequencies between 20–35 kHz. For example, the Misonix BoneScalpel employs interchangeable sharp tips for aggressive bone penetration and blunt tips for controlled sculpting [82-84,93-95,98].

Hollow Surgical Tips

Hollow tips incorporate an internal channel for irrigation and/or aspiration, enabling simultaneous tissue fragmentation and removal. This is advantageous in neurosurgery, oncology, and ophthalmology, where continuous cooling of the surgical site is required to prevent thermal injury [98]. The lumen diameter is optimised to balance flow rate, prevent clogging, and maintain mechanical stiffness. Material selection prioritises fatigue strength under cyclic loading and resistance to corrosion from irrigants [83-84,98].

Wire and Rod Tips

Slender ultrasonic wires or semi-flexible rods are employed in minimally invasive surgical applications such as vascular recanalisation and lithotripsy, where their small diameter enables navigation through narrow anatomical pathways. However, the introduction of bent or curved geometries alters wave propagation behaviour and

promotes the excitation of non-longitudinal vibration modes (Figure 2.6), including flexural and torsional components.

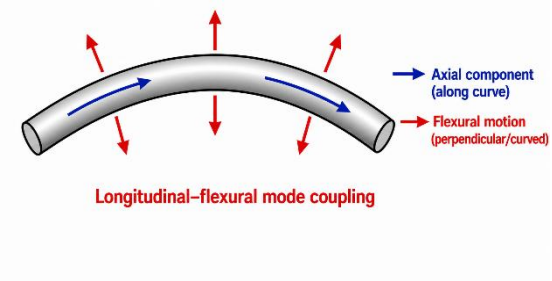


Figure 2.6 – Non-longitudinal vibration mode in a rod.

This modal coupling reduces the efficiency of axial energy transmission and can introduce unintended lateral motion at the tip, thereby increasing the risk of off-target tissue interaction [83-84]. These effects arise because curvature breaks the axial symmetry of the structure, causing part of the longitudinal input energy to be redistributed into transverse deformation modes. To mitigate these challenges, design strategies such as enclosing the wire within a stabilising sheath or incorporating tuned damping mechanisms are employed to suppress unwanted resonances and maintain predominantly longitudinal motion at the distal tip [83–84,98].

Probes

In long-reach or laparoscopic ultrasonic systems, probes function as mechanical transmission elements between the horn and the surgical tip. For efficient energy transfer, probes are typically designed to resonate at an integer multiple of half-wavelengths of the operational frequency, ensuring impedance matching and minimising reflective losses along the transmission path. The probe diameter plays a critical role in determining both mechanical strength and acoustic impedance [98]. Larger diameters increase stiffness and load-bearing capacity but may limit accessibility, whereas smaller diameters improve manoeuvrability at the expense of reduced rigidity and increased susceptibility to bending-induced mode conversion. Materials such as Ti-6Al-4V are commonly selected due to their high stiffness-to-weight ratio, corrosion resistance, and superior fatigue performance under cyclic ultrasonic loading. Achieving an appropriate balance between structural rigidity and minimal cross-sectional area is therefore essential to maintain efficient energy delivery while preserving accessibility in confined surgical environments [83–84,98].

2.5. Ultrasonic surgical devices: miniaturisation and its challenges

Miniaturisation in ultrasonic surgical devices is driven by the need for improved surgical access, reduced patient trauma, and compatibility with minimally invasive and robotic-assisted procedures. In laparoscopic and endoscopic surgery, device diameter and length directly influence surgeon dexterity, access to deep or confined anatomical sites, and the size of the surgical incision. Smaller devices also facilitate integration with robotic surgical systems, enabling precise manipulation in constrained spaces [4,96].

A widely recognised commercial example is the Harmonic Ace® (Johnson & Johnson) as shown in Figure 2.7, which employs a BLT in conjunction with the da Vinci® robotic system. The Harmonic Ace demonstrates how industry-leading devices have been adapted for robotic platforms, offering precise cutting and coagulation in a compact handpiece.

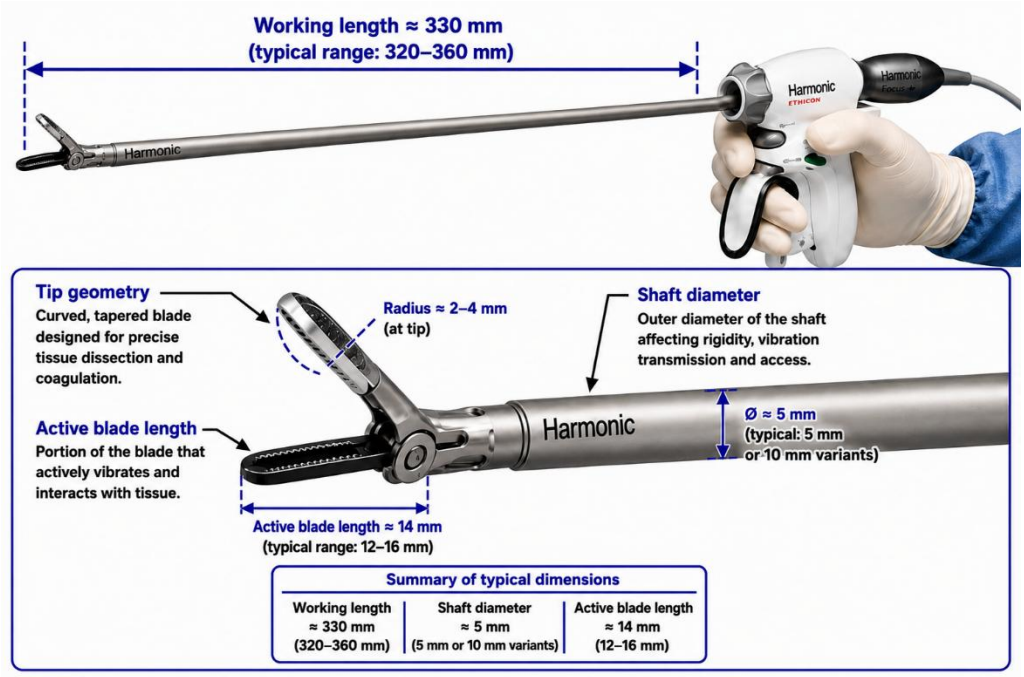


Figure 2.7 - The Harmonic scalpel [84].

However, as with most BLT-based devices, miniaturisation is constrained by the requirement for the transducer length to correspond to an integer multiple of half-wavelengths of the longitudinal vibration mode. Since the wavelength is defined by:

$$\lambda = c/f \qquad (2.8)$$

This limits further size reduction without compromising resonance behaviour [4, 96].

Class IV flextensional transducer designs (Figure 1.6a) offer an alternative approach to miniaturisation. These devices achieve displacement amplification through flexural

deformation of the shell structure rather than relying solely on longitudinal standing waves. As a result, high displacement amplitudes can be achieved at shorter device lengths and lower resonance frequencies. This enables the development of more compact surgical devices while maintaining effective cutting performance. Additionally, flextensional designs provide greater flexibility in geometry and material selection, allowing adaptation to specific surgical requirements [37-39].

2.6. Evolution of flextensional transducers

The term "flextensional" was first introduced in a publication by Toulis in the early 1960s, combining the words ‘flexural’ and ‘extensional’ to describe the operational mode of this type of transducer. There are seven distinct classes of flextensional transducers, named classes I to VII, as shown in Figure 2.8, differing in their geometric and material configurations [39, 100]. Their development dates back to the late 1920s, the first was built and tested in 1929 at the Anacostia Naval Research Laboratories (NRL) in Washington, D.C. Toulis patented the first flextensional electroacoustic transducer in 1966 after refining his design throughout the 1950s [38]. Toulis’ patents also referenced an earlier 1936 patent by Hayes titled “Sound Generating and Directing Apparatus,” which described the theory and design of a flextensional transducer resembling an archer's bow. This bow-like transducer is now known as the class IV transducer [83].

All flextensional transducers (classes I-VII) are based on Hayes' original design, which employed a high mechanical or acoustic impedance transduction material (piezoelectric or magnetostrictive) to drive a low impedance shell [40]. Hayes' design was used in foghorns operated by the Lighthouse Service, and he later developed a ring transducer that was more durable than the original design. This ring transducer (class VI) was used as altitude and drift meters for lighter-than-air ships and was funded by the U.S. Navy [39]. The ring transducer (class VI) proved more rugged and cost-effective than the original flextensional transducer, offering the same electroacoustic efficiency [39-40].

Howard C. Merchant, working alongside Toulis, developed a flextensional transducer design employing convex shells, referred to as a class II configuration, in contrast to the concave shell geometry used in Toulis’ original class I design [39-40,100]. As illustrated in Figure 2.8, class I transducers utilise an inward-curving shell profile, where the shell walls curve towards the central axis [39-40]. Under axial excitation from the piezoelectric driver, this geometry promotes flexural deformation of the shell, resulting in significant displacement amplification

and making it highly effective for generating large acoustic outputs in applications such as underwater sonar and communication systems [100].

The class II design employs an outward-curving shell, where the structure bulges away from the central axis, as shown in Figure 2.8. This configuration increases the structural stiffness of the shell, improving mechanical coupling between the piezoelectric driver and the surrounding structure. As a result, energy transfer efficiency is enhanced, although the degree of flexural displacement amplification is reduced compared to the concave configuration. Additionally, the increased rigidity of the convex shell allows it to better withstand higher compressive pre-stress levels, though excessive stiffening may reduce overall acoustic output [39-40,83-84].

As highlighted in Figure 2.8, both configurations rely on the same fundamental mechanism: axial motion generated by the piezoelectric driver is converted into flexural motion of the shell, which in turn produces amplified displacement at the output region. The primary distinction between the two classes lies in the direction of shell curvature and the resulting balance between displacement amplification and structural stiffness [39-40]. Both designs have been widely applied in underwater acoustic projection systems, while class II configurations have also found use in certain air-based applications due to their improved driver–shell coupling efficiency [83-84].

The classification of flextensional transducers was developed by Brigham and Royster, and initially included five classes. Later, two additional classes were added. Class VI, for example, incorporates two concave end-caps and was designed to operate at greater underwater depths than the class V transducer. As shown in Figure 2.8, class IV and class VII transducers share an identical conical shell mechanism, with the only difference being the orientation of the shell. In the class IV design, the cone opens away from the driver, whereas in the class VII the geometry is inverted, with the cone opening towards the driver, resulting in different output characteristics despite the same underlying flexural mechanism [39-40,83-84].

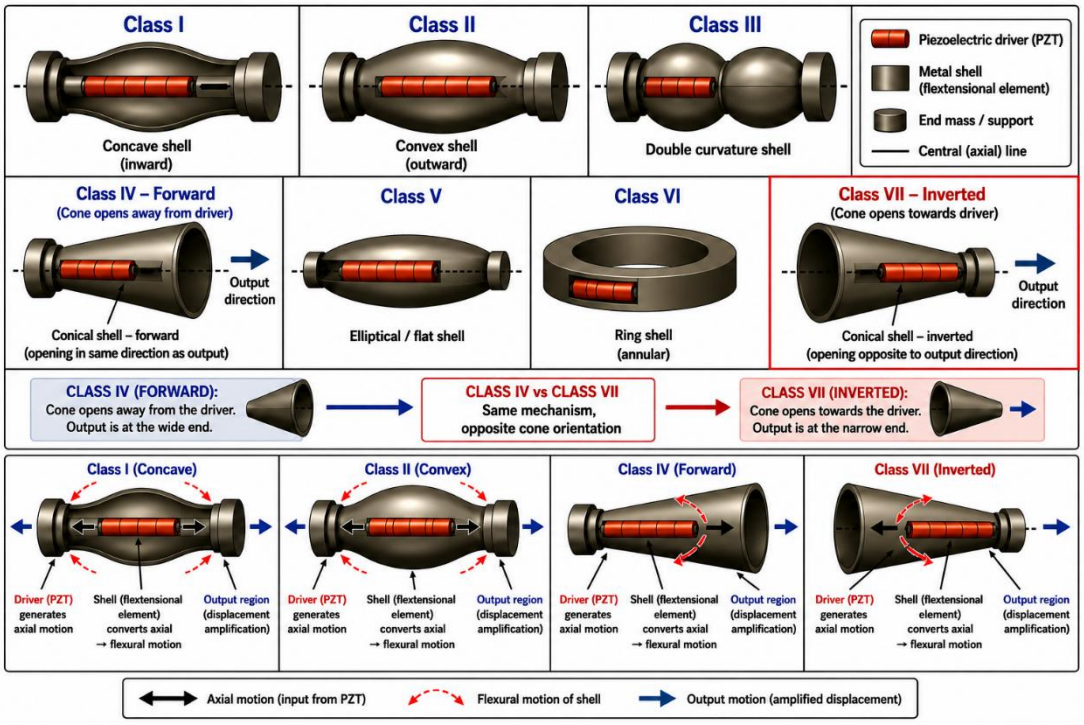


Figure 2.8 - Classes of flextensional transducers [84].

The class I transducer, often called the "football" transducer, features a cylindrical stack of piezoceramic discs compressed along its major axis by a surrounding, barrel-shaped shell. The piezoceramic stack acts as the primary driver, generating longitudinal vibrations that are transferred to the shell. The shell geometry converts this axial motion into amplified flexural displacement through its curved profile. As the piezoelectric driver expands and contracts along the axial direction, it induces bending of the shell walls. Due to the curvature of the shell, this bending deformation results in transverse motion at the edges, producing displacement amplification at the output regions [39,101-103].

The class II flextensional transducer is a modified version of the class I “football” type, retaining the elongated curved shell geometry but extending the major axis to accommodate a greater volume of piezoceramic material. This increase in ceramic volume enhances the power-handling capability, making class II more suitable for applications requiring higher acoustic output in the low-frequency range (typically 1–1.5 kHz). The smooth curvature of the shell distributes mechanical stresses more evenly compared to convex or more rigid shell configurations, reducing stress concentrations that could otherwise initiate cracks in the shell or ceramic stack under cyclic loading. This improved stress distribution enhances the fatigue resistance of the device, which is particularly important for long-duration underwater

operations where the device may undergo millions of vibration cycles under constant hydrostatic pressure [39,101-103].

While class I and class II designs excel in low-frequency, high-displacement underwater applications (e.g., naval sonar, sub-sea communication), their large size, low operating frequency, and long wavelength make them unsuitable for ultrasonic frequencies (>20 kHz) without significant redesign [100,103]. At ultrasonic frequencies, the wavelength becomes much shorter as defined by equation 2.8, requiring proportional downsizing of the shell and driver to maintain resonance, which would drastically reduce the achievable displacement amplitude, counteracting one of the primary benefits of the flextensional configuration [101-102]. This limitation is a key reason why surgical ultrasonic devices should employ alternative flextensional configurations, such as the class IV type, which can achieve high-frequency operation while retaining mechanical amplification [101-102].

The class III design combines two class I shells in a back-to-back configuration to form a double-resonance system. Each shell is driven by a shared piezoelectric stack positioned between them, and the mechanical coupling between the shells creates two distinct flexural resonance modes. These resonances are closely spaced in frequency due to the interaction between the in-phase vibration of both shells (asymmetric mode) and the out-of-phase vibration (symmetric mode) as shown in Figure 2.9.

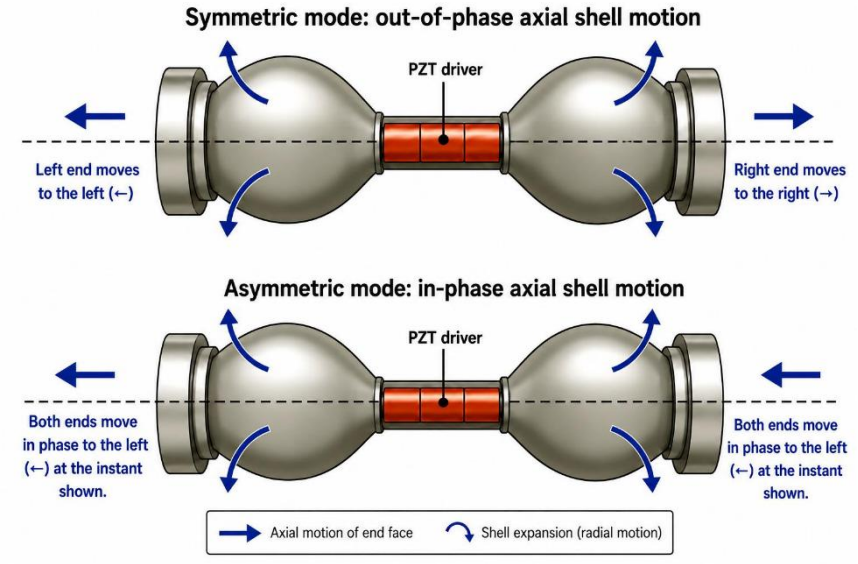


Figure 2.9 - Mode shapes of the class III flextensional transducer.

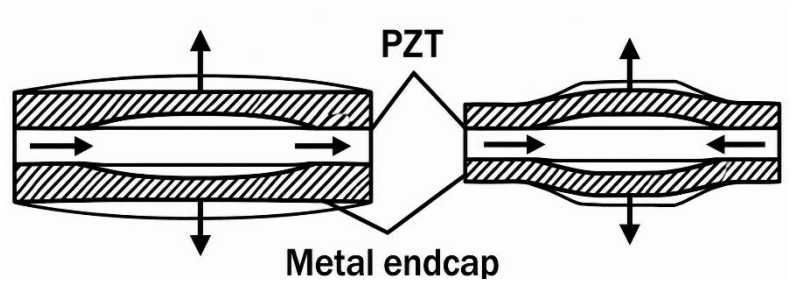
The proximity of these two resonances broadens the overall operational bandwidth of the transducer, enabling efficient acoustic output over a wider range of frequencies compared to single-shell designs. This broader bandwidth is advantageous in applications such as

underwater communications and sonar, where frequency agility improves signal clarity and adaptability to varying propagation conditions. While class III designs typically operate in the low-kilohertz range for underwater applications, their underlying principles could, in theory, be adapted for higher-frequency airborne or medical ultrasound systems, although the increased shell mass and geometry constraints would make such miniaturisation challenging [100,102-103].

Abbott introduced a flying saucer-shaped flextensional transducer in 1955, which was driven by a ceramic disc. He also explored other driver materials for concave and convex shells. Abbott's design became known as the cymbal class V transducer [39,101] which was originally developed as a mini-actuator for multilayer and bimorph actuation [104].

The Moonie transducer, developed in the late 1980s by the Materials Research Laboratory at Pennsylvania State University, is a miniature flextensional device consisting of a shallow, dome-shaped cap bonded to each side of a piezoceramic disk as shown in Figure 2.10a. The domed caps act as mechanical transformers, converting the small radial motion of the ceramic into amplified axial displacement. The Moonie design is compact and lightweight, making it suitable for sensor applications and certain low-power actuation roles [104]. However, its relatively shallow dome depth limits the mechanical amplification factor, and the manufacturing process requires precision bonding of the dome caps to the ceramic disk, which can increase production complexity [104-105].

The cymbal transducer as shown in Figure 2.10b is a modified form of the Moonie design, characterised by deeper, cymbal-shaped caps. This increased dome height and cavity depth significantly increases mechanical amplification, allowing greater displacement output and improved force generation compared to the Moonie. Cymbals can achieve displacement gains ranging between 15-40 times relative to the free strain of the piezoelectric element, depending on cap thickness, dome angle, and material stiffness [104-105]. Values exceeding this range are generally limited by structural instability, increased localised stress and potential yielding within the cap, which restrict practical amplification under cyclic excitation. Figure 2.10 shows the geometry and the mechanical displacement transfer concept of Moonie and cymbal transducers.



(a) Moonie transducer. (b) Cymbal transducer.

Figure 2.10 - Comparison of class V flextensional architectures. The horizontal arrows represent the axial expansion of the piezoelectric elements. The vertical arrows represent the flexural motion of the shells [106].

The cymbal transducer is easier to mass-produce than the Moonie because its cap geometry can be stamped from sheet metal in a single forming operation, reducing machining requirements. In addition, the bonding process is more tolerant to minor dimensional variations, improving manufacturing yield. The simplified assembly process and reduced number of critical tolerances make cymbal transducers more cost-effective for large-scale production, particularly for array-based sonar or sensing applications [104-105].

Although cymbal transducers can generate large mechanical displacements (several to tens of micrometres) relative to the small size of their piezoelectric element, their acoustic performance is limited by their high reactance and low radiation resistance [106]. The transducer impedance can be represented as:

$$Z = R+jX \qquad (2.9)$$

R is the resistive component associated with real power transfer and X is the reactive component associated with stored energy. High reactance indicates that a substantial proportion of the input energy is stored cyclically within the electromechanical structure rather than being converted into radiated acoustic power [104-105]. The radiated acoustic power can be expressed as:

$$P=0.5R_r v^2 \qquad (2.10)$$

R_r is the radiation resistance, and v is the vibration velocity at the radiating surface. Low radiation resistance indicates poor coupling between the transducer and the surrounding medium, reducing the fraction of mechanical vibration converted into propagating sound waves [104-105].

In this context, high reactance indicates that a substantial portion of the input electrical energy is stored within the transducer's electromechanical structure, manifesting as oscillating

electrical and mechanical fields rather than being efficiently converted into acoustic energy. Low radiation resistance reflects the transducer's poor ability to transfer vibrational energy into the surrounding medium as propagating sound waves. This is primarily due to the small radiating surface area of the end-caps and the low stiffness of the structure, which reduce acoustic coupling efficiency [107].

In 1997, a double-resonance cymbal transducer was developed by incorporating asymmetry. The first configuration used end-caps of different materials (steel and brass), while the second configuration used end-caps of the same material but with different shapes. For the double-resonance cymbal, the bandwidth doubled compared to a single-resonance device by lowering the mechanical quality factor [107]. In the double-resonance cymbal configuration, the bandwidth is increased compared to a single-resonance device due to a reduction in the mechanical quality factor. The mechanical quality factor Q is defined as:

$$Q = 2\pi \text{ (stored energy/energy dissipated per cycle)} \quad (2.11)$$

And is inversely related to the bandwidth of the system through:

$$Q = f_r/\Delta f \quad (2.12)$$

where f_r is the resonance frequency and Δf is the frequency bandwidth. A lower Q therefore corresponds to increased energy dissipation and a broader frequency response. In double-resonance cymbal transducers, two closely spaced resonance modes are introduced through structural design, allowing their frequency responses to overlap. This results in an effectively wider operational bandwidth compared to single-resonance systems, where the response is typically narrow and sharply peaked [106-107].

Asymmetric end-caps with different materials or shapes, offer more flexibility for driving in resonance without requiring complex tracking electronics, making it easier to adjust the operating frequency range of cymbal transducers [107].

Due to its thin end-caps and convex structure, the standard cymbal transducer, Figure 2.10b, is typically used for shallow water applications. If the hydrostatic pressure exceeds a certain threshold, the end-caps can permanently deform, causing it to collapse. Cymbal transducers can feature concave end-caps to improve pressure tolerance and reliability under high hydrostatic pressure. This concave version is the "double-dipper" cymbal and dramatically improves pressure resistance [108].

The traditional cymbal transducer, as patented by Newnham and Dogan in 1998, features metal end-caps with shallow cavities on their inner surfaces. A high-strength epoxy resin bonds the

piezoceramic disc to the end-caps, converting radial displacements to flexural motion solely through mechanical coupling [36,109].

Newnham's cymbal transducer offers several advantages over the traditional Moonie transducer, including high piezoelectric coefficients, increased vibrational displacement, and sensitivity at low frequencies. Its cost-effective manufacturing process also allows for easy modifications of desired properties by selecting appropriate end-cap and driver materials [36,109-110].

Cymbal transducers are also known to display double-resonance behaviour due to minor asymmetries in the dimensions of the end-caps or irregularities in the epoxy resin bond layer as shown in Figure 2.11. The resonance modes manifest as out-of-phase and in-phase vibrations of the end-caps, representing symmetric and asymmetric modes, respectively. The operational range of cymbal transducers can be influenced by factors such as the type of piezoceramic material, which determines the maximum voltage before depolarisation, and the strength of the epoxy resin bond, which may fail under high displacement [109-110].

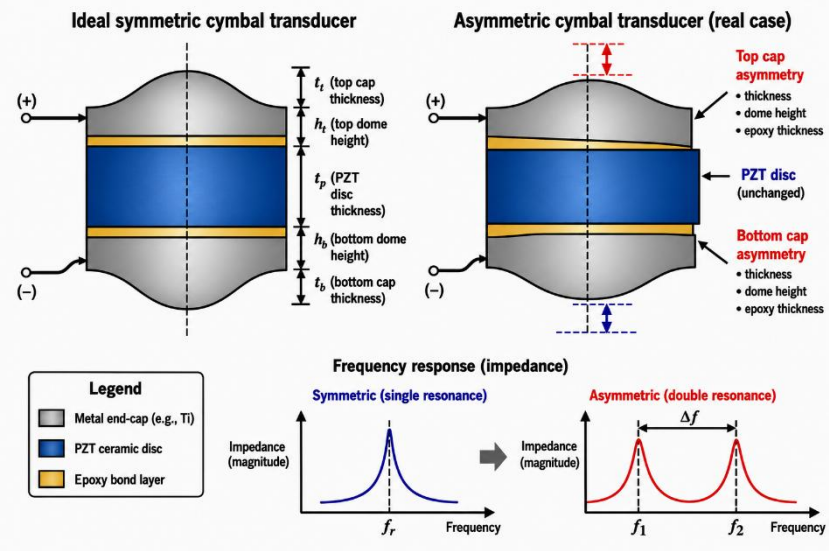


Figure 2.11 - Schematic illustration of symmetry effects in cymbal transducers.

An evolution in cymbal transducer design was introduced by Lin in 2010 featuring a driver consisting of a ceramic disc bonded to a metal ring. A later ultrasonic surgical cutting version of this cymbal, shown in Figure 2.12, was a one-sided modification [111-113]. The end-cap and balancing back-shell are attached to a metal ring with screws, improving mechanical coupling and reducing stress in the epoxy layer. This addresses the limitations in power handling, allowing the device to operate at higher displacements. [111-113]. The end-cap includes a threaded stud to incorporate a cutting insert (IM2A®) from Mectron S.p.A (Italy).

This allows the radial motion of the piezoelectric disc to be converted into an amplified axial motion of the cutting insert [54,109-110].

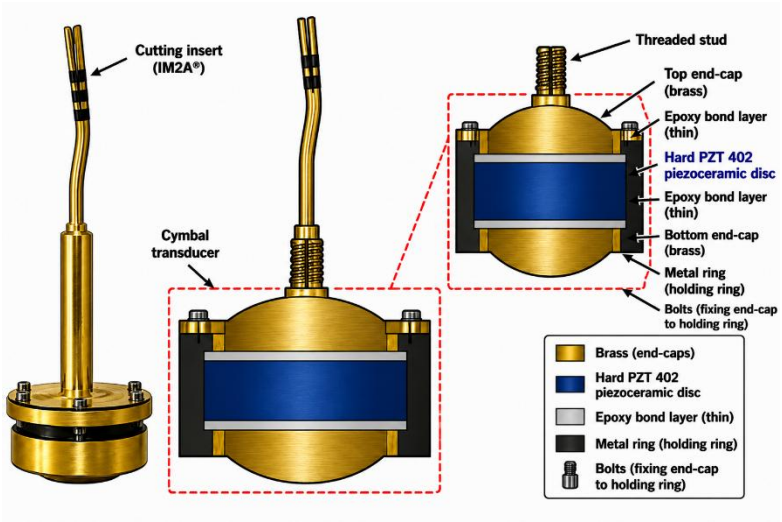


Figure 2.12 - Modified cymbal transducer with commercial cutting insert [36].

In this study, the performance of the modified cymbal transducer and cutting insert (Figure 2.12) was evaluated and compared with that of a conventional power sagittal saw by assessing cell viability around the cut area, indicating that the ultrasonic cymbal device has potential to enable faster healing [109-110].

In addition to its use in arrays, sonar, and ultrasonic surgical applications, the cymbal transducer has been adapted for tuneable frequency applications by integrating Nitinol, an SMA as the end-cap material. Nitinol exhibits a solid-state phase transformation between its martensite and austenite forms when exposed to thermal or mechanical stimuli, altering its elastic modulus [16-17,19]. In one experimental study, cymbal transducers were fabricated with 200 µm and 250 µm Nitinol sheets bonded to the end-caps. At room temperature, in the martensitic phase, the fundamental resonance of the 200 µm design was approximately 22.5 kHz. After heating through the transformation range to A_F (29–40 °C), the increase in end-cap stiffness shifted the resonance to 28.3 kHz, a 25% increase without altering the transducer's physical dimensions [114]. This behaviour is consistent with previous studies on SMAs, where the transformation from martensite to austenite results in a significant increase in Young's modulus, leading to an increase in structural stiffness and a corresponding upward shift in resonance frequency. Similar temperature-dependent frequency tuning has been reported in SMA-integrated cymbal transducers and adaptive structures, where stiffness modulation enables passive control of dynamic response [27-30].

Beyond thermal activation, Nitinol's mechanical responsiveness was evaluated under hydrostatic pressure. The SMA-modified end-caps retained their shape and frequency response up to 4.8 MPa; above this threshold, the end-cap experienced permanent deformation, preventing it from recovering its original shape and compromising functional displacement transmission. At pressures exceeding 2 MPa, a gradual reduction in the hydrostatic piezoelectric coefficient (d_h) was observed [114], the hydrostatic piezoelectric coefficient d_h characterises the charge response of the material under uniform pressure and is defined as:

$$d_h = d_{33} + 2d_{31} \qquad (2.13)$$

d_{33} is the longitudinal piezoelectric coefficient in the poling direction and d_{31} is the transverse coefficient. This parameter reflects the effective electromechanical coupling of the piezoceramic under hydrostatic loading conditions [27-29].

The displacement response of the transducer may also be expressed through an effective displacement coefficient:

$$d_v = \Delta h/V \qquad (2.14)$$

Δh is the measured axial displacement, and V is the applied voltage. In flextensional configurations such as cymbal transducers, the end-cap geometry mechanically amplifies the intrinsic strain of the piezoceramic, resulting in enhanced effective displacement coefficients compared to the free ceramic element accompanied by a 24% decrease in displacement amplitude. After heating above the martensite to austenite transition temperature, the resonance frequency, displacement magnitude, and the flat profile of the end-cap returned to their original values, and the hydrostatic piezoelectric coefficient was restored. This demonstrated that shape recovery is linked to the resonance frequency, cap profile, and d_h values [114].

The class IV is the most widely studied flextensional transducer with successful applications in low-frequency underwater technologies and high-power underwater acoustic sources [38-39,100].A class IV transducer has previously been designed for bone biopsy. A boss, defined as a local protruding cylindrical feature used for mechanical attachment, is fitted to the output surface of the end-cap to enable secure connection of a biopsy needle [41]. The needle (made from Ti-6Al-4V) is a slender, typically hollow cylindrical structure with a sharpened cutting tip, designed for tissue sampling. Its geometry plays a critical role in vibration transmission and cutting efficiency, as its length and diameter influence the propagation of longitudinal vibrations and stress distribution along the shaft [115].

The device incorporates a rectangular cavity profile and a tapered transition section at the base of the needle, as shown in Figure 2.13, to promote uniform displacement amplitude and reduce stress concentrations. Two geometrically similar flextensional devices were evaluated. The

first used epoxy resin as a coupling medium between the Pz26 piezoceramic material, end-cap, and back mass. While epoxy provides compliant bonding, it can introduce damping and variability due to non-uniform distribution, leading to reduced vibrational symmetry. The second device employed an interference fit, defined as a press-fit assembly where components are joined through elastic deformation, producing a tight mechanical interface. This method improves mechanical coupling and energy transmission, although excessive stiffness may constrain vibration.

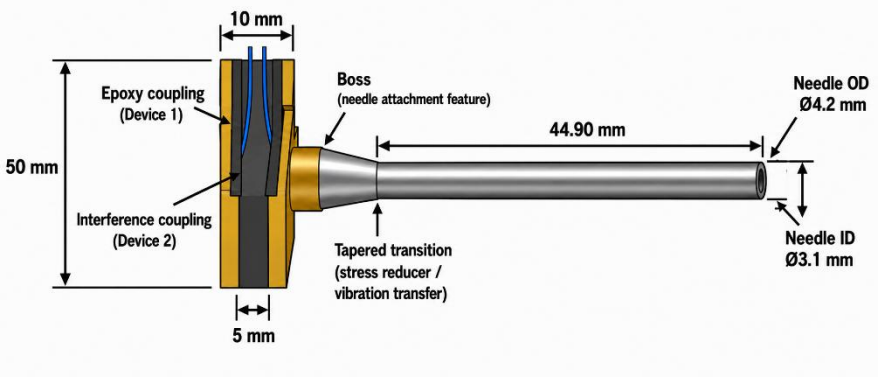


Figure 2.13 – Concept class IV flextensional transducer with biopsy needle [41].

The study reported that the epoxy resin provided effective mechanical coupling between the end-cap and the Pz26 bar. However, non-uniform epoxy distribution introduced variability in the vibrational response of the end-caps, which was observed as a reduction in vibrational symmetry. For example, variations in epoxy thickness led to measurable differences in displacement amplitude across the output surface, with reductions of up to 20–30% in localised regions compared to uniformly bonded configurations. In the case of this class IV flextensional transducer with an integrated biopsy needle, the asymmetric geometry of the device itself further complicates the assessment of whether these effects arise solely from epoxy distribution or from inherent structural asymmetry.

For the interference-fit version, poor mechanical coupling between the end-cap and the Pz26 bar resulted in insufficient energy transfer, with observed reductions in displacement amplitude of approximately 15–25% compared to epoxy-bonded configurations. This made the design unsuitable for high-power ultrasonic needle applications. These results highlight the need for an optimised end-cap–piezoceramic coupling strategy to ensure efficient vibration transmission and stable performance [41].

2.7. The history of SMAs and further applications

The discovery of SMAs can be traced back to research conducted by Martens in the 1890s, who identified martensite in steels [116]. The martensitic transformation was one of the most studied phenomena in metallurgy throughout the 20th century, initially viewed as an irreversible process in the Fe-C system [116]. However, in 1949, Kurdjumov and Khandros observed a reversible martensitic structure in CuAl and CuZn alloys. Later, in 1953, a thermoelastic martensitic transformation was also noted in InTl alloys [116]. InTl alloys, despite demonstrating reversible transformations, were unsuitable for engineering applications due to brittleness and thallium toxicity [116]. These studies nonetheless provided valuable insights into transformation mechanisms that informed later development of commercially viable SMAs, such as Nitinol.

The SMA, Nitinol, was discovered in 1963 by William Buehler and his team at the Naval Ordnance Laboratory. Research in the 1960s further explored the effects of heat treatment, composition, and microstructure on Nitinol [21,24]. In 1965, the addition of elements such as Co or Fe to the NiTi system resulted in a decrease in transformation temperatures. This led to the first commercial application of Nitinol, Cryofit, a material used for pipe couplings in F-14 aircraft. These couplings were stored in liquid nitrogen to prevent actuation before assembly due to their low transformation temperatures [117].

In the 1980s, niobium (Nb) was added to NiTi to create NiTiNb alloys, which became widely used in applications requiring large temperature hysteresis [118-119]. The addition of Nb introduces Nb-rich second phases and internal stress fields that impede the motion of the martensite–austenite interface, thereby increasing the thermal energy required for reverse transformation and resulting in a wider hysteresis. In the late 1970s, research into Nitinol's fatigue properties showed that adding copper (Cu) to the alloy reduced stress hysteresis without significantly altering transformation temperatures. In 1999, Miyazaki demonstrated that NiTiCu alloys exhibited enhanced fatigue resistance, making them suitable for industrial applications due to their lower cost compared to conventional NiTi alloys [118–120].

CoNiAl alloys, formed by adding cobalt (Co) to NiAl or nickel (Ni), exhibit good oxidation and corrosion resistance. These alloys transform from a cubic parent structure to a tetragonal martensite phase [121]. A specific composition, $CoNi_{33}Al_{29}$, exhibits austenite and martensite finish temperatures of −26 °C and −57 °C, respectively, and maintains superelasticity over a temperature range of approximately 150 °C above A_F. Superelasticity arises from a reversible, stress-induced martensitic transformation, in which applied stress converts austenite to

martensite and unloading drives the reverse transformation, enabling recovery of large strains [18]. However, the recoverable strain in CoNiAl alloys is typically limited to approximately 0.06%, significantly lower than the 6–8% achievable in NiTi-based alloys, which restricts their use in applications requiring large deformation recovery [121-123].

Among the most studied magnetic shape memory alloys (MSMAs) are NiMnGa alloys. In 1996, it was suggested that magnetic field-induced shape memory effects could be achieved with these materials, and field-induced reorientation strains of up to 0.2 % were observed in stress-free martensitic Ni_2MnGa single crystals [124]. A limitation of MSMAs is their relatively low blocking stress (the stress at which magnetic reorientation is suppressed), with values ranging from 6-10 MPa. Despite this, Ni_2MnGa alloys can experience compressive strains of up to 4 % during pseudoelastic transformations, and field-induced transformations of up to 0.5 % have been observed with a unique combination of pseudoelastic behaviour and an external magnetic field [125].

SMAs have found applications in aerospace applications, particularly in fixed-wing aircraft. Two notable examples include the Smart Wing programme and the smart aircraft and marine propulsion system (SAMPSON) demonstration [126]. In these programmes, SMAs were used as wire tendons to actuate hingeless ailerons on a scaled-down F-18 aircraft, which were incorporated into torque tubes to induce wing twist. Although SMA torque tubes could actuate the wing model at one-sixth the size of a full-scale aircraft (1:6 scale). While the demonstration confirmed that SMA actuation could achieve the desired wing twist in the model, the generated forces and displacements were insufficient to meet the requirements of a full-scale aircraft without further optimisation of the actuator design and material properties [126-127].

SMAs have been employed to tailor propulsion systems due to their ability to undergo large, reversible shape changes driven by temperature-dependent phase transformations. This enables adaptive modification of aerodynamic components, such as engine inlets and chevrons, using the thermal environment of the engine, thereby reducing the need for complex mechanical actuation systems. Their high force-to-weight ratio, compact integration, and smooth, continuous deformation make them particularly well-suited for controlling airflow characteristics and improving propulsion efficiency under varying operating conditions [126-127]. In the SAMPSON programme, SMAs were also employed to tailor propulsion systems, such as modifying the geometry of an F-15 engine inlet. Full-scale experiments using bundles of 34 SMA wires/rods generated a force of 26.7 kN, which rotated the inner cowl by 9°. Additionally, SMA actuation was tested to change the shape of the inlet lip [126].

SMAs have been embedded in chevrons to reduce engine noise and enhance performance. During low-altitude, low-speed flights, SMA beams cause the chevrons to bend, promoting exhaust gas mixing and reducing noise. In high-altitude applications, SMA beams cool into martensite and straighten the chevrons, improving engine performance [128]. SMAs have also been explored for rotorcraft applications, such as blade actuation, with torque tubes used to alter the twist of rotor blades on tiltrotor aircraft [129].

SMAs have been used in space applications for release mechanisms in low-pressure aerospace environments and for vibration damping during spacecraft launches. In addition to actuation, SMAs are also utilised for vibration damping, particularly during spacecraft launch conditions. Their damping capability arises from the hysteretic nature of stress-induced phase transformations. During cyclic loading, mechanical energy is dissipated as heat through the repeated transformation between austenite and martensite, as well as through internal friction caused by the reorientation of martensitic variants. As a result, part of the vibration energy is absorbed within the material rather than being transmitted through the structure, reducing vibration amplitudes and helping to protect sensitive components under high dynamic loading conditions. In satellites, SMA actuators are employed in low-shock release mechanisms, and, due to the scalability of SMA actuators, they are ideal for compact release mechanisms in smaller satellites. Devices such as the Micro Sep-Nut and Qwknut use the shape memory effect for rotary actuation, providing an angle of 90° in components as small as 5 mm [130].

SMA actuators, such as the lightweight flexible solar array (LFSA), are also found in solar panel components. SMA strips are used as torsional elements to deploy solar panels upon heating in 30 seconds [131-132]. On the Mars Pathfinder mission in 1997, SMA actuators were employed to rotate a dust cover over a specific region of a solar cell, preventing dust from settling and protecting the power output. This allowed for comparative analysis of clean and dust-covered areas of the panel to evaluate the impact of dust on solar cell performance [133].

SMAs such as Nitinol have also seen extensive use in biomedical applications, including in stents and grafts for orthodontic, cardiovascular, and neurosurgical procedures. Nitinol's application in power ultrasonics applications is mainly in the studies of tuneable frequency devices and a Langevin transducer configuration [34-35].

More recent advancements have focused on adaptive SMA-based actuation in soft robotics, demonstrating high displacement capabilities in spatially constrained environments and under complex loading conditions [134]. In parallel, additive manufacturing techniques now enable the fabrication of phase-tuned Nitinol components with locally tailored microstructures, allowing stiffness, and functional fatigue life through process parameter selection [135]. These

developments have shown that SMA structures can be engineered for mechanical responses such as vibration attenuation, controllable compliance, and thermal adaptivity.

Comparable progress in precision ultrasonic actuation has reinforced the potential of material adaptivity for developing compact and tuneable surgical devices [136]. Within this context, Nitinol's ability to reversibly transition between martensite and austenite offers a unique pathway for thermally or stress-controlled tuning of ultrasonic transducers, supporting devices that maintain performance stability while adapting dynamically to changing surgical environments.

2.8. Challenges of Nitinol

One of the primary failure modes of Nitinol components is fatigue, as these materials are often subjected to cyclic loading. Fatigue failure can cause significant damage, with estimates suggesting that 50-90 % of all failures are attributed to fatigue [137].

Fatigue failure is common in Nitinol not only due to cyclic loading, but also because repeated stress-induced phase transformations cause localised strain accumulation within the microstructure. During each cycle, martensite reorientation and transformation to austenite generates internal defects, such as dislocations and microcracks at grain boundaries, progressively reducing structural integrity and limiting fatigue life [137].

The failure process in Nitinol consists of two main stages: crack initiation and crack propagation. The initiation of cracks occurs at a slower rate compared to the propagation stage [138].

The fatigue behaviour of Nitinol is more complex than other metals due to its shape memory effect and superelasticity. This arises from the material's phase transformations and structural phases [138]. Nitinol fatigue can be classified into three categories [139]:

1. Structural Fatigue**:** This type of fatigue refers to reduced strength under cyclic loading. With repeated stress, Nitinol experiences a loss of strength and may fail at stress levels lower than its nominal tensile strength [140].
2. Functional Fatigue: This form of fatigue results in a decrease in the functionality of Nitinol due to cyclic deformation. Research has suggested that a symmetry-dictated non-phase transformation pathway can lead to defect generation, which causes a loss of dimensional stability during transformation cycling [141]. Functional fatigue occurs when the local stress (a combination of internal and external stresses) exceeds a critical threshold during the martensitic phase, activating symmetry-dictated non-phase transformation pathways and generating dislocations in the austenite matrix. This leads

to the functional degradation of the material. However, the term “functional fatigue” is not universally accepted within the fatigue research community [138]. Many materials undergo cyclic instability, leading to softening, hardening, or stabilising mechanical properties. These microstructural changes typically occur during the initial cycles of fatigue, and Nitinol often stabilises within the first 100 cycles without failure [137].

3. Thermal Fatigue: Thermal fatigue refers to microstructural evolution under cyclic thermal loading, including the accumulation of dislocations and defects within the lattice [142]. These changes modify the material’s physical properties, such as transformation temperatures and phase stability, thereby altering its thermal response. For example, Miyazaki et al. [143] linked the reduction in transformation temperatures has been linked to defect accumulation, which hinders the martensitic transformation and affects the reversibility of phase transitions.

Microstructural factors, such as grain size, lattice defects, and inclusions, influence the fatigue behaviour of Nitinol. Grain size, for instance, affects stress concentrations at grain boundaries, which can lead to permanent deformation and crack initiation. High-stress locations, like inclusions, voids, and laminations, are more prone to micro-crack formation under cyclic or thermal loading [138].

For instance, in strain-life fatigue analysis, the fatigue resistance of superelastic Nitinol (above the A_F temperature) decreases as the temperature increases. However, an opposite trend is observed in stress-life fatigue analysis, with fatigue resistance improving as the temperature increases, due to an increased stress plateau at higher temperatures [138].

Figure 2.14 illustrates the various phases of superelastic Nitinol.

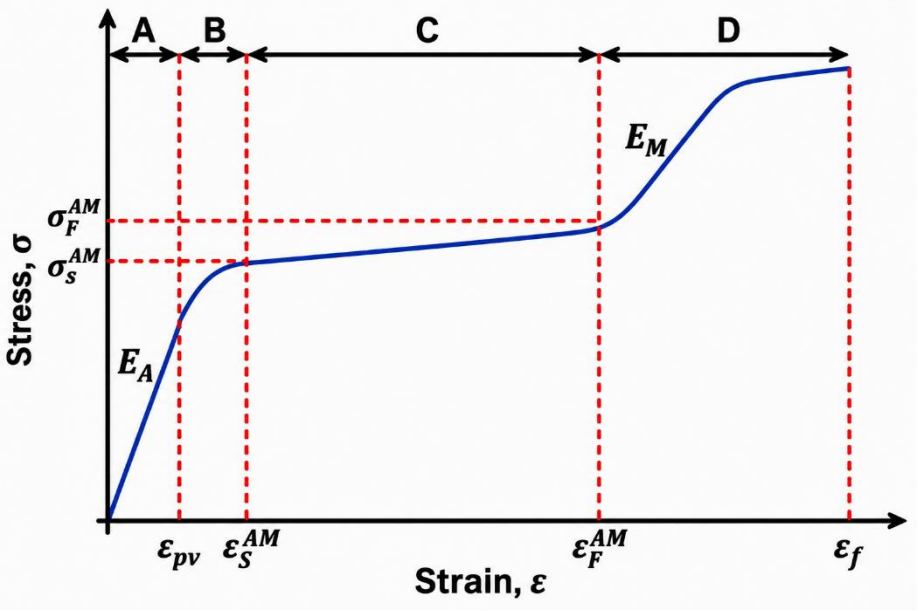


Figure 2.14 - Multiple phases of superelastic Nitinol [138].

The fatigue behaviour of superelastic Nitinol can be categorised into four distinct regions:

1. Region A – Austenitic linear elastic region: In this region, the material is fully austenitic and follows linear elastic behaviour, typically described by Hooke's law ($\sigma = E_A\varepsilon$), where E_A is the elastic modulus of austenite. The strain remains below the proportional limit, and no phase transformation occurs [138].
2. Region B – Transition from linear elastic to stress plateau region: This region marks the onset of stress-induced martensitic transformation, occurring between the transformation start and finish stresses (σ_s^{AM} *to* σ_f^{AM}) [137]. The material begins transitioning from austenite to martensite, resulting in nonlinear behaviour and increasing strain with relatively small increases in stress.
3. Region C – Stress plateau region: In this region, the material undergoes significant strain at approximately constant stress due to the continued transformation of austenite into martensite. Fatigue behaviour in this region is predominantly governed by stress rather than strain amplitude, and the strain–life response becomes less sensitive to changes in strain amplitude.
4. Region D – Fully detwinned martensitic region: In this region, the material is fully transformed into detwinned martensite and exhibits predominantly elastic behaviour characterised by the martensitic modulus ($\sigma = E_M\varepsilon$). As strain amplitude increases in this region, fatigue life decreases, often following a logarithmic trend due to accumulated plastic deformation and microstructural damage.

Biomedical devices, such as peripheral vascular stents made from Nitinol, are designed to withstand 10^8 to 10^9 fatigue cycles without failure during the patient's lifetime [144]. Fatigue design and life prediction methods often rely on total life analyses incorporating stress-life and strain-life data. A summary of findings [144] includes:

1. Under stress-controlled conditions, superelastic Nitinol exhibits higher fatigue limits and longer life than thermal martensite. This is due to the difference in plateau strength between the austenite and martensite phases at the test temperature.
2. In stress-controlled conditions, deformation occurs in repeated cycles, increasing peak strain at a constant stress amplitude.
3. Under strain-controlled conditions, the fatigue life of martensite exceeds that of superelastic Nitinol. This is because less stress is needed to deform thermal martensite at a given strain amplitude compared to transforming austenite to martensite in superelastic conditions.
4. Repeated cycles may induce cyclic hardening in strain-controlled conditions, where stress increases at a constant strain amplitude. This is caused by increased dislocation density with increasing cycles, which reduces the extent of cyclic phase transformation in the material.
5. For superelastic Nitinol, fatigue life is primarily driven by strain amplitude rather than mean or peak strain. Fatigue life improves as mean strain increases, up to the end of the phase transformation plateau.

While foundational studies such as [144] provide a valuable basis for understanding Nitinol fatigue, they are now nearly four decades old and do not reflect significant advancements in material design and manufacturing. More recent developments in SMA actuator technology have demonstrated that fatigue life can be substantially improved through enhanced microstructural stability and optimisation of the phase-transformation pathway [134]. In particular, careful control of heat treatment, alloy composition, and ageing processes has enabled designers to stabilise martensite/austenite interfaces and reduce localised strain concentrations, both of which are key drivers of crack initiation.

In parallel, advances in precision additive manufacturing have enabled the fabrication of phase-tuned Nitinol structures with reduced defect density and controlled grain morphology, leading to further improvements in cyclic performance [135, 145]. These innovations enable SMAs to be engineered with tailored transformation temperatures and stiffness profiles through controlled variation of alloy composition, heat treatment, and additive manufacturing parameters. For example, adjustments in Ni/Ti ratio and the addition of alloying elements such

as Cu or Nb can shift transformation temperatures and modify hysteresis behaviour, while thermal processing influences precipitate formation and phase stability. In additive manufacturing, process parameters such as laser power and scan speed affect microstructure, porosity, and residual stress, thereby altering mechanical stiffness and fatigue performance. Architected geometries with graded density can be used to tune the effective stiffness of the structure [118-120,135,145]. Such improvements are especially relevant for ultrasonic surgical applications, where components experience millions of high-frequency loading cycles and therefore require both stable stiffness control and resistance to functional degradation over time.

2.9. Machining of Nitinol

Machining Nitinol is a complex process due to its stiffness and the titanium oxide layer that coats this metal alloy. Chapter 1 highlighted standard machining methods for Nitinol, including waterjet cutting, wire-EDM, and laser cutting. Laser cutting of metals offers advantages such as high accuracy, speed, precision, and a lack of physical contact, which minimises the risk of damage or contamination [146-149]. However, laser cutting Nitinol introduces several challenges, such as forming HAZs around the cut [59-61, 146-149]. These HAZs can alter the material's thermal properties, compromise its corrosion resistance, and affect surface roughness. Additionally, the residual stress generated from thermal expansion and contraction during the cutting process can impact the dimensional accuracy and mechanical properties of the machined Nitinol [147-148]. Laser cutting can also induce microcracks and delamination in Nitinol components due to thermal damage. The process is slow when cutting thick Nitinol samples, and costly due to expensive equipment and the need for specialised expertise. Environmental concerns also arise, given the hazardous fumes and waste materials that require careful and secure disposal [149]. Waterjet cutting uses a high-pressure pump to create a concentrated jet of water directed to a workpiece to shape or remove material. This process effectively cuts thick parts and produces complex geometries with high precision. Abrasive particles like silicon carbide and aluminium oxide are used to machine Nitinol components. An advantage of waterjet cutting is that it eliminates heat, which reduces the risk of thermal damage to Nitinol workpieces. However, challenges arise when creating small structures from thin Nitinol sheets because silicon carbide abrasive particles used in the waterjet process can become embedded in the surface. This contamination leads to increased surface roughness, deteriorated corrosion resistance, and compromised mechanical integrity, which are particularly problematic for medical or high-precision application [150]. Additionally,

controlling the milling depth can be difficult when using water jet cutting on Nitinol [59-61,150].

Wire-EDM was used in this study for machining the Nitinol end-caps of the class IV flextensional transducers. This process uses an electric discharge to vaporise workpiece material through a voltage applied between the workpiece and the electrode, which creates craters flushed by dielectric fluid. The advantages of wire-EDM, and why this method was chosen for machining the Nitinol end-caps, is that it can precisely and accurately machine intricate shapes for Nitinol components. With Nitinol SMAs machined by the wire-EDM process, the shape memory effect is typically limited to approximately 8% bending strain because, beyond this threshold, excessive microstructural distortion can induce plastic deformation or irreversible dislocation movements. These changes reduce recoverability and can lead to functional degradation of the SMA [151]. Another advantage is that a smooth surface finish can be produced. Although wire-EDM has desirable properties compared to the other mentioned machining methods, it poses negative environmental impacts such as production of sludge, harmful gases and particulate matter released into the atmosphere during the machining process. If not properly recycled, the dielectric fluid can also lead to environmental harm [151-152].

Other machining methods for Nitinol, particularly in biomedical applications, include vacuum induction melting (VIM), vacuum arc melting (VAM), and plasma arc melting (PAM). The VIM process involves a graphite crucible mounted in a steel shell connected to a vacuum. The eddy currents in the crucible and the electrodynamic forces help stir and mix the melt. VIM is the most widely used method for producing commercial-grade Nitinol because it provides greater control over homogeneity and alloy composition than other melting processes. It also offers flexibility in terms of time, pressure, temperature, and mass transport, all contributing to material homogeneity. However, carbon contamination is a potential issue in VIM, as the process uses a graphite crucible. In VAM, an electrode is continuously remelted in an arc within a vacuum environment. VAM is effective for producing high-purity Nitinol components and is often used to purify VIM ingots. However, achieving the desired homogeneity with VAM typically requires several melts of the VIM ingots [153].

PAM uses elemental metals placed in a copper, water-cooled crystalliser, which is then moved beneath an argon plasma burner utilising a screw. Nitinol components produced by PAM generally have better corrosion resistance and higher purity than those made by VIM. However, the homogeneity of PAM-produced Nitinol is typically poorer than that of VIM-produced

components, and multiple PAM furnace torches are needed to achieve a level of homogeneity comparable to VIM [154].

2.10. Additive manufacturing of Nitinol

The use of Nitinol in biomedical applications is often limited by the challenges associated with producing complex Nitinol parts. High ductility, the rebound effect, and work hardening make it challenging to create high-quality, precision components [155]. The conventional manufacturing methods, combined with the sensitivity of Nitinol's transformation temperatures, which are influenced by the relative concentrations of nickel and titanium, pose significant difficulties when fabricating custom, intricate geometries [156]. Additionally, turning, milling, forging, and casting are ineffective for manufacturing complex Nitinol structures, further limiting its applications [157].

Selective laser melting (SLM), an additive manufacturing technique, has been explored for fabricating Nitinol parts from powdered material. In SLM, functional and complex parts are created by selectively melting powdered layers with a laser beam. The laser follows a pattern controlled by software that slices the 3-D computer aided design (CAD) model of the desired part [158]. To achieve high-quality products, the powders used in SLM must have specific properties. These include good flowability, spherical particle shapes, minimal moisture or gas content to avoid defects, and an appropriate size distribution to ensure efficient layer deposition [158].

A thermal analysis of specimens produced by SLM showed that the transformation temperatures of Nitinol shifted to higher values after processing, with temperature rises of up to 16 °C observed during heating and cooling [156]. This was attributed to the evaporation of nickel at high temperatures during the laser melting process. Cyclic testing on SLM-manufactured Nitinol parts revealed irreversible strains on the order of 0.5–1% during the initial cycles, with the shape memory effect deteriorating in the first few cycles. However, the effect stabilised after approximately 50–100 cycles, with reduced accumulation of residual strain. This suggests that SLM holds promise for producing Nitinol parts with complex geometries [156].

Maintaining low impurity levels in Nitinol ensures its performance, particularly for medical applications. Impurities can adversely affect the phase transformation temperatures and the structural and functional properties of the material [159-161]. SLM systems can control impurity content by managing the process environment. While conventional methods use recycled argon in the process chamber, a more effective approach is to flood the chamber with

fresh argon, reducing impurity uptake significantly. This method has been shown to reduce oxygen levels by 60 % and nitrogen by 85 % [162].

Additive manufacturing, specifically SLM, has been found to produce higher-quality medical-grade Nitinol compared to conventional methods like metal injection moulding [163-164]. SLM offers advantages over casting and powder metallurgy (PM) in producing Nitinol components. Casting involves high-temperature melting, which can increase impurity content, forming detrimental Ti-rich phases such as TiC and $Ti_4Ni_2O_x$. These secondary phases degrade the functional properties of Nitinol. Additionally, machining processes used to shape cast Nitinol can result in excessive tool wear due to the material's super-ductility [165]. Although helpful in producing near-net-shaped devices (components produced with geometries that are close to the final design, requiring only minor finishing operations), powder metallurgy also suffers from impurity accumulation and limitations in the complexity and porosity of the parts produced [166].

However, caution must be exercised when setting SLM processing parameters. Low laser power combined with high scanning speeds can result in incomplete fusion of the Nitinol powder, leading to increased porosity and compromised material properties. Conversely, high laser power and low scanning speed can create deep, narrow keyholes, which may result in defects due to instability at the tip of the keyhole [144,167].

SLM has also been shown to be a safe manufacturing method for biomedical applications, as it reduces nickel release from the fabricated structures after implantation. The concentration of nickel must remain well below cytotoxic levels (25×10^6Ng/ml) to avoid harming the body. A study by Habijan et al. demonstrated the safety of SLM-manufactured Nitinol implants by culturing human mesenchymal stem cells (hMSC) on an SLM-fabricated Nitinol component [168]. After eight days of incubation, viable cells were found not only on the surface but also inside the pores of the implants. This confirmed that nickel ion release from the implant was well below cytotoxic levels, highlighting SLM as an attractive and safe method for producing Nitinol structures for biomedical applications.

Despite the advantages of SLM in producing complex Nitinol geometries, additively manufactured parts often exhibit higher porosity and residual stress levels compared to wrought Nitinol where the material is produced through thermomechanical processes such as forging, rolling, and drawing, followed by heat treatment. These processes result in a more refined and homogeneous microstructure with fewer defects, leading to improved fatigue performance in long-term cyclic applications relevant to ultrasonic transducer operation [135,145]. These microscale features act as fatigue initiation sites, reducing fatigue life particularly under high-

frequency cyclic loading. Recent studies have shown that optimised heat treatment and post-processing (e.g., hot isostatic pressing) can partially recover fatigue performance; however, AM Nitinol typically still underperforms compared to conventionally manufactured material in long-term cyclic applications relevant to ultrasonic transducer operation [135,145]. Therefore, while AM Nitinol is a promising route for future transducer miniaturisation, current fatigue limitations must be carefully considered when targeting long-term reliability under ultrasonic actuation.

2.11. Summary of literature and research gaps

While the literature demonstrates an understanding of BLT-based surgical devices and various flextensional configurations for sonar and sensing applications, there is an absence of surgical devices employing flextensional architectures in the commercial ultrasonic surgical devices market. Existing studies on class IV designs focus on underwater or airborne acoustics, with no reported adaptation for surgical cutting. This gap is significant given the inherent advantages of flextensional designs in mechanical amplification and the potential for miniaturisation, two features highly desirable for modern surgical tools.

SMAs such as Nitinol introduce a further opportunity: the ability to tune the resonant frequency through reversible phase transformation. However, the practical integration of Nitinol into ultrasonic devices is complicated by its challenging machinability stemming from Nitinol's known high toughness, work-hardening behaviour, and low thermal conductivity, which are widely recognised to cause surface finish imperfections and introduce internal stresses during processing. While these limitations are well-established in the broader SMA manufacturing literature, their implications for integrating Nitinol components into class IV flextensional ultrasonic transducers, where precise geometry and surface integrity directly influence modal amplification and acoustic coupling, have not yet been fully explored. This gap provides a key motivation for the design choices and material integration strategies undertaken in this thesis.

In a class IV flextensional shell, where precise geometry directly governs modal amplification and acoustic coupling, such imperfections can significantly reduce performance. These effects become even more critical when miniaturising devices to meet the dimensional constraints of laparoscopic or robotic surgery and diameters are typically limited to approximately 2–5 mm (limiting available piezoelectric volume) imposes strict design limitations [169]. The key gaps and research questions addressed in this thesis are:

Key gaps in knowledge

1. Absence of surgical flextensional devices. No published designs or commercial products currently implement flextensional transducers for surgical cutting.
2. Unexplored integration of Nitinol into flextensional architectures. While Nitinol has been applied in other ultrasonic contexts, its integration into class IV flextensional shells for tuneable resonance has not been studied.
3. Limited understanding of Nitinol machining constraints for ultrasonic applications. There is little data on how manufacturing defects from Nitinol machining affect vibration efficiency and frequency stability in miniaturised flextensional designs.

Research questions addressed in this thesis

1. How can a class IV flextensional ultrasonic transducer be designed and manufactured for surgical applications?
2. Can Nitinol be integrated into a class IV flextensional design to enable tuneable resonance frequency for surgical cutting?
3. How do the machining and fabrication constraints of Nitinol influence the final vibrational performance of a class IV flextensional ultrasonic transducer?

Chapter 3

Material characterisation of Nitinol end-caps and wires

The integration of SMAs into ultrasonic transducers introduces material behaviours that are not present in conventional engineering metals such as titanium, aluminium, and stainless steel. Unlike these materials, Nitinol exhibits temperature-dependent thermomechanical behaviour associated with reversible phase transformations between martensite/rhombohedral and austenite [29]. These transformations influence material properties such as stiffness, damping, and mechanical response [27-29,47], which can affect the dynamic performance of ultrasonic transducers [27-29]. Understanding the material behaviour of Nitinol is therefore essential before assessing its suitability for ultrasonic transducer applications.

This chapter presents the material characterisation of the Nitinol end-caps and wires used throughout this study. Differential scanning calorimetry (DSC) was employed to determine transformation temperatures and assess transformation behaviour. Energy dispersive X-ray spectroscopy (EDXS) was conducted to evaluate elemental composition and material uniformity. In addition, static tensile testing and dynamic mechanical analysis (DMA) were performed to characterise the mechanical response of Nitinol under applied and cyclic loading conditions, respectively.

The objective of this chapter is to establish a fundamental understanding of the thermomechanical behaviour of Nitinol and to provide material-level context for the transducer investigations presented in subsequent chapters. By characterising transformation behaviour, composition, stiffness, damping, and deformation mechanisms, this chapter provides a framework for interpreting how Nitinol may influence the performance of ultrasonic transducers under varying electrical, mechanical, and thermal operating conditions.

3.1. Methodology

3.1.1. DSC

DSC is an experimental technique used to determine the transformation temperatures of material samples and is useful for characterising SMAs like Nitinol [18,27-30]. DSC was performed in this chapter to characterise the transformation behaviour of the Nitinol end-caps and wires used in the class IV flextensional transducers in Chapters 4-6. This analysis is

essential for this study because Nitinol is a phase-transforming SMA, and its thermo-mechanical properties depend strongly on whether it is in the martensite or austenite phase. These phases differ in stiffness, internal damping, and recoverable strain behaviour, properties that directly influence the vibration characteristics of an ultrasonic transducer [27-30].

DSC can provide a method to determine when these phase transitions occur and how sharply they take place [18,27-28]. By establishing the start, peak, and finish temperatures of phase transformations, the DSC results provide the material context needed to interpret the unique behaviour of the Nitinol transducers (Chapters 4-5) under cycling and elevated temperatures.

All DSC tests were conducted using a differential scanning calorimeter (Diamond DSC, Perkin Elmer, Waltham, MA, USA). A simplified diagram of the DSC setup is shown in Figure 3.1. Before testing, the instrument was calibrated using an indium standard. Indium is commonly employed as a calibration material because its melting temperature and enthalpy of fusion are well established. Calibration against an indium standard ensures the accuracy of both the temperature and heat-flow measurements obtained during DSC testing [27-28].

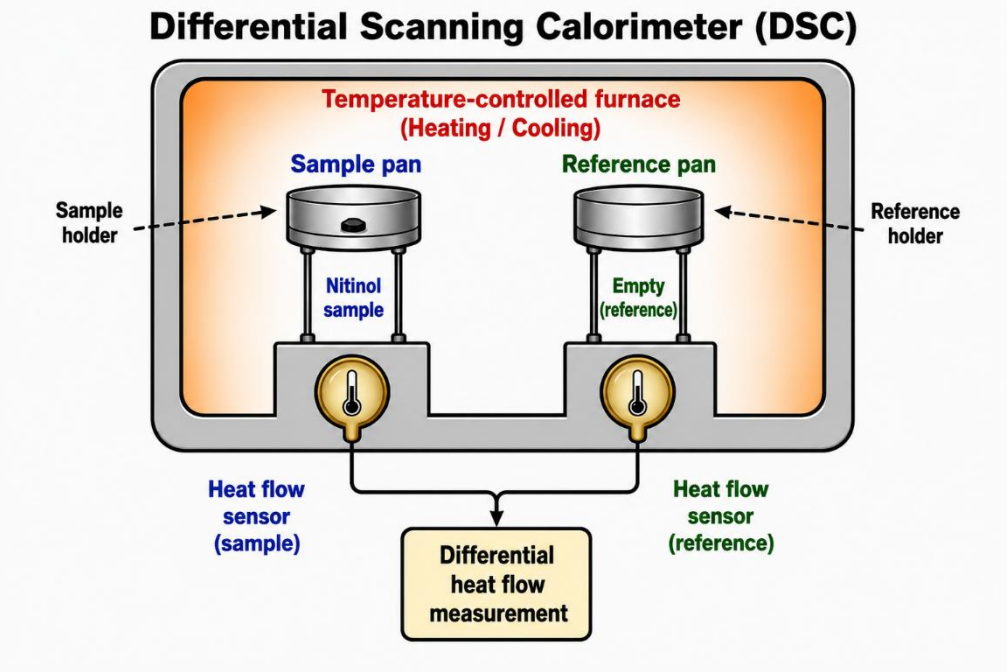


Figure 3.1 - Simplified diagram of DSC setup.

The DSC setup consists of two pans housed within a temperature-controlled furnace. The sample pan contains the Nitinol specimen, while the reference pan remains empty. Both pans are subjected to identical heating and cooling cycles, and the instrument measures the difference in heat flow required to maintain both pans at the same temperature. This differential

heat flow is associated with phase transformations occurring within the specimen and is used to identify the transformation temperatures of the material [18,28]. The use of a reference pan eliminates baseline effects and improves the sensitivity of the measurement to subtle thermal events [27-28].

A total of 31 specimens were extracted from a single Nitinol end-cap using wire-EDM. The cutting path was designed to obtain material from different locations within the end-cap, as shown in Figure 3.2. Owing to the tapered geometry of the component, perfectly uniform specimens could not always be obtained, and specimen volumes ranged between approximately 2-3 mm^3. This specimen size was selected to provide sufficient thermal uniformity while maintaining adequate heat-flow signal strength during testing. The use of 31 specimens enabled transformation behaviour to be assessed across multiple regions of the end-cap, providing a detailed evaluation of material homogeneity and allowing any location-dependent variations in transformation temperatures to be identified.

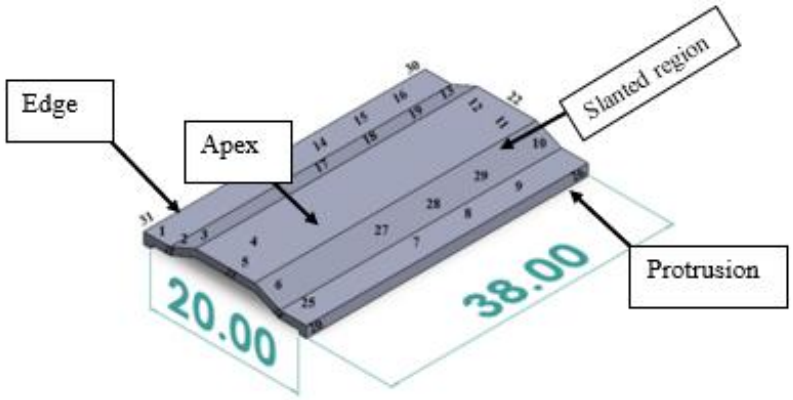


Figure 3.2 – Regions of the Nitinol end-cap from where the cubic samples were taken. Dimensions in mm.

The Nitinol sheet used to produce the DSC specimens was sourced from Kellogg's Research Labs (NH, USA) and had a specified A_F of 35 °C. The specimens were machined from the same batch of Nitinol sheet used to fabricate the Nitinol end-caps examined in Chapters 4-5. As only the A_F temperature was provided on the material certificate, DSC mapping of multiple positions was performed to evaluate material homogeneity and determine whether local variations in transformation behaviour could contribute to the dynamic responses observed in the flextensional transducers.

A heating and cooling rate of 10 °C min^{-1} was employed throughout the study. This scan rate is widely used for the thermal characterisation of Nitinol because it provides clear resolution

of transformation peaks while maintaining practical testing durations. Faster scan rates can introduce kinetic effects that shift apparent transformation temperatures and alter peak morphology, whereas slower scan rates offer limited additional benefit while increasing experiment duration and susceptibility to baseline drift [18,27-30].

The DSC measurements were performed over a temperature range of −20 °C to 100 °C. This range was selected to ensure potential capture of both the martensitic and austenitic transformations. The lower temperature limit was chosen to try to ensure that transformation to martensite was completed, while the upper temperature limit ensured that the reverse transformation to austenite had fully occurred. The resulting thermograms were used to determine the start, peak, and finish temperatures associated with the martensitic, austenitic, and R-phase transformations.

Similar to the investigation conducted on the Nitinol sheet with an A_F of 35 °C, a further set of 31 specimens was extracted from a Nitinol sheet with an A_F of 45 °C using wire-EDM. This material originated from the same Nitinol sheet used to manufacture the A_F of 45 °C Nitinol end-caps described in Chapter 4. The DSC tests were conducted using the same heating and cooling rate of 10 °C min^{-1} and the same temperature range of −20 °C to 100 °C employed for the A_F of 35 °C specimens. As with the A_F of 35 °C material, the supplier's material certificate provided only the A_F temperature, and therefore DSC characterisation was required to determine the complete transformation behaviour of the material, including the martensitic, austenitic, and any intermediate phase transformations.

The purpose of conducting DSC tests on Nitinol material with a higher transformation temperature was to investigate the presence of the SME. The SME in Nitinol refers to the material's ability to recover a previously imposed deformation upon heating [29], driven by a reversible solid-state phase transformation between martensite and austenite [27-30]. In DSC, the presence of the SME during heating is commonly identified by a two-stage endothermic response, corresponding to successive phase transformations, which may appear as two distinct troughs in the heating curve.

DSC tests were also conducted on the Nitinol wire specimens used in the class IV flextensional transducers (Chapter 5). Seven specimens were cut from a 1 mm diameter Nitinol wire supplied by Nexmetal Corporation. According to the manufacturer, the wire possessed an A_F of 30 °C. The DSC measurements were performed under the same experimental conditions as those used for the end-cap specimens, employing a heating and cooling rate of 10 °C min^{-1} over a temperature range of −20 °C to 100 °C.

3.1.2. EDXS of Nitinol end-caps and Nitinol wire specimens

EDXS was employed to assess the chemical uniformity of the Nitinol end-cap and wire specimens and to determine whether local variations in nickel–titanium composition could contribute to the transformation behaviour identified by DSC. While DSC provides insight into transformation temperatures and phase transition, it cannot distinguish whether observed variability arises from thermomechanical effects or from compositional inhomogeneity introduced during material processing or machining. EDXS therefore, complements the thermal analysis by enabling spatially resolved verification of elemental composition.

A single machined Nitinol end-cap (A_F 35 °C) was sectioned into representative regions corresponding to the apex, protrusions, slanted regions, and edges (Figure 1.6b). These regions were selected based on their functional significance within the class IV transducer and their differing local geometries. By analysing multiple regions within a single Nitinol end-cap, the influence of geometry-dependent processing effects could be isolated from batch-to-batch material variability.

EDXS was also performed on representative Nitinol wire specimens to confirm bulk compositional consistency and to verify that the wire material did not exhibit local nickel enrichment or depletion that could independently influence transformation temperatures [18]. The EDXS results support interpretation of the transducer-level measurements by excluding compositional heterogeneity as a primary driver of the observed behaviour. The Nitinol wire was incorporated as a simplified representation of a surgical attachment connected to the transducer end-cap. It also enabled the influence of a discrete transformation-capable Nitinol element on the dynamic response of the transducer to be investigated (Chapter 5).

To prepare the Nitinol end-cap specimen (A_F 35 °C) for EDXS, the end-cap was sectioned into seven parts using a Qcut 200A (Brilliant 220) precision saw that provided smooth cut edges and dimensional accuracy. Following sectioning, the samples were vacuum impregnated with epoxy resin, which was cured at 45 °C for three hours. They were then left to cure for a further twelve hours at room temperature to allow the epoxy to harden before polishing. The polishing process began with a 1-micron diamond suspension on a Buehler MicroCloth pad for three minutes. This was followed by polishing with a 0.3-micron aluminium oxide suspension on a Buehler MasterTex pad for three minutes. Finally, the samples underwent a final polish using a 0.05-micron aluminium oxide suspension on a MasterTex pad for five minutes. The wire samples were polished using the same process.

For these samples, both the cut wire face and its length were scanned. Sample imaging and chemical mapping were performed on polished Nitinol end-cap and wire samples, which were coated with a 20 nm layer of carbon. Carbon was selected as the conductive coating because it provides sufficient electrical conductivity while introducing minimal interference with EDXS elemental analysis. This was carried out using a Zeiss Sigma variable pressure field emission-gun scanning electron microscope, equipped with an Oxford Instruments X-Max 80 mm^2 silicon drift energy dispersive detector.

Backscattered electron (BSE) imaging and EDXS analysis were conducted under high vacuum and high current conditions, with an accelerating voltage of 20 kV. The working distance for both EDXS and BSE imaging was set to 9 mm, with an aperture size of 60 µm and a tilt angle of 70 ° was used. Oxford Instruments Aztec software was employed to acquire and process the EDXS mapping data. BSE images of the wire and end-cap sections were obtained.

Due to project time constraints, EDXS was not conducted on the seven sections of the Nitinol end-cap with an A_F of 45 °C. As a result, the influence of local compositional variations on the measured transformation behaviour could not be assessed. Future work should combine DSC and EDXS analyses to establish whether variations in elemental composition contribute to the observed differences in transformation temperatures across the end-cap as done with the Nitinol end-cap with an A_F of 35 °C.

3.1.3. Static mechanical characterisation

Given the integration of Nitinol into ultrasonic transducers, a detailed understanding of the material response under applied loading is required. Static tensile testing was performed to characterise the fundamental stress–strain behaviour of the Nitinol material. These tests provide information regarding the elastic response, the stress-induced transformation region, and the post-transformation stiffening behaviour of the SMA [12,14]. Such information is important because the deformation mechanisms activated during tensile loading influence the manner in which the material accommodates strain and stores mechanical energy.

Under uniaxial loading, the engineering stress σ, and engineering strain ε, are defined as:

$$\sigma = F/A_0 \quad (3.1)$$

$$\varepsilon = \Delta L/L_0 \quad (3.2)$$

where F is the applied force, A_0 is the original cross-sectional area, ΔL is the change in gauge length, and L_0 is the original gauge length. Within the initial elastic region, the stress and strain are related through Hooke's law:

$$\sigma = E\varepsilon \qquad (3.3)$$

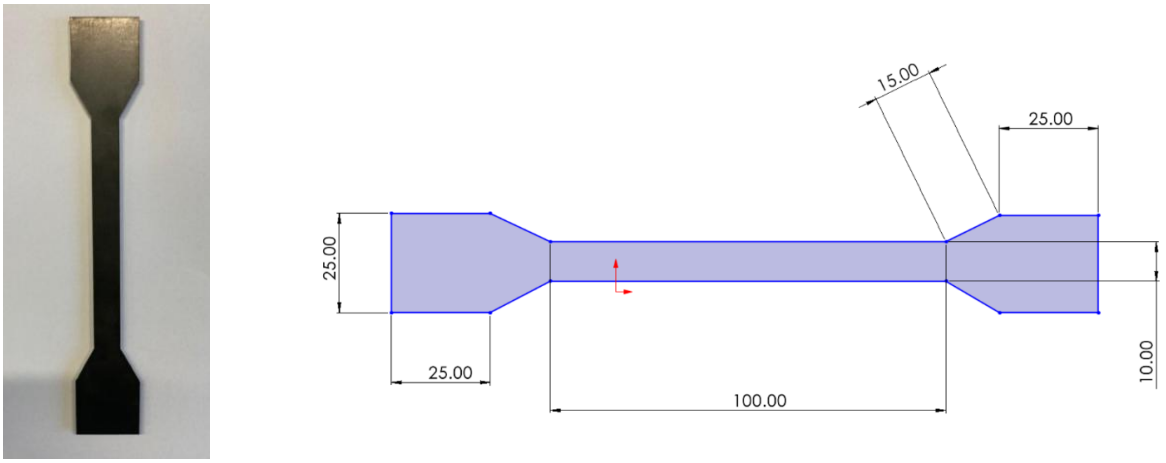
Where E is the Young's modulus. Unlike conventional metal alloys, Nitinol exhibits a nonlinear stress-strain response due to stress-induced martensitic transformation [12,14]. As the applied stress increases, the material transitions from elastic deformation into a transformation plateau, followed by post-transformation hardening at higher strains. Static tensile testing provides information regarding the elastic stiffness, transformation behaviour, strain accommodation mechanisms, and overall mechanical response of the material under monotonic loading conditions [12,14,16].

Nitinol sheets with a specified A_F of 55 °C were obtained from Resonetics Smart Materials Inc. (New Hartford, NY, USA). These sheets were machined into dogbone specimens using a WAZER waterjet cutter (Solid Print3D Ltd, UK). An example of a machined dogbone specimen is shown in Figure 3.3. The feed rates for cutting varied between 6.80 and 8 mmmin^{-1}, depending on whether the sections were angled or flat. Following fabrication, the specimens were cleaned and deburred using a diamond file to ensure safe handling and minimise edge defects.

Four dogbone specimens were produced, consisting of one sacrificial specimen and three test specimens (#1–3). Each dogbone specimen had a thickness of 2 mm. Tensile testing was then conducted using an Instron 3367 universal testing machine, as shown in Figure 3.4. Four tensile tests were conducted with a fixed cross-head speed of 2 mmmin^{-1} in for each test, allowing the stress–strain response to be compared directly across specimens. The first specimen served as a sacrificial sample to estimate the failure load of the Nitinol. This test indicated that failure occurred at approximately 22 kN. A clip-on extensometer was attached to the specimen up to 10 kN, which was then removed to prevent instrument damage while maintaining reliable strain measurement in the elastic and transformation regimes.

It should be noted that the Nitinol material used for the static tensile and dynamic characterisation tests were not sourced from the same material batches or suppliers used to manufacture the Nitinol end-caps with A_F temperatures of 35 °C and 45 °C or the Nitinol wire with an A_F of 30 °C investigated in the chapters 4-5. This approach was adopted owing to the limited availability of the original end-cap, wire materials and time constraints. The static and dynamic characterisation results should be interpreted as providing a representative

understanding of the thermomechanical behaviour of Nitinol rather than a direct characterisation of the specific materials used in the transducer fabrication.



(a) Waterjet cut Nitinol specimen.

(b) Dimensions of Nitinol dogbone, mm.

Figure 3.3 – Nitinol dogbone.

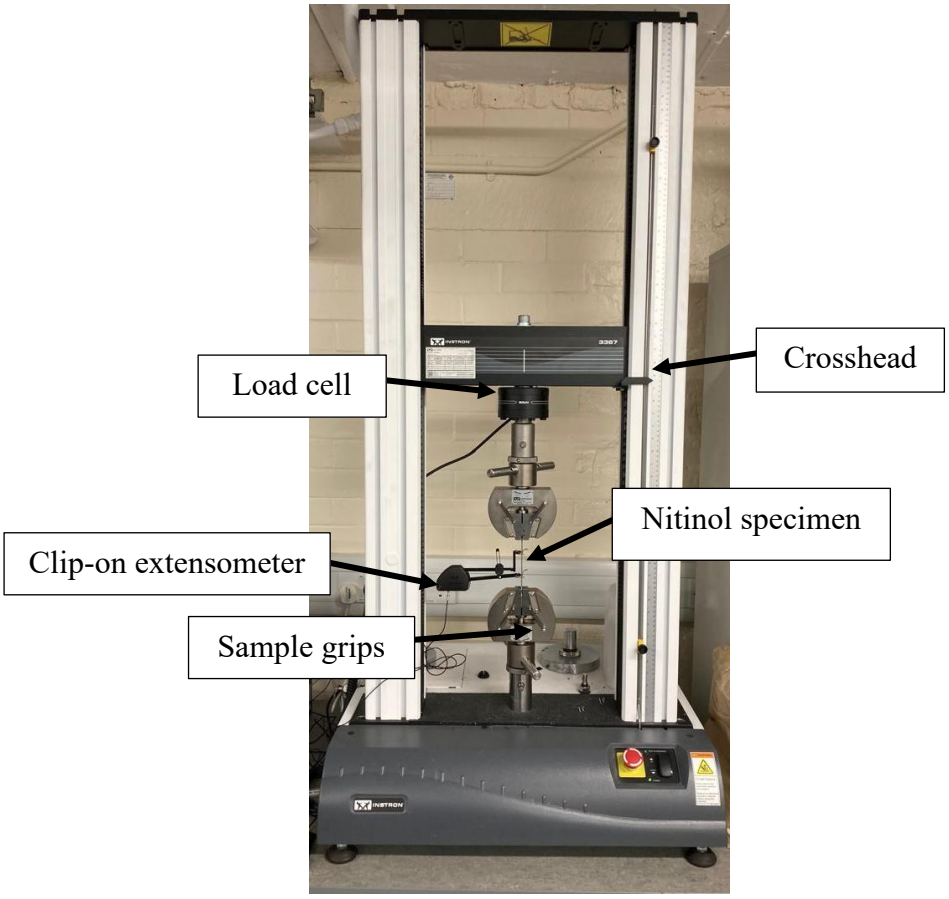


Figure 3.4 – Tensile test setup.

3.1.4. Dynamic mechanical characterisation

While static tensile testing characterises the material response under applied loads, ultrasonic transducers operate under cyclic loading conditions where energy storage and dissipation mechanisms become dominant. DMA was employed to investigate the temperature-dependent dynamic behaviour of the Nitinol specimens. DMA enables direct measurement of displacement amplitude, storage modulus, loss modulus, and mechanical loss factor (*tan δ*) under controlled oscillatory loading. These parameters describe how stiffness and damping evolve with temperature and provide a quantitative assessment of how mechanical energy is stored and dissipated within the material.

In DMA, a sinusoidal strain is applied according to:

$$\varepsilon(t) = \varepsilon_0 \sin(\omega t) \qquad (3.4)$$

where ε_0 is the strain amplitude and ω is the angular frequency. The resulting stress response is phase shifted and can be expressed as:

$$\sigma(t) = \sigma_0 \sin(\omega t + \delta) \qquad (3.5)$$

Where σ_0 is the stress amplitude and δ is the phase lag between stress and strain. This phase lag arises due to internal energy dissipation mechanisms within the material and forms the basis for determining the dynamic mechanical properties.

The dynamic response of the material can be separated into elastic and dissipative components through the storage modulus, E', and loss modulus, E'' [170-172]. The storage modulus represents the elastic energy stored and recovered during each loading cycle and is given by:

$$E' = (\sigma_0 / \varepsilon_0) \cos \delta \qquad (3.6)$$

The loss modulus quantifies the energy dissipated during cyclic deformation and is defined as:

$$E'' = (\sigma_0 / \varepsilon_0) \sin \delta \qquad (3.7)$$

The damping behaviour of the material is commonly expressed through the loss factor, *tan δ*:

$$\tan \delta = E''/E' \qquad (3.8)$$

which represents the ratio of dissipated energy to stored energy during each loading cycle. These parameters provide insight into how the stiffness, damping, and energy dissipation characteristics of Nitinol evolve with temperature. Such measurements are particularly relevant for ultrasonic transducer applications, where resonance behaviour, vibration amplitude, and energy transfer efficiency are strongly influenced by the dynamic mechanical properties of the constituent materials [170-172].

DMA is particularly suitable for characterising Nitinol because the alloy exhibits significant temperature-dependent variations in stiffness and internal friction associated with phase transformation and microstructural rearrangement [170-172]. By measuring the storage modulus, loss modulus, and *tan δ*, DMA captures both the elastic and dissipative components of material behaviour that cannot be fully resolved through static tensile testing alone. The displacement amplitude measurements additionally provide insight into changes in material compliance with temperature, which is relevant to understanding the temperature-dependent vibration response of ultrasonic transducers.

Rectangular specimens were fabricated from the same Nitinol sheets used to produce the tensile test specimens. The samples measured 30 × 6 × 1.5 mm and were machined using the same waterjet cutting process. DMA measurements were conducted using a DMA 8000 system (Perkin Elmer, MA, USA). The specimens were mounted within the instrument clamps as shown in Figure 3.5.

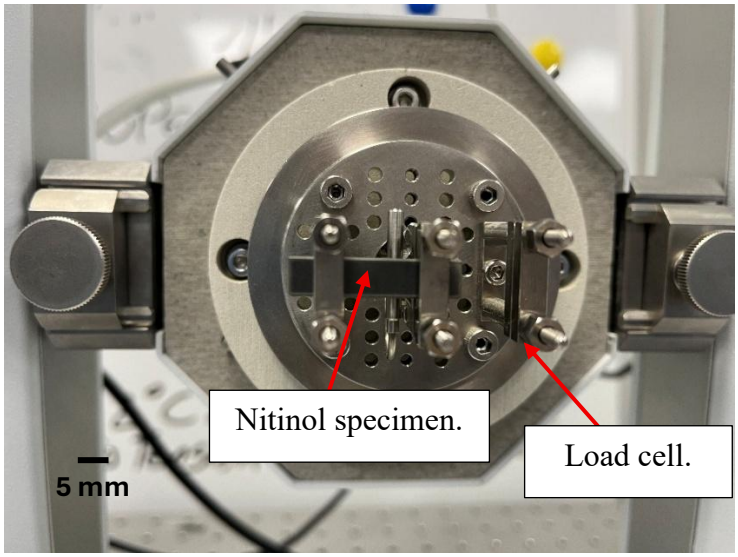


Figure 3.5 – Nitinol sample mounted on load cell of DMA 8000.

DMA was performed over a temperature range of 25–75 °C in order to span temperatures below, through, and above the A_F temperature of 55 °C. This range enabled continuous observation of changes in displacement amplitude, stiffness, and damping as the material progressed through the phase transformation regime. Temperature increments of 3 °C were selected to provide sufficient resolution to identify transformation-related trends while maintaining experimental stability and practical testing durations.

A static force of 0 N was applied to avoid preloading the specimen and to ensure that the measured response reflected intrinsic temperature-dependent behaviour rather than

stress-induced effects. A dynamic force amplitude of 2 N was selected to maintain oscillatory loading within the linear viscoelastic regime, allowing reversible material behaviour to be characterised without inducing permanent deformation or detwinning. The test frequency was set to 1 Hz to characterise the low-frequency dynamic mechanical response of Nitinol under quasi-static cyclic loading conditions. At this frequency, inertial effects are negligible and the measured response is governed primarily by viscoelastic and phase-transformation-related mechanisms.

Together, the static tensile and dynamic mechanical analyses provide complementary information regarding the behaviour of Nitinol. The tensile tests establish the fundamental stress–strain response and transformation characteristics under monotonic loading, whereas DMA characterises the evolution of stiffness and damping under cyclic loading conditions. Collectively, these techniques provide a mechanical framework for interpreting the temperature-dependent electromechanical behaviour observed in the Nitinol-based ultrasonic transducers.

3.2. Results from experimental characterisations

3.2.1. Results from DSC

DSC thermograms were generated for the 31 samples. A DSC thermogram, such as the example shown in Figure 3.6, shows measured heat flow as a function of temperature during controlled cooling and heating. A sample is subject to a cycle of heating and cooling and the endothermic reaction on heating shows the transition from the austenite start (A_S) to the A_F; the austenite peak (A_P) is also identified. From Figure 3.6, the A_F value of sample #9 is 35 °C which matches with the A_F value of the Nitinol sheet provided by the supplier.

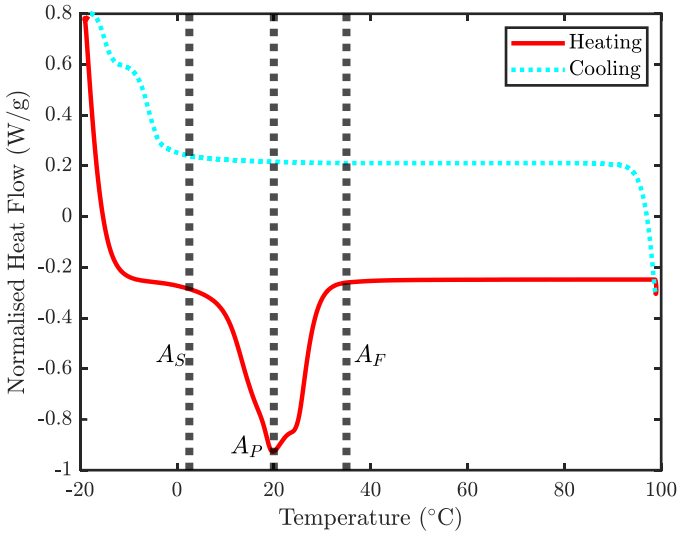
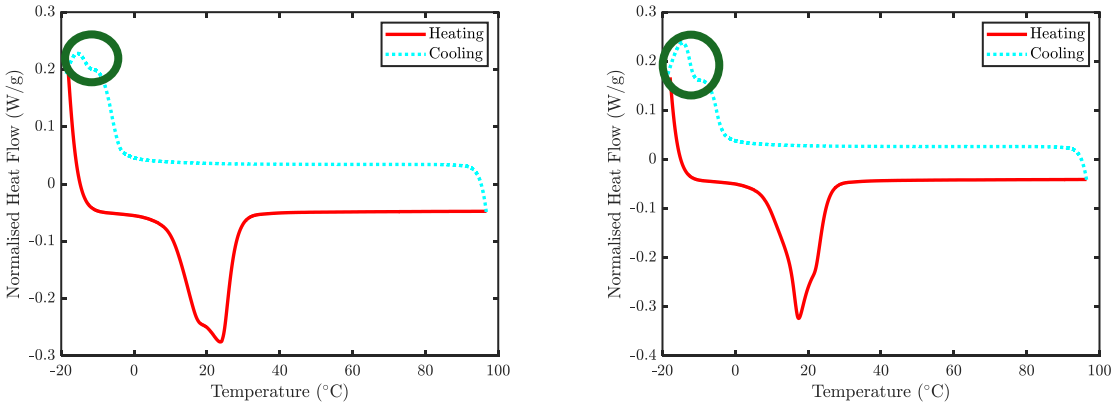


Figure 3.6 – DSC thermogram of sample #9 (edge region).

As can be seen in Figure 3.6, a double peak occurs with A_P being identified with the more dominant (larger negative heat flow) peak. Double peaks were observed in many of the thermograms, for samples #2, 6, 9-10, 13, 17, 21-22, 24-26, and 30-31, two of which are shown in Figure 3.7. In some cases, A_P was at a higher temperature peak and in some cases at a lower temperature as seen in the figure. In some samples # 1, 5, 7-8, 11, 14, and 16, a double peak also occurred at the end of the cooling cycle (green circles).



(a) Sample # 13 (slanted region). (b) Sample # 11 (apex surface).

Figure 3.7 – DSC thermogram of samples with additional peaks before/after the A_P temperature.

The double peaks shown during heating reflect the occurrence of an intermediate transformation stage, namely the R-phase. The R-phase is well documented for NiTi alloys as a transitional phase between martensite and austenite [7,12,27-29]. Its presence in a DSC

thermogram indicates that the Nitinol end-caps undergo a multi-step transformation sequence rather than a single-phase transition. The *Ms* and M_F temperatures were not supplied by the manufacturer and the thermograms also show that the martensite transformation was not fully captured by the temperature range of the tests. However, it was sufficient to confirm the multiphase transformation behaviour of the Nitinol end-caps.

Figure 3.8 presents the DSC thermogram of wire sample #1, showing an A_F of 29.61 °C.

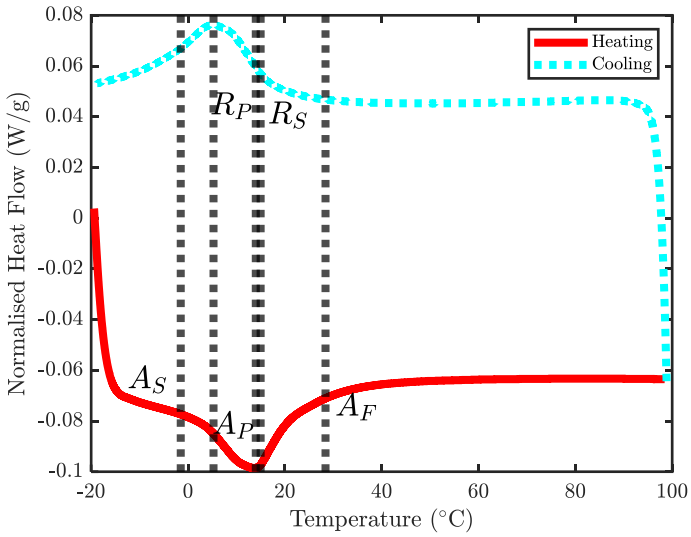


Figure 3.8 – DSC thermogram of wire sample #1.

As seen in Figure 3.8, the A_S, A_P, A_F, rhombohedral start (R_S) and peak (R_P) temperatures were identified. The rhombohedral finish temperature (R_F) could not be identified within the temperature range.

The thermal hysteresis between the endothermic and exothermic reactions in Nitinol is a key indicator of the type of phase transformation occurring. Thermal hysteresis is defined as the temperature separation between corresponding transformation features observed during heating and cooling and is indicative of the energy barrier associated with a phase transformation. While martensitic transformations in Nitinol are typically associated with large hysteresis windows due to the significant lattice strain involved, the R-phase transformation is characterised by a much smaller hysteresis, reflecting its low-strain and more reversible crystallographic nature [29]. In the DSC measurement of the Nitinol wire (Figure 3.8), the

transformation features exhibit a narrow hysteresis and small enthalpy changes, together with subtle peak morphology. These characteristics are consistent with an austenite–R-phase transformation rather than a martensitic transformation. The absence of large transformation peaks and wide hysteresis windows indicates that martensitic behaviour was not activated within the measured temperature range, while the presence of small, reversible features confirms the occurrence of an intermediate R-phase transformation [27-29].

Figure 3.9 shows a DSC thermogram for Nitinol end-cap samples (A_F 45˚C).

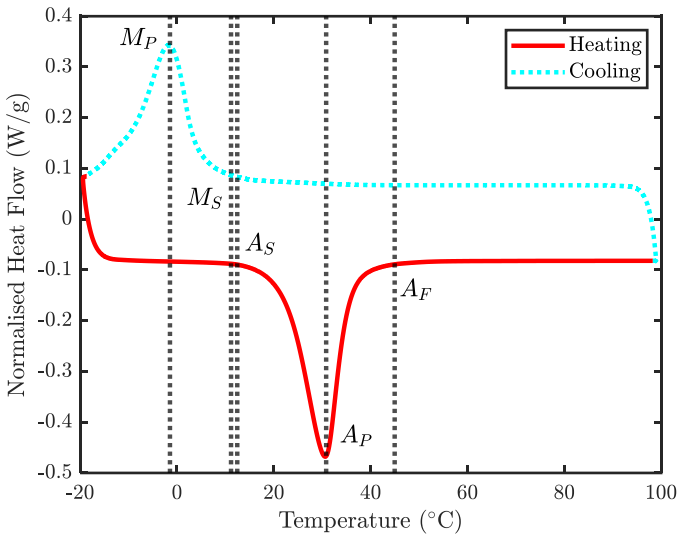
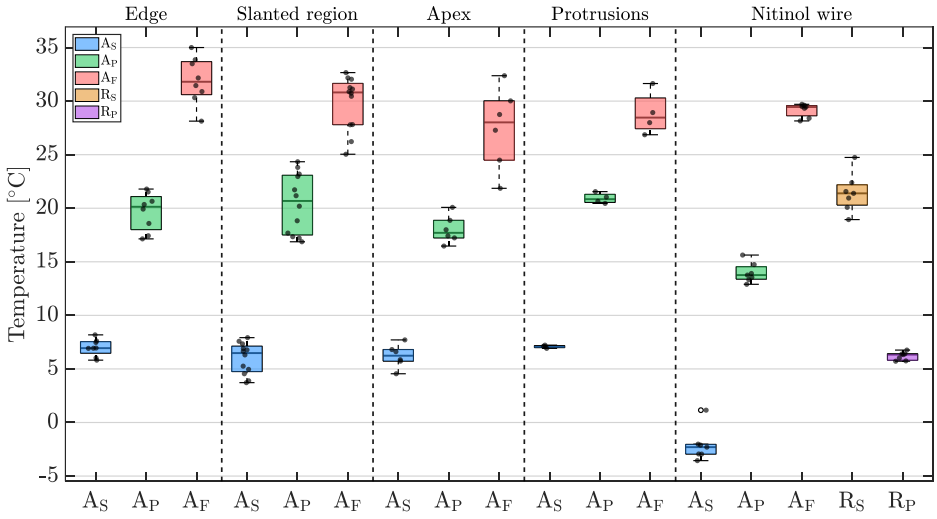


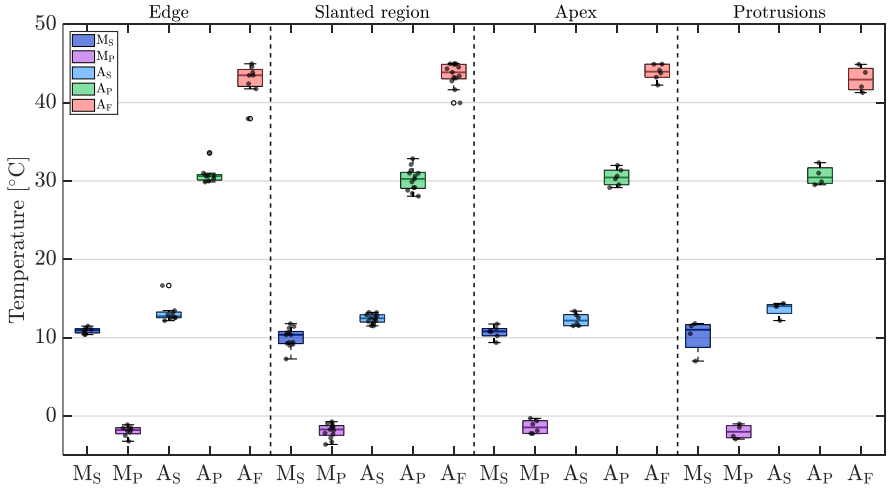
Figure 3.9-DSC thermogram of end-cap sample #1 (Edge region).

From Figure 3.9, the A_F of the Nitinol end-cap edge sample is 44.96 °C which closely matches with the 45 °C A_F temperature value provided by Kellogg's Research Labs. From Figure 3.9, the martensite peak during cooling and the austenite trough during heating can be clearly seen and are well separated from the surrounding baseline. This clear peak–trough structure was observed consistently across all 31 Nitinol samples tested with a higher transformation temperature, allowing the transformation temperatures to be identified with clarity. The thermograms shown in Figures 3.6-3.7 exhibit less distinct features, with additional peaks that obscure the individual transformation events. As a result, the martensite peak and austenite trough are not as clearly observable in these lower transformation temperature samples, highlighting the improved clarity of the phase transformation signatures at the higher transformation temperature.

Figure 3.10 gives a box and whiskers plot for the transformation temperatures of 31 samples from different regions of the Nitinol end-caps (A_F: 35 °C and 45 °C) and seven Nitinol wire specimens (A_F: 30 °C). The box-and-whisker plots for the A_F 35 °C end-cap and A_F 30 °C wire configurations have been presented as a grouped set, as this particular end-cap and wire attachment combination was selected for extensive evaluation in Chapter 4, followed by wire integration in Chapter 5 and surgical cutting assessments in Chapter 6.



(a) Transformation temperatures of the A_F 35 °C Nitinol end-cap regions and the A_F 30 °C Nitinol wire specimens.



(b) Transformation temperatures of the A_F 45 °C Nitinol end-cap regions.

Figure 3.10 - Box and whiskers plots for transformation temperatures of end-caps (A_F 35 °C and A_F 45 °C) and Nitinol wire (A_F 30 °C).

Figure 3.10a presents box-and-whisker plots of the transformation temperatures measured from 31 Nitinol end-cap specimens with an A_F of 35 °C together with seven Nitinol wire specimens having an A_F of 30 °C. The end-cap specimens were grouped according to their extraction location within the component, namely the edge, slanted region, apex, and protrusions. For each group, the As, A_P, and A_F temperatures were obtained from DSC analysis. The wire specimens were additionally characterised by the presence of an R-phase transformation, allowing determination of the R_P and Rs temperatures.

The results demonstrate that transformation behaviour varied across the different end-cap regions (A_F of 35 °C). The edge region exhibited relatively consistent transformation temperatures, with As values between 5.8 and 8.18 °C, A_P values between 17.14 and 21.79 °C, and A_F values between 28.13 and 35.0 °C. The protrusion specimens displayed the narrowest distributions among the end-cap regions, with A_P values ranging from 20.45 to 21.55 °C and A_F values ranging from 26.86 to 31.64 °C indicating comparatively uniform local transformation behaviour within the protrusion features. While the A_P values remained relatively consistent, the A_F values were lower than those measured at the edge, indicating that completion of the austenitic transformation occurred at lower temperatures within the protrusion region.

Greater variability was observed within the slanted and apex regions. The slanted region exhibited the greatest overall spread across the austenite transformation temperatures, with As ranging from 3.72 to 7.92 °C, A_P ranging from 16.87 to 24.34 °C, and A_F ranging from 25.04 to 32.66 °C. The apex region displayed the largest variability in A_F with values ranging from 21.86 to 32.37 °C. The lower A_F values observed in portions of the apex suggest that localised variations in material condition may exist within this region. Although the slanted and apex regions both exhibited broader transformation temperature distributions than the edge and protrusion regions, the apex displayed the most pronounced reduction in A_F temperature.

The Nitinol wire specimens exhibited lower variability than the fabricated end-cap specimens. The wire As, A_P, and A_F temperatures ranged from −3.56 to 1.15 °C, 12.9 to 15.63 °C, and 28.15 to 29.7 °C, respectively. In addition, a distinct R-phase transformation was consistently observed, with R_P temperatures between 5.72 and 6.76 °C and R_s temperatures between 18.94 and 24.74 °C. The comparatively narrow distributions of both the austenite and R-phase

transformation temperatures indicate that the wire material retained a more uniform thermomechanical condition than the fabricated end-cap specimens.

An analysis of variance (ANOVA) followed by Bonferroni post-hoc testing was performed to evaluate statistical differences between groups. The analysis showed that the wire A_S and A_P temperatures were significantly different ($p < 0.05$) from those measured within the end-cap specimens. However, this result was expected because the wire material originated from a different supplier and possessed an A_F temperature approximately 5 °C lower than that of the end-cap material. For the end-cap regions, the only statistically significant difference identified was between the A_F temperatures of the edge and apex groups. No statistically significant differences were observed between the wire A_F temperatures and those of the end-cap regions, indicating substantial overlap between the measured A_F distributions despite their differing nominal transformation temperatures.

The observed transformation temperature variability may arise from local material heterogeneity together with manufacturing-induced effects associated with the wire-EDM fabrication process. Wire-EDM is known to introduce residual stresses and local HAZs that may influence phase transformation behaviour in Nitinol [151-152]. These effects can alter the local thermomechanical state of the material and contribute to regional differences in transformation temperatures. The statistically significant difference observed between the edge and apex A_F temperatures suggests that such localised variations may be present within portions of the fabricated end-cap [151-153].

A limitation of the present study (Figure 3.10a) is that only 31 end-cap specimens and seven wire specimens were analysed. While this sample population was sufficient to identify general trends and perform statistical comparisons, a larger number of specimens would be required to establish the full extent of regional variability and improve statistical confidence. No DSC measurements were performed on the as-received end-cap stock material prior to wire-EDM fabrication. The relative contributions of inherent material variability and manufacturing-induced effects could not be isolated and should be investigated in future work.

The A_F 45 °C end-cap exhibited relatively uniform transformation behaviour across all investigated regions (Figure 3.10b). The edge specimens showed M_S, M_P, A_S, A_P, and A_F temperatures of approximately 10.43–11.48 °C, –3.21 to –1.11 °C, 12.18–16.66 °C, 29.88–33.58 °C, and 37.96–44.96 °C, respectively. With the exception of a single lower A_F value, the

majority of specimens exhibited A_F temperatures above 40 °C, indicating consistent transformation characteristics within this region.

The slanted region displayed the greatest overall spread in transformation temperatures, with M_S ranging from 7.29–11.79 °C, M_P from –3.62 to –0.72 °C, A_S from 11.51–13.23 °C, A_P from 28.06–32.85 °C, and A_F from 39.97–44.96 °C. Despite this broader distribution, the measured values remained clustered within relatively narrow temperature ranges and overlapped with those of the other regions.

The apex and protrusion regions exhibited transformation temperatures comparable to those measured in the edge and slanted regions. The apex specimens showed A_F temperatures between 42.24 and 44.91 °C, while the protrusions exhibited A_F temperatures between 41.28 and 44.89 °C. Although some local variability was observed, particularly within the slanted region, the overall distributions were similar across all regions.

ANOVA performed on the M_S, M_P, A_S, A_P, and A_F temperatures identified no statistically significant differences between the edge, slanted region, apex, and protrusion groups ($p > 0.05$). Bonferroni testing likewise revealed no statistically significant pairwise differences between any regions. These results indicate that the observed regional variations were small relative to the overall specimen-to-specimen variability and suggest that the A_F 45 °C end-cap exhibited a largely homogeneous transformation response throughout the fabricated component.

Despite the difference in nominal transformation temperature, several similarities were observed between the A_F 35 °C and A_F 45 °C end-cap materials. In both cases, measurable variability in transformation temperatures was present between specimens extracted from different regions of the end-cap, with the slanted region generally exhibiting the broadest distributions. The transformation temperatures measured within the edge, slanted, apex, and protrusion regions showed substantial overlap, indicating that the materials did not consist of distinct transformation-temperature populations. While the A_F 35 °C end-cap exhibited a statistically significant difference between the edge and apex A_F temperatures, no statistically significant regional differences were identified for the A_F 45 °C end-cap.

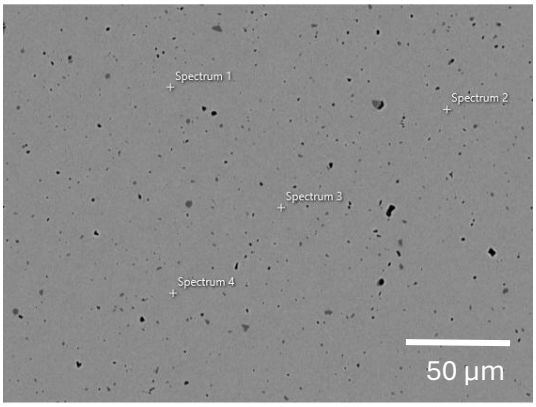
3.2.2. Results from EDXS

BSE images of individual Nitinol endcap and wire sections were obtained, and randomly distributed spectrum locations were assigned as specified in Figure 3.11. An EDXS elemental spectrum was created for each location (Figure 3.11), and Table 3.1 in the lists the determined elemental composition in weight percent (wt%).

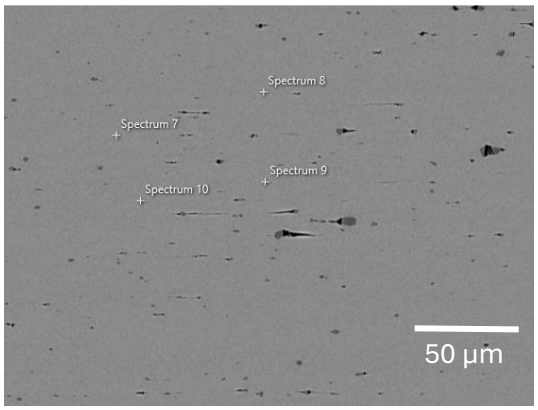
The spectra represent specific locations or regions of interest within the end-cap sections or wire specimens. Spectrum numbers are automatically assigned by the Oxford Instruments Aztec software. From each spectrum, elemental plots are generated, providing the elemental composition (wt%) of the end-cap and wire specimens.

EDXS identifies the elements present at each measurement location from their characteristic X-ray energies. In an EDXS spectrum, the x-axis represents X-ray energy in kiloelectronvolts (keV), while the y-axis represents the detected X-ray count rate per unit energy, expressed as counts per second per electronvolt (cps/eV). Peaks occurring at characteristic energies correspond to specific elements, while their relative intensities provide an indication of the relative abundance of those elements. The detected peaks are quantified to determine the elemental composition at each spectrum location, which is reported here as weight percentage (wt%) [18,20-21].

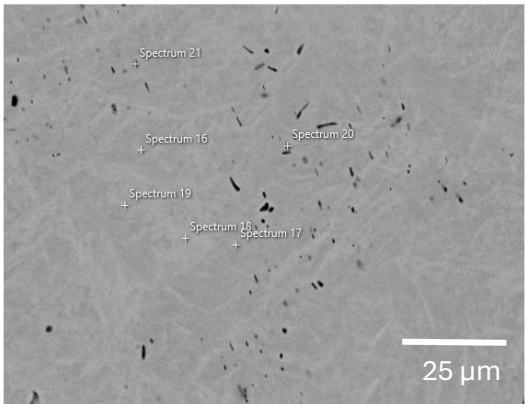
An EDXS spectrum was obtained for each location shown in Figure 3.11, and the resulting elemental compositions are presented in Table 3.1. Comparison of the spectra therefore enables local variations in the elemental composition of the Nitinol end-cap and wire specimens to be identified. Examples of the EDXS results for the wire face, wire length, end-cap edge, apex, protrusion and slanted regions are presented in Figures 3.12-3.16.



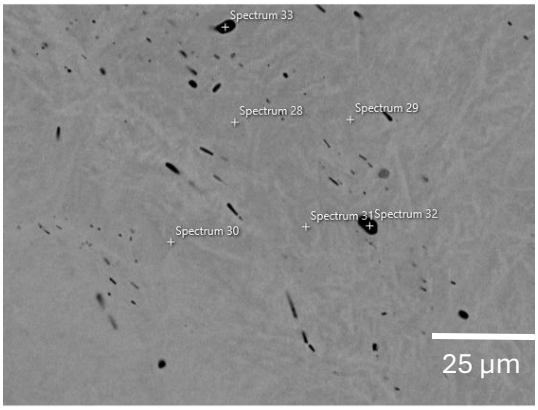
(a)



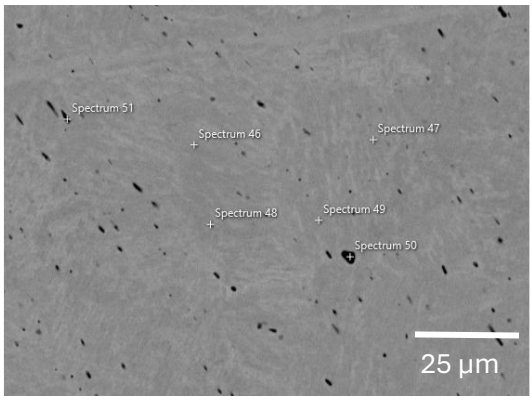
(b)



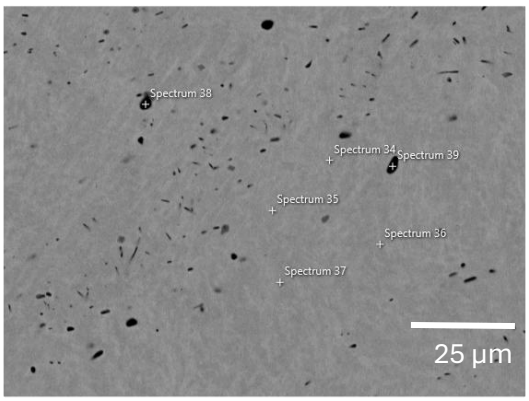
(c)



(d)

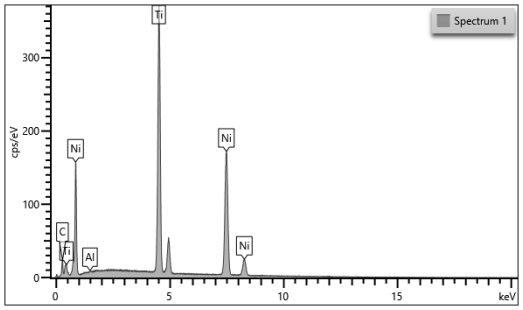


(e)

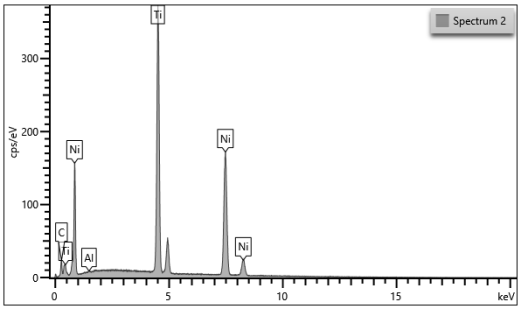


(f)

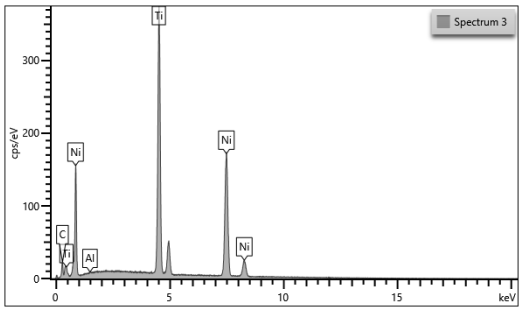
Figure 3.11 - BSE images and spectrum positions of (a) wire face, (b) wire length, (c) endcap edge, (d) apex, (e) protrusion and (f) slanted region.



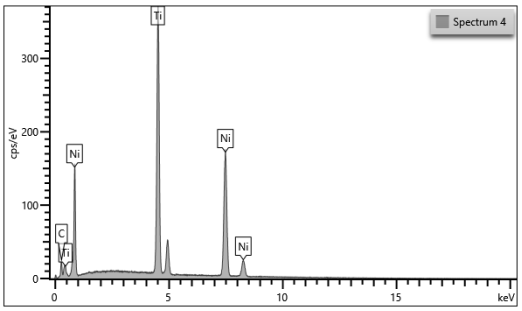
(a)



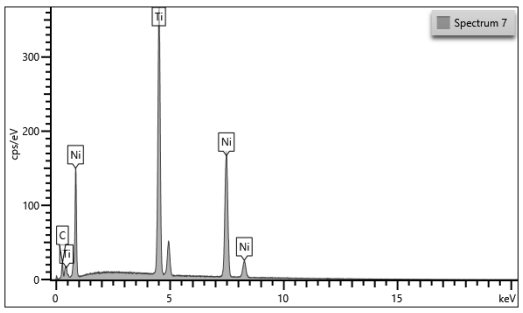
(b)



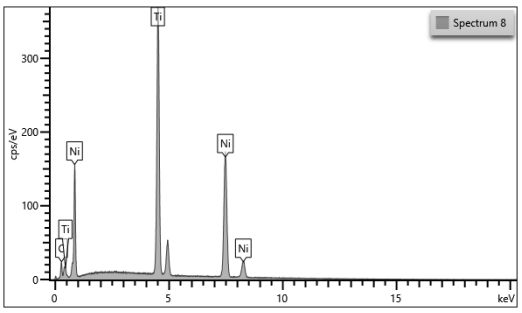
(c)



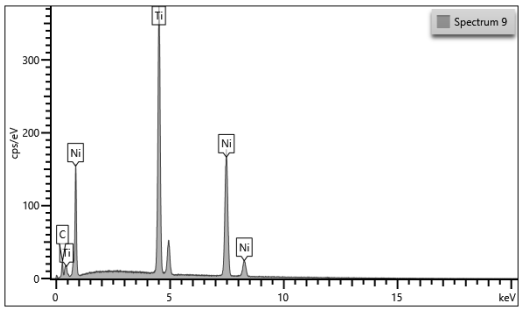
(d)



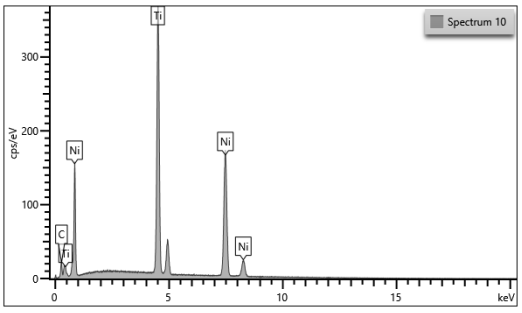
(e)



(f)

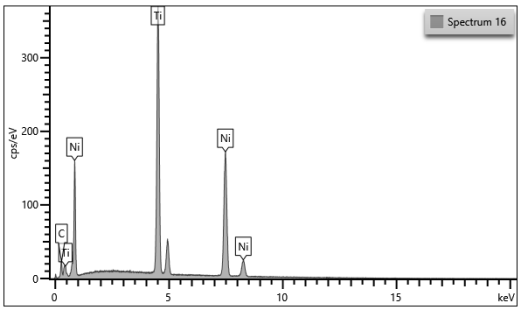


(g)

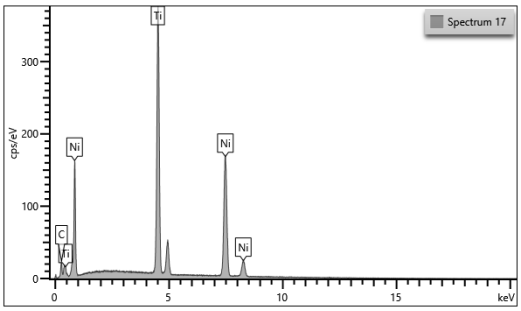


(h)

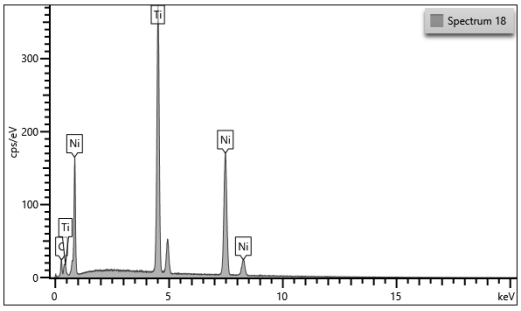
Figure 3.12 - Elemental composition of (a-d) wire face spectra 1-4 and (e-h) wire length spectra 7-10.



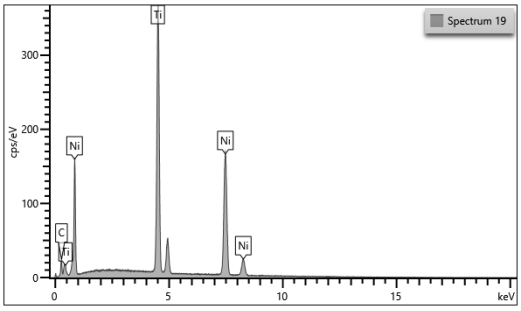
(a)



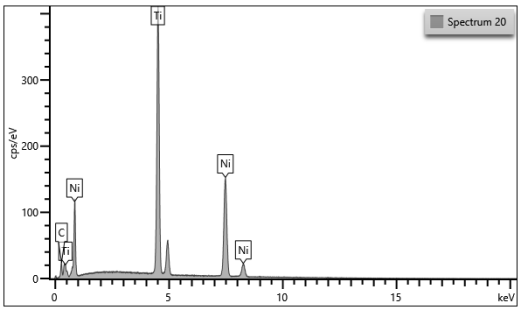
(b)



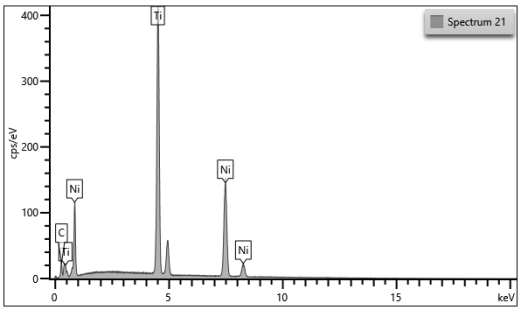
(c)



(d)

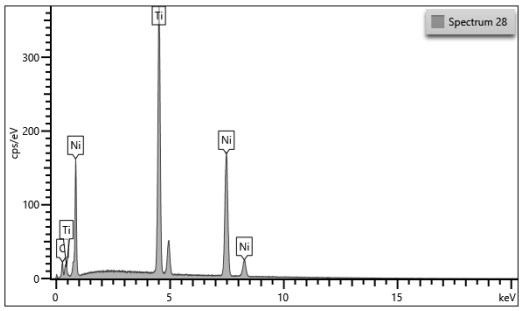


(e)

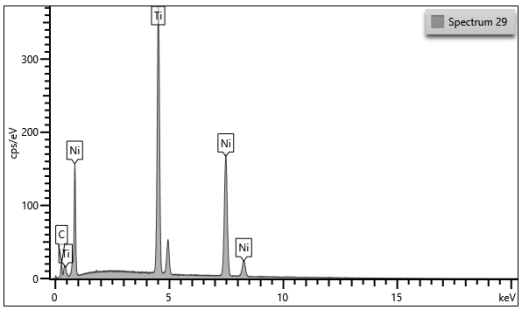


(f)

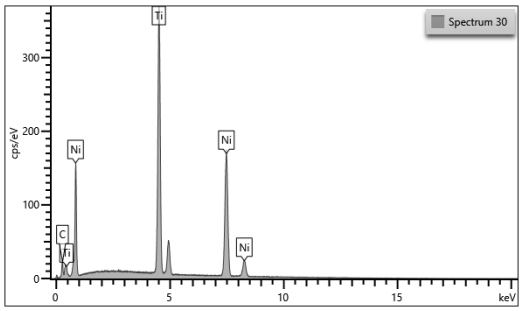
Figure 3.13 - Elemental composition of (a-f) end-cap edge spectra 16-21.



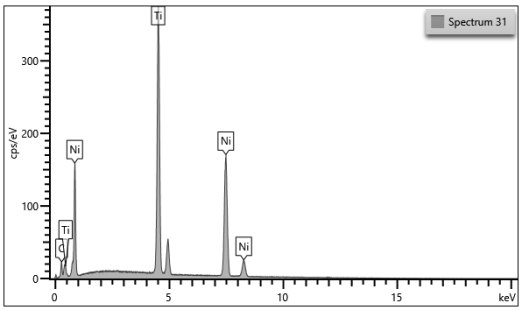
(a)



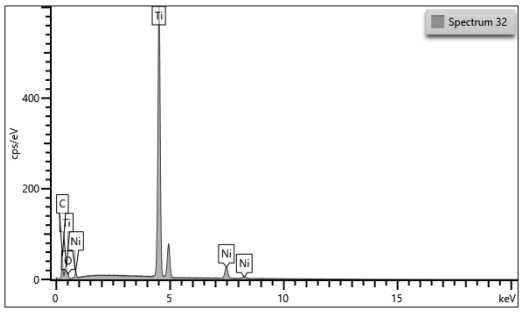
(b)



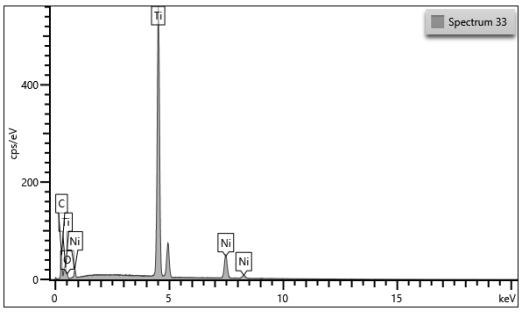
(c)



(d)

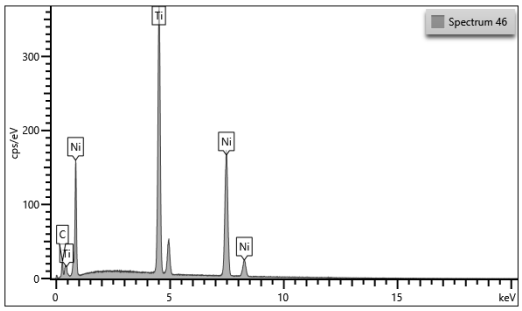


(e)

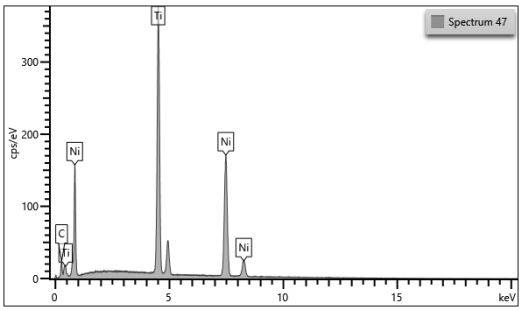


(f)

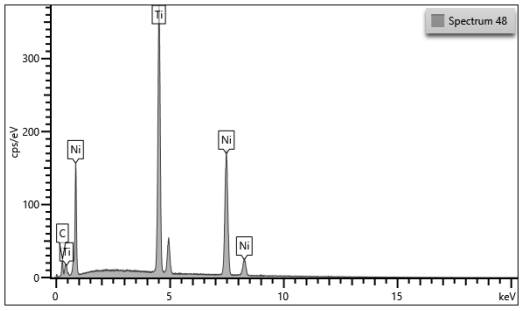
Figure 3.14 - Elemental composition of (a-f) end-cap apex spectra 28-33.



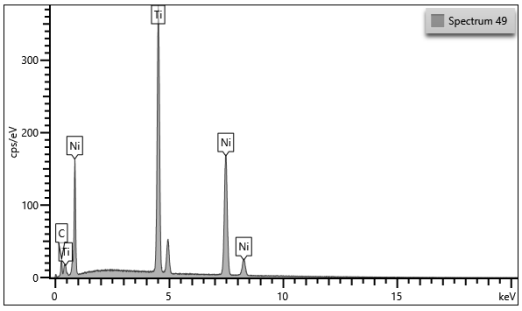
(a)



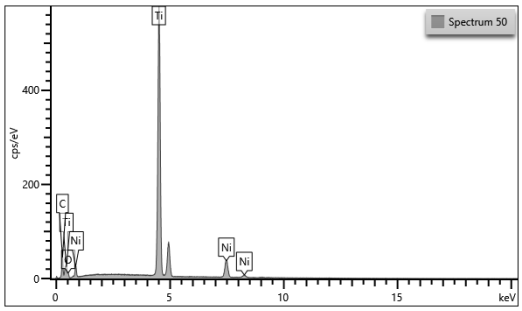
(b)



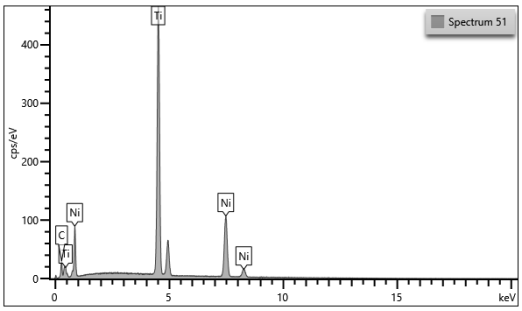
(c)



(d)

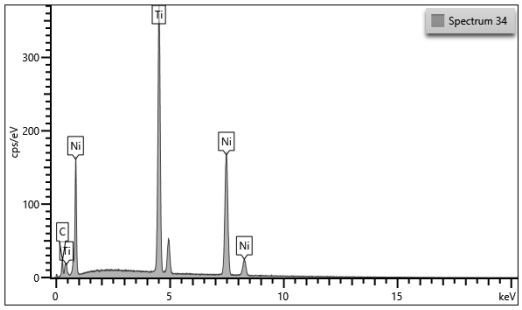


(e)

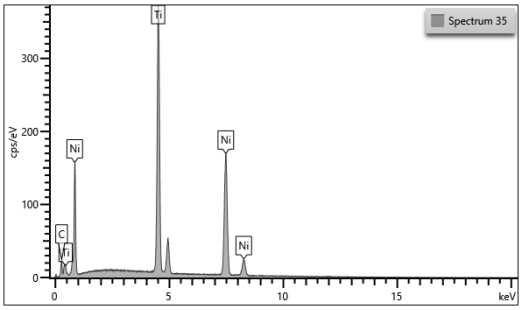


(f)

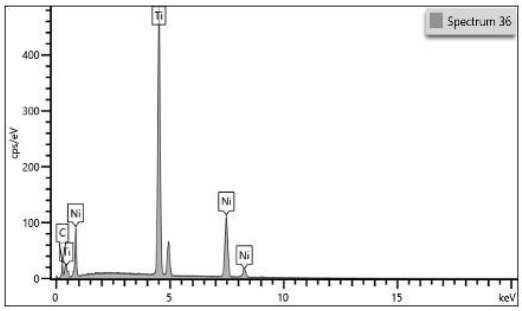
Figure 3.15 - Elemental composition of (a-f) end-cap protrusion spectra 46-51.



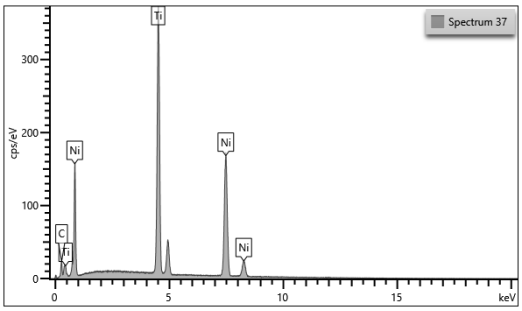
(a)



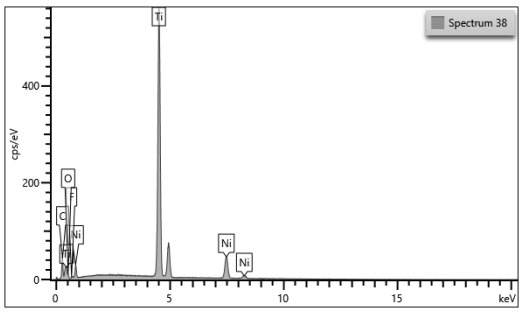
(b)



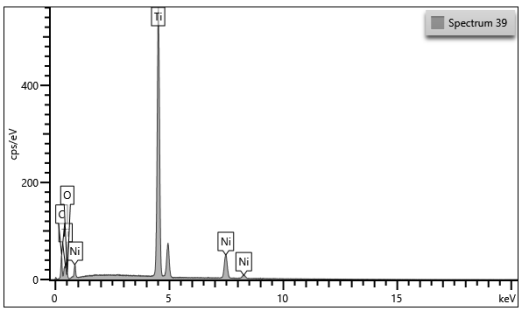
(c)



(d)



(e)



(f)

Figure 3.16 - Elemental composition of (a-f) end-cap slanted region spectra 34-39.

Location	spectrum	Ni (wt%)	Ti (wt%)	O (wt%)	Fe (wt%)
Wire face	1	55.43	44.57	NA	NA
Wire face	2	55.12	44.88	NA	NA
Wire face	3	55.30	44.70	NA	NA
Wire face	4	55.19	44.81	NA	NA
Wire length	7	55.46	44.54	NA	NA
Wire length	8	55.16	44.84	NA	NA
Wire length	9	55.11	44.89	NA	NA
Wire length	10	55.16	44.84	NA	NA
Endcap edge	16	55.02	44.98	NA	NA
Endcap edge	17	54.95	45.05	NA	NA
Endcap edge	18	54.92	45.08	NA	NA
Endcap edge	19	54.85	45.15	NA	NA
Endcap edge	20	49.74	50.26	NA	NA
Endcap edge	21	48.55	51.45	NA	NA
Endcap apex	28	55.02	44.98	NA	NA
Endcap apex	29	54.68	45.32	NA	NA
Endcap apex	30	55.16	44.84	NA	NA
Endcap apex	31	54.79	45.21	NA	NA
Endcap apex	32	9.51	81.13	9.36	NA
Endcap apex	33	17.67	74.53	7.8	NA
Endcap protrusion	46	54.98	45.02	NA	NA
Endcap protrusion	47	54.86	45.14	NA	NA
Endcap protrusion	48	55.02	44.98	NA	NA
Endcap protrusion	49	55.03	44.97	NA	NA
Endcap protrusion	50	13.93	77.12	8.95	NA
Endcap protrusion	51	38.07	61.93	NA	NA
Endcap slanted	34	55.11	44.89	NA	NA
Endcap slanted	35	54.72	45.28	NA	NA
Endcap slanted	36	54.86	45.14	NA	NA
Endcap slanted	37	54.81	45.19	NA	NA
Endcap slanted	38	16.77	73.82	6.82	2.59
Endcap slanted	39	18.31	74.34	7.35	NA

Table 3.1- Wt% compositions of wire face, wire length, and end-cap cross-section, protrusion, apex, and slanted region spectra.

The EDXS spectra (Figures 3.12-3.16) confirmed the presence of Ni and Ti, with minor contributions from C and Al. The carbon and aluminium signals are attributed to the polishing and sample preparation and are therefore not considered in Table 3.1. In addition, all the spectra (Figure 3.12-3.16) exhibit a minor Ti Kβ peak adjacent to the main Ti Kα peak, corresponding to a secondary characteristic X-ray emission line of titanium alloys [173]. Such secondary peaks are commonly observed in EDXS analyses of titanium-containing materials and arise from electron transitions between different atomic energy levels following inner-shell ionisation. The presence of the Ti Kβ peak is an expected feature of the titanium spectrum and serves to further confirm the presence of titanium within the analysed specimens rather than indicating the presence of an additional phase or elemental constituent [173].

Literature indicates that variations in the Ni and Ti content of Nitinol (Ni-Ti) can influence the transformation temperatures of the SMA. An increase in Ni content relative to Ti lowers the transformation temperature [174-175], whereas a higher Ti content relative to Ni raises it [161]. The elevated Ni concentrations of up to 55.5 %wt are consistent with a comparatively low A_F of 30 °C (wire) and 35 °C (end-cap), determined by DSC measurements.

However, the BSE and EDXS analysis revealed the presence of impurities in the end-cap specimens, visible as dark areas in Figure 3.11, resulting in a non-equiatomic Ni-Ti composition where particularly in the end-cap apex, protrusion and slanted regions the wt% of Ni fell below 20%, accompanied by substantially higher Ti concentrations. The magnitude of these local variations is greater than the relatively small changes in Ni/Ti composition discussed in the literature [161,174-175], and the cited studies do not report Ni/Ti variations of a comparable magnitude. The low-Ni (wt% of Ni <20%) measurements should not be interpreted as evidence of uniform Ni depletion from the Ni–Ti lattice throughout the end-cap. Instead, they indicate discrete, chemically distinct regions within the analysed surface. EDXS alone cannot determine whether these variations result from Ni removal from the Ni–Ti lattice or from the presence of a distinct local phase or surface region; therefore, the precise mechanism responsible for the observed Ti-rich and Ni-depleted compositions cannot be established from the present measurements.

These spatial variations in Ni/Ti ratios, together with measurable oxygen and iron content (Figures 3.12–3.16 and Table 3.1), suggest local material inhomogeneity, at least at the surface, which may be related to the Wire-EDM fabrication process and associated residual stresses and local heat-affected zones (HAZs) [153,162,174–175]. In addition, the presence of oxygen

(Table 3.1) is a common impurity in Nitinol arising from the melting and processing stages and is known to stabilise the austenite phase, thereby lowering transformation temperatures and degrading superelastic and shape memory performance while increasing hardness and brittleness [174-176]. Iron impurities similarly reduce transformation temperatures by substituting for nickel in the Ni–Ti matrix and can further diminish the SME and corrosion resistance at elevated concentrations [174-176].

For ultrasonic transducers incorporating Nitinol components, these findings have important design and modelling implications. The sensitivity of transformation temperatures to trace impurities means that nominally identical Nitinol parts may exhibit different thermomechanical responses if processing routes are not tightly controlled. In the context of ultrasonic operation, this can lead to variations in stiffness, damping, and effective boundary conditions as temperature changes, even when bulk composition remains within specification. From a practical standpoint, the integration of Nitinol into ultrasonic transducers benefits from careful control of material condition and processing history. The use of aged (heat-treated to stabilise its microstructure and transformation behaviour) or fully annealed (heat-treated to relieve internal stresses and maximise ductility) Nitinol [135], minimisation of oxygen ingress during machining, and sourcing material with certified narrow transformation temperature ranges would reduce component-to-component variability.

3.2.3. Results from static tests

Figure 3.17 illustrates the stress-strain relationship derived from the measured data. All tensile tests are presented in terms of engineering stress-strain and were conducted at room temperature.

The stress-strain curves for Specimens #1 and #2 terminate at 8% strain because these tests were intentionally conducted within a conservative loading range and were stopped well below the failure load, with the maximum applied load limited to approximately 10 kN. Specimen #3 was loaded to approximately 20 kN, close to the ultimate failure load of 22 kN, to fully characterise the post-transformation hardening behaviour of the material. Only Specimen #3 captures the complete stress-strain response through Region D.

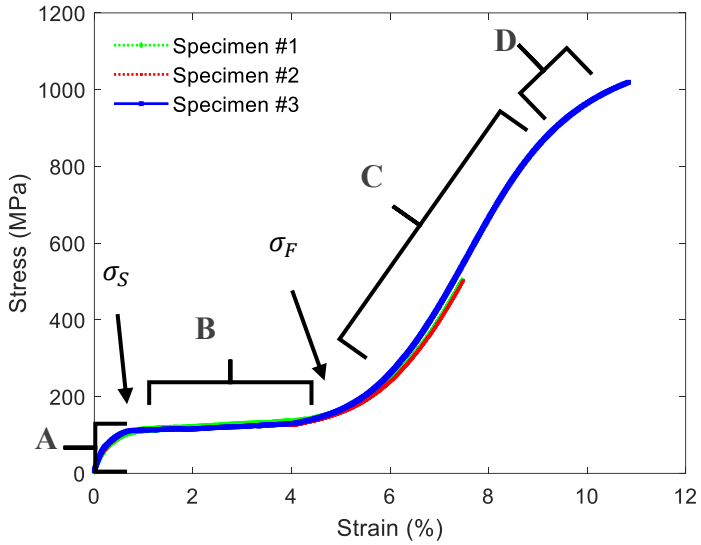


Figure 3.17 – Stress-strain relationship for three dogbone samples.

The stress-strain curves divide into three regions A-C plus a fourth region, D for specimen #3, These regions are:

A. The twinned martensite (M^t) region (refer to Figure 1.2). In this region, the material exists in the twinned martensite phase. A martensitic variant refers to a martensitic crystal with a distinct orientation direction, and Nitinol can have up to 24 different martensitic variants [12,14,22]. The twinned martensite phase incorporates a network of twin boundaries that help accommodate strain during transformation [12,14]. When mechanical load is applied, the structure can be detwinned, meaning the martensitic variants reorient to form detwinned martensite (region C). If the Nitinol sample is heated above its A_F temperature, it returns to its original shape due to the SME. For all the dogbone samples, the twinned martensite region extends from 0 to 103.7 MPa (0.55 % strain).

B. The detwinning region. Detwinning is a deformation mechanism in which the twinned martensite phase reorients, eliminating twinned variants [13]. The stress required to initiate this process is called the detwinning start stress (σ_s) which occurs at 105.7 MPa for all samples. As stress increases, detwinning progresses until completion at the detwinning finish stress (σ_F) which is 141.3 MPa. During this process, strain increases as the twin boundaries shift under stress [12,14]. In Figure 3.13, the strain increases up to 4.5 % until detwinned martensite is formed.

C. Detwinned martensite (M^d). In this region, another variant of martensite exists. The Young's modulus of detwinned martensite is higher than that of twinned martensite,

as the latter slips more easily under stress [12-14,22]. If Nitinol is cooled under a mechanical stress greater than σ_s in the austenite phase, the detwinned martensite forms [22]. Shape recovery occurs if the sample is reheated while the stress remains. For specimens #1 and #2, the detwinned martensite phase extends from 150 MPa at 4.83% strain to 500 MPa at 7.49% strain. For specimen #3, the detwinned martensite phase was captured up to 920 MPa at 9.50% strain by retaining the extensometer of the sample up to 20 kN load.

D. In this region, the sample undergoes elongation and necking, leading to fracture. EDXS tests were conducted on specimens extracted from both the fractured regions and the non-fractured dogbone head sections of each tensile sample. The fractured regions represent material that experienced severe localised deformation and damage leading to failure, while the dogbone head sections correspond to regions that were mechanically loaded but did not fracture. This comparative approach enabled assessment of potential regional variations in elemental composition and microstructural response associated with different stress and deformation histories within the same specimen. All fractures occurred outside the central gauge section; this failure location is consistent with the mechanical behaviour of Nitinol dogbone specimens. Unlike conventional metals such as titanium, Nitinol undergoes large, recoverable strains associated with martensitic reorientation and detwinning [12,14], which leads to significant strain accommodation within the gauge length. As a result, stress localisation can occur near geometric transitions between the gauge section and the wider head regions, where stiffness and constraint change abruptly. In these regions, the material experiences a combination of axial stress and local stress concentration, making fracture initiation at or near the specimen heads more likely. The observed failure locations therefore reflect the unique deformation mechanisms of Nitinol.

The EDXS specimens were sectioned using the WAZER waterjet cutter (Solid Print3D Ltd, UK). Figure 3.18 shows the BSE images of the fractured/non-fractured regions of the three dogbones.

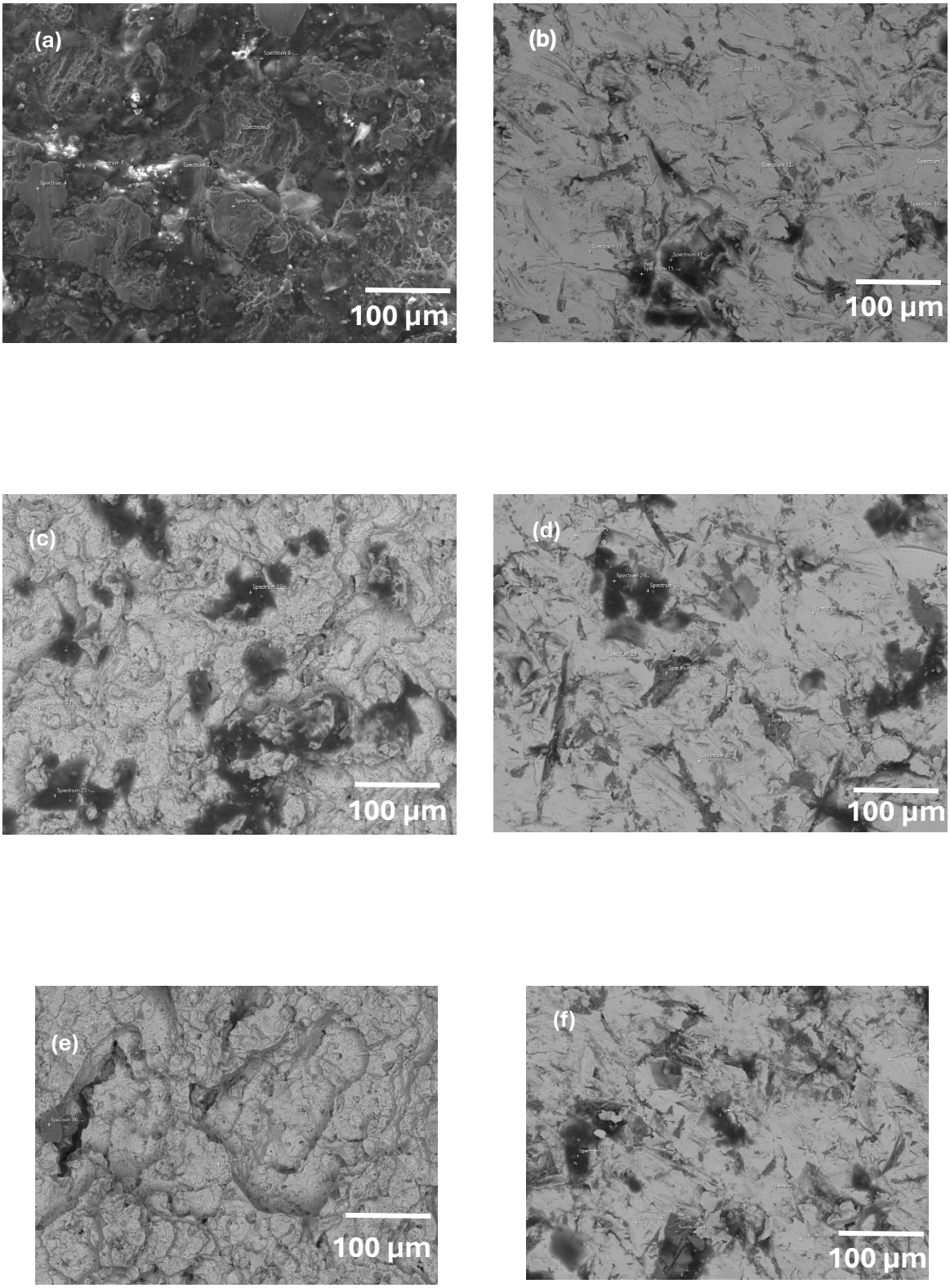


Figure 3.18 – BSE images of dogbone specimens. (a) Fractured area for specimen #1. (b) Unfractured area for specimen #1. (c) Fractured area for specimen #2. (d) Unfractured area for specimen #2. (e) Fractured area for specimen #3. (f) Unfractured area for specimen #3.

From Figure 3.18, the grey regions corresponded to EDXS measurement locations containing substantial concentrations of silicon and iron, with sulphur additionally detected at one location. Spectrum 16 (Figure 3.18b) contained 19.14 wt% Si and 28.63 wt% Fe, spectrum 30 (Figure 3.18d) contained 20.59 wt% Si and 32.24 wt% Fe, while spectrum 40 (Figure 3.18f) contained 19.34 wt% Si, 1.11 wt% S and 37.94 wt% Fe. These measurements demonstrate that the grey-contrast regions exhibit a local elemental composition distinct from the surrounding Ni–Ti matrix. The precise origin of the Si, S and Fe cannot be established from the post-fracture EDXS measurements alone. These elements may have been present within the material prior to testing or introduced during material processing, machining or specimen preparation; therefore, their source cannot be conclusively determined from the present analysis.

In the fracture zones, a higher percentage of oxygen was also detected. Titanium possesses a strong affinity for oxygen, and previous studies have reported the formation of TiO_2 precipitates, oxygen-rich zones, and oxide particles within Nitinol alloys subjected to thermomechanical processing and service environments [174–176]. These oxygen-containing features have been associated with changes in the local mechanical behaviour of the material and have been identified as potential sites for crack initiation in Nitinol alloys [174–176].
It should be noted that EDXS measurements were only performed on the dogbone post-fracture. The elemental distributions present prior to fracture were not characterised, and it is therefore not possible to determine whether the observed silicon-, sulphur-, iron-, or oxygen-rich regions existed in the same form before mechanical testing or whether they directly contributed to crack initiation. The local stress distributions associated with these regions were not measured. As a result, the observed elemental concentrations should be interpreted as post-fracture compositional observations rather than definitive evidence of the fracture mechanism.
The Nitinol dogbone specimen tests give insights into how the mechanical behaviour of the Nitinol material affects the performance of an ultrasonic transducer incorporating this material. They show that the Nitinol can exhibit martensitic and austenitic phase transitions under stress [16]. As the stiffness of Nitinol increases in the austenite phase, the ultrasonic transducer will experience an increase in the resonance frequency. From the stress-strain relationships (Figure 3.17), the detwinning process (105.69 MPa to 141.30 MPa) and subsequent high-stress regions show that the material has high energy absorption and shape recovery properties. This means that if Nitinol is incorporated in a transducer, which undergoes repeated stress cycles, the material can exhibit good fatigue resistance. The repeatable stress–strain response observed

across the three dogbone specimens indicates consistent material behaviour under controlled loading, providing confidence in the predictability of the mechanical response. These results emphasise the importance of maintaining operating stresses within the reversible transformation regime to avoid accumulated damage. The tensile characterisation supports informed design decisions regarding allowable strain levels, geometry selection, and stress distribution in Nitinol-based ultrasonic transducers, contributing to reliable and repeatable dynamic performance within safe operational limits.

3.2.4. Results from dynamic tests

Figure 3.19 reveals key insights into the phase transitions of the Nitinol specimen.

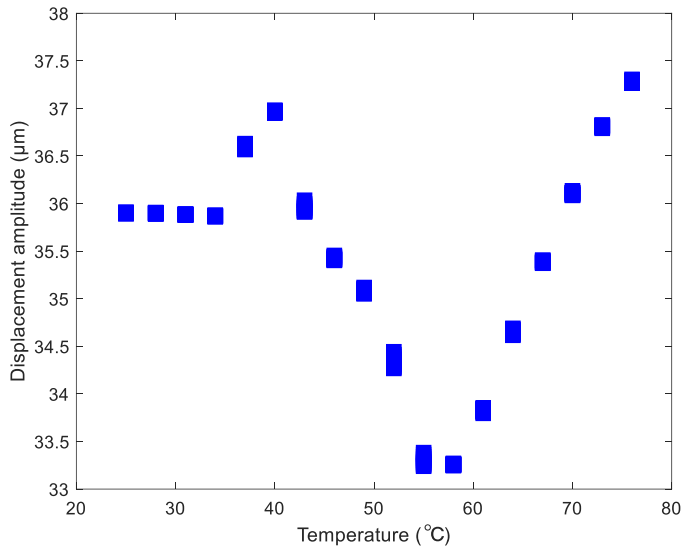


Figure 3.19 – DMA analysis of Nitinol specimen with A_F of 55 ˚C.

The displacement amplitude measured during DMA provides an indirect measure of the Nitinol specimen's dynamic compliance under a constant oscillatory load. For a fixed dynamic force amplitude, variations in displacement amplitude reflect changes in the material's stiffness, which is known to differ between the martensitic and austenitic phases. Between 25 and 35 °C, the displacement amplitude remains approximately constant, indicating that the specimen remains predominantly in the martensitic phase, where the material exhibits lower stiffness.

From 35 to 40 °C, the detwinned martensite begins to initiate the transformation into austenite. At 40 °C, the A_S temperature is reached at the displacement amplitude peak. This displacement peak is caused by a microstructural change within the lattice as the twinned boundaries of the martensitic crystals reorient. Between 40 and 55 °C, as the material progresses from the A_S to

the A_P temperature, the displacement amplitude gradually decreases. This decrease signifies a loss of energy as the material completes its transition into the austenite phase. Rather than representing a direct loss of energy, this reduction in displacement is consistent with an increase in material stiffness during the transformation, since a stiffer specimen undergoes a smaller displacement under the same applied dynamic load. During this transformation, the lattice structure changes to a body centred cubic (BCC) crystal structure, which reduces lattice length and increases the material's stiffness, characterised by a higher Young's modulus [12-14]. The material has lower stiffness in the martensitic phase at 25–35 °C. Therefore, in this temperature range, an ultrasonic transducer incorporating this Nitinol material would have a lower resonance frequency. Above 40 °C, the resonance frequency would be higher. This change in mechanical properties is crucial for optimising Nitinol-based transducers operating across different temperature ranges.

DMA also enables the measurement of tan δ, E'', and E'. tan δ measures a material's internal friction or damping characteristics, defined as the ratio of the loss modulus to the storage modulus [170-172]. E' represents the ability of a material to store mechanical energy during cyclic deformation, quantifying the amount of energy stored and recovered in each cycle. Meanwhile, E'' describes the viscous energy dissipation of the material, representing the energy lost as heat due to internal friction during deformation [170-172]. These tests were carried out at three distinct temperatures: 25 °C (room temperature), 55 °C (transformation temperature), and 75 °C (final test temperature). Three samples were tested and all tests were conducted under a dynamic stress of 2.8 MPa. Table 3.2 presents the values of these three parameters at the specified temperature points.

Temperature (°C)	tan (δ)	Storage Modulus (E') (MPa)	Loss Modulus (E'') (MPa)
25	0.015	28.72	0.442
55	0.0048	35	0.164
75	0.0047	34.44	0.164

Table 3.2 - DMA presents tan δ, E' and E'' of Nitinol samples at three different temperatures.

At 25 °C, corresponding to the martensitic temperature region, the Nitinol exhibited the lowest measured E' of 28.72 MPa and the highest tan δ value of 0.015. The corresponding E'' of 0.442 MPa was also higher than those measured at 55 and 75 °C. These results indicate lower

stiffness and greater internal damping at 25 °C and are consistent with the greater mobility of the martensitic microstructure, which can accommodate deformation through internal rearrangement and consequently dissipate a greater proportion of the applied mechanical energy during cyclic loading [170–172].

At 55 °C, E' increased to 35.00 MPa, compared with 28.72 MPa at 25 °C, while a similar value of 34.44 MPa was measured at 75 °C. The higher E' measured at both 55 and 75 °C is consistent with the increased stiffness associated with transformation towards the austenitic phase. However, because E' was measured at only three discrete temperatures, the present data are insufficient to establish that E' stabilises continuously over the 55–75 °C temperature range. Rather, the results demonstrate that similar E' values were obtained at the two higher measurement temperatures.

Over the same measurements, E'' decreased from 0.442 MPa at 25 °C to 0.164 MPa at 55 °C and remained at 0.164 MPa at 75 °C. Similarly, tan δ decreased from 0.015 at 25 °C to 0.0048 at 55 °C, with a similar value of 0.0047 measured at 75 °C. These results indicate that mechanical energy dissipation and internal damping were lower at the two higher test temperatures than at 25 °C. This behaviour is consistent with the change in dynamic mechanical response accompanying transformation from the B19′ monoclinic martensitic structure towards the B2 cubic austenitic structure [12–14].

Overall, the displacement amplitude, E', E'' and tan δ measurements provide complementary information on the temperature-dependent dynamic mechanical behaviour of Nitinol. The increase in E' between 25 and 55 °C is consistent with an increase in stiffness, while the corresponding reductions in E'' and tan δ indicate reduced mechanical energy dissipation and internal damping at the higher test temperatures. These properties are directly relevant to Nitinol-containing ultrasonic transducers, since changes in stiffness can influence resonance frequency, while changes in damping affect mechanical energy dissipation and vibration response under cyclic excitation [48].

3.3. Summary

Chapter 3 provides a comprehensive characterisation of Nitinol materials relevant to their integration into ultrasonic transducers, combining thermal, static, and dynamic mechanical testing to link microstructural behaviour with functional performance. DSC confirmed the transformation temperatures and revealed batch-level variability associated with processing and machining, while tensile testing established the stress–strain response and deformation mechanisms under quasi-static loading. DMA further quantified the temperature-dependent

stiffness and damping behaviour, demonstrating how phase transformation governs both elastic energy storage and internal dissipation under cyclic excitation.

Together, these results show that the mechanical response of Nitinol is strongly phase-dependent, with martensitic states exhibiting lower stiffness and higher damping, and austenitic states exhibiting higher stiffness and reduced damping. For ultrasonic transducer applications, this implies that resonance frequency is primarily controlled by phase-dependent stiffness [27-29]. The combined experimental evidence establishes clear design-relevant trends that enable informed material selection and operating-temperature control when integrating Nitinol into ultrasonic devices subjected to cyclic loading.

Building on this material-level understanding, Chapter 4 shifts the focus from characterisation of the Nitinol material to the design, fabrication, and experimental evaluation of class IV flextensional transducers incorporating Nitinol end-caps. The chapter investigates how the unique thermomechanical characteristics of Nitinol influence the electromechanical behaviour of the transducers, including resonance frequency, electrical impedance, mechanical quality factor, displacement amplitude, and power consumption. By comparing Nitinol with conventional end-cap materials such as titanium (Ti-6Al-4V), aluminium (grade 1050A), and stainless steel (grade 316), the chapter establishes the baseline performance of Nitinol-based class IV transducers and provides the foundation for the subsequent integration of Nitinol wires examined in Chapter 5.

Chapter 4

Design, fabrication and characterisation of a class IV transducer

Chapter 4 presents the design, modelling, and experimental validation of a baseline class IV flextensional ultrasonic transducer with end-caps fabricated from titanium (Ti-6Al-4V), aluminium (grade 1050A), stainless steel (grade 316), and Nitinol. Finite element modelling (FEM) is used to predict resonance behaviour and mode shapes, followed by experimental modal analysis (EMA) to validate the dynamic response of the devices. Harmonic response analysis is conducted to evaluate performance under operating conditions, examining how mechanical quality factor, power density, and electrical impedance vary with applied voltage. In addition, the influence of temperature on resonance frequency, mechanical quality factor, and impedance is investigated to assess the suitability of the transducer for tuneable and thermally responsive operation.

4.1. Methodology

4.1.1. Design of class IV transducer

The three essential components required for modelling and fabricating the class IV flextensional transducer are end-caps, piezoelectric ceramic material and a mechanical coupling mechanism (a mixture of epoxy resin and a catalyst). Small geometric differences in end-cap dimensions can produce significant variations in performance, especially when combined with differences in speed of sound between materials. In this study, four geometrically identical class IV flextensional transducers were fabricated and characterised with end-caps made from the following materials:

1. Nitinol (Ni-Ti).
2. Aluminium (1050A).
3. Stainless Steel (grade 316).
4. Titanium (Ti-6Al-4V).

Finite element analysis (FEA) was employed to predict the dynamic behaviour of the class IV flextensional ultrasonic transducers and to support the iterative design process prior to fabrication. The transducers were modelled using the FEA software package (Abaqus-Simulia, Dassault Systèmes, France). The simulations provided insight into the resonance frequencies,

mode shapes, displacement distributions, and electromechanical response of the transducers under varying material conditions. In addition to performance prediction, FEA enabled optimisation of the end-cap geometry and material selection before experimental manufacture and testing.

The operation of the class IV flextensional transducer begins with the piezoelectric plate (geometry commonly used in the class IV transducers [36]), Figure 4.1, which converts electrical excitation into mechanical strain.

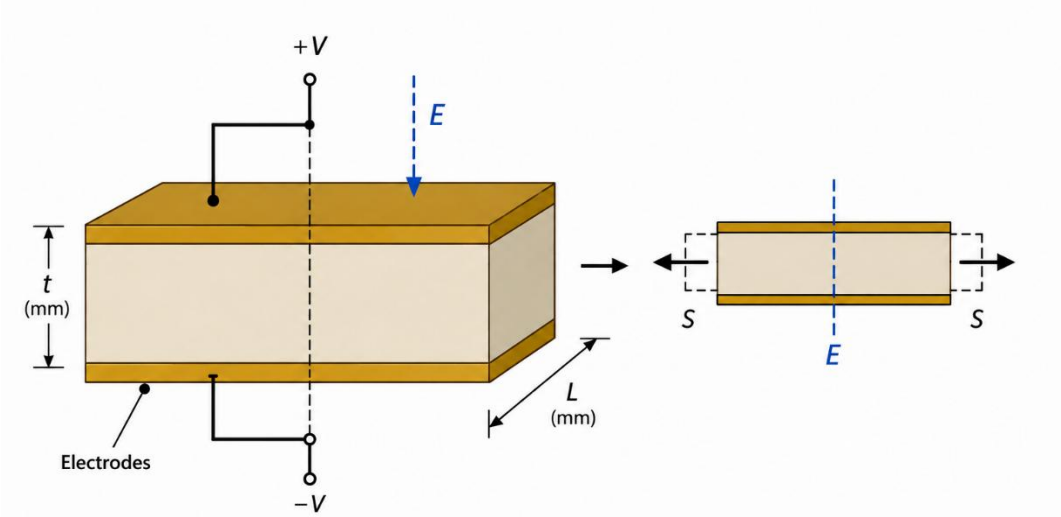


Figure 4.1- Schematic of a piezoelectric plate showing the generation of longitudinal strain and vibration under an applied alternating electric field.

When an alternating electric field is applied across the piezoelectric material, cyclic strain is generated according to:

$$S = dE_{field} \qquad (4.1)$$

where S is the induced mechanical strain, d is the piezoelectric coefficient, and E_{field} is the applied electric field. This cyclic strain produces longitudinal vibration within the piezoelectric element, which is transferred into the surrounding transducer structure [1-3,58,63].

The cyclic strain described by Equation 4.1 causes the piezoelectric plate to undergo repeated expansion and contraction under an alternating electric field. However, because the piezoelectric element has finite length, width and thickness dimensions, this vibration can occur in several characteristic resonant modes. These plate-mode resonances correspond to different deformation directions within the piezoelectric element, with the principal modes comprising length-extensional, width-extensional and thickness modes, as illustrated in Figure 4.2 [58-59].

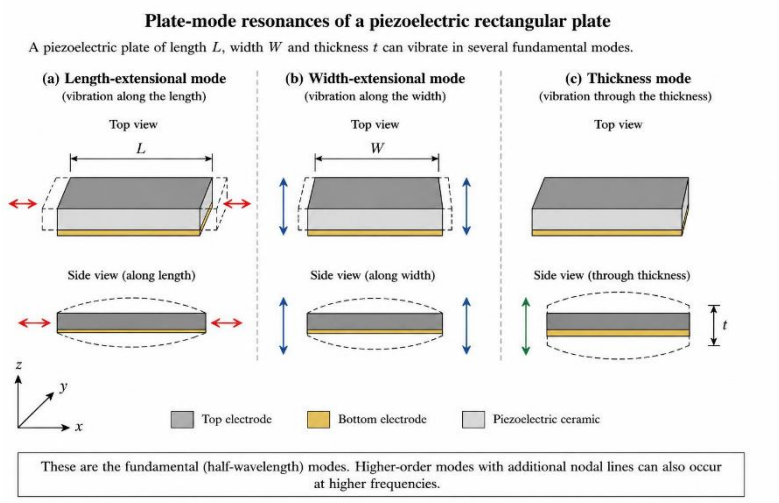


Figure 4.2- Schematic representation of the fundamental plate-mode resonances of a rectangular piezoelectric element.

The fundamental resonance frequency associated with each plate mode is governed by the corresponding plate dimension and the relevant elastic wave velocity within the piezoelectric material. For a rectangular piezoelectric plate of length L, width W, and thickness t, the fundamental length-extensional, width-extensional and thickness-mode resonance frequencies may be approximated respectively as [58-59]:

$$f_L = c_L/2L \quad (4.2)$$

$$f_W = c_W/2W \quad (4.3)$$

$$f_t = c_t/2t \quad (4.4)$$

Where f_L, f_W and f_t are the fundamental resonance frequencies associated with the length, width and thickness modes, respectively while c_L, c_W and c_t are the corresponding elastic wave velocities. These relationships arise from the fundamental standing-wave condition in which the relevant plate dimension corresponds approximately to one-half of the wavelength:

$$\lambda = 2X \quad (4.5)$$

Where X represents the relevant plate dimension (L,W or t). Since wave velocity is related to frequency and wavelength (Equation 2.8), the resonance frequency is inversely proportional to the corresponding plate dimension. For a plate in which the thickness is substantially

smaller than its in-plane dimensions ($t << L,W$), the fundamental thickness-mode resonance generally occurs at a higher frequency than the fundamental in-plane modes.

At the system level, the dynamic behaviour of the transducer is governed by the relationship between effective stiffness and mass, where the natural frequency may be approximated as [1,58-59]:

$$f_n = 1/2\pi \times (k_s/m_{eff})^{0.5} \quad (4.6)$$

where k_s is the effective structural stiffness and m_{eff} is the effective vibrating mass. Variations in end-cap material properties therefore influence the resonance behaviour of the transducer by modifying both stiffness and mass distribution.

In class IV flextensional transducers, the end-cap geometry converts the longitudinal vibration generated by the piezoelectric plate into amplified flexural displacement. The flexural behaviour of the end-caps is governed by the bending rigidity [106]:

$$D = Eh^3/12(1-\nu^2) \quad (4.7)$$

where D is the flexural rigidity, h is the end-cap thickness, and ν is Poisson's ratio. Increasing the bending rigidity increases structural stiffness and alters the flexural resonance behaviour of the transducer [106].

A traditional class IV transducer, Figure 1.6a (Chapter 1), has been modified to enable it to be used for future miniaturised power ultrasonic devices [36]. The modification involved replacing the oval shells with metal end-caps that incorporated protrusions, Figure 4.3, to be affixed to the piezoceramic material with epoxy resin. The end-cap design in Figure 4.3 was implemented for the four transducers and inspired by previous work done with the class IV bone biopsy needle [41].

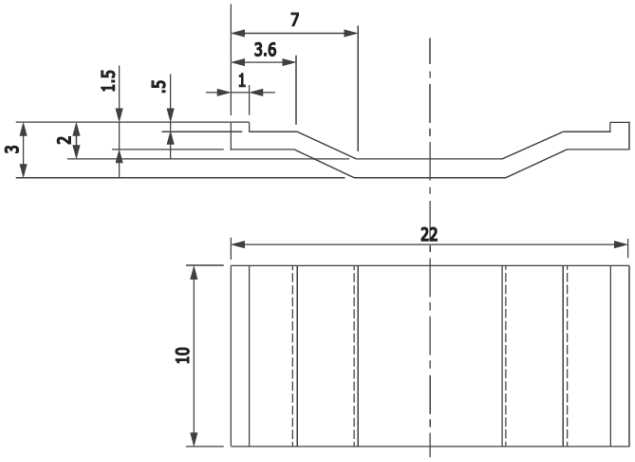


Figure 4.3- End-cap dimensions for class IV flextensional transducers, dimensions in mm.

The end-caps incorporate small protrusions (0.5 mm in height) to enhance mechanical coupling between the piezoceramic and the end-cap. These features locally reduce the effective contact area, thereby increasing the contact pressure according to:

$$P=F/A \quad (4.8)$$

F is the applied preload, and A is the contact area. The increased pressure improves interfacial conformity by reducing microscopic gaps and surface asperities [106].

Improved contact leads to higher interfacial stiffness, which may be approximated as:

$$K_i=EA/L \quad (4.9)$$

K_i is the interfacial stiffness, E is the Young's modulus, A is the effective contact area, and L is the thickness of the interface. A higher interfacial stiffness enables more efficient transmission of vibrational energy from the piezoceramic to the metallic end-cap by minimising losses due to local compliance at the interface. In addition, improved contact reduces acoustic impedance mismatch, promoting better energy transfer into the end-cap structure. These effects collectively enhance vibrational coupling and help maintain stable mechanical contact during both operation and manufacturing [36].

Three-dimensional (3-D) models were developed to accurately capture the geometric complexity of the class IV flextensional transducers. The transducers were modelled as individual components consisting of the end-caps, piezoelectric plate, and epoxy coupling layer. All models incorporated a 0.1 mm thick epoxy layer positioned between the piezoelectric ceramic and the end-cap surfaces. For the metallic end-caps and epoxy resin, the material properties required by the FEA model included density, Young's modulus, and Poisson's ratio and are found in Table 4.1.

Property	Titanium	Aluminium	Stainless Steel	Nitinol	Epoxy resin
Density [kg/m^3]	4,430	2,699	7,850	6,450	1,496
Young's Modulus [GPa]	110	70	200	80	2.75
Poisson's Ratio	0.33	0.33	0.30	0.33	0.35

Table 4.1 - Mechanical properties of end-cap materials and epoxy resin [177-181].

The piezoelectric ceramic required additional dielectric, elastic, and piezoelectric coefficients, which were obtained from the manufacturer's datasheet [182]. The piezoelectric properties of the Pz26 plate are provided in Table 4.2.

Thickness [mm]	3
Length [mm]	20
Breadth [mm]	10
Density [kg/m^3]	7,700
Piezoelectric Radial Charge Coefficient d_{31} [pC/N]	-130
Poisson's Ratio	0.33
Piezoelectric Longitudinal Charge Coefficient d_{33} [pC/N]	300
Mechanical Quality Factor $Q_{m,t}$	>1,000
Curie Temperature T_C [°C]	330

Table 4.2 – Pz26 specimen dimensions and material properties [182].

The material properties listed in Table 4.2 define the electromechanical and structural behaviour of the piezoelectric plate and are critical in determining the performance of the ultrasonic transducer. The geometric parameters (thickness, length, and breadth) define the physical dimensions of the piezoceramic and influence its resonance characteristics and integration within the transducer assembly.

The piezoelectric charge coefficients describe the electromechanical coupling behaviour of the material. The radial coefficient d_{31} represents the strain generated in a direction perpendicular to the applied electric field, while the longitudinal coefficient d_{33} describes the strain in the direction of the applied field [29]. These coefficients determine the efficiency with which electrical energy is converted into mechanical deformation. The mechanical quality factor (Q_m) represents the ratio of stored to dissipated mechanical energy per cycle and is an indicator of damping within the material. A high Q_m corresponds to low internal losses and sharper resonance peaks, which is desirable for efficient ultrasonic energy transmission. Finally, the Curie temperature (T_c) defines the maximum operating temperature of the piezoelectric material, above which it loses its polarisation and piezoelectric properties, making it a critical parameter for ensuring thermal stability during operation [182-183]. This material was chosen due to its simultaneously high T_c, enabling thermal stability under high-power ultrasonic conditions; mechanical quality factor which improves mechanical energy transfer efficiency; its low dielectric loss, reducing electrical dissipation and improving long-term performance consistency and its ability to deliver stable performance over time [183].

In addition to stiffness and piezoelectric coupling, ultrasonic transducer performance is influenced by material losses. These include mechanical losses, which account for internal friction and energy dissipation within the ceramic and end-cap materials, and dielectric losses, which describe energy leakage in the piezoceramic under alternating electric fields [28]. Thermal effects may also contribute, particularly for metallic end-caps such as Nitinol, where hysteresis during phase transformation can introduce additional damping [18,28-29]. While the FEA models used in this study did not directly incorporate all loss mechanisms, their influence was considered qualitatively when comparing simulated results with experimental measurements. Particular attention was given to the symmetric flexural vibration mode, in which the end-caps deform out-of-phase about the central axis as shown in Figure 4.4. This mode is of primary interest for ultrasonic surgical applications because it maximises flexural displacement amplification at the end-cap surfaces, enabling efficient vibration transmission to surgical end-effectors such as cutting blades.

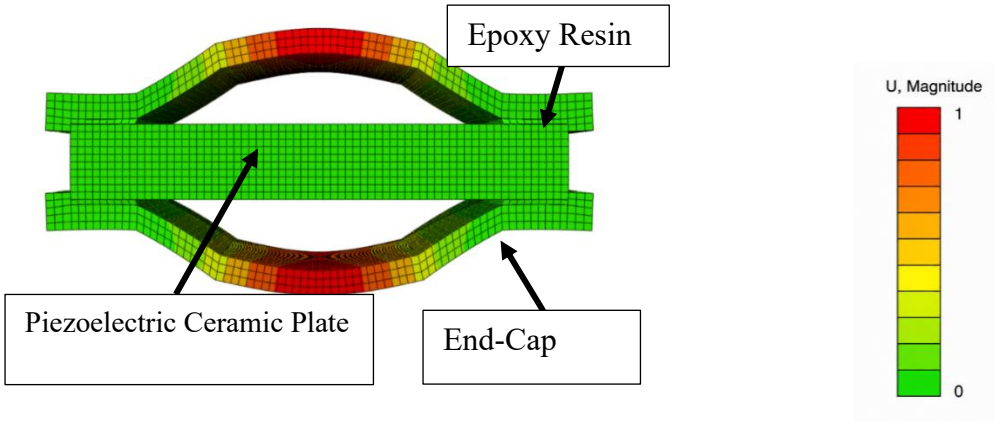


Figure 4.4 - FEA model of the transducer in its symmetric vibration mode. Colour bar illustrating the normalised displacement magnitude (U) used in the FEA contour plot. Values range from 0 (green) to 1 (red), representing minimum to maximum relative displacement, respectively.

The transducer structures were discretised using tetrahedral elements to accurately represent the curved geometries of the flextensional end-caps. A mesh convergence study, Figure 4.5, was performed to ensure that the predicted resonance frequencies and mode shapes were independent of mesh density. Coarse meshes produced inaccurate resonance predictions, whereas excessively fine meshes significantly increased computational expense with minimal improvement in accuracy.

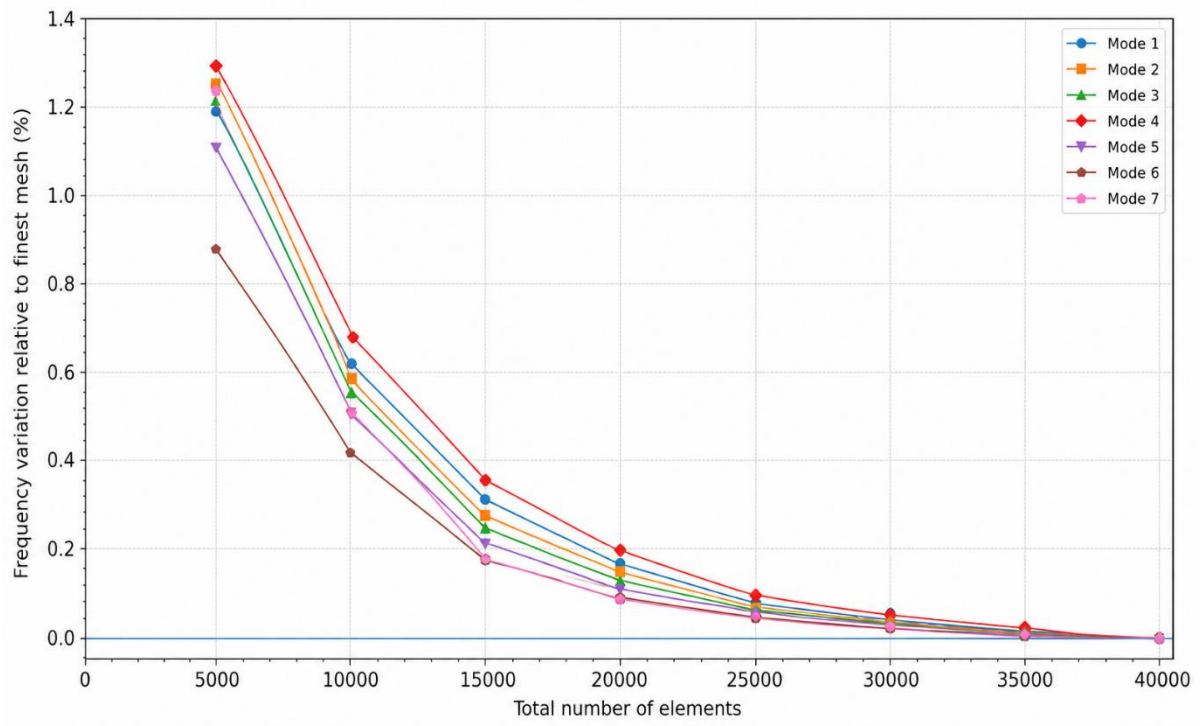
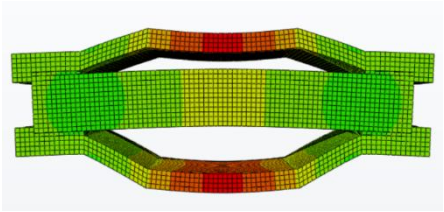
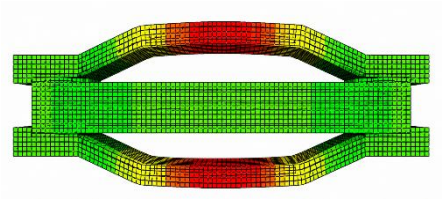


Figure 4.5 - Mesh convergence study showing variation in modal frequencies with increasing element count for the aluminium class IV transducer.

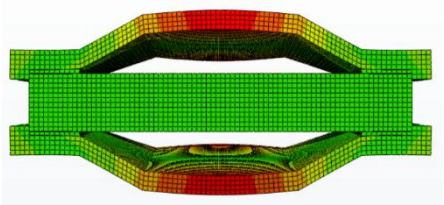
The mesh convergence study demonstrated that beyond approximately 25,000 elements, the variation in the predicted resonance frequencies of the first seven vibration modes remained below 0.5%. A global seed size of 0.0003 m, corresponding to 38,000 elements, was therefore selected as it provided accurate prediction of the transducer vibration modes while maintaining reasonable computational efficiency. The final mesh density was therefore considered sufficiently converged for accurate prediction of the transducer dynamic behaviour, and additional mesh refinement was not pursued due to the minimal improvement in solution accuracy relative to the increased computational expense. The mode shapes of modes 1-7 are visualised in Figure 4.6.



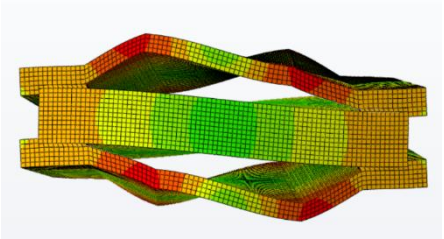
(a) Mode 1: asymmetric mode (23.293 kHz).



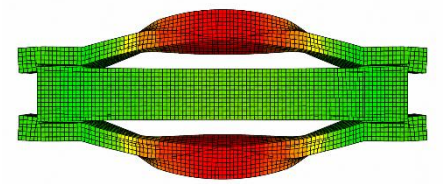
(b) Mode 2: symmetric mode (31.240 kHz).



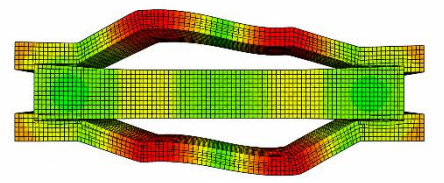
(c) Mode 3: asymmetric flexural mode (32.325 kHz).



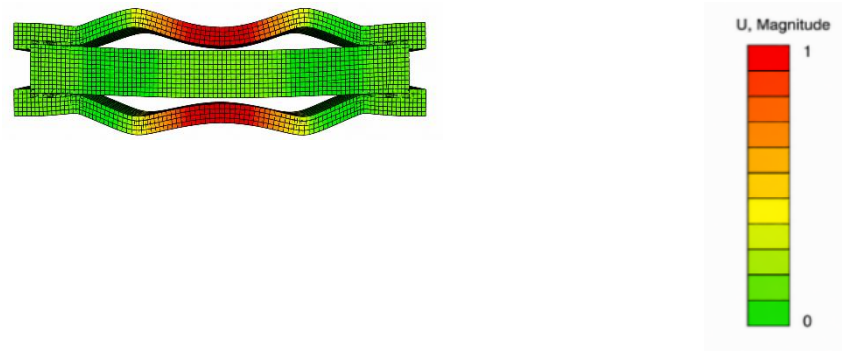
(d) Mode 4: torsional mode (38.374 kHz).



(e) Mode 5: symmetric (thickness-breathing) mode (45.345 kHz).



(f) Mode 6: higher order flexural mode (55.452 kHz).



(g) Mode 7: second-order symmetric flexural mode (60.350 kHz).

Figure 4.6 - Finite element modal analysis results showing the vibration mode shapes of the class IV flextensional transducer having alumnium end-caps.

4.1.2. Fabrication and assembly of transducers

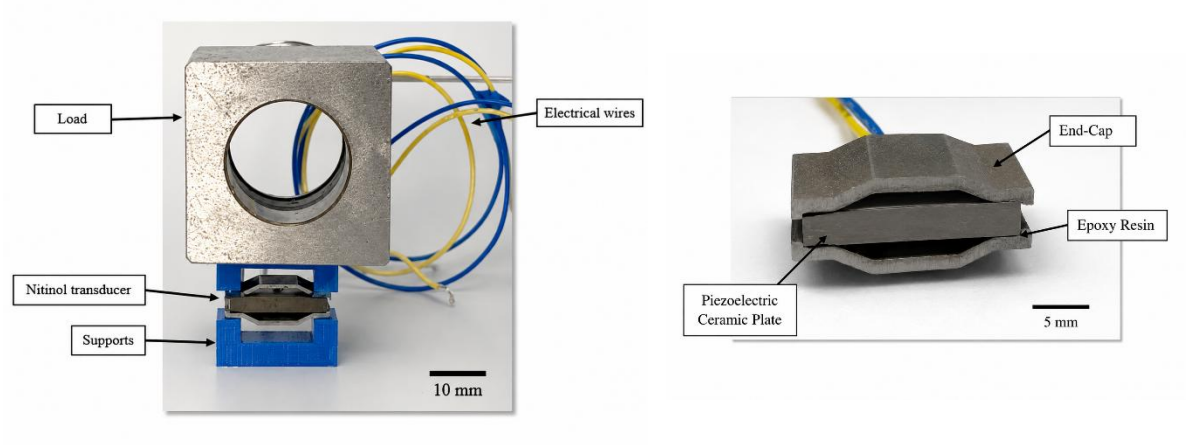
A Pz26 piezoelectric plate was diced to produce four piezoelectric ceramic plates with specified dimensions in Table 4.2 using the DISCO automated dicing saw (DAD 3350). The dicing saw used a synthetic diamond blade (Z09 series). Electrical wires were then soldered onto the piezoelectric ceramic plate's top and bottom electrode surfaces. During the soldering process, care was taken to ensure that heat was applied for a minimum amount of time. The integrity of the four PZ26 piezoelectric samples was verified using EIA. This was done to ensure that the soldering process did not damage the functionality of the piezoelectric ceramic samples [46].

After wires were soldered onto the piezoelectric plates, the bonds between the electrical wires and the surfaces of the piezoelectric samples were further strengthened by coating the solder spots with a thin layer of epoxy resin (Eccobond 45 LV High Strength, Ellsworth Adhesives Ltd., UK). The epoxy was mixed at a ratio of one part epoxy resin to one part 15 LV resin catalyst hardener and left to cure at room temperature for 24 hours.

A limitation found in flextensional transducers is the difficulty in achieving repeatable and precise deposition of the epoxy layer for mechanical coupling. For the class IV transducers, that mechanical coupling is between the end-caps and the piezoelectric ceramic plate surfaces, and uses the same epoxy as used to coat the solder. To aim for a reliable bond, air bubbles are removed before application, as they can reduce the strength of the bond. Although vacuum degassing is typically recommended to eliminate entrapped air bubbles and improve bond consistency, it was not available during fabrication. Instead, the epoxy was carefully mixed and applied to minimise air inclusion. The epoxy resin was deposited on the flanges of each end-cap surface. Once the transducers were assembled, the epoxy was allowed to cure for 24

hours. The assembled transducer, Figure 4.7a, was mounted in a custom 3-D printed support with a loading mass for 24 hours to strengthen the epoxy bond between the piezoceramic surface and the end-caps. The quality and thickness of the epoxy bond between the piezoceramic and the end-caps can influence the dynamic response of the transducer. The epoxy layer forms part of the mechanical transmission path between the piezoceramic and the metallic end-caps and, because of its comparatively low stiffness, variations in bond-layer thickness can alter the effective compliance of the interface. From the simplified relationship for axial stiffness, (Equation 4.9), an increase in the effective thickness, L, of the bonding layer reduces the interfacial stiffness when the elastic modulus and contact area remain constant. Variations in epoxy-layer thickness can modify the mechanical coupling between the piezoceramic and end-caps and thereby influence the resonance and vibration response of the assembled transducer [27-30,107-108]. Variations in the manually applied epoxy layer represent one possible source of differences in the measured responses of nominally similar transducers. However, the cured epoxy-layer thickness was not measured for each fabricated transducer; therefore, epoxy-layer variation cannot be established as the principal cause of the observed differences. Other manufacturing tolerances and material variations may also have contributed to the measured response.

Therefore, care was taken to apply a uniform layer of epoxy under controlled pressure to ensure consistent bonding across the piezoceramic surface. The fabricated transducer is shown in Figure 4.7b.



(a) Assembled Nitinol transducer mounted on supports with a load applied to it.

(b) Assembled Nitinol transducer once the loads and supports are removed.

Figure 4.7 – A Nitinol class IV transducer produced in this work.

Insulating epoxy resins like Eccobond ® are preferred to conductive epoxy resins, which are silver-filled, as they are stronger and provide good coupling at high displacement amplitudes.

A Nitinol sheet was procured from Kellogg's Research Labs (NH, USA) to machine the Nitinol end-caps for the modified class IV flextensional transducer. According to the manufacturer, the A_F of the Nitinol sheet was 35 °C. The dimensions of the sheet were 150 mm by 25 mm by 4 mm. The sheet was machined using the wire-EDM process.

The aluminium, titanium, and stainless steel end-caps were manufactured in the university workshop using conventional machining processes from supplied sheet metal stock.

4.1.3. Resonance frequency characterisation

Resonance frequency characterisation was conducted using an impedance gain/phase analyser. Information such as the resonance (f_r), anti-resonance (f_a) frequencies, electrical impedance magnitude and phase angles were measured using the Agilent 4294A Impedance/Gain Phase Analyser, with an Agilent 42941A probe. The impedance analyser was calibrated to ensure measurement accuracy and reliability by attaching two load-heads to the probe. One head is called the 'short', 0 Ω (Agilent HRM 504) and the other head is called the 'load', 50 Ω (Agilent HRM 601). The electrical connection fixture consisted of two crocodile clips attached to the impedance probe, which were used to connect the transducer electrode wires to the impedance analyser. The fixture was calibrated using open- and short-circuit compensation procedures with the clips attached but without the transducer connected. Once these calibration steps were followed, the transducers were connected to the impedance analyser. The flextensional transducers were shorted every time before being connected to the impedance analyser (IA).

A swept signal of 1 $V_{p\text{-}p}$ was applied over the frequency range 10–50 kHz. This range was selected to encompass the predicted resonance band of the transducers, with FEA indicating that the symmetric flexural vibration mode (Figure 4.4 and 4.6b) of interest would occur within the 20–35 kHz range. The wider sweep range also provided sufficient margin to capture potential frequency shifts arising from fabrication tolerances and material variability.

From the data obtained from the impedance analyser, the effective electromechanical coupling coefficient (k_{eff}), can be calculated using the resonance and anti-resonance frequencies. The Q_m can be obtained using the resonance frequencies obtained from the impedance analyser and applying the half power bandwidth (HPBW) relationship. The electromechanical coupling coefficients and the mechanical quality factors are obtained by applying equations 4.10 and 4.11 (similar to equation 2.12), respectively.

$$k_{eff}^2 = (f_a^2 - f_r^2)/f_a^2 \qquad (4.10)$$

$$Q_m = f_r/(f_2 - f_1) \qquad (4.11)$$

The calculation of the k_{eff} and the Q_m provides critical insight into the performance of the class IV flextensional transducers. While k_{eff} quantifies the efficiency of electrical-to-mechanical energy conversion, Q_m reflects the damping behaviour and energy losses of the device. For equation 4.8, The values f_2 and f_1 are the frequencies that correspond with the value of $\sqrt{2}$ of the maximum amplitude at the resonance frequency f_r [82]. This relationship is known as the half power bandwidth (HPBW).

Devices that exhibit high k_{eff} and large Q_m are expected to deliver greater vibration amplitudes for a given electrical input while dissipating less energy as heat. Together, these parameters provide valuable insight into the transducers' performance and indicate their potential suitability for high-power ultrasonic surgical applications.

4.1.4. Experimental modal analysis

EMA is a vibration analysis technique that measures the vibrational response of the transducer surfaces in the form of frequency response functions (FRFs) from which the modal parameters, mode shape, frequency and damping can be extracted. By combining EMA with finite element analysis, the accuracy of simulated resonance predictions can be confirmed against measured vibration responses of the class IV flextensional transducers.

A 3-D laser Doppler vibrometer (LDV) can measure the modal parameters of a transducer. LDVs utilise two important principles, the Doppler effect and interferometry. The Doppler effect describes the frequency shift of a wave in relation to the source frequency. In laser Doppler vibrometry, the measured Doppler frequency shift depends on the component of surface velocity along the laser beam direction and may be expressed as:

$$f = 2v\cos\theta/\lambda \quad (4.12)$$

where f is the Doppler frequency shift, v is the surface velocity, θ is the angle between the laser beam and vibration direction, and λ is the laser wavelength. For normal incidence ($\theta = 0^{\circ}$), this simplifies to:

$$f = 2v/\lambda \quad (4.13)$$

To conversely determine the velocity of an object, the Doppler frequency shift must be measured at a known wavelength, achieved using a laser interferometer. A laser beam is split into a reference beam and a measurement beam. The measurement beam is directed at a vibrating surface, which is reflected, collected, and then recombined with the reference beam [184].

This principle is represented by equation 4.14, where I_{TOT} is the resultant interference intensity measured at the detector. I_1 and I_2 are the intensities of the reference and measurement beams,

respectively. The reference beam has optical path length r_1, which is kept constant, while the measurement beam has optical path length r_2, which varies with the displacement of the vibrating sample. Changes in r_2 alter the path length difference (r_1-r_2), producing a phase change in the interference signal measured by the detector.

$$I_{TOT} = I_1 + I_2 + 2[I_1 I_2 \cos 2\pi(r_1-r_2)/\lambda]^{0.5} \quad (4.14)$$

A schematic of the LDV setup is shown in Figure 4.8.

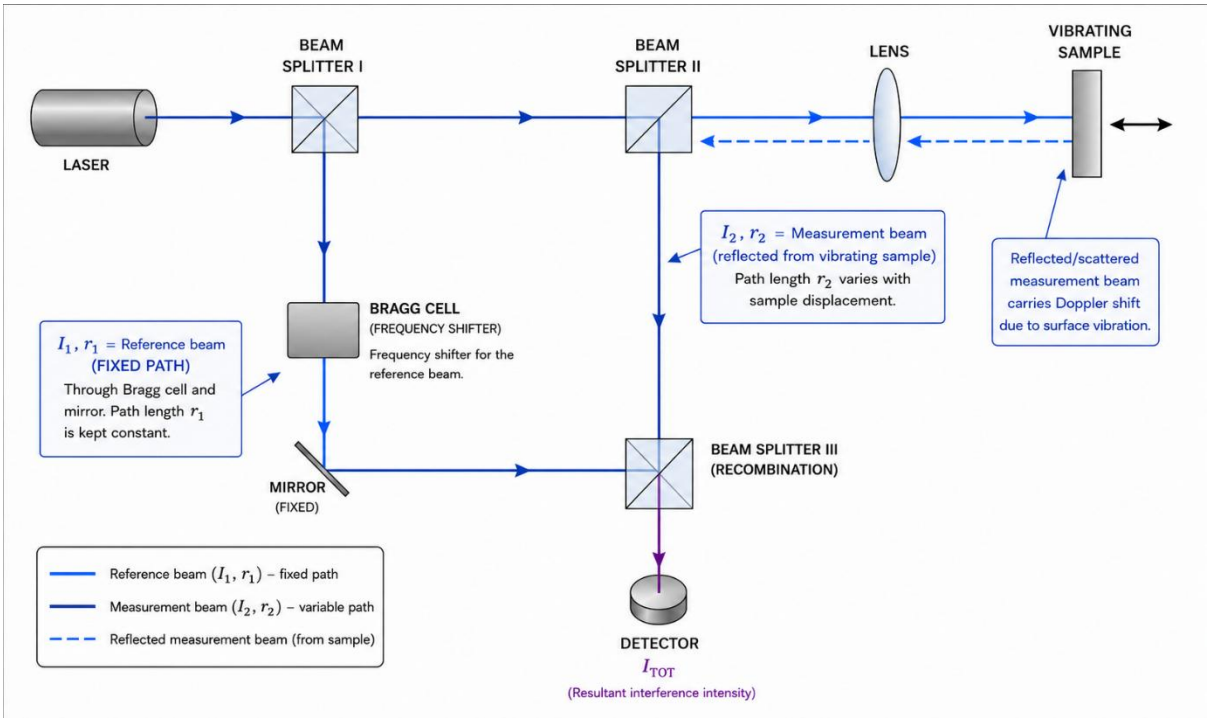


Figure 4.8 - Schematic of LDV setup [185].

The vibration of an object produces a fringe pattern based on the principle of interferometry [184]. Each fringe corresponds to a half-wavelength displacement of the test object. The modulation frequency of this fringe pattern is directly related to the surface vibration velocity of the vibrating object, though the phase cannot be determined from this alone. To determine the phase, a Bragg cell shifts the frequency of the light when the test object is stationary. As a result, any change in the test object's position enables the determination of its direction of movement [184]. The schematic in Figure 4.8 shows that the laser beam is split by beam splitter I into a reference beam and a measurement beam. After passing through beam splitter II, the measurement beam is focused onto the sample, where it is reflected. The reflected measurement beam is redirected by beam splitter III and recombined with the reference beam before reaching the detector Since the optical path of the reference beam (r_1) remains constant, any movement of the sample (r_2) generates a light/dark interference pattern on the detector. Each light/dark

cycle on the detector corresponds to a displacement of the object equal to half the wavelength of the light used [178]. For harmonic motion, the vibration velocity amplitude is proportional to both the displacement amplitude and vibration frequency, and may be expressed as:

$$v=2\pi fs \quad (4.15)$$

where v is the vibration velocity amplitude, f is the vibration frequency, and s is the displacement amplitude. Together, these relationships form the mathematical foundation of EMA, linking the optical measurement to the vibration response of the transducer. EMA was performed using a scanning 3-D LDV (LDV-MSA-100-3-D, Polytec GmbH, Germany), shown in Figure 4.9. The scanning profile, measurement mesh, vibration mode shapes, and associated frequencies were controlled and analysed using the associated acquisition software (PSV 10.1, Polytec). The scanning profile was generated by defining the surface region of interest on the transducer geometry, after which a measurement mesh consisting of discrete scan points was created across the surface. The density of the measurement mesh was selected according to the geometric complexity of the transducer and the spatial resolution required to accurately capture the vibration modes. During measurement, the LDV sequentially directed the laser beam to each scan point using automated scanning mirrors and recorded the vibration velocity response at each location. The measured responses were subsequently processed within the PSV software to reconstruct the operational deflection shapes and resonance mode shapes of the transducers at their corresponding resonance frequencies. The transducers were mounted on a foam block which was securely held to the scanning stage to prevent the foam from moving during the scanning process.

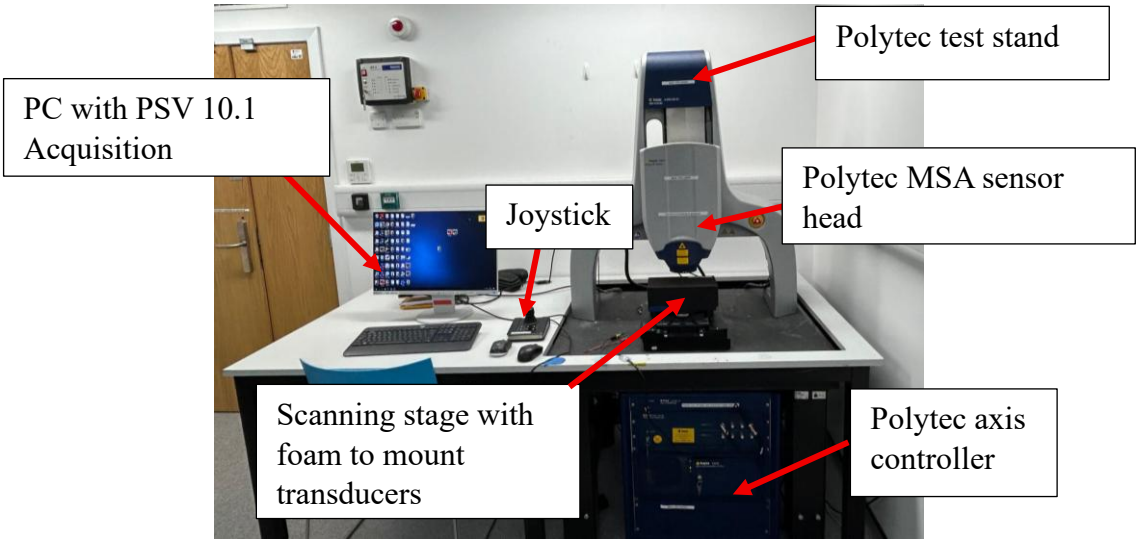


Figure 4.9 – EMA experimental set up.

For the transducer scans, For the transducer scans, a linear periodic chirp excitation signal with an amplitude of 16 $V_{p\text{-}p}$ was applied over the frequency range 10–50 kHz to generate a sufficient

vibration response while minimising nonlinear and thermal effects. The chirp signal consisted of a sinusoidal waveform with continuously increasing frequency across the selected sweep range, enabling broadband excitation of the transducer resonance modes within a single measurement. The excitation was repeated periodically to improve the signal-to-noise ratio through synchronous averaging within the PSV acquisition software. Chirp excitation was selected because it enables efficient identification of multiple resonance frequencies and associated vibration mode shapes while maintaining stable excitation energy across the frequency sweep.

4.1.5. Harmonic response analysis

Figure 4.10 illustrates the experimental setup for the harmonic analysis tests. The displacement amplitudes of the transducers were measured using a 1-D LDV system. The harmonic response analysis tests were carried out to evaluate the nonlinear vibration behaviour of the class IV transducers.

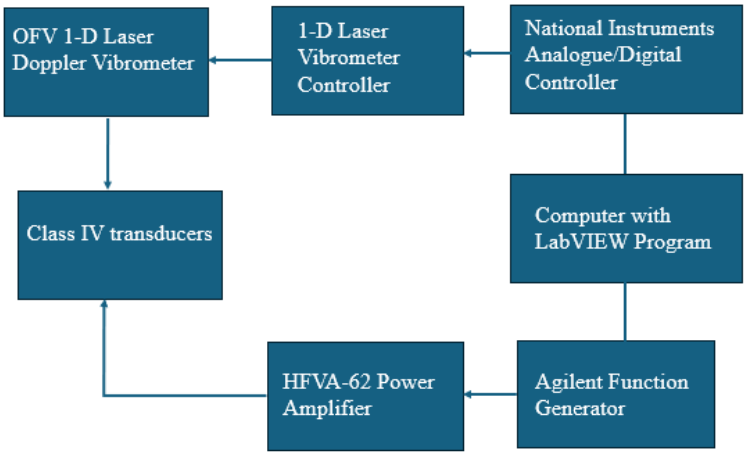


Figure 4.10 – Harmonic response analysis experimental setup.

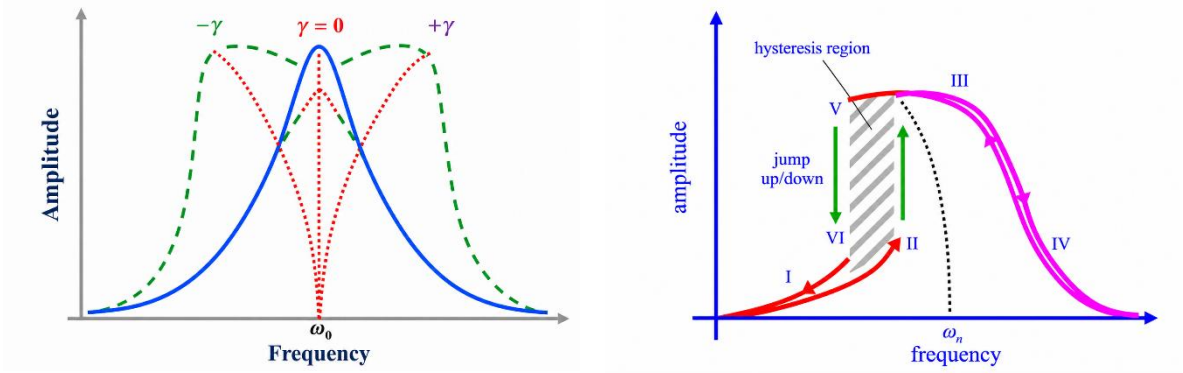
Nonlinear vibration behaviour may arise in dynamic systems due to changes in material properties, nonlinear restoring forces, geometric nonlinearities, or amplitude-dependent damping mechanisms. Unlike linear systems, where the response amplitude is directly proportional to the excitation input and the resonance frequency remains constant, nonlinear systems may exhibit amplitude-dependent resonance behaviour and shifts in resonance frequency with increasing excitation level [83].

Power ultrasonic transducers can exhibit duffing-type nonlinear behaviour at elevated excitation amplitudes. For a single-degree-of-freedom system, the nonlinear equation of motion may be expressed as:

$$m\ddot{x}+c\dot{x}+kx+\gamma x^3 = F(t) \quad (4.16)$$

where m is the effective mass, c is the damping coefficient, k is the linear stiffness,x is displacement, γx^3 represents the nonlinear stiffness term, and $F(t)$ is the harmonic excitation force. The nonlinear stiffness coefficient γ determines whether the system exhibits hardening or softening behaviour, Figure 4.11a.When $\gamma > 0$, the effective stiffness increases with vibration amplitude, producing a hardening response in which the resonance frequency shifts towards higher frequencies. When $\gamma < 0$, the effective stiffness decreases with increasing amplitude, producing a softening response and a shift in resonance frequency towards lower frequencies [83].

Systems exhibiting duffing-type behaviour may also display hysteresis and jump phenomena as illustrated in Figure 4.11b.



(a) Frequency responses for varying γ. (b) Jump phenomenon and hysteretic region.

Figure 4.11 - Duffing like behaviour [83].

Within certain frequency regions, multiple vibration amplitudes may exist for the same excitation frequency, resulting in abrupt transitions between stable response branches during frequency sweeps. Such nonlinear effects have been reported in high-power ultrasonic systems due to nonlinear piezoelectric coupling, material hysteresis, adhesive layer losses, and interfacial frictional effects [4,18,27-28,83].

In the present study, harmonic response analysis was conducted to investigate potential nonlinear effects associated with increasing excitation voltage, including resonance frequency shifts, changes in impedance behaviour, and amplitude-dependent vibration response of the class IV flextensional transducers.

By applying a controlled voltage range above and below resonance, the tests aimed to capture these nonlinear effects. The excitation was provided by a burst sine signal generated by a signal generator (Agilent Technologies, USA) and amplified using a power amplifier (Foneng Technology Industry Co., China). Vibration data was measured from the centre of the end-cap

apex with a 1-D LDV. The excitation signal to the transducers was controlled using LabVIEW software. For each test, the burst sine signal had a fixed number of oscillation cycles and a three-second time interval between successive bursts to reduce heating effects. The applied voltage was changed for each new frequency sweep, from 10 to 60 $V_{(rms)}$ in increments of 10 $V_{(rms)}$. All the transducers were tested over a 3,500 Hz frequency range with a data resolution of 5 Hz. To ensure a free-boundary condition was approximated, the transducers were held by their wires as shown in Figure 4.12. The stability of the suspended transducer was monitored during excitation, and no movement or rotation of the transducer was observed throughout the frequency sweeps. The transducer therefore maintained a stable orientation, with the LDV measurement location remaining centred on the end-cap apex during the measurements.

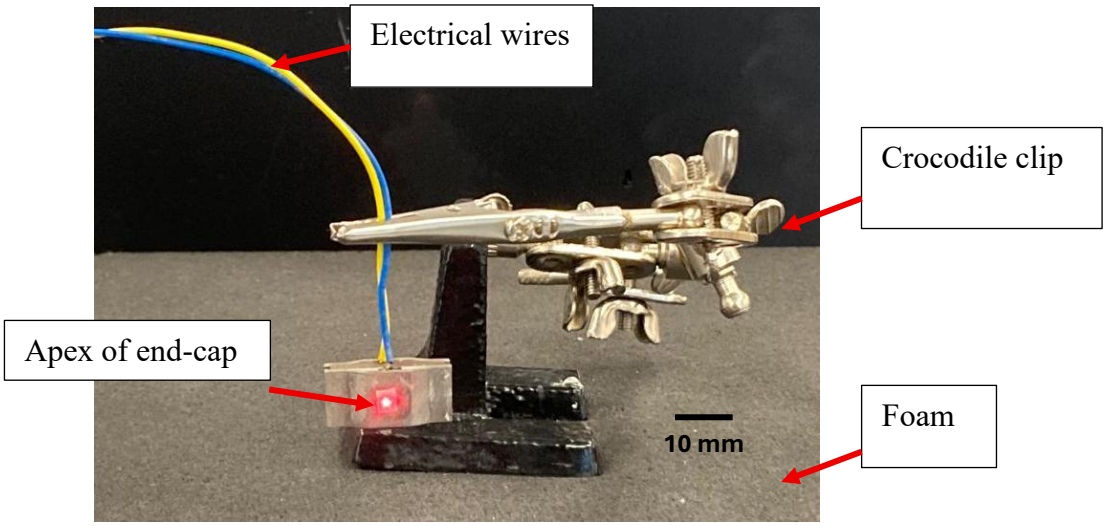


Figure 4.12 – Experimental setup for free boundary condition.

4.1.6. Temperature studies

The performance of ultrasonic transducers is sensitive to operating temperature. Temperature fluctuations can alter the material properties of both the end-caps, epoxy coupling and the piezoceramic plates, directly affecting resonance frequency, impedance, and power transfer efficiency [27-28,36-37,83]. For the Nitinol end-caps, the influence of temperature is even more pronounced due to the phase transitions, which can change stiffness and the dynamic response of a Nitinol incorporated ultrasonic transducer [27-30].

This study was therefore undertaken to evaluate how the resonance frequency and corresponding impedance values vary with temperature, providing insights into the stability and reliability of each transducer design. Specifically, the aim was to assess whether:

- Resonance frequency varies across the investigated temperature range, influencing the dynamic stability of the transducer response.

- Impedance variations occur that may reduce power transfer efficiency.
- Temperature-dependent material behaviour (particularly in Nitinol) contributes to tuneability in the device response.

To achieve this, the four transducers underwent cooling and heating stages over a temperature range of -5 to 65 °C, in 5 °C increments. Cooling was performed by placing the transducers in a freezer, while heating was achieved using a commercial dehydrator (Andrew James, UK). A K-type thermocouple (RS-1384, RS PRO, UK) was used to monitor the temperature of the transducers. The probe was placed in direct contact with the flange of the transducer end-caps, ensuring that the recorded values closely reflected the bulk temperature of the metallic end-caps. Impedance measurements were taken using the impedance analyser at 5-minute intervals once thermal equilibrium was reached.

4.2. Results

4.2.1. Results from electrical impedance analysis

The impedance magnitude and phase of the transducers are shown in Figure 4.13. The k_{eff} and Q_m were obtained for all the transducers at ambient room temperature and are recorded in Table 4.3. The FEA results of the resonance frequency of the symmetric vibration mode are shown in Table 4.4.

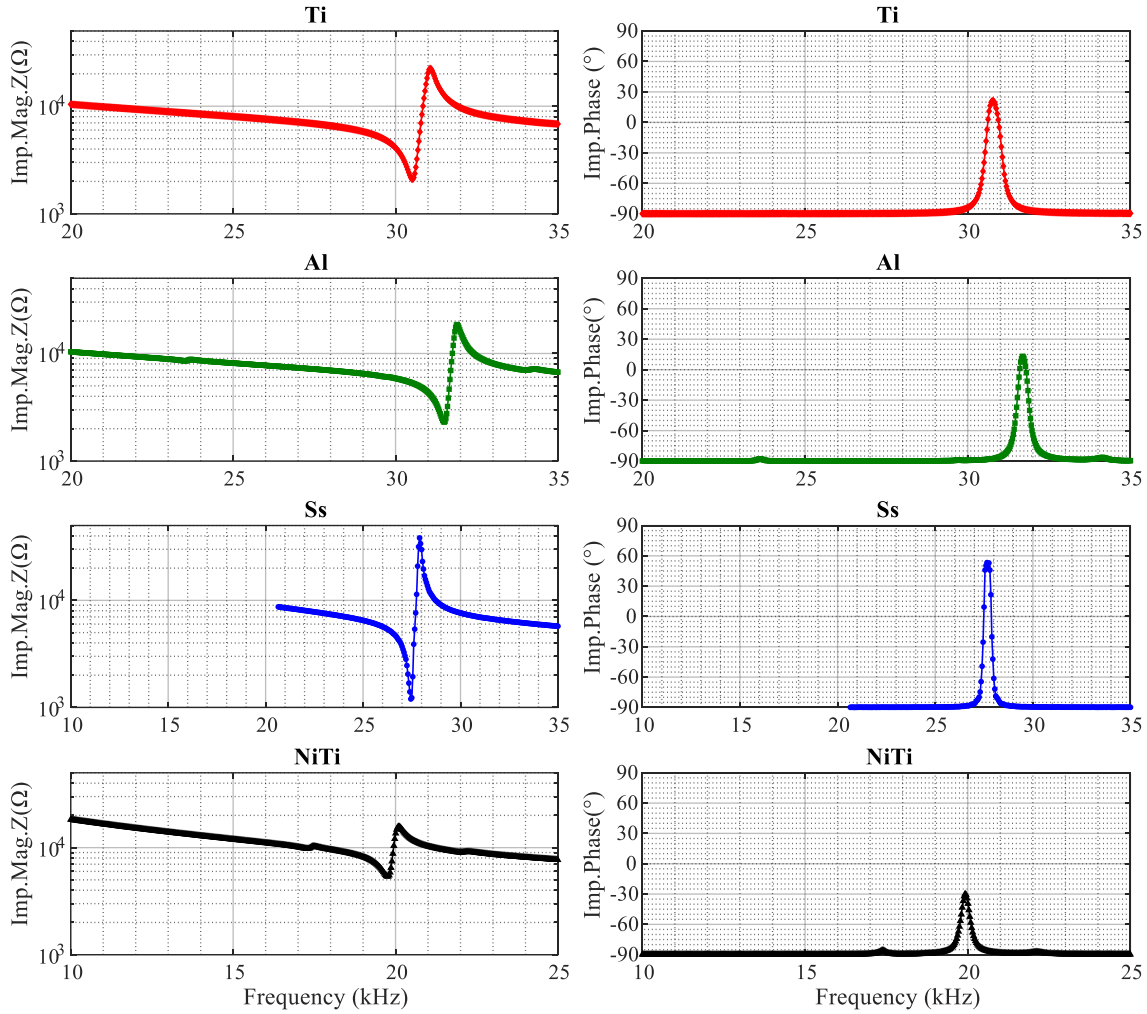


Figure 4.13 - Measured impedance magnitude and phase spectra of the flextensional transducers. Ti - transducer with titanium end-caps, Al- transducer with aluminium end-caps, Ss- transducer with stainless steel end-caps and NiTi- transducer with Nitinol end-caps.

Transducer End-Cap Material	f_r (kHz) [EIA]	f_a(kHz) [EIA]	Phase at resonance frequency	Speed of sound (m/s)	Q_m	k_{eff}
Titanium	30.475	31.050	-39°	5,214	76	0.192
Aluminium	30.883	31.353	-27°	5,088	54	0.172
Stainless Steel	27.156	27.656	9°	5,050	108	0.189
Nitinol	20.062	20.343	-62°	3,522	71	0.165

Table 4.3 – Electromechanical characteristics of class IV flextensional transducers with different end-cap materials measured from EIA.

Transducer End-Cap Material	f_r (kHz) [FEA]
Titanium	30.783
Aluminium	31.240
Stainless Steel	27.003
Nitinol	20.148

Table 4.4 – Resonance characteristics of class IV flextensional transducers with different end-cap materials measured from FEA.

From Equation 2.4, the resonance behaviour of the class IV transducers scales with the speed of sound in the metal end-caps. As the Nitinol end-caps have the lowest speed of sound (3,522 ms^{-1}) compared to the other transducer end-caps, its resonance frequency was the lowest (20.062 kHz), corresponding with the experimental data shown in Table 4.3. Based on the speed of sound value of the titanium end-caps (5,214 ms^{-1}), it is expected that the titanium transducer would have the highest resonance frequency but from the experimental data (Table 4.3), it had the second highest resonance frequency value (30.475 kHz). The aluminium transducer had the highest resonance frequency value (30.883 kHz) and the second highest speed of sound (5,088 ms^{-1}). The stainless steel transducer had the third highest resonance frequency (27.156 kHz) which corresponded with it having the third highest speed of sound value (5,050 ms^{-1}). The variation in resonance frequency and the speed of sound values for the titanium and aluminium transducers occurs due to the variation in the amount of epoxy resin that was deposited between the end-caps and the piezoceramic surfaces or minimal geometrical variations in the design of the end-caps.

In the FEA model, the aluminium transducer exhibited a slightly higher resonance frequency (31.240 kHz - Table 4.4) than the titanium transducer (30.783 kHz - Table 4.4). Although titanium possesses a higher Young's modulus and therefore greater structural stiffness, aluminium has a lower density, resulting in a lower effective vibrating mass at the flexural apex regions of the transducer (refer to Table 4.1). Since the resonance frequency is governed by relationship 2.3, the reduction in vibrating mass associated with aluminium produced a greater influence on the predicted resonance frequency than the increase in stiffness provided by titanium. The FEA model assumes idealised conditions, including perfect bonding between the piezoceramic and end-caps, uniform material properties, and geometrically symmetric structures, without the imperfections introduced during fabrication. The simulated resonance frequencies represent idealised behaviour and may differ slightly from experimentally

measured values due to manufacturing tolerances, epoxy distribution, and assembly-induced asymmetry [28,37,41].

The phase at resonance frequency values (Table 4.3) provides information about whether the electrical impedance of the device behaves in a more capacitive (negative phase) or inductive (positive phase) manner [179]. For example, the Nitinol transducer showed a strongly negative phase angle (–62°), indicating capacitive-dominant behaviour, while the stainless steel transducer displayed a positive phase (9°), suggesting inductive-like characteristics. The Q_m (Table 4.3) quantifies how efficiently the transducer vibrates by comparing stored vibrational energy to energy lost per cycle. Higher Q_m values indicate lower damping and reduced energy loss. The stainless steel transducer exhibited the highest Q_m (108), implying the lowest vibrational damping among the materials tested, while the aluminium transducer had the lowest Q_m (54), reflecting greater mechanical losses during operation. Higher k_{eff} values correspond to more effective energy transfer. The titanium transducer (0.192) and stainless steel transducer (0.189) demonstrated the strongest electromechanical coupling, suggesting they are more efficient at energy conversion than the aluminium transducer (0.172) and the Nitinol transducer (0.165).

The combined influence of damping and capacitive behaviour is particularly important for resonance tuneability and operational stability. Increased damping, as observed in the aluminium and Nitinol transducers, dissipates vibrational energy more rapidly, reducing the Q_m and broadening the resonance response. The relationship between resonance bandwidth and quality factor is expressed in Equations 2.11-2.12 and 4.11. Lower Q_m values produce broader resonance peaks, making the transducers less frequency-selective but more tolerant to small variations in loading and boundary conditions [4,83,96].

Similarly, capacitive-dominant behaviour, such as that observed in the Nitinol transducer, increases the sensitivity of the electrical impedance response to changes in material stiffness, dielectric properties, stress, and temperature. In Nitinol-based structures, temperature-dependent phase transformation between martensite and austenite alters the elastic modulus and damping characteristics of the transducer, producing corresponding shifts in impedance and resonance behaviour [28]. This provides an inherent mechanism for resonance tuneability, although often at the expense of lower electromechanical coupling and reduced mechanical quality factor compared with titanium or stainless steel transducers.

The stainless steel and titanium transducers offer the most efficient energy conversion with low losses, the aluminium transducer provides the highest resonance frequencies despite higher damping, and the Nitinol transducer, while less efficient, uniquely offers capacitive behaviour

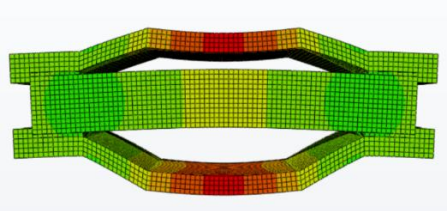
and damping-induced bandwidth broadening, making it a promising candidate for tuneable ultrasonic applications.

It should be noted that the conclusions drawn from the EIA are based on a limited number of fabricated prototypes, with only one transducer manufactured for each end-cap material. The observed differences in resonance behaviour, impedance response, damping characteristics, and mechanical quality factor may also be influenced by fabrication tolerances, epoxy distribution, assembly variability, and local geometric asymmetry. Future work should include the fabrication and testing of multiple transducers for each material to evaluate repeatability and quantify experimental variability more rigorously.

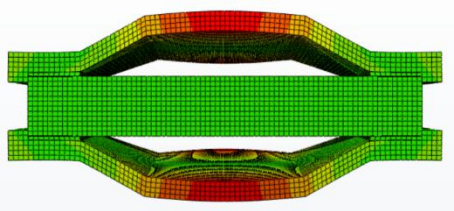
Alongside the symmetric vibration mode, three additional resonance modes were also identified through the impedance-magnitude and phase spectra (Figure 4.13) and visualised through FEA simulations. These included an asymmetric mode (Figure 4.14a), an asymmetric flexural mode (Figure 4.14b), and a torsional mode (Figure 4.14c).

In contrast to the symmetric flexural mode shown in Figure 4.4 and Figure 4.6b, where the upper and lower end-caps vibrate in a balanced and mechanically symmetric manner to generate uniform displacement amplification, the additional vibration modes identified in Figure 4.14 exhibit non-uniform structural deformation. In the asymmetric mode (Figure 4.14a), the vibration response differs between the upper and lower end-caps, producing unequal displacement amplitudes and loss of vibrational symmetry. Similarly, the asymmetric flexural mode (Figure 4.14b) involves flexural deformation of the end-caps, but the motion is distributed unevenly across the structure, resulting in non-uniform displacement amplification. In the torsional mode (Figure 4.14c), the transducer undergoes rotational twisting motion about its longitudinal axis rather than the predominantly flexural motion associated with the desired symmetric operating mode. These modes are less suitable for ultrasonic surgical operation, where controlled and uniform displacement amplification is required at the transducer end-cap surfaces.

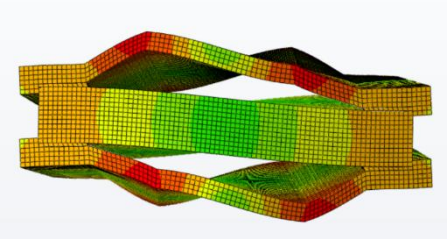
Although these modes were not the primary operational modes of interest, their identification demonstrates the complex dynamic behaviour of the class IV flextensional transducer and provides additional confidence in the validity of the finite element predictions. The experimentally observed resonance peaks obtained from the electrical impedance analysis corresponded closely with the resonance frequencies predicted by the FEA simulations, confirming the presence of these additional structural vibration modes within the transducer system.



(a) FEA prediction of asymmetric mode (23.293 kHz).



(b) FEA prediction of asymmetric flexural mode (32.325 kHz).



(c) FEA prediction of torsional mode (38.374 kHz).

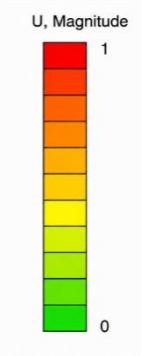


Figure 4.14 – FEA predictions of additional vibration modes in the aluminium class IV flextensional transducer. The shared U-magnitude scale represents normalised displacement, with warm colours indicating higher displacement and green regions indicating lower displacement.

Table 4.5 presents the resonance frequencies of the additional vibration modes that were identified from the impedance analysis and verified by FEA for the class IV flextensional transducers.

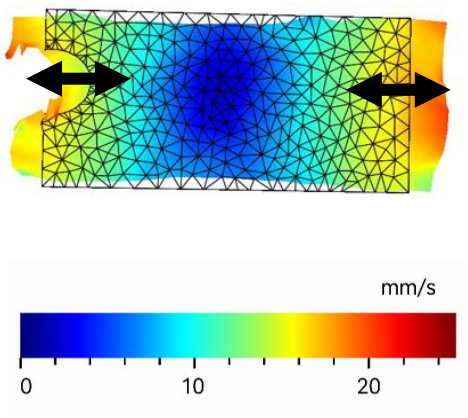
Transducer end-cap material	Vibration mode	f_r (kHz) [EIA]	f_r (kHz) [FEA]
Nitinol	Asymmetric	17.279	17.537
Nitinol	Asymmetric flexural	22.177	22.577
Aluminium	Asymmetric	23.525	23.293
Aluminium	Asymmetric flexural	33.025	32.325
Aluminium	Torsional	39.350	38.374

Table 4.5 – Resonance frequencies of additional vibration modes in the transducers with different end-cap materials as identified by EIA and FEA.

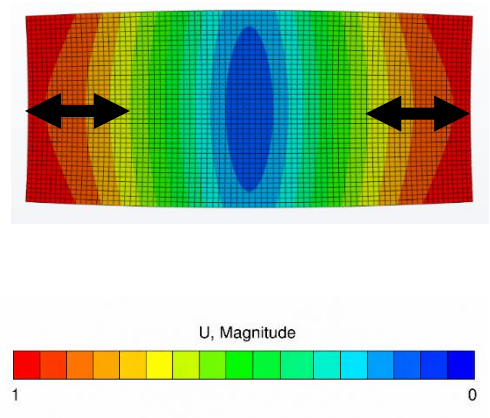
The neighbouring modes such as the asymmetric, asymmetric flexural and torsional modes of the end-caps and the PZT plates were not visible in the impedance analysis (Figure 4.13) for the titanium and stainless steel transducers. This is likely due to the low excitation voltage during impedance analysis which was not sufficient to excite these modes. The importance for this work is that energy is not leaked into these modes in the transducers. The symmetric mode is maintained and there is no bending of the PZT plate.

4.2.2. Results from experimental modal analysis

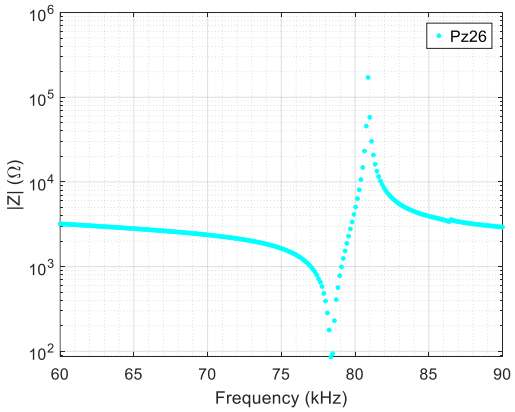
Figure 4.15 illustrates the extensional motion of the piezoceramic plate, which is then converted into flexural motion of the end-caps (Figure 1.6a). The resonance frequency and mode shapes of the piezoceramic plate, as determined by EMA (Figure 4.15a) and FEA (Figure 4.15b), are compared in Figure 4.15. A profile surface scan was carried out on the piezoceramic bar (Figure 4.15a), with the d_{31} piezoelectric coefficient being a key parameter for the class IV flextensional transducer study. This coefficient relates to the longitudinal expansion and contraction of the piezoceramic material.



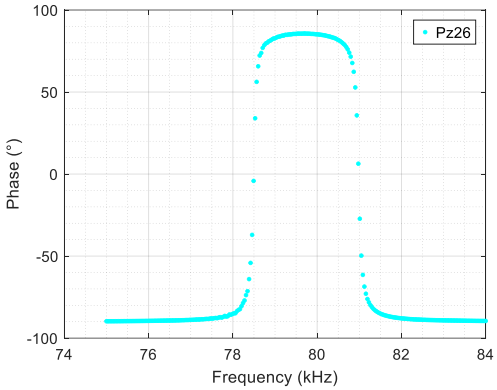
(a) EMA result of the extensional mode of the piezoceramic at 77.773 kHz, measured using LDV (mm/s). Blue regions indicate low or near nodal vibration velocity, while red regions indicate maximum vibration velocity, with intermediate colours representing increasing velocity magnitude. Black arrows indicate the direction of displacement.



(b) FEA result at 77.683 kHz showing the normalised displacement magnitude, where red regions represent higher normalised displacement and blue regions represent lower normalised displacement. Black arrows indicate the direction of displacement.



(c) Impedance magnitude of piezoelectric plate (78.480 kHz).



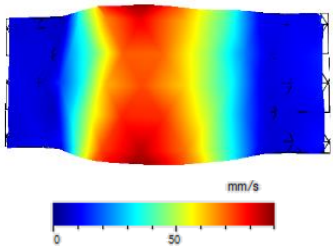
(d) Phase of the piezoelectric plate.

Figure 4.15 – Experimental and numerical comparison of the extensional vibration mode of the piezoceramic plate.

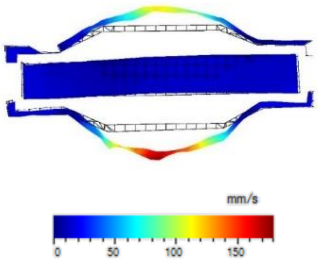
The resonance frequency obtained from EMA (Figure 4.15a) of the extensional vibration mode of the piezoceramic plate showed good agreement with both the FEA prediction (Figure 4.15b) and the EIA measurement (Figure 4.15c). The experimentally measured resonance frequency differed from the FEA-predicted value by 0.16%, while the difference between the EMA and

EIA measurements was 0.90%. These results provide strong validation of both the finite element model and the experimentally identified extensional vibration mode of the piezoceramic plate. In addition to the close resonance frequency agreement, qualitative correlation was observed between the EMA-reconstructed vibration velocity distribution and the FEA-predicted normalised displacement mode shape. Both approaches identified maximum vibration response near the lateral regions of the piezoceramic plate and a lower vibration region near the centre of the structure. It should be noted that the EMA measurements represent relative vibration velocity distributions reconstructed from LDV measurements, whereas the FEA results correspond to normalised relative displacement magnitudes. The comparison focused primarily on resonance frequency agreement and qualitative mode shape correlation rather than direct displacement amplitude matching.

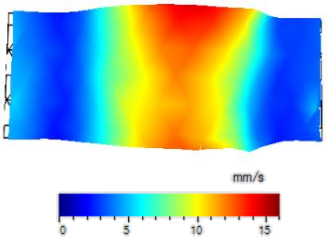
Two types of EMA scans were conducted for the class IV transducers. These scans were end-cap surface (Figure 4.16 a,c,e and g) transducer side face (Figure 4.16 b,d,f and h) scans.



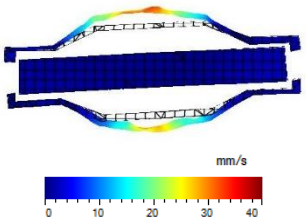
(a) Ti: 30.408 kHz.



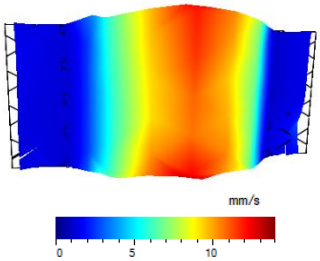
(b) Ti: 30.140 kHz.



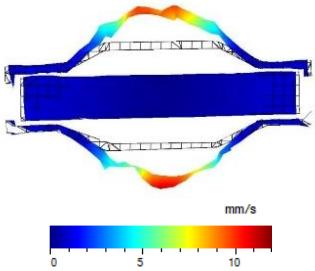
(c) Al: 30.633 kHz.



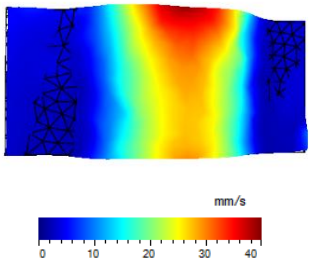
(d) Al: 30.453 kHz.



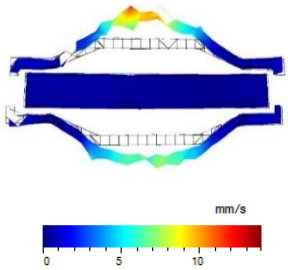
(e) Ss: 27.0 kHz.



(f) Ss: 27.406 kHz.



(g) NiTi: 20.148 kHz.



(h) NiTi: 20.195 kHz.

Figure 4.16 - Modal response and frequency of the symmetric mode from LDV scans. EMA scale showing the velocity response of the end-caps and transducer surfaces measured using laser vibrometry (mm/s). Dark blue regions correspond to low or near-nodal vibration velocity, while red regions indicate areas of maximum vibration velocity response

In Figure 4.16, the underlying wireframe mesh represents the undeformed reference geometry of the transducer end-cap and side face surfaces, while the coloured surface illustrates the exaggerated operational deflection shape reconstructed from the LDV measurements. The operational deflection shapes reconstructed from the LDV measurements were visually scaled within the PSV software (scale-up feature) to exaggerate the displacement field for improved visualisation of the vibration mode shapes. The displayed deformation amplitudes do not represent true physical displacement magnitudes but rather scaled relative modal displacements.

Figures 4.16 a,c,e and g demonstrate that the apex regions of the end-caps exhibit the highest relative vibration response associated with the symmetric vibration mode presented in Figure 4.17.

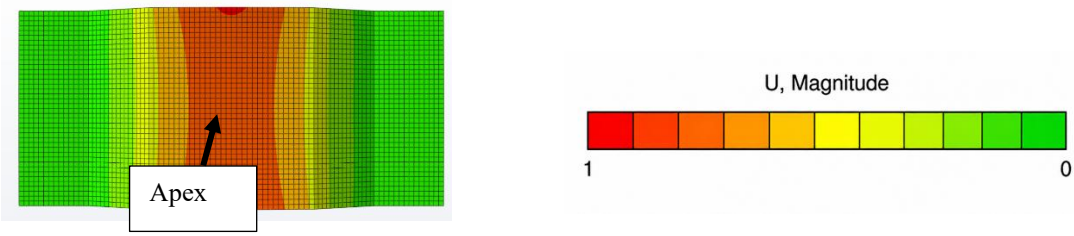


Figure 4.17 - FEA displacement magnitude of the end-cap in the symmetric vibration mode, showing an antinode at the apex. Red regions indicate maximum normalised displacement magnitude, while green regions indicate lower displacement magnitude. Vibration response of the end-cap of the flextensional transducer in its symmetric vibration mode.

The resonance frequencies predicted by EIA (Table 4.3) and FEA simulations (Table 4.4) showed good agreement with those measured using EMA (Figure 4.16). The percentage

differences between the EMA and FEA resonance frequencies were below 2% for all end-cap materials, while the EMA and EIA measurements differed by less than 1%. The greatest deviation between EMA and FEA was observed for the aluminium transducer (1.98%), whereas the stainless steel and Nitinol transducers showed near-identical agreement (0 to 0.01%). These results provide confidence in the validity of the finite element model and the experimentally identified symmetric vibration modes.

The EMA measurements primarily provided relative vibration velocity distributions and operational deflection shapes rather than directly calibrated displacement amplitudes. The comparisons between EMA and FEA were based principally on resonance frequency correlation and qualitative agreement in mode shape behaviour.

It is not uncommon for there to be a slight difference in the resonance frequencies of the symmetric vibration modes measured using EIA and EMA which stems from the different excitation voltage levels used for these tests. For the Nitinol (Figure 4.16h), aluminium (Figure 4.16d) and titanium (Figure 4.16b) transducers, the symmetric mode is not entirely symmetric, with one end-cap vibration response being more dominant than the other in the mode shape. This lack of symmetry is less evident in the stainless steel (Figure 4.16f) transducer. The differences in vibration responses may be attributed to variations in the thickness of the epoxy layers between the end-caps and the piezoceramic surfaces, or slight differences in the geometry of the two end-caps [27-30]. This suggests that the optimal placement for a surgical attachment would be at the centre of the apex, Figure 4.17, where the highest relative vibration response occurs. The flexural motion generated at the apex of the end-cap may therefore provide effective vibration transmission to a surgical attachment or cutting interface for ultrasonic surgical applications.

4.2.3. Results from harmonic response analysis

Figure 4.18 shows the results of the harmonic response analysis of the four transducers conducted in ambient room temperature. Figure 4.19 shows the maximum displacement amplitudes of the transducers at incrementally increasing excitation voltages.

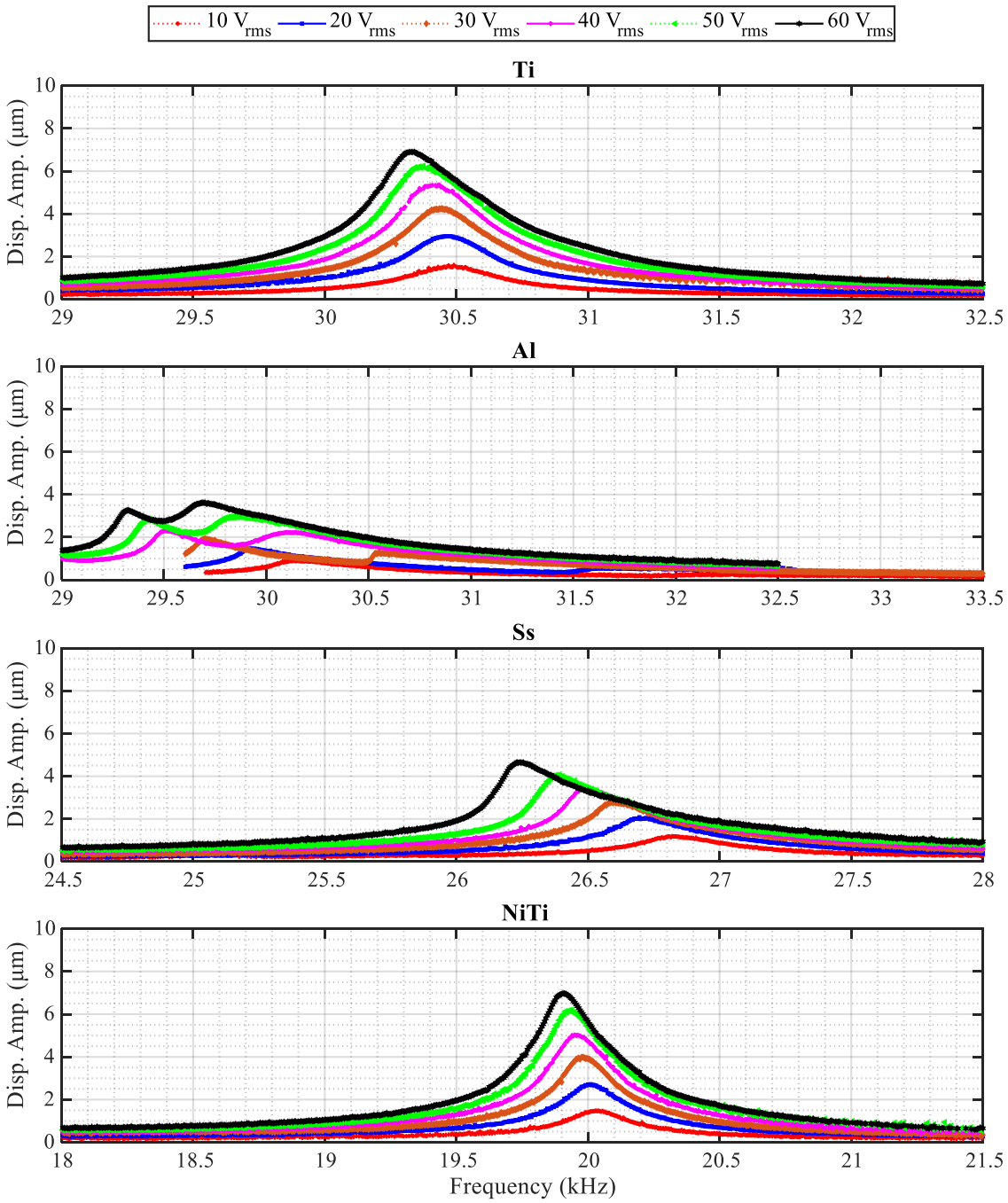


Figure 4.18 – Harmonic response analysis results from the transducers.

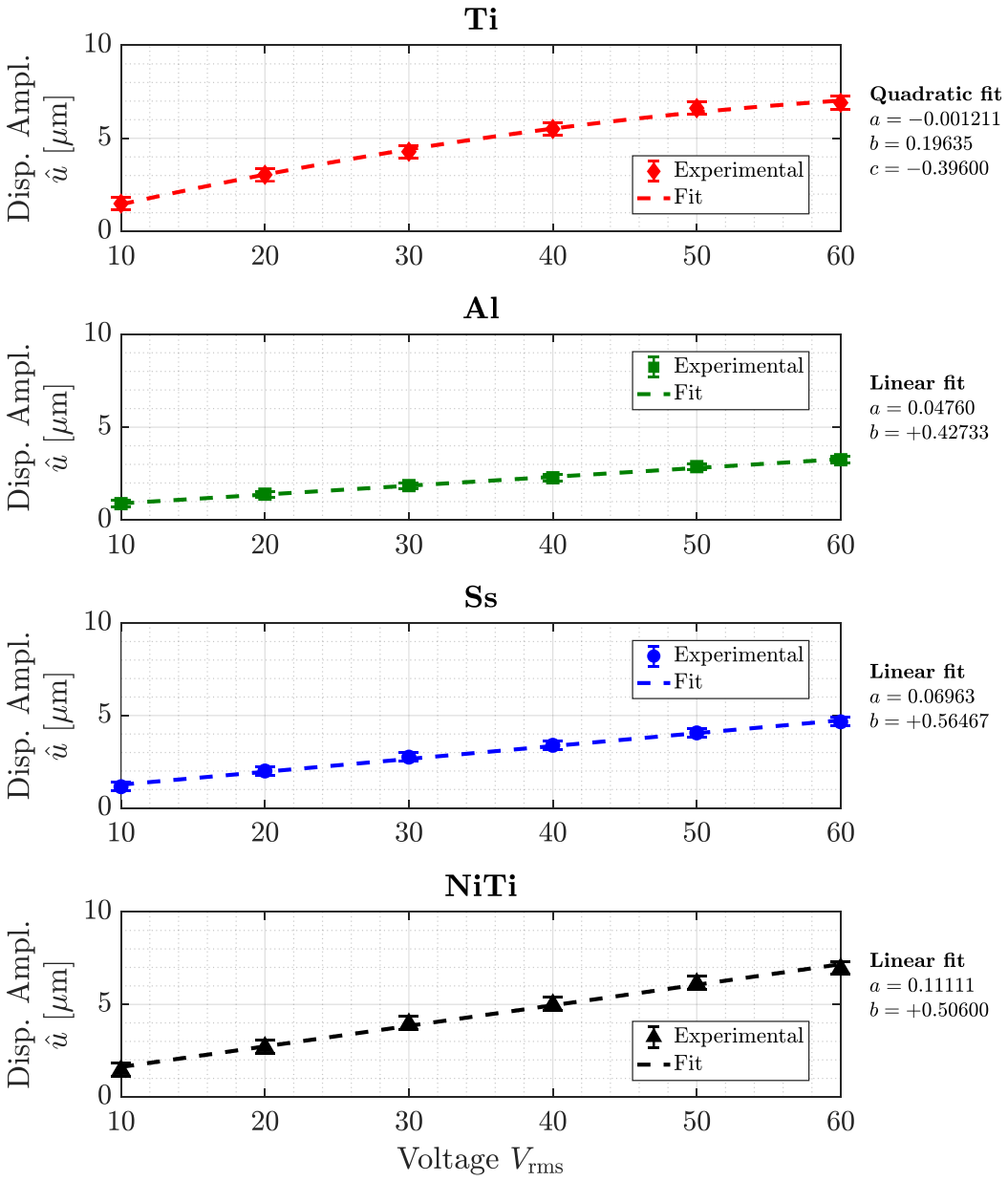


Figure 4.19 - Maximum displacement amplitude of the symmetric vibration mode for transducers at incrementally increasing voltage levels.

The harmonic response analysis revealed distinct trends in the dynamic behaviour of the four class IV transducers (Figure 4.18). In this study, softening behaviour refers to a reduction in resonance frequency with increasing excitation voltage and displacement amplitude [83]. All four transducers exhibited varying degrees of resonance-frequency softening with increasing voltage; however, the magnitude of this behaviour differed substantially and may have been influenced by end-cap material properties, epoxy layer variation and electromechanical coupling.

The displacement amplitude increased with excitation voltage over the investigated range of 10–60 $V_{(rms)}$ for all four transducers (Figure 4.18). Linear regression provided a good representation of the displacement responses of the aluminium, stainless steel and Nitinol transducers, with coefficients of determination (R^2) of 0.9976, 0.9962 and 0.9955, respectively. For the titanium transducer, a quadratic fit provided a better representation of the measured response than a linear fit, increasing R^2 from 0.9719 to 0.9963 and reducing the RMSE from 0.3239 µm to 0.1171 µm. The residuals for the quadratic fit were also smaller and more evenly distributed than those obtained using the linear fit, supporting the use of the quadratic model for the titanium transducer. Error bars in Figure 4.18 represent an estimated ±5% experimental uncertainty, which is within the <10% measurement error reported for related experimental measurements in [182].

The fitted linear gradients provide a quantitative comparison of the displacement response of the aluminium, stainless steel and Nitinol transducers to increasing excitation voltage. The Nitinol transducer exhibited the greatest linear displacement-voltage gradient of 0.1111 µm/$V_{(rms)}$, followed by the stainless steel transducer at 0.0696 µm/$V_{(rms)}$ and the aluminium transducer at 0.0476 µm/$V_{(rms)}$. A single displacement-voltage gradient is not reported for the titanium transducer because its response was better represented by a quadratic relationship. The mild curvature observed in the titanium displacement response should be distinguished from the nonlinear softening behaviour identified from the resonance-frequency changes (Figure 4.18).

At 60 $V_{(rms)}$, the titanium and Nitinol transducers achieved comparable displacement amplitudes of 6.91 µm and 6.98 µm, respectively. The Nitinol transducer maintained an approximately linear displacement response over the investigated voltage range, whereas mild curvature was observed in the titanium response. These comparable displacement amplitudes were obtained despite differences in the resonance frequency and electromechanical characteristics of the two configurations presented in Table 4.3.

In [169], a titanium class IV transducer that did not incorporate epoxy resin as a coupling mechanism but instead used structural prestress to couple the shells to the piezoceramic plate achieved displacement amplitudes of 10–15 µm at the same excitation voltage of 60 $V_{(rms)}$. The lower displacement amplitude of 6.91 µm obtained for the titanium transducer in the present study may therefore be partly associated with additional damping introduced by the epoxy layer.

The resonance-frequency behaviour demonstrates the relative stability of the titanium and Nitinol configurations. The Nitinol transducer exhibited a resonance-frequency shift of only

100 Hz across the investigated voltage range, while the titanium transducer exhibited a shift of 140 Hz. These frequency changes were smaller than those observed for the aluminium and stainless steel configurations, indicating greater resonance-frequency stability over the investigated excitation range.

The stainless steel transducer exhibited a lower displacement response than the titanium and Nitinol transducers, with a fitted gradient of 0.0696 μm/$V_{(rms)}$ and an R^2 value of 0.9962. At 60 $V_{(rms)}$, its maximum displacement amplitude was 4.66 μm, approximately 33% lower than the corresponding displacement amplitudes of both the titanium and Nitinol transducers. Despite the approximately linear displacement-voltage relationship, its resonance frequency decreased by 440 Hz across the investigated voltage range. The greater resonance-frequency shift indicates stronger softening of the coupled transducer system than observed for the titanium and Nitinol configurations. Thus, the nonlinear behaviour of the stainless steel configuration was manifested primarily through the resonance-frequency response rather than through a strongly nonlinear relationship between displacement amplitude and excitation voltage.

The aluminium transducer exhibited the lowest displacement response and the largest resonance-frequency shift (805 Hz) of the four configurations. Its fitted displacement-voltage gradient was 0.0476 μm/$V_{(rms)}$, approximately 57% lower than the linear gradient of the Nitinol transducer, while its displacement-voltage response was well represented by a linear relationship (R^2 = 0.9976). Although aluminium has a relatively high speed of sound (Table 4.3), second only to titanium, the aluminium transducer's harmonic response was affected by interaction with a neighbouring asymmetric flexural mode. At 50 and 60 $V_{(rms)}$, the displacement amplitude of this neighbouring mode surpassed that of the intended symmetric vibration mode (Figure 4.18). The symmetric mode exhibited displacement amplitudes of 2.88 and 3.25 μm at 50 and 60 $V_{(rms)}$, respectively, whereas the neighbouring mode reached 2.98 and 3.62 μm at the corresponding excitation levels.

According to the impedance analysis, this neighbouring mode occurs at 32.9 kHz (Figure 4.13), where it appears as a minor impedance minimum following the symmetric vibration mode. Figure 4.20 shows the corresponding asymmetric flexural mode shape obtained using the experimental setup described in Figure 4.12. As the excitation voltage increased, this asymmetric mode became increasingly prominent relative to the symmetric mode, particularly over the 30–60 $V_{(rms)}$ range. This behaviour indicates modal coupling, whereby vibrational energy is redistributed between the intended symmetric mode and the neighbouring parasitic mode rather than remaining concentrated in the symmetric response. This redistribution

reduces the effective displacement amplitude of the intended mode and provides an explanation for the comparatively low displacement-voltage gradient of the aluminium transducer. The modal interaction is also consistent with its substantially greater resonance-frequency shift and less stable harmonic response at elevated excitation voltages.

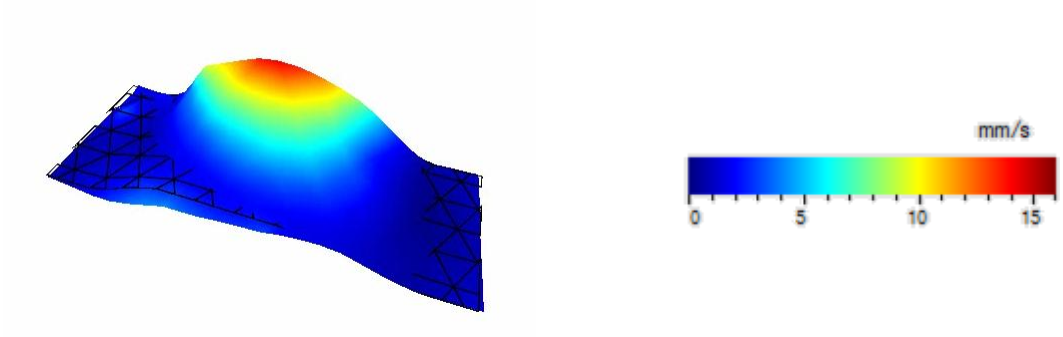


Figure 4.20 – EMA result of the asymmetric flexural mode of the aluminium transducer at 32.468 kHz, reconstructed from LDV measurements. Warm colours indicate regions of higher vibration velocity, while cooler colours indicate lower vibration velocity or near-nodal regions.

Although the Nitinol transducer exhibited neighbouring vibration modes within the electrical impedance spectrum (Figure 4.13), including modes at 16.85 kHz and 21.9 kHz, the harmonic response analysis was conducted over the frequency range 18–21.5 kHz, centred around the selected symmetric operating mode. The influence of these neighbouring modes on the measured harmonic response behaviour was not directly investigated. EMA measurements were primarily focused on vibration modes occurring within the harmonic response analysis frequency range of interest rather than performing a comprehensive modal characterisation of all neighbouring modes identified from the impedance spectra. For this reason, EMA investigation of the asymmetric flexural mode was performed for the aluminium transducer because this neighbouring mode occurred within the selected harmonic response operating range, making its influence on the transducer response more significant. These observations indicate that the influence of neighbouring vibration modes is dependent on both material selection and their proximity to the chosen operating frequency range. Future harmonic response analysis and EMA investigations could involve expanding the analysed frequency range to further evaluate modal interactions between the symmetric operating mode and neighbouring asymmetric vibration modes, particularly for the Nitinol transducer.

Figure 4.21 shows the variation in mechanical quality factor with excitation voltage for the four class IV transducers, together with fitted relationships where supported by the experimental data. The mechanical quality factor was determined using the half-power bandwidth method, as described by Equation 4.11, where Q_m is defined as the ratio of resonance frequency to the corresponding half-power bandwidth. Therefore, a reduction in Q_m, for an approximately constant resonance frequency, corresponds to an increase in resonance bandwidth. Measuring Q_m across increasing excitation voltages provides insight into changes in the resonance response and effective mechanical losses under progressively higher drive conditions [82–83].

For an ideal linear resonator with constant stiffness and damping, Q_m is expected to remain approximately independent of excitation amplitude. For a lightly damped, approximately linear single-mode resonator, Q_m is also inversely proportional to the damping ratio, as expressed by the approximate relationship ($Q_m \approx 1/2\zeta$) where ζ represents the damping ratio [83].

The voltage-dependent changes in Q_m observed in Figure 4.21 therefore indicate changes in the effective resonance characteristics of the transducers under increasing excitation. These changes may be associated with amplitude-dependent mechanical losses, nonlinear dynamic behaviour, or modal interactions, depending on the transducer configuration. However, these theoretical relationships do not prescribe a linear or second-order polynomial dependence of Q_m on excitation voltage. Consequently, the fitted relationships were selected as empirical descriptions of the measured trends, with model selection guided by goodness-of-fit parameters, residuals, and the observed physical behaviour.

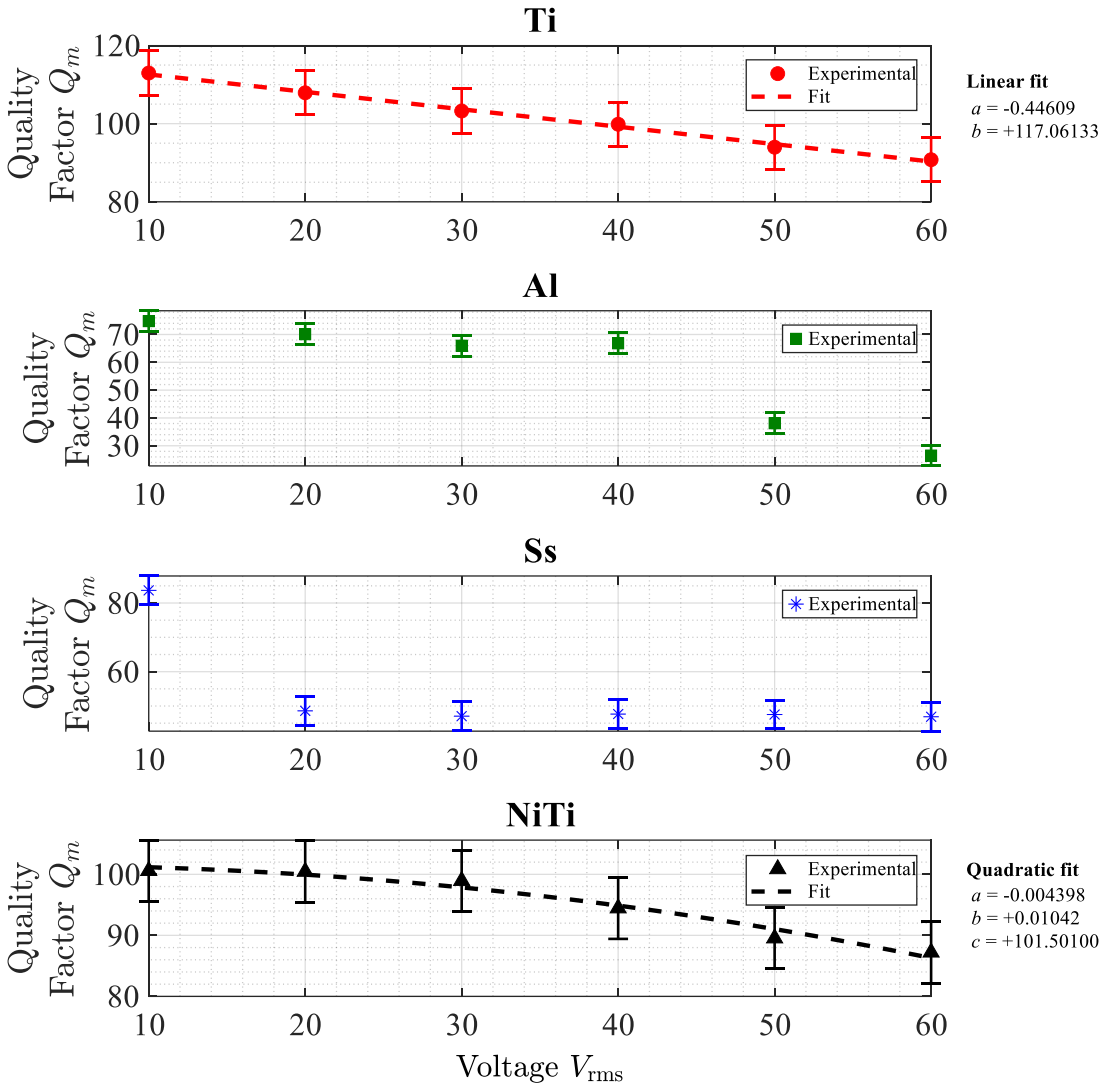


Figure 4.21 – Mechanical quality factor Q_m as a function of excitation voltage.

The titanium transducer exhibited the clearest approximately linear reduction in Q_m over the investigated voltage range. A linear fit produced an R^2 value of 0.9954, while examination of the residuals showed only small deviations from the fitted relationship. A second-order polynomial provided only a negligible improvement (R^2 =0.9960), and therefore the simpler linear model was retained. The fitted gradient was -0.446 $Q_m/V_{(rms)}$, with Q_m decreasing from 112.96 at 10 $V_{(rms)}$ to 90.77 at 60 $V_{(rms)}$. The titanium transducer also maintained the highest Q_m values throughout the investigated voltage range, indicating comparatively low effective damping associated with the measured resonance response.

The Nitinol transducer also exhibited a gradual reduction in Q_m, from 100.58 at 10 $V_{(rms)}$ to 87.21 at 60 $V_{(rms)}$. However, unlike the titanium transducer, the reduction was not strictly linear. The linear model produced an R^2 value of 0.9265, while a second-order polynomial increased this to 0.9697 and reduced the root mean square error (RMSE) from 1.43 to 0.92. Examination of the residuals similarly indicated some deviation from a purely linear relationship. A second-order polynomial was retained as an empirical description of the mildly nonlinear response. This polynomial is not intended to represent a fundamental physical relationship but provides a more appropriate representation of the measured trend over the investigated voltage range. Together with the relatively small resonance-frequency shift observed during harmonic response analysis (Figure 4.18), the gradual reduction in Q_m indicates comparatively stable dynamic behaviour. This behaviour may be associated with the intrinsic damping characteristics of the SMA [34-35].

The aluminium transducer exhibited substantially different behaviour. Q_m decreased gradually from 74.79 at 10 $V_{(rms)}$ to 66.81 at 40 $V_{(rms)}$, before decreasing sharply to 38.09 and 26.50 at 50 and 60 $V_{(rms)}$, respectively. A single linear fit did not adequately represent the complete response (R^2 =0.8290). Although a second-order polynomial increased the R^2 value to 0.9368, the corresponding residuals retained substantial deviations around the 40–50 $V_{(rms)}$ region. Therefore, no fitting function was applied to the aluminium transducer data in Figure 4.21. Applying a higher-order polynomial to obtain a closer numerical fit would provide an increasingly empirical description of the limited number of experimental points without an established physical basis. The measured response was instead interpreted directly in terms of the distinct change in behaviour at elevated excitation voltage.

The high-voltage reduction in Q_m for the aluminium transducer corresponds to the excitation range in which interaction with the neighbouring asymmetric flexural mode became increasingly prominent (Figures 4.18 and 4.20). The response indicates that vibrational energy was no longer concentrated solely within the intended symmetric mode, providing a physical basis for the deterioration in the measured resonance response at elevated excitation. Furthermore, because Q_m was determined using the HPBW method, the increasing asymmetry and modal interaction must be considered when interpreting the calculated values, since this method is most applicable to a well-defined isolated resonance. The high-voltage Q_m values for the aluminium transducer should be interpreted as

characterising an increasingly complex resonance response rather than as evidence of a simple continuous voltage-dependent relationship.

The stainless steel transducer exhibited a further distinct response. Q_m decreased sharply from 83.69 at 10 $V_{(rms)}$ to 48.58 at 20 $V_{(rms)}$, after which it remained comparatively stable between 47.06 and 46.86 over the range 30–60 $V_{(rms)}$. Neither a global linear model (R^2=0.4565) nor a second-order polynomial (R^2=0.8014) adequately represented this behaviour. In particular, the second-order polynomial introduced curvature that was not representative of the approximately constant Q_m measured after the initial decrease. Therefore, no fitting function was applied to the stainless steel data in Figure 4.21. As with the aluminium transducer, applying higher-order polynomial functions to increase the goodness of fit would not provide additional physical understanding and would risk fitting the individual experimental points rather than describing an underlying relationship. The stainless steel transducer response was interpreted directly as a rapid initial reduction followed by a comparatively stable lower-Q_m region.

The reduction in Q_m observed across the transducers indicates that increasing excitation can alter the resonance bandwidth and mechanical-loss behaviour of the coupled transducer system. This voltage-dependent behaviour departs from the approximately amplitude-independent quality factor expected for an ideal linear resonator with constant stiffness and damping. However, the present analysis demonstrates that the nature of this response is material- and configuration-dependent. The titanium transducer exhibited a well-defined approximately linear decrease while maintaining the highest Q_m, whereas the Nitinol transducer exhibited a gradual, mildly nonlinear decrease that was better represented empirically by a second-order polynomial. The aluminium transducer exhibited a deterioration at elevated excitation associated with modal interaction, while the stainless steel transducer exhibited a sharp initial reduction followed by an approximately stable lower- Q_m regime. A common fitting function or comparison based solely on linear gradients was not appropriate for all four transducers. The fitting functions presented in Figure 4.21 were therefore selected only where they provided an adequate representation of both the measured response and its physical behaviour.

The electrical power consumed by the class IV transducers is a critical parameter in assessing their operational efficiency and suitability for ultrasonic surgical applications. Higher power consumption generally indicates increased electrical demand on the driving

amplifier, greater thermal loading and reduced energy-conversion efficiency. A transducer that delivers high displacement amplitudes while drawing comparatively low power is more efficient, more stable under continuous operation and better suited to compact surgical systems where thermal constraints and power-supply limits are significant [169,183]. Therefore, quantifying power consumption across excitation voltages provides further insight into each material's electromechanical performance and practical operating limits. Figure 4.22 illustrates the electrical power consumed by the transducers from the power amplifier.

All four transducers exhibited an increasing power density with increasing excitation voltage, although the response was nonlinear rather than approximately linear. Electrical power was calculated by the experimental measurement system according to $P = V_{(rms)}^2/R$, while power density was obtained by normalising the electrical power by the volume of piezoelectric material. Since the piezoelectric volume remained constant for each transducer, a second-order dependence on excitation voltage was considered as the physically motivated candidate relationship, provided that the effective electrical resistance did not vary substantially with excitation.

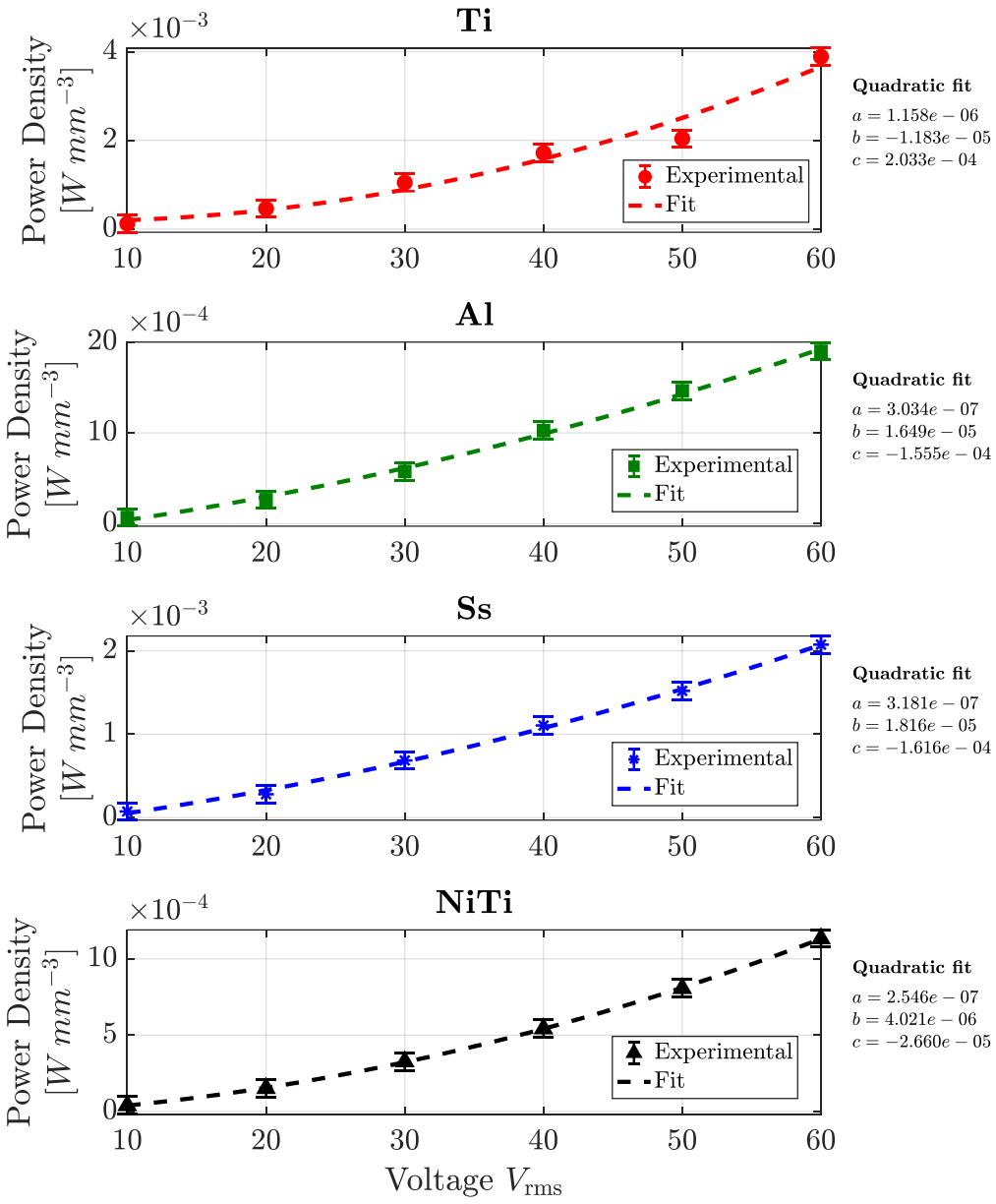


Figure 4.22 – Power density of flextensional transducers as a function of excitation voltage.

The titanium transducer exhibited the highest power density over the investigated voltage range, reaching 3.89 × 10^{-3} Wmm^{-3} at 60 $V_{(rms)}$. A second-order fit produced an R^2 value of 0.9656 and an RMSE of 2.30 × 10^{-4} Wmm^{-3}, indicating that the expected nonlinear increase provided a reasonable representation of the overall response. However, greater deviation from the fitted relationship was observed for the titanium transducer than for the other transducers, particularly at 50 $V_{(rms)}$, where the deviation exceeded the estimated ±5% experimental uncertainty. The second-order fit was considered representative of the overall voltage-dependent behaviour rather than an exact description of each experimental point. A higher-

order polynomial was not introduced to accommodate this deviation because no corresponding physical basis was identified.

The aluminium and stainless steel transducers exhibited lower power densities than the titanium transducer, reaching 1.90 and 2.08 × 10^{-3} Wmm^{-3}, respectively, at 60 $V_{(rms)}$. Their responses were represented well by second-order fits, with R^2 values of 0.9974 for aluminium and 0.9984 for stainless steel transducers. The corresponding RMSE values were 3.29 × 10^{-5} and 2.75 × 10^{-5} Wmm^{-3} respectively, and the residuals remained small relative to the estimated experimental uncertainty. The fitted relationships provide good agreement with the expected nonlinear increase in power density for both transducers over the investigated excitation range.

The Nitinol transducer exhibited the lowest power density throughout the investigated voltage range, reaching 1.13 × 10^{-3} Wmm^{-3} at 60 $V_{(rms)}$. The Nitinol transducer response showed the closest agreement with the expected second-order relationship, with R^2 =0.9999 and an RMSE of 2.88 × 10^{-6} Wmm^{-3}. The residuals were also substantially smaller than the estimated experimental uncertainty. The Nitinol transducer data provided the strongest agreement with a second-order voltage-dependent power-density response of the four transducers.

At 60 $V_{(rms)}$, the measured power densities followed the order Ti > Ss > Al > NiTi. The differences in power density should not, however, be interpreted independently as a direct measure of electromechanical conversion efficiency. The titanium transducer exhibited the highest power density, while the titanium and Nitinol transducers achieved comparable displacement amplitudes at 60 $V_{(rms)}$, despite the Nitinol transducer exhibiting the lowest power density. Assessment of electromechanical performance requires consideration of the electrical power demand together with the resulting mechanical displacement response rather than assuming that a greater power density necessarily corresponds to greater conversion efficiency.

The power consumed by the transducers is also related to their electrical behaviour at increasing excitation voltage, as examined through the electrical impedance measurements presented in Figure 4.23. Changes in impedance near resonance influence the current drawn by the transducer and therefore the electrical power required at a given excitation voltage. The measured power-density differences should consequently be considered together with the voltage-dependent impedance, mechanical losses and electromechanical response of each configuration [30,36,83]. These relationships are important when assessing amplifier

requirements and identifying transducer configurations that provide an appropriate balance between electrical power demand and mechanical displacement output.

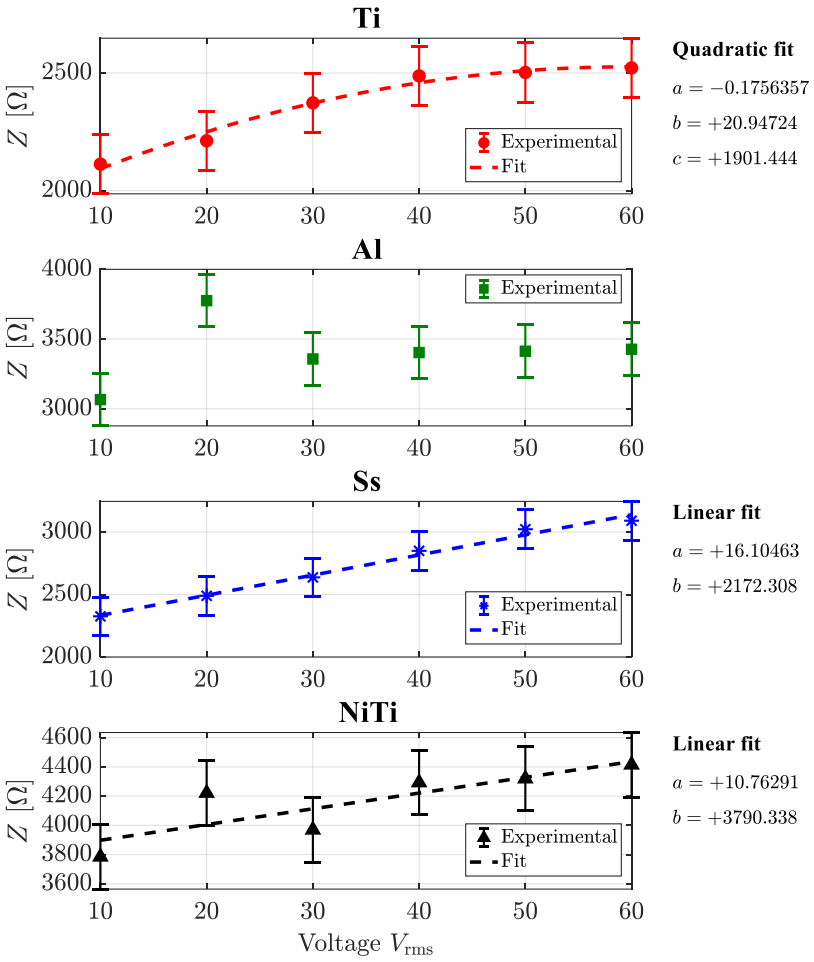


Figure 4.23 – Electrical impedance measured across excitation voltages for the flextensional transducers.

The titanium transducer exhibited the lowest overall electrical impedance values throughout the investigated voltage range, increasing from 2,112.88 Ω at 10 $V_{(rms)}$ to 2,521.71 Ω at 60 $V_{(rms)}$. The response was not strictly linear, with the rate of impedance increase becoming progressively smaller at higher excitation levels. A linear fit produced an R^2 value of 0.9017, whereas a second-order fit increased the coefficient of determination to 0.9810 and reduced the RMSE from 48.78 Ω to 21.45 Ω. The residuals from the second-order fit were also comparatively small. A second-order empirical fit was therefore considered more appropriate for describing the measured response. The resulting curvature captures the progressive increase in impedance followed by partial stabilisation at higher excitation levels. This comparatively smooth impedance response is consistent with the stable harmonic behaviour of the titanium

transducer, which exhibited only a small resonance-frequency shift and maintained a comparatively high mechanical quality factor throughout the investigated voltage range. The second-order relationship was therefore retained as an empirical representation of the observed impedance curvature, which may reflect voltage-dependent changes in the electromechanical resonance characteristics of the assembled transducer, although the present measurements do not establish a specific underlying mechanism.

The aluminium transducer exhibited a distinctly different impedance response. The impedance increased from 3,066.16 Ω at 10 $V_{(rms)}$ to 3,775.32 Ω at 20 $V_{(rms)}$, before decreasing to 3,357.24 Ω at 30 $V_{(rms)}$ and remaining comparatively stable at around 3.4 kΩ between 30 and 60 $V_{(rms)}$. Neither a linear (R^2=0.0326) nor a second-order (R^2=0.1781) relationship adequately represented the complete response. No global fitting function was applied to the aluminium transducer data. The use of a higher-order polynomial would accommodate individual data points without an established physical basis and would risk overfitting the limited dataset. The aluminium transducer response is more appropriately described as a pronounced low-voltage variation followed by a comparatively stable impedance regime. The absence of a simple voltage-dependent impedance relationship is consistent with the more complex harmonic behaviour observed for this transducer. In particular, resonance broadening, the reduction in mechanical quality factor and the increasing contribution of the neighbouring asymmetric flexural mode indicate that the aluminium transducer response became progressively influenced by modal interaction at elevated excitation. These effects provide a plausible physical basis for the absence of the smooth impedance-voltage behaviour observed for titanium and stainless steel transducers.

The stainless steel transducer exhibited the clearest approximately linear impedance response, increasing from 2,325.60 Ω at 10 $V_{(rms)}$, to 3,090.84 Ω at 60 $V_{(rms)}$. Linear regression produced an R^2 value of 0.9874, while the residuals showed only small deviations from the fitted relationship. Although a second-order fit increased the R^2 slightly to 0.9911, this improvement was insufficient to justify the additional fitting parameter. The simpler linear relationship was retained. The stainless steel transducer results demonstrate a consistent voltage-dependent increase in electrical impedance. Unlike the aluminium transducer, the stainless steel transducer did not exhibit the same neighbouring-mode interaction within the investigated excitation range, which may account for its smoother impedance response. However, its larger resonance-frequency variation and lower mechanical quality factor compared with the titanium

transducer indicate that the transducer nevertheless experienced greater voltage-dependent changes in its mechanical resonance behaviour.

The Nitinol transducer exhibited the highest electrical impedance values over most of the investigated voltage range, increasing overall from 3,784.76 Ω at 10 $V_{(rms)}$ to 4,414.46 Ω at 60 $V_{(rms)}$. Point-to-point variation was observed, particularly between 20 and 40 $V_{(rms)}$. A linear fit produced an R^2 value of 0.7028, while a second-order fit provided only a small improvement to 0.7174. The additional curvature therefore did not provide sufficient improvement to justify the more complex model. A linear fit was retained only as a representation of the overall increasing trend and should not be interpreted as evidence of a strongly defined linear relationship. Despite the local impedance variations, the Nitinol transducer exhibited the smallest resonance-frequency shift of the four configurations and maintained comparatively high displacement amplitudes. The comparatively high intrinsic damping characteristics commonly associated with Nitinol structures may contribute to its distinct electromechanical response [34,35,187]. Such damping may assist in limiting abrupt resonance changes and the development of strong modal interactions, although the present measurements do not independently isolate the contribution of material damping from the other electromechanical mechanisms within the assembled transducer.

The impedance analysis (Figure 4.23) demonstrated that the four transducer configurations exhibited distinctly different voltage-dependent responses and could not appropriately be described using a common fitting model. The titanium transducer exhibited a nonlinear increase followed with a progressively decreasing rate of increase at higher excitation levels, the aluminium transducer showed a pronounced low-voltage variation followed by a comparatively stable response, the stainless steel transducer demonstrated a well-defined approximately linear increase, and the Nitinol transducer exhibited an overall increasing trend accompanied by greater experimental scatter. The differences in impedance behaviour corresponded with differences in resonance-frequency variation, mechanical quality factor and modal behaviour, indicating that the electrical response was closely associated with the material-dependent dynamic behaviour of the assembled transducers. The selection of different empirical fitting models was therefore informed by the observed differences in resonance and modal behaviour, rather than solely by the coefficients of determination. These fitted relationships describe the measured voltage-dependent trends and are not intended to establish the underlying physical mechanisms responsible for the observed responses.

All four configurations exhibited resonance-frequency softening with increasing excitation voltage; however, the magnitude of the frequency shift and the associated changes in displacement amplitude, mechanical quality factor, power density, electrical impedance and modal behaviour differed substantially between the investigated end-cap materials. These differences indicate that the high-excitation behaviour resulted from the combined influence of material properties, mechanical losses, electromechanical coupling and the interaction of neighbouring vibration modes.

The titanium and Nitinol transducers exhibited the most stable resonance-frequency responses, with resonance-frequency shifts of 140 Hz and 100 Hz, respectively. At 60 $V_{(rms)}$, the titanium transducer achieved a displacement amplitude of 6.91 µm, comparable to the 6.98 µm achieved by the Nitinol transducer and maintained the highest mechanical quality factor throughout the investigated voltage range. Its displacement-voltage response was better represented by a quadratic relationship, while its comparatively smooth impedance response exhibited a progressively smaller rate of increase at higher excitation levels. These characteristics indicate that the titanium configuration maintained a well-defined mechanical response with comparatively low mechanical losses as excitation increased. The titanium transducer also exhibited the highest power density, indicating that its mechanical output was accompanied by the greatest electrical power demand of the investigated configurations.

The aluminium transducer exhibited the strongest nonlinear and modal behaviour. Its resonance frequency decreased by 805 Hz across the investigated voltage range, while the displacement amplitude reached only 3.25 µm at 60 $V_{(rms)}$. The increasing contribution of the neighbouring asymmetric flexural mode at elevated excitation was accompanied by resonance broadening and a pronounced reduction in mechanical quality factor. These observations are consistent with increasing redistribution of vibrational energy between interacting vibration modes rather than its remaining concentrated in the intended symmetric response. The irregular impedance behaviour provides further evidence that the electromechanical response of the aluminium configuration could not be described by a single simple voltage-dependent relationship. Modal coupling therefore provides a physically plausible explanation for the comparatively unstable high-excitation response of the aluminium transducer.

The stainless steel transducer exhibited intermediate behaviour. Its displacement amplitude reached 4.66 µm at 60 $V_{(rms)}$, while the resonance-frequency shift of 440 Hz was greater than those measured for titanium and Nitinol but substantially smaller than that of aluminium. The

sharp initial reduction in mechanical quality factor followed by a lower- Q_m plateau indicates increased mechanical losses relative to the titanium transducer, although the stainless steel transducer did not exhibit the pronounced neighbouring-mode interaction observed for the aluminium transducer. Its electrical impedance increased smoothly and approximately linearly with excitation voltage. The stainless steel results therefore demonstrate that substantial changes in mechanical damping and resonance behaviour can occur even when the corresponding electrical impedance response remains comparatively regular.

The Nitinol transducer exhibited a distinct combination of comparatively stable resonance behaviour and high mechanical displacement. Its resonance-frequency shift of 100 Hz was the smallest of the four configurations, while its displacement amplitude reached 6.98 μm at 60 $V_{(rms)}$, comparable to the 6.91 μm achieved by the titanium transducer. The gradual reduction in mechanical quality factor, absence of the modal interaction observed for the aluminium transducer, and comparatively small resonance-frequency variation suggest that the Nitinol transducer maintained a relatively stable vibration response as excitation increased. The Nitinol transducer also exhibited the lowest power density while maintaining comparatively high displacement, together with the highest overall electrical impedance. The intrinsic damping characteristics associated with Nitinol [34,35,187] may contribute to suppressing abrupt resonance instability and strong modal interaction; however, the present results do not independently quantify the extent to which this behaviour arises from intrinsic material damping rather than the complete electromechanical transducer configuration.

Overall, the titanium and Nitinol transducers exhibited comparable displacement amplitudes at 60 $V_{(rms)}$, while demonstrating different high-excitation characteristics. The titanium transducer maintained the highest mechanical quality factor and comparatively stable resonance behaviour, whereas the Nitinol transducer demonstrated the smallest resonance-frequency variation and maintained comparable displacement at the lowest measured power density. The aluminium transducer was most strongly affected by modal interaction and resonance instability, whereas the stainless steel transducer exhibited intermediate mechanical behaviour without the pronounced modal coupling observed for the aluminium transducer. The combined results indicate that neighbouring vibration modes, material-dependent damping, mechanical losses and electromechanical coupling can collectively influence the high-excitation response of flextensional ultrasonic transducers. These parameters should be considered collectively, rather than individually, when selecting end-cap materials and optimising future transducer designs.

4.2.4. Results from temperature studies

Figure 4.24 shows how the resonance frequency of the transducers varied with temperature.

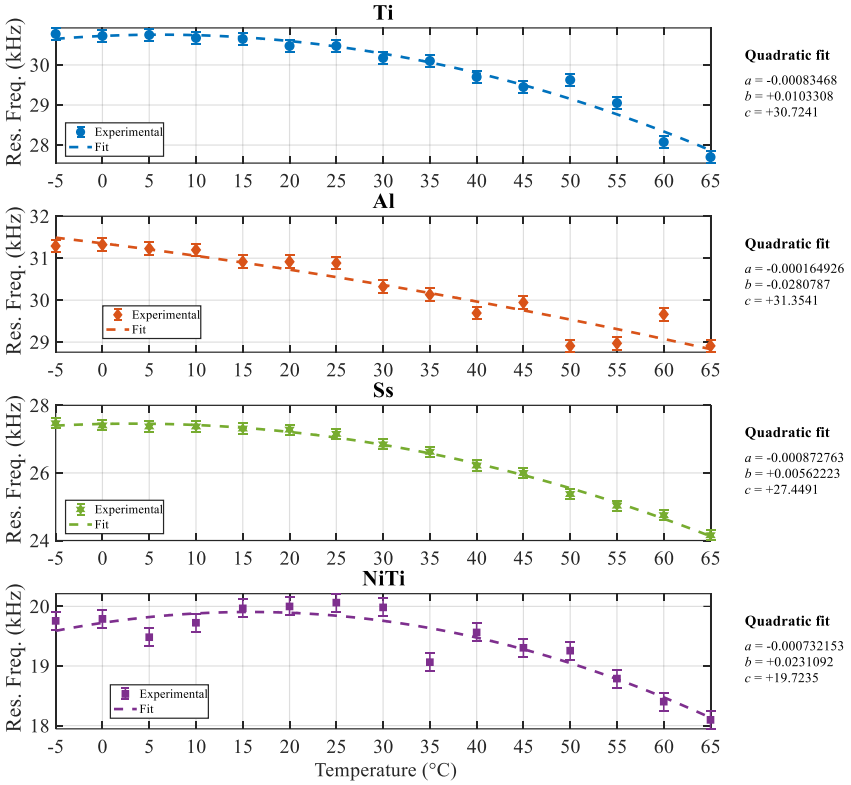


Figure 4.24 – Change in the resonance frequency as a function of temperature as identified by EIA.

The titanium transducer exhibited a nonlinear decrease in resonance frequency with increasing temperature, from 30.775 kHz at −5 °C to 27.7 kHz at 65 °C. The response was comparatively shallow at lower temperatures before the rate of frequency reduction increased progressively at elevated temperatures. A second-order relationship provided a strong representation of this behaviour, with $R^2 = 0.9653$ and an RMSE of 0.1756 kHz. The residuals were generally small, although greater deviations were observed from 50–65 °C. The fitted curvature is consistent with a temperature sensitivity that became increasingly negative as temperature increased. The titanium transducer response was therefore characterised by a progressively increasing sensitivity of resonance frequency to temperature rather than a constant frequency-temperature gradient.

The aluminium transducer exhibited an overall decrease in resonance frequency from 31.291 kHz at −5 °C to 28.910 kHz at 65 °C, accompanied by appreciable point-to-point

variation, particularly at elevated temperatures. A second-order polynomial fit was applied to maintain consistency with the fitting approach adopted for the other transducer configurations, producing an R^2 value of 0.8959 and an RMSE of 0.2806 kHz. This represented only a marginal improvement over the linear fit (R^2 = 0.8897, RMSE = 0.2888 kHz). The relatively small quadratic coefficient (a = −0.000164926 kHz/°C²) indicates that the temperature-dependent response remained approximately linear over much of the investigated range, with modest curvature. The residuals demonstrated greater scatter than those observed for the titanium and stainless steel transducers, particularly at higher temperatures. Consequently, the fitted relationship should be interpreted as an empirical representation of the overall temperature-dependent resonance behaviour rather than a precise prediction of resonance frequency at individual temperatures.

The stainless steel transducer exhibited a pronounced nonlinear reduction in resonance frequency, decreasing from 27.469 kHz at −5 °C to 24.156 kHz at 65 °C. The resonance frequency changed relatively slowly at lower temperatures before decreasing at a progressively greater rate as temperature increased. A second-order relationship represented the measured response particularly well, producing R^2 = 0.9947 and an RMSE of 0.0786 kHz. The small residual deviations further supported the suitability of the fitted relationship. The fitted curvature indicates that the temperature sensitivity of the stainless steel configuration increased substantially in magnitude with increasing temperature and therefore cannot appropriately be characterised using a single constant frequency-temperature gradient.

The Nitinol transducer exhibited a distinctly different temperature-dependent response. The resonance frequency remained comparatively stable across the lower-temperature range, with values close to approximately 20 kHz, before decreasing more strongly at elevated temperatures. The resonance frequency was 19.757 kHz at −5 °C and decreased to 18.096 kHz at 65 °C. A second-order relationship captured the overall nonlinear behaviour, producing R^2 = 0.8684 and an RMSE of 0.2112 kHz. Experimental scatter remained, particularly around 35 °C, and the fitted relationship should be regarded as an empirical representation of the overall temperature-dependent response rather than a precise predictive model. Nevertheless, the fitted curvature captures the change from the comparatively stable lower-temperature behaviour to an increasingly negative temperature sensitivity at elevated temperatures.

The Nitinol end-cap exhibited an A_F of 35 °C, while previous investigations of Nitinol cymbal and Langevin-type ultrasonic transducers have reported temperature-dependent resonance behaviour associated with the thermomechanical properties of Nitinol [27–30,34,35]. Although the measured response became more strongly temperature dependent across the elevated-temperature region, no discrete resonance-frequency shift was observed at 35 °C that could be directly associated with A_F. The present measurements therefore do not independently demonstrate that the nonlinear resonance response resulted from the martensitic-to-austenitic transformation. Instead, the response may reflect the combined influence of the temperature-dependent mechanical properties of the Nitinol end-cap and the dynamic behaviour of the complete transducer assembly. Residual stresses introduced during Wire-EDM processing may additionally influence the transformation characteristics of Nitinol [47]. The resonance-frequency response provides evidence of a distinct temperature dependence for the Nitinol configuration, but the contribution of the Nitinol phase transformation cannot be isolated from the present measurements.

More generally, the temperature-dependent resonance-frequency response represents the behaviour of the complete flextensional transducer assembly. Resonance frequency is governed by the dynamic characteristics of the assembled structure, and temperature-dependent changes in structural stiffness, mechanical losses, the piezoceramic elements, adhesive layers, structural interfaces and electromechanical coupling may therefore contribute to the observed behaviour. Previous studies have demonstrated that temperature can influence the dielectric, elastic and piezoelectric properties of piezoceramic materials [188–190], providing an additional mechanism through which temperature may alter transducer resonance behaviour. Since the individual temperature-dependent properties of the piezoceramic material, epoxy layer and end-cap materials were not independently characterised during operation, their respective contributions cannot be isolated from the present measurements.

Overall, the temperature-dependent resonance behaviour differed substantially between the four transducer configurations. Titanium and stainless steel transducers exhibited nonlinear decreases in resonance frequency, with the magnitude of their temperature sensitivity increasing at elevated temperatures. The aluminium transducer exhibited an approximately linear overall decrease accompanied by greater experimental scatter. The Nitinol transducer exhibited a distinct nonlinear response, characterised by comparatively stable resonance behaviour at lower temperatures followed by a greater frequency reduction at elevated

temperatures. These results demonstrate that the four end-cap material configurations exhibited differences in both the magnitude and form of the temperature-dependent dynamic response of the assembled class IV flextensional transducers.

Figure 4.25 shows how the electrical impedance of the transducers varied with temperature.

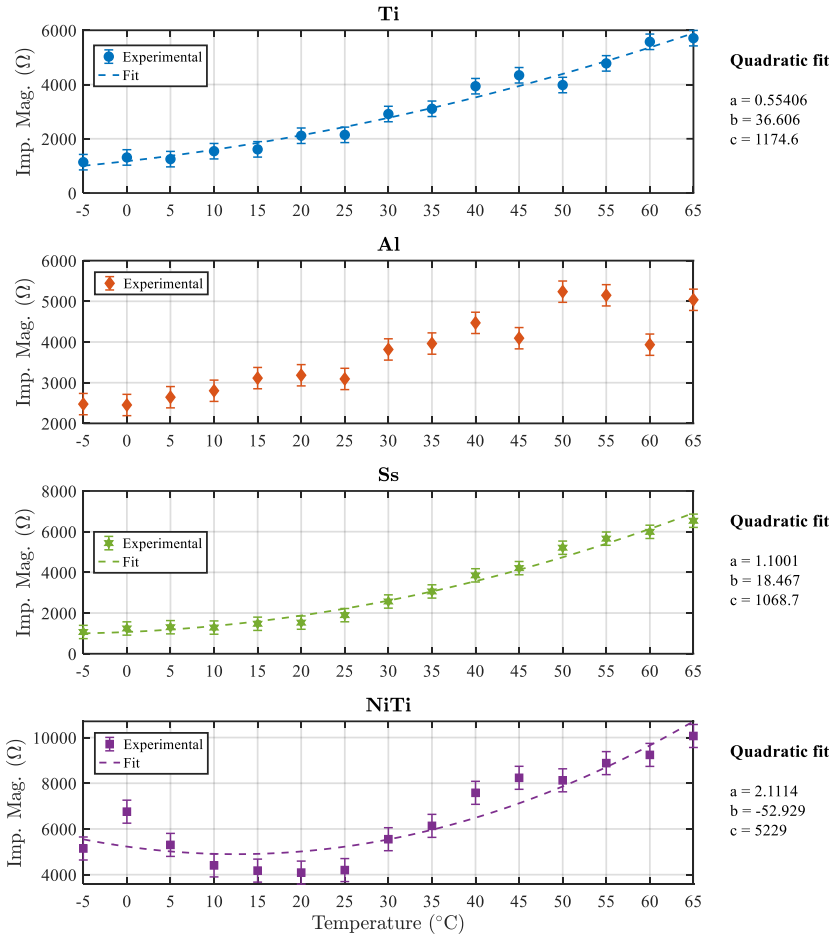


Figure 4.25 – Electrical impedance as a function of temperature.

The titanium transducer exhibited an overall nonlinear increase in electrical impedance magnitude with increasing temperature, from 1,137.86 Ω at −5 °C to 5,709.28 Ω at 65 °C. The increase was comparatively gradual at lower temperatures and became progressively greater as temperature increased. A second-order relationship provided a strong representation of the overall response, with $R^2 = 0.9777$ and an RMSE of 230.6 Ω. Although some point-to-point deviations remained, particularly at elevated temperatures, the residuals were distributed about the fitted response without altering the overall curvature of the measured trend. The second-order relationship therefore indicates that the impedance-temperature sensitivity of the titanium configuration was not constant but increased progressively with temperature.

The aluminium transducer exhibited an overall increase in electrical impedance magnitude with temperature but with substantially greater point-to-point variation than the titanium and stainless steel configurations. The impedance increased from 2,474.26 Ω at −5 °C to 5,037.37 Ω at 65 °C, although pronounced deviations from a smooth temperature-dependent response occurred at elevated temperatures. Neither a global linear nor a second-order relationship adequately represented the measured behaviour, while a two-region representation did not provide sufficient physical or statistical justification for assigning separate temperature-dependent regimes. No global fitting function was applied to the aluminium data. The aluminium response is therefore more appropriately interpreted directly from the experimental measurements rather than by assigning a single impedance-temperature sensitivity to the configuration.

The stainless steel transducer exhibited a pronounced nonlinear increase in electrical impedance magnitude, from 1,069.70 Ω at −5 °C to 6,536.80 Ω at 65 °C. The impedance changed comparatively gradually over the lower-temperature range before increasing more rapidly at elevated temperatures. A second-order relationship represented this behaviour strongly, producing $R^2 = 0.9846$ and an RMSE of 234.9 Ω. The residual analysis showed that the fitted relationship captured the principal curvature of the experimental response despite some local deviations. The fitted curvature indicates that the temperature sensitivity of the stainless steel configuration increased substantially as temperature increased and therefore cannot appropriately be represented by a single constant impedance-temperature gradient.

The Nitinol transducer exhibited a complex temperature-dependent impedance response. Unlike the predominantly increasing responses observed for titanium and stainless steel, the Nitinol transducer impedance was comparatively high at the lowest temperatures, decreased across part of the lower-temperature range and subsequently increased strongly at elevated temperatures. The impedance magnitude was 5,145.04 Ω at −5 °C and reached 10,068.60 Ω at 65 °C. A second-order empirical relationship captured the broad nonlinear form of this response, with $R^2 = 0.8548$ and an RMSE of 749.4 Ω. However, the residuals were substantially larger than those obtained for the titanium and stainless steel fits, demonstrating considerable point-to-point variation that was not captured by the fitted relationship. The second-order relationship should be regarded as an empirical description of the overall nonlinear response rather than a precise predictive model. Nevertheless, it captures the broad progression from decreasing or comparatively weak impedance variation at lower temperatures to a pronounced increase in impedance magnitude at elevated temperatures.

The temperature-dependent behaviour of the Nitinol configuration is particularly relevant in relation to the thermomechanical properties of the end-cap material. Nitinol can exhibit substantially greater internal friction and damping than conventional structural metals, with its mechanical behaviour also varying with temperature and phase state [12,187]. These characteristics may contribute to the distinct electromechanical response observed for the Nitinol transducer. However, the measured electrical impedance magnitude represents the response of the complete piezoelectric transducer and does not independently establish that the nonlinear impedance behaviour resulted directly from changes in Nitinol damping or from the martensitic-to-austenitic transformation. The independently measured A_F of 35 °C provides additional context for interpreting the response. Above this temperature, the Nitinol end-cap would be expected to be predominantly austenitic on heating, while the impedance magnitude exhibited a pronounced overall increase across the elevated-temperature region. However, the impedance measurements did not exhibit a discrete change at A_F and considerable variation was present across the transformation-temperature region. Therefore, although the increasing impedance at elevated temperatures occurs within the predominantly austenitic temperature range, the measurements do not provide evidence of a distinct transformation-induced impedance shift at 35 °C. Instead, the results indicate that the electromechanical response of the Nitinol transducer became increasingly temperature dependent at elevated temperatures, potentially reflecting the combined influence of the temperature-dependent Nitinol material state and changes in the piezoceramic properties, structural stiffness, mechanical losses, adhesive layers and interfaces within the assembled transducer.

More generally, the temperature-dependent electrical impedance represents the response of the complete flextensional transducer assembly rather than the end-cap material in isolation. The measured electrical impedance is coupled to the mechanical response of the transducer and may therefore be influenced by temperature-dependent changes in structural stiffness, mechanical losses, resonance behaviour and electromechanical coupling. Temperature-dependent changes in the dielectric, elastic and piezoelectric properties of the piezoceramic elements may also contribute to the measured response [188–190]. In addition, changes associated with the adhesive layers and structural interfaces may influence the mechanical boundary conditions of the assembled device. Since these individual temperature-dependent contributions were not independently characterised during operation, the differences observed between the four transducers cannot be attributed solely to the intrinsic properties of their respective end-cap materials. The second-order fitting functions were therefore used as empirical representations of the overall nonlinear impedance–temperature responses, rather

than as theoretical models of the underlying electromechanical mechanisms. No global fitting function was applied to the aluminium transducer because its irregular temperature-dependent response could not be adequately represented by the investigated polynomial models.

The variation in mechanical quality factor with temperature is shown in Figure 4.26.

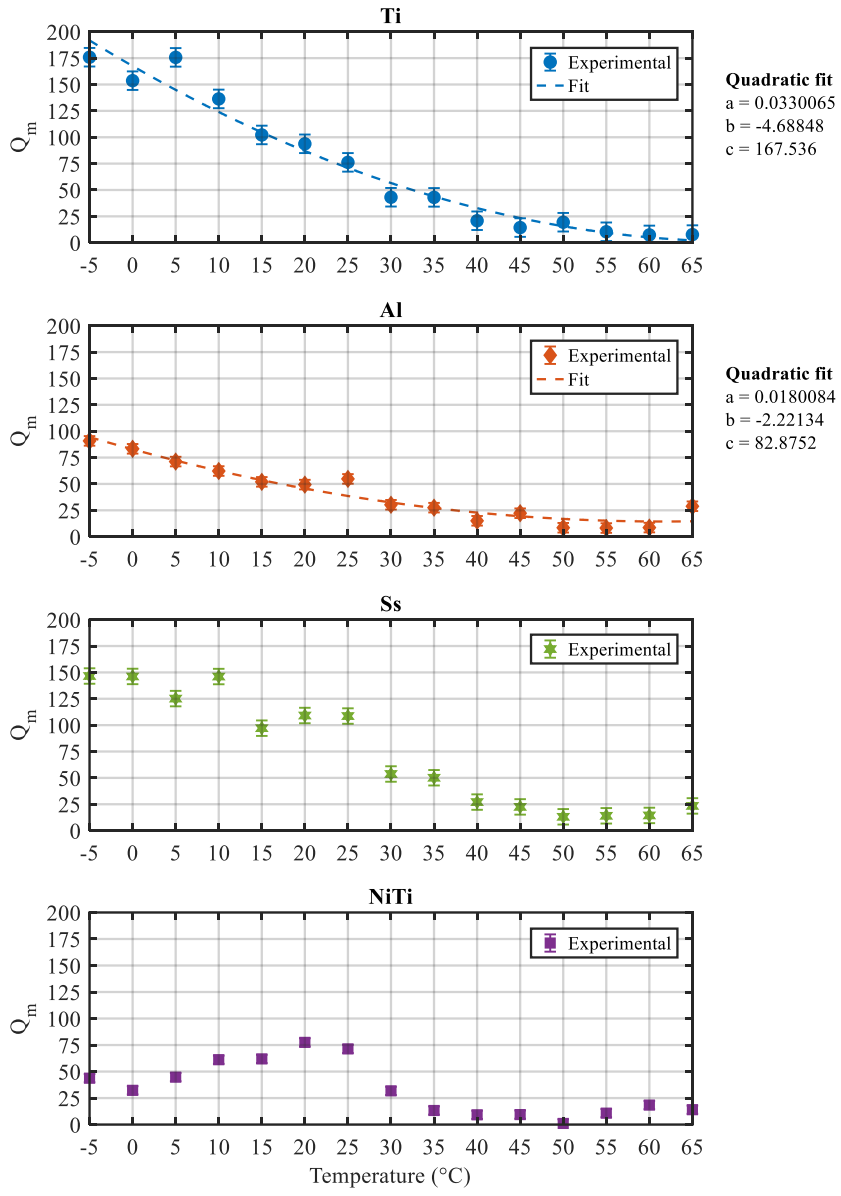


Figure 4.26 – Mechanical quality factor as a function of temperature.

The titanium transducer exhibited the highest Q_m values at the lower temperatures and a pronounced reduction with increasing temperature. Q_m decreased overall from 175.86 at −5 °C to 7.69 at 65 °C, although appreciable point-to-point variation was present, particularly at lower temperatures. A linear relationship produced $R^2 = 0.9129$ and an RMSE of 18.07, whereas a

second-order relationship increased the coefficient of determination to R^2 =0.9629 and reduced the RMSE to 11.79. The second-order relationship was therefore considered more appropriate for representing the overall temperature-dependent behaviour. The fitted curvature indicates that the rate of reduction in Q_m was not constant with temperature. The substantial decrease in Q_m indicates a progressive reduction in resonance sharpness, consistent with increased effective mechanical losses within the assembled transducer as temperature increased.

The aluminium transducer also exhibited an overall reduction in Q_m, decreasing from 90.80 at −5 °C and reaching generally low values at elevated temperatures, although an increase to 28.83 was observed at 65 °C. A linear fit produced R^2 =0.8539 and an RMSE of 10.19, while a second-order relationship increased R^2 to 0.9323 and reduced the RMSE to 6.94. The second-order empirical relationship therefore provided a better representation of the overall measured response. Nevertheless, point-to-point variation remained, particularly at elevated temperatures, and the increase observed at 65 °C was not captured by the general decreasing behaviour. The fitted relationship should therefore be regarded as an empirical representation of the overall temperature dependence rather than a precise prediction of Q_m at individual temperatures.

The stainless steel transducer exhibited an overall reduction in Q_m from 146.58 at −5 °C to 23.43 at 65 °C, accompanied by substantial point-to-point variation. A linear relationship produced R^2= 0.8956 and an RMSE of 16.79, while a second-order relationship provided only a modest improvement to R^2= 0.9079 and an RMSE of 15.77. Although both relationships captured the overall reduction in Q_m, neither adequately represented the pronounced local variations within the measured response. The relatively small improvement obtained using the additional second-order term was therefore considered insufficient to justify application of a global nonlinear fitting relationship. No global fit was retained for the stainless steel data. The experimental measurements nevertheless show an overall reduction in Q_m with increasing temperature, indicating reduced resonance sharpness, consistent with increased effective mechanical losses within the assembled transducer at elevated temperatures.

The Nitinol transducer exhibited a distinctly different temperature-dependent Q_m response. Rather than decreasing monotonically with increasing temperature, Q_m increased from 43.76 at −5 °C to a maximum measured value of 77.51 at 20 °C before decreasing substantially at higher temperatures. A linear relationship provided a poor representation of the measured behaviour, with R^2=0.4440 and an RMSE of 18.19. A second-order relationship provided only a small improvement, producing R^2=0.4852 and an RMSE of 17.51. Neither relationship adequately represented the complete measured response, and no global fitting function was

therefore applied. The Nitinol response is more appropriately described directly from the experimental measurements as an initial increase in Q_m, followed by a pronounced reduction at elevated temperatures.

The non-monotonic response of the Nitinol configuration is particularly relevant when considered in relation to the temperature-dependent thermomechanical characteristics of Nitinol. Previous investigations of Nitinol-based ultrasonic transducers have reported temperature-dependent changes in dynamic behaviour associated with the thermomechanical properties of the material [27–30,34,35]. In the present investigation, the Nitinol end-cap exhibited an independently measured A_F of 35 °C. However, the maximum Q_m occurred at 20 °C and no discrete change in Q_m was observed at A_F. The measurements therefore do not independently establish that the observed non-monotonic response resulted directly from the martensitic-to-austenitic transformation. Instead, the response may reflect the combined influence of the temperature-dependent properties of the Nitinol end-cap and the dynamic behaviour of the complete transducer assembly. Nitinol can also exhibit comparatively high internal friction and damping, which may further influence its dynamic response [12,187], although the contribution of material damping cannot be independently isolated from the present measurements.

The temperature-dependent variations observed in resonance frequency, electrical impedance and mechanical quality factor for the A_F 35 °C Nitinol transducer can be considered in relation to the material-characterisation results presented in Chapter 3. The DSC box-and-whisker plot (Figure 3.10a) demonstrated that the martensitic-to-austenitic transformation occurred over a finite temperature range and varied between the four investigated end-cap regions, providing material context for the gradual temperature-dependent changes observed in the transducer response rather than suggesting a discrete response at a single transformation temperature. EDXS also identified variations in nickel content between regions of the end-cap, particularly at the apex, protrusion and slanted regions, together with minor oxygen- and iron-containing regions (spectra 32–33, 50–51 and 38–39 of Table 3.1). These compositional variations indicate local chemical heterogeneity within the investigated Nitinol end-cap regions and may provide additional material context for the complex temperature-dependent behaviour observed in the assembled transducer. However, their influence on the local transformation characteristics cannot be established from the present EDXS measurements. Residual stresses introduced during Wire-EDM processing may additionally influence the transformation characteristics of Nitinol [47]. However, the respective contributions of material composition,

processing, phase transformation and other temperature-dependent characteristics of the complete transducer assembly cannot be isolated from the present measurements.

More generally, the measured mechanical quality factor represents the behaviour of the complete flextensional transducer assembly rather than the intrinsic damping characteristics of the end-cap material in isolation. Q_m may be influenced by temperature-dependent changes in structural stiffness, mechanical losses, piezoceramic behaviour, adhesive layers, structural interfaces and electromechanical coupling. Temperature-dependent changes in the dielectric, elastic and piezoelectric properties of piezoceramic materials may also contribute to changes in the dynamic response of the assembled transducer [188–190]. Since these individual contributions were not independently characterised during operation, the differences in Q_m observed between the four configurations cannot be attributed solely to the intrinsic properties of their respective end-cap materials.

When the resonance frequency, electrical impedance and mechanical-quality factor measurements are considered together, the Nitinol transducer exhibited a temperature-dependent electromechanical response that differed from those of the titanium, aluminium and stainless steel configurations. The resonance frequency remained comparatively stable across the lower-temperature region before decreasing more strongly at elevated temperatures, the electrical impedance exhibited a complex nonlinear response, and Q_m initially increased before subsequently decreasing. These observations demonstrate that the Nitinol configuration exhibited distinct temperature-dependent dynamic characteristics. However, the absence of a discrete response at A_F across these measurements means that the contribution of the martensitic-to-austenitic transformation cannot be independently distinguished from the other temperature-dependent mechanisms present within the assembled transducer.

Overall, the temperature study demonstrated that the four end-cap material configurations exhibited differences in both the magnitude and form of the thermal response of the class IV flextensional transducers. Titanium, aluminium and stainless steel transducers predominantly exhibited reductions in resonance frequency and mechanical quality factor together with increasing electrical impedance as temperature increased, although the detailed response differed between the configurations. The Nitinol transducer exhibited more complex nonlinear behaviour, particularly in its resonance frequency, impedance and Q_m responses. The material-characterisation results provide a physical context in which these differences may be interpreted, but they do not establish that the transducer response was governed solely by the Nitinol phase transformation. The results therefore demonstrate a distinct temperature-dependent electromechanical response associated with the Nitinol end-cap configuration while

recognising the combined influence of the material properties and the complete assembled transducer structure [27–30,34,35,47].

4.2.5. Results of Nitinol transducers with A_F temperatures of 35 °C and 45 °C

In Figure 4.24, the Nitinol transducer did not exhibit an expected shift in resonance frequency when heated above its A_F temperature (35 °C). To investigate this behaviour further, a second geometrically identical Nitinol transducer was fabricated and assembled. The end-caps were manufactured using the same wire-EDM process as the original transducer; however, they were produced from a different Nitinol sheet material (same supplier) with a higher A_F of 45 °C, compared with 35 °C for the original transducer. The resonance frequency, electrical impedance, and mechanical quality factor responses of the two Nitinol transducers were compared over a temperature range of -5 °C to 65 °C to evaluate the influence of transformation temperature on the dynamic behaviour of the Nitinol transducers.

The change in the resonance frequency of the Nitinol transducers with temperature are shown in Figure 4.27.

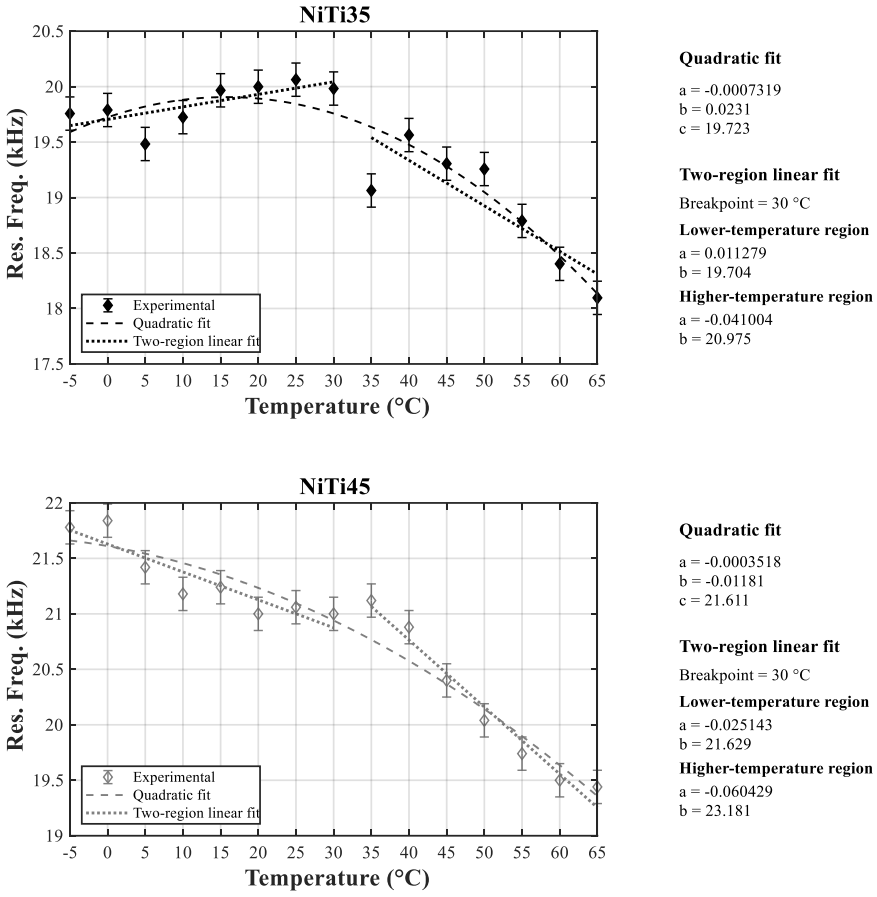


Figure 4.27 - Resonance frequency of Nitinol transducers.

The comparison between the 35 °C A_F and 45 °C A_F Nitinol transducers demonstrated that the temperature-dependent resonance-frequency responses differed between the two Nitinol end-cap conditions. Although both configurations exhibited an overall reduction in resonance frequency with increasing temperature, differences were observed in the form and magnitude of their temperature dependence. For consistency, both second-order polynomial and two-region linear fitting relationships were evaluated for each configuration, as presented in Figure 4.27.

The 35 °C A_F transducer exhibited a nonlinear response. The resonance frequency remained close to approximately 20 kHz across the lower-temperature region, increasing slightly from 19.757 kHz at −5 °C to a maximum measured value of 20.063 kHz at 25 °C before decreasing at elevated temperatures to 18.096 kHz at 65 °C. The second-order empirical relationship represented the broad nonlinear response with R^2 = 0.8682 and an RMSE of 0.2113 kHz. The two-region linear relationship, with a breakpoint at 30 °C, provided a marginally improved fit (R^2 = 0.8797, RMSE = 0.2019 kHz). However, the improvement was relatively small, and the

second-order relationship provided a continuous empirical representation of the broad maximum and subsequent reduction in resonance frequency without introducing a breakpoint. Appreciable local deviations remained, particularly around 35 °C, and both fitting relationships should therefore be interpreted as empirical approximations rather than precise predictive models.

The 45 °C A_F transducer exhibited a different temperature-dependent response. The resonance frequency decreased from 21.780 kHz at −5 °C to 19.440 kHz at 65 °C, with the rate of reduction becoming substantially greater at elevated temperatures. A global second-order model provided a strong representation of the response (R^2 = 0.9393, RMSE = 0.1845 kHz); however, the two-region linear relationship provided an improved empirical description, with R^2 = 0.9747 and an RMSE of 0.1191 kHz. The lower-temperature region exhibited a gradient of approximately −25.1 Hz °C^{-1}, whereas the higher-temperature region exhibited a greater negative gradient of approximately −60.4 Hz °C^{-1}. The magnitude of the fitted temperature sensitivity therefore increased by a factor of approximately 2.41 between the two regions.

The two-region linear relationships for both configurations employed a breakpoint at 30 °C. These breakpoints should not be interpreted as direct measurements of the Nitinol phase-transformation temperatures. The independently characterised end-caps exhibited A_F temperatures of 35 °C and 45 °C, respectively, while the resonance-frequency measurements represent the response of the complete assembled transducers. Although the two-region relationships provided useful empirical descriptions of changes in temperature sensitivity, they do not establish discrete changes in material properties at the selected breakpoints. In particular, no discrete resonance-frequency shift was observed precisely at 45 °C that could independently establish a direct transformation-induced response.

Comparison of the two Nitinol configurations therefore demonstrates that increasing the end-cap transformation temperature did not simply translate the 35 °C A_F response to a higher temperature. The 35 °C A_F transducer exhibited a broad shallow maximum followed by an increasingly negative temperature dependence, whereas the 45 °C A_F transducer exhibited a negative temperature dependence across the investigated range, with a greater reduction rate at elevated temperatures. Although the two-region linear relationships produced higher R^2 values for both configurations, the second-order relationship was considered a more appropriate continuous representation of the broad nonlinear response of the 35 °C A_F transducer. Conversely, the two-region relationship provided a closer empirical representation of the change in temperature sensitivity observed for the 45 °C A_F transducer. These differences should not necessarily be attributed to distinct phase-transformation mechanisms, since the

measured resonance response also reflects the coupled behaviour of the piezoceramic elements, structural stiffness, mechanical losses, adhesive interfaces and the wider assembled structure [27–30,169].

Overall, the comparison demonstrates that the two Nitinol end-cap conditions produced measurably different resonance-frequency responses under thermal excitation. Applying both fitting approaches consistently allowed their relative suitability to be assessed using the measured trends and fitting statistics. The second-order relationship provided a reasonable continuous description of the 35 °C A_F response, whereas the two-region linear relationship more closely represented the changing temperature sensitivity of the 45 °C A_F response. Nevertheless, neither empirical fitting relationship independently identifies the underlying phase-transformation behaviour, and the resonance-frequency measurements alone cannot isolate the contribution of Nitinol from the response of the complete transducer assembly.

The change in the electrical impedance of the Nitinol transducers with temperature are shown in Figure 4.28.

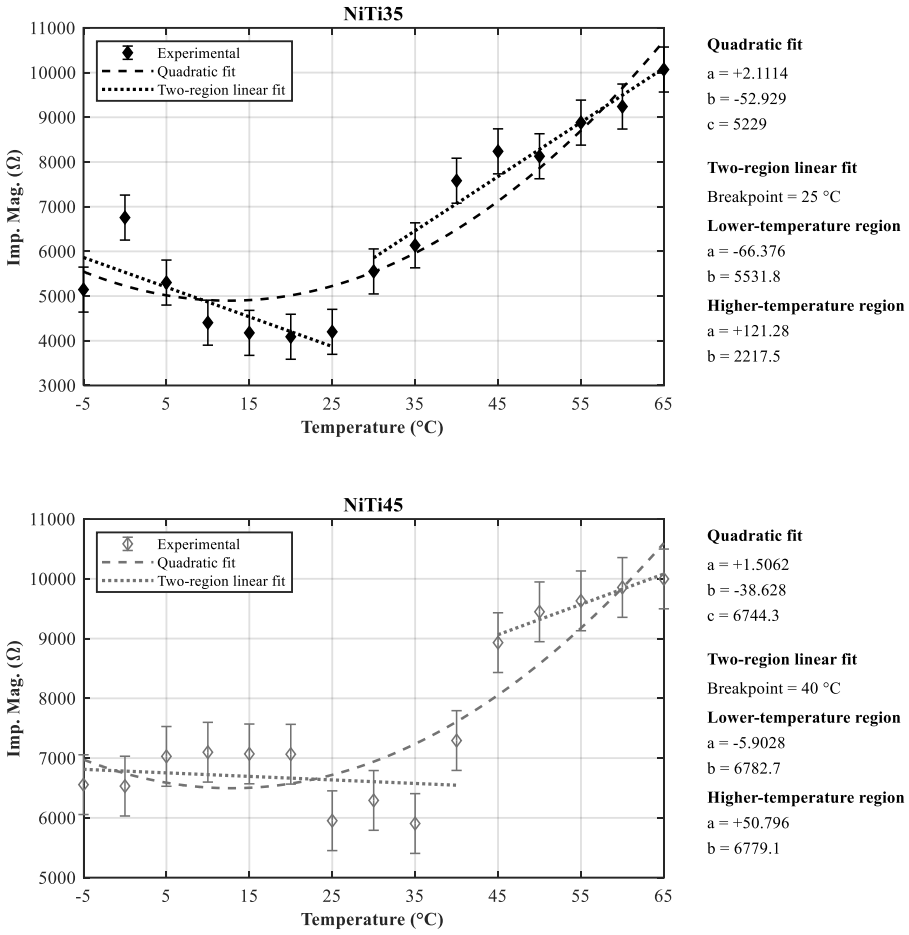


Figure 4.28 - Electrical impedance magnitude of Nitinol transducers.

Figure 4.28 compares the electrical impedance magnitude of the two Nitinol transducers as a function of temperature. Both second-order polynomial and two-region linear fitting relationships were evaluated for each configuration to compare their suitability in representing the measured temperature-dependent responses.

The 35 °C A_F Nitinol transducer exhibited a pronounced nonlinear response, with the impedance magnitude decreasing to a minimum measured value of 4,090.04 Ω at 20 °C before increasing to 10,068.60 Ω at 65 °C. A second-order empirical relationship represented the broad form of this response, with R^2 = 0.8548 and an RMSE of 749.4 Ω. However, the two-region linear relationship provided a closer empirical fit, with R^2 = 0.9421 and an RMSE of 473.2 Ω, using a breakpoint at 25 °C. Although the two-region relationship improved the fitting statistics, the second-order relationship provided a continuous representation of the overall decrease followed by an increase in impedance magnitude. Considerable point-to-point

variation remained, particularly within the lower-temperature region, indicating that neither fitting relationship should be interpreted as a precise predictive model.

The 45 °C A_F Nitinol transducer exhibited a different temperature-dependent response. Its impedance magnitude remained comparatively stable overall across much of the lower-temperature range, despite local variation and a minimum measured value of 5,905.44 Ω at 35 °C, before increasing to 9,997.93 Ω at 65 °C. The second-order relationship produced $R^2 = 0.7961$ and an RMSE of 648.0 Ω, whereas the two-region linear relationship provided an improved empirical representation, with $R^2 = 0.9267$ and an RMSE of 388.6 Ω. The lower-temperature region exhibited only a weak overall gradient of −5.90 Ω °C^{-1}, whereas the higher-temperature region exhibited a positive gradient of 50.80 Ω °C^{-1}, indicating a stronger temperature dependence at elevated temperatures.

The mathematically selected breakpoints for the two-region relationships occurred at 25 °C and 40 °C for the 35 °C A_F and 45 °C A_F transducers, respectively. Although the latter lies close to the independently measured A_F of 45 °C, these breakpoints should not be interpreted as direct measurements of the Nitinol phase transformation. Rather, they identify changes in the empirical temperature dependence of the electrical response. Similarly, the minimum measured impedance values of the two transducers did not occur directly at their respective AF temperatures. The electrical impedance therefore does not exhibit a simple one-to-one correspondence with the independently measured transformation temperatures.

Comparison of the two configurations demonstrates that changing the Nitinol transformation characteristics did not simply shift an otherwise identical impedance–temperature response along the temperature axis. The 35 °C A_F transducer exhibited a broader nonlinear decrease followed by an elevated-temperature increase, whereas the 45 °C A_F transducer exhibited comparatively weak overall variation across much of the lower-temperature range followed by a stronger increase at elevated temperatures. Although the two-region linear relationships provided improved fitting statistics for both configurations, the second-order relationships offered continuous empirical descriptions of their overall nonlinear responses. The two-region relationships were useful for quantifying changes in temperature sensitivity but should not be interpreted as evidence of discrete material transitions. These differences indicate that the two Nitinol end-cap conditions exhibited different temperature-dependent electromechanical responses. However, because the measured impedance represents the complete flextensional transducer assembly, the observed differences cannot be attributed solely to the Nitinol

transformation temperature and may also reflect temperature-dependent changes in structural stiffness, mechanical losses, piezoceramic properties, adhesive layers and structural interfaces.

The change in the mechanical quality factors of the Nitinol transducers with temperature are shown in Figure 4.29.

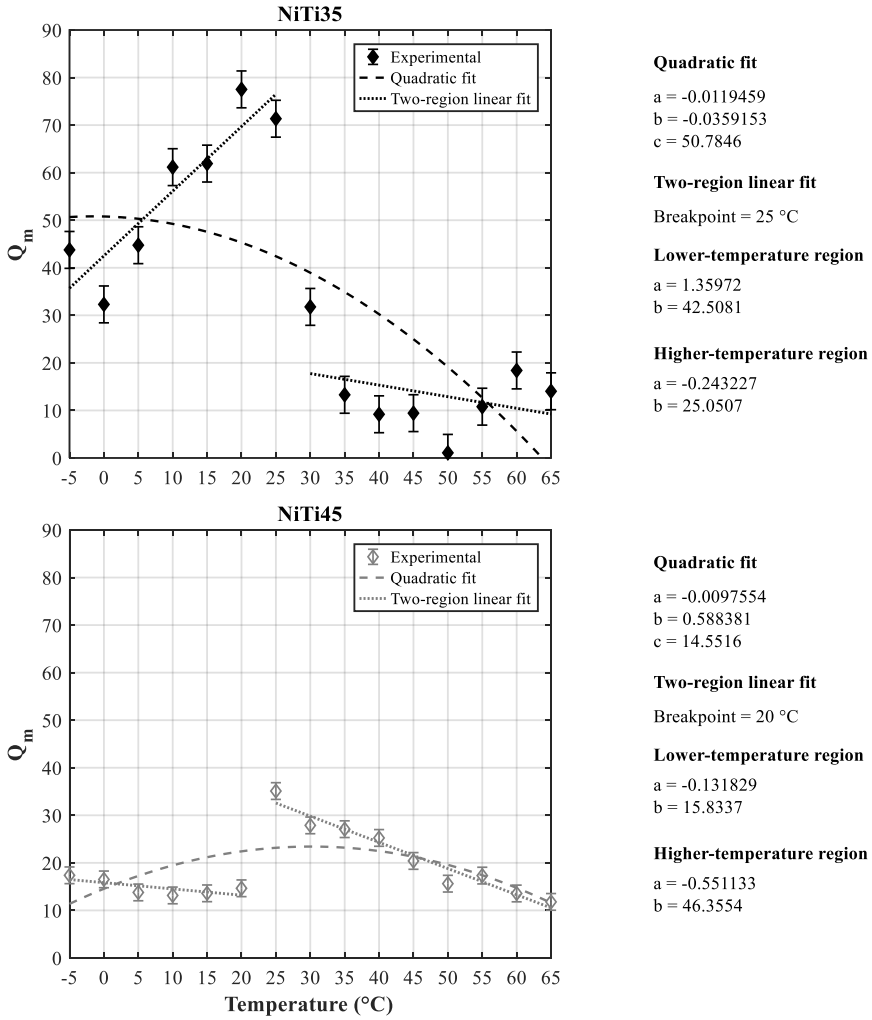


Figure 4.29 - Mechanical quality factors of Nitinol transducers.

Figure 4.29 compares the variation in mechanical quality factor with temperature for the two Nitinol transducers. The 45 °C A_F Nitinol transducer generally exhibited lower mechanical quality factor values than the 35 °C A_F transducer. The 35 °C A_F transducer reached a maximum measured Q_m of 77.51 at 20 °C, whereas the 45 °C A_F transducer reached a lower maximum of 35.10 at 25 °C. In both configurations, the maximum Q_m occurred below the respective A_F, and neither dataset exhibited an abrupt change in mechanical quality factor precisely as the independently measured A_F was exceeded.

The strongly non-monotonic behaviour, including the pronounced changes in mechanical quality factor over relatively narrow temperature intervals, could not be adequately represented by a single global linear or second-order polynomial relationship. Consequently, both second-order and two-region linear relationships were evaluated for each configuration to assess their suitability in describing the measured temperature-dependent responses.

For the 35 °C A_F transducer, the global linear and second-order relationships produced R^2 = 0.4440 and R^2 = 0.4852, respectively. The second-order relationship therefore provided only a limited representation of the measured response, particularly the pronounced reduction in Q_m following its maximum. A two-region empirical relationship provided a substantially stronger representation, with R^2 = 0.9108 and an RMSE of 7.29. The lower-temperature region exhibited an overall positive gradient of 1.36 $Q_m°C^{-1}$, whereas the higher-temperature region exhibited a negative gradient of −0.243 $Q_m°C^{-1}$. This relationship better represented the contrasting temperature-dependent regimes observed experimentally, although the fitted regions should not be interpreted as evidence of a discrete physical transition.

The 45 °C A_F transducer exhibited a different response. A global linear relationship provided essentially no representation of the measured temperature dependence (R^2 = 0.0001), while the second-order relationship remained comparatively weak (R^2 = 0.3729). The second-order relationship could not adequately represent the relatively low Q_m values at lower temperatures, followed by the pronounced increase around 25 °C and subsequent reduction. A two-region empirical relationship represented the response considerably more strongly, with R^2 = 0.9499 and an RMSE of 1.48. The lower-temperature region exhibited a small negative gradient of −0.132 $Q_m°C^{-1}$, whereas the higher-temperature region exhibited a greater negative gradient of −0.551 $Q_m°C^{-1}$. The latter region therefore describes the overall reduction in mechanical quality factor following the local maximum observed at 25 °C.

The mathematically selected breakpoints occurred at 25 °C for the 35 °C A_F transducer and 20 °C for the 45 °C A_F transducer. These values should not be interpreted as transformation temperatures. Neither breakpoint coincided with the independently measured A_F of the corresponding Nitinol material. Furthermore, the independently fitted linear regions do not necessarily form continuous relationships at their respective breakpoints. The two-region fits should therefore be regarded as empirical approximations of the measured behaviour rather than physical models describing abrupt changes in the mechanical properties of Nitinol. The Q_m measurements do not demonstrate a direct one-to-one correspondence between completion of the martensitic-to-austenitic transformation and a distinct change in the mechanical quality factor of the assembled transducer.

More broadly, comparison of the resonance-frequency, electrical impedance and Q_m measurements demonstrates that increasing A_F from 35 °C to 45 °C did not simply shift an otherwise identical transducer response towards higher temperature. The two configurations differed in their absolute resonance frequencies, impedance magnitudes and mechanical quality factors, as well as in the detailed temperature dependence of these parameters. Neither transducer exhibited a discrete resonance-frequency shift as its respective A_F was exceeded. Similarly, the impedance and Q_m measurements exhibited broad and non-monotonic changes rather than abrupt transitions at the independently measured transformation temperatures. The dynamic response of the Nitinol flextensional transducers therefore cannot be described by nominal A_F alone.

Manufacturing-related effects may contribute to this behaviour. Residual stresses introduced during Wire-EDM processing can influence the transformation behaviour of Nitinol [47]. Compositional variation and the finite transformation-temperature ranges identified during the material characterisation may also contribute to differences between the end-caps. However, the present transducer measurements do not independently isolate these mechanisms. Furthermore, resonance frequency, electrical impedance and Q_m represent properties of the complete electromechanical assembly and may also be affected by the piezoceramic elements, end-cap stiffness, mechanical losses, adhesive layers and structural interfaces. The observed differences between the 35 °C and 45 °C A_F configurations should therefore be interpreted as differences in the coupled temperature-dependent response of the complete transducers rather than as direct measurements of the Nitinol phase transformation.

From an application perspective, neither configuration demonstrated a discrete thermally induced resonance shift comparable to that previously reported for Nitinol-based cymbal transducers [27–30]. The present results do not demonstrate a clear advantage of either configuration for active frequency tuning based solely on its A_F. Nevertheless, the distinct temperature-dependent responses demonstrate that the two Nitinol end-cap configurations exhibited different behaviour within the assembled flextensional transducers. Further work in which the Nitinol material state and transducer response are characterised simultaneously would be required to separate transformation-related effects from the other temperature-dependent contributions within the device.

The thermomechanical processing history of the Nitinol sheet materials prior to wire-EDM machining was not available and therefore could not be accounted for in the present study. Since the transformation behaviour of Nitinol is highly sensitive to prior thermal and

mechanical processing, differences in manufacturing history may have influenced the phase-transformation characteristics of the Nitinol and may therefore represent an additional source of variability in the dynamic response of the finished transducers. The results suggest that manufacturing processes, residual stresses and material processing history may contribute to the behaviour of Nitinol-based flextensional transducers and should therefore be considered alongside transformation temperature during future transducer design and optimisation.

This finding has important implications for the future development of Nitinol-based ultrasonic surgical devices. International medical device quality management standards such as ISO 13485 emphasise design control, process validation, traceability, risk management, and the ability to consistently manufacture devices that meet their intended performance requirements. A comprehensive understanding of Nitinol material history, including prior thermomechanical processing, heat treatment, and manufacturing-induced residual stresses, will therefore be important for achieving predictable transducer performance, manufacturing repeatability, and regulatory compliance throughout the device development lifecycle. Improved traceability of material processing history would also assist in distinguishing intrinsic material effects from manufacturing-induced variability, thereby supporting the development of robust and reproducible ultrasonic surgical devices suitable for future clinical translation [191].

4.3. Summary

The work presented in this chapter established the design, fabrication, and baseline characterisation of class IV flextensional transducers incorporating Nitinol, titanium (Ti-6Al-4V), stainless steel (grade 316), and aluminium (1050A) end-caps. The four geometrically identical configurations enabled the influence of end-cap material selection on transducer performance to be investigated. Under increasing drive voltage, material-dependent differences were observed in displacement amplitude, electrical impedance, mechanical quality factor, and power consumption, demonstrating the influence of end-cap material on the electromechanical response of the transducer. Temperature-dependent measurements further demonstrated distinct material-dependent behaviour in resonance frequency, electrical impedance, and mechanical quality factor, highlighting the influence of end-cap material selection on the thermal response of the assembled transducers. Collectively, these results establish a baseline understanding of how end-cap material selection influences the electromechanical and temperature-dependent behaviour of class IV flextensional transducers.

Although the Nitinol transducer exhibited temperature-dependent variations in resonance frequency, electrical impedance, and mechanical quality factor, a discrete resonance-frequency shift associated with exceeding the independently measured A_F was not observed. Investigation of a second geometrically identical Nitinol transducer with a higher A_F similarly did not produce a distinct transformation-induced resonance shift. Furthermore, changing the Nitinol transformation characteristics did not simply shift an otherwise identical temperature-dependent response to a higher temperature, with the two Nitinol configurations exhibiting differences in their resonance-frequency, impedance, and mechanical-quality-factor responses. These findings indicate that the temperature-dependent dynamic behaviour of the assembled flextensional transducer cannot be described by the Nitinol transformation temperature alone. Other factors may contribute, including manufacturing-induced residual stresses, material processing and compositional variability, together with temperature-dependent changes in the piezoceramic elements, structural stiffness, mechanical losses, adhesive layers, and interfaces within the complete transducer assembly.

Building on this foundation, Chapter 5 investigates an alternative approach to incorporating Nitinol into the flextensional transducer through the integration of Nitinol wire attachments. In addition to modifying the transducer boundary conditions and vibration behaviour, the wire-integrated configuration provides an opportunity to investigate whether transformation-related resonance behaviour can be more effectively exploited through a discrete Nitinol element rather than through the end-cap structure itself. Direct comparison between the transducers without wire and their wire-integrated counterparts therefore extends the understanding of how Nitinol components may be functionally incorporated into ultrasonic surgical transducers and informs the development of future tuneable and thermally adaptive ultrasonic device configurations.

Chapter 5

Design, fabrication and characterisation of class IV transducers with wires

To further investigate the incorporation of Nitinol into flextensional transducers, an alternative integration strategy was considered. Rather than using Nitinol as the end-cap material, a discrete Nitinol wire was attached to the transducer structure. This approach was also motivated by the eventual development of an ultrasonic surgical device, where a surgical attachment or end-effector would typically be connected to one of the transducer end-caps. The addition of a wire provides a simplified representation of such a surgical attachment while simultaneously enabling the influence of a transformation-capable Nitinol element on the transducer response to be investigated.

An additional motivation for this approach was to determine whether a different method of integrating Nitinol into the transducer could produce measurable transformation-related changes in dynamic behaviour. Since the anticipated resonance frequency shift was not observed when Nitinol was incorporated into the end-caps, the wire-integrated configuration provided an opportunity to investigate whether the SME could be more effectively coupled to the vibration response through a discrete Nitinol element. If successful, such an approach could provide a mechanism for thermally induced resonance tuning, adaptive vibration control, or frequency adjustment within ultrasonic transducers.

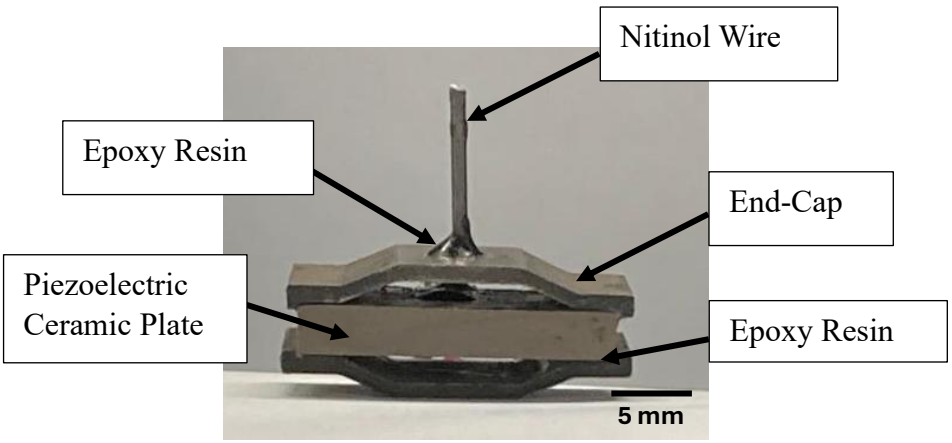
Nitinol wires have been widely studied for biomedical and interventional applications owing to their flexibility, superelasticity, and shape memory behaviour. Previous studies have investigated wire-based devices for applications including arterial tissue perforation, clot disruption, and guidewire-assisted recanalisation procedures [192–196]. Motivated by these applications, this chapter examines the design, fabrication, and characterisation of class IV flextensional transducers incorporating Nitinol wire attachments. Particular attention is given to the influence of the wire on boundary conditions, vibration behaviour, energy transfer, and temperature-dependent transducer performance, allowing direct comparison with the wire-free transducers investigated in Chapter 4.

5.1. Incorporating Nitinol wires to the class IV flextensional transducers

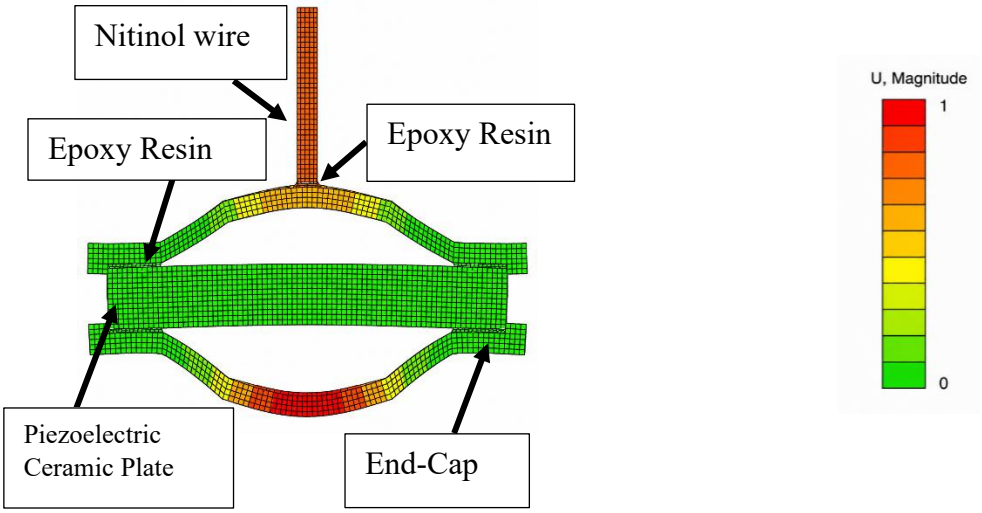
The Nitinol wire used in this study was supplied by Nexmetal Corporation (USA) and had a length of 10 mm, a diameter of 1 mm, and an A_F of 30 °C, as specified by the manufacturer. To investigate the influence of wire integration on transducer performance, four geometrically identical class IV flextensional transducers were fabricated using the titanium (Ti-6Al-4V), aluminium (1050A), stainless steel (grade 316), and Nitinol end-cap materials described in Chapter 4. To accommodate the Nitinol wire attachment, a 1.2 mm diameter hole was introduced at the centre of the apex region of each end-cap.

The Nitinol wires were bonded to the end-caps using a thin layer of epoxy resin (Eccobond 45 LV High Strength, Ellsworth Adhesives Ltd., UK). The adhesive was prepared using a 1:1 mixing ratio of epoxy resin and 15 LV catalyst hardener. This bonding mechanism was selected to maintain consistency with the fabrication procedures used in Chapter 4, where the same epoxy was employed to bond the end-caps to the piezoceramic surfaces and to encapsulate the soldered electrical connections on the piezoceramic electrodes. For the FEA of the wire-integrated transducers, the Nitinol wire geometry was incorporated into the existing models developed in Chapter 4. A mesh seed size of 0.0003 m was used throughout the wire-integrated models, ensuring consistency with the mesh discretisation employed for the wire-free transducers and enabling direct comparison between the numerical predictions presented in Chapters 4 and 5.

Figure 5.1a shows a fabricated Nitinol transducer with a Nitinol wire in place and the associated FEA model is shown in Figure 5.1b showing the symmetric mode at 20,233 Hz.



(a) Transducer with Nitinol end-caps incorporating a Nitinol wire.



(b) FEA model of the device in its symmetric vibration mode at 20.233 kHz. The normalised displacement magnitude is shown by the accompanying U-magnitude scale, where warm colours represent higher displacement and green regions represent lower or near-nodal displacement.

Figure 5.1- Fabricated Class IV flextensional transducer with an embedded Nitinol wire and corresponding FEA symmetric vibration mode.

5.2. Results from electrical impedance analysis

The impedance magnitude and phase spectra were obtained from impedance analysis for the four flextensional transducers with Nitinol wires with end-caps made from titanium (Ti-6Al-4V), aluminium (1050A), stainless steel (grade 316), and Nitinol. The impedance magnitude and the phase of the transducers with wires were compared against transducers without wires and are shown in Figure 5.2.

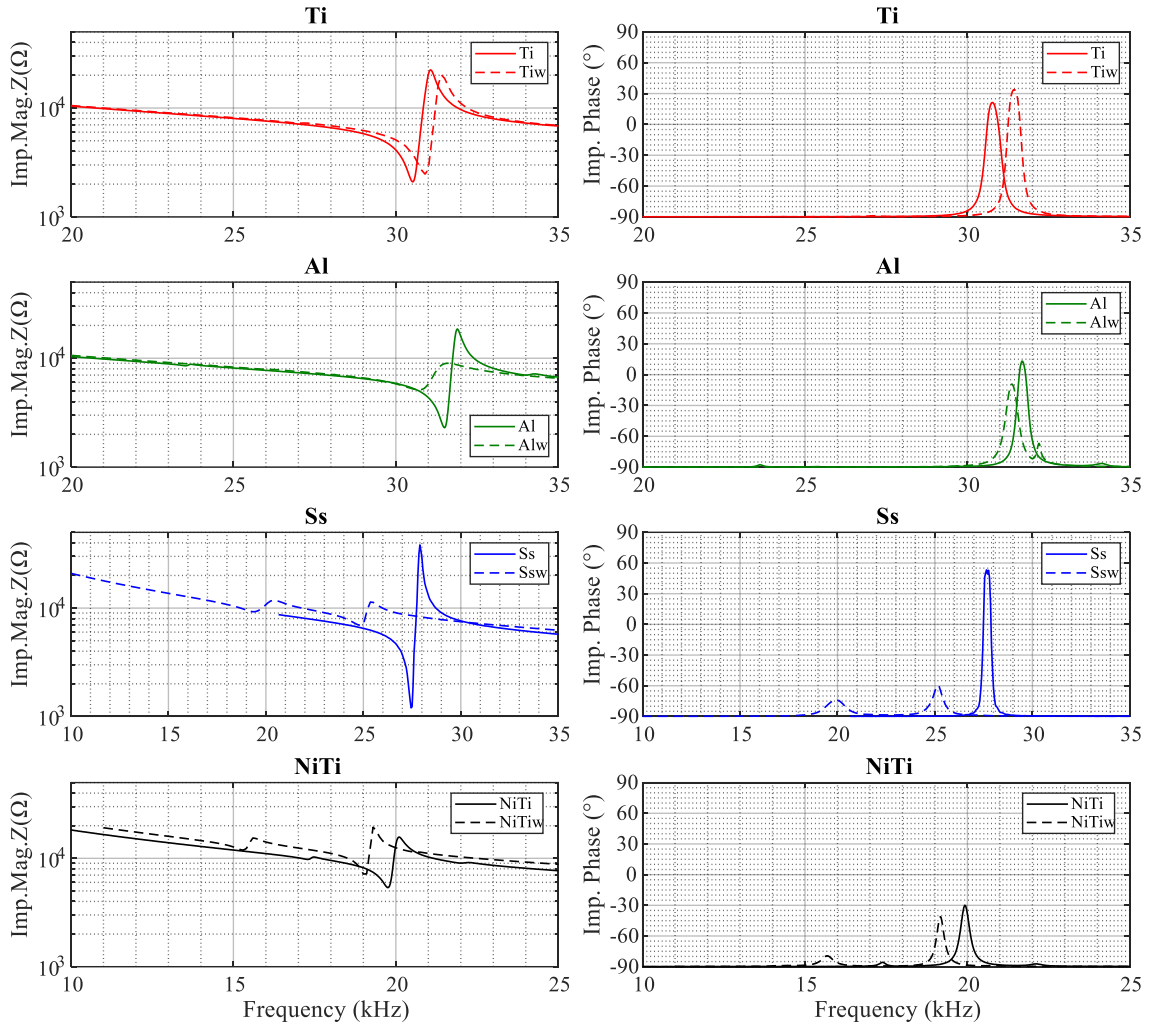


Figure 5.2 – Comparison of the measured impedance magnitude and phase spectra of the class IV flextensional transducers with and without Nitinol wire end-effectors. Tiw - transducer with titanium end-caps and Nitinol wire, Alw- transducer with aluminium end-caps and Nitinol wire, Ssw- transducer with stainless steel end-caps and Nitinol wire and NiTiw- transducer with Nitinol end-caps and Nitinol wire

From the impedance magnitude and phase of the transducers incorporating a Nitinol wire, the symmetric mode and the neighbouring mode are not as distinct as the same vibration mode of the transducers without the wires. The Nitinol and stainless steel transducers with wires have a vibration mode close in frequency to the symmetric vibration modes (Figure 5.2). This mode is the asymmetric vibration mode, where the end-caps vibrate in-phase (rather than out-of-

phase as for the symmetric mode), predicted by FEA [Nitinol transducer with wire] and shown in Figure 5.3.

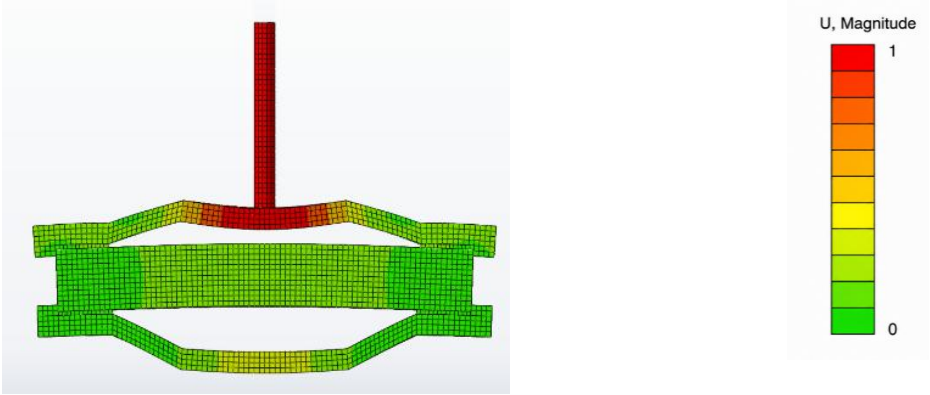


Figure 5.3 – FEA model of class IV flextensional transducer with a Nitinol wire at its asymmetric vibration mode at 14.750 kHz. The normalised displacement amplitude is indicated by the U-magnitude scale, where warm colours represent higher displacement and green regions represent lower or near-nodal displacement.

Table 5.1 lists the anti/resonance frequencies of the symmetric vibration modes, the phase, FEA results of the resonance frequency as well as the derived k_{eff} and Q_m values for transducers with and without the Nitinol wires.

Transducer End-Cap Material	f_r (kHz) [EIA]	f_a(kHz) [EIA]	f_r (kHz) [FEA]	Phase at resonance frequency	Q_m	k_{eff}
Titanium	30.475	31.050	30.783	-39°	76	0.192
Titanium with wire	31.195	31.675	30.258	-27°	113	0.172
Aluminium	30.883	31.353	31.240	-27°	54	0.172
Aluminium with wire	31.125	31.600	30.430	-51°	59	0.163
Stainless Steel	27.156	27.656	27.003	9°	108	0.189
Stainless Steel with wire	24.932	25.436	25.100	-68°	26	0.193
Nitinol	20.062	20.343	20.148	-62°	71	0.165
Nitinol with wire	19.619	19.862	20.233	-46°	41	0.156

Table 5.1 - Electromechanical characterisation of transducers using EIA.

From Table 5.1, the incorporation of the Nitinol wire influenced the resonance frequency of the transducers in a material-dependent manner. The titanium transducer exhibited a slight increase in resonance frequency, whereas aluminium, stainless steel, and Nitinol transducers with wires showed reductions. The largest decrease was observed in the stainless steel transducer. These results indicate that the addition of the wire altered the dynamic response of the transducers, although the magnitude and direction of the change varied depending on the end-cap material.

The phase angle at resonance was also affected by wire integration. Titanium and Nitinol transducers exhibited phase values that moved closer to 0˚ (inductive), while aluminium and stainless steel transducers showed more negative phase angles (capacitive) following the addition of the wire. The most pronounced change occurred in the stainless steel transducer, where the phase shifted from 9˚ to -68º. Overall, the results demonstrate that the wire modified the electrical-mechanical interaction within the transducer, with the extent of the change varying between materials [169].

The effect of the wire on the mechanical quality factor was strongly dependent on the end-cap material. Titanium and aluminium transducers exhibited increases in Q_m, with titanium showing the largest improvement. The stainless steel and Nitinol transducers experienced substantial reductions in Q_m, indicating a less pronounced resonant response [83]. These findings suggest that the influence of the wire on mechanical losses and energy storage within the transducer is dependent on the material used for the end-cap.

The effective electromechanical coupling coefficient generally decreased following the addition of the wire. Reductions in k_{eff} were observed for the titanium, aluminium, and Nitinol transducers, while stainless steel exhibited a slight increase. The results indicate that wire integration can influence the efficiency of energy conversion between the electrical and mechanical domains of the transducer [196-198].

The resonance frequencies predicted by the FEA models showed good agreement with the experimentally measured EIA resonance frequencies, with percentage differences ranging from 0.43% to 3.13%. For the transducers without wires, the differences were particularly small, ranging between 0.43% and 1.16%, demonstrating that the numerical models accurately captured the dynamic behaviour of the structures. The addition of the Nitinol wire generally resulted in slightly larger discrepancies, with the largest differences observed for the Nitinol-with-wire (3.13%) and titanium-with-wire (3.00%) transducers. Nevertheless, all predicted resonance frequencies remained within ±3.2% of the experimental values. These small deviations are likely attributable to modelling assumptions regarding the epoxy bonding layer, wire attachment conditions, material property variations, and manufacturing tolerances, which are difficult to replicate exactly in the FEA models. Overall, the close agreement between the experimental and numerical results provides confidence in the validity of the developed FEA models.

Overall, these findings suggest that titanium is the most promising material for integration with Nitinol wires, as it combines an increase in Q_m, stable k_{eff}, and only minor impedance and phase changes. The aluminium transducer also shows potential, with small improvements in Q_m and enhanced capacitive behaviour. The Nitinol transducer, while maintaining stable resonance, suffers from increased damping that could limit efficiency, and the stainless steel transducer performs poorly under wire loading due to excessive impedance growth and quality factor reduction. For ultrasonic surgical applications, where high vibrational stability, low damping, and predictable frequency response are critical, the titanium transducer and to a lesser extent, the aluminium transducer emerge as the most viable end-cap materials for flextensional transducers incorporating Nitinol wires.

5.3. Results from experimental modal analysis

Experimental modal analysis was conducted with the experimental setup shown in section 4.1.4. The mode shapes and frequencies of the transducers with wires were compared against the transducers without the wires as shown in Figure 5.4.

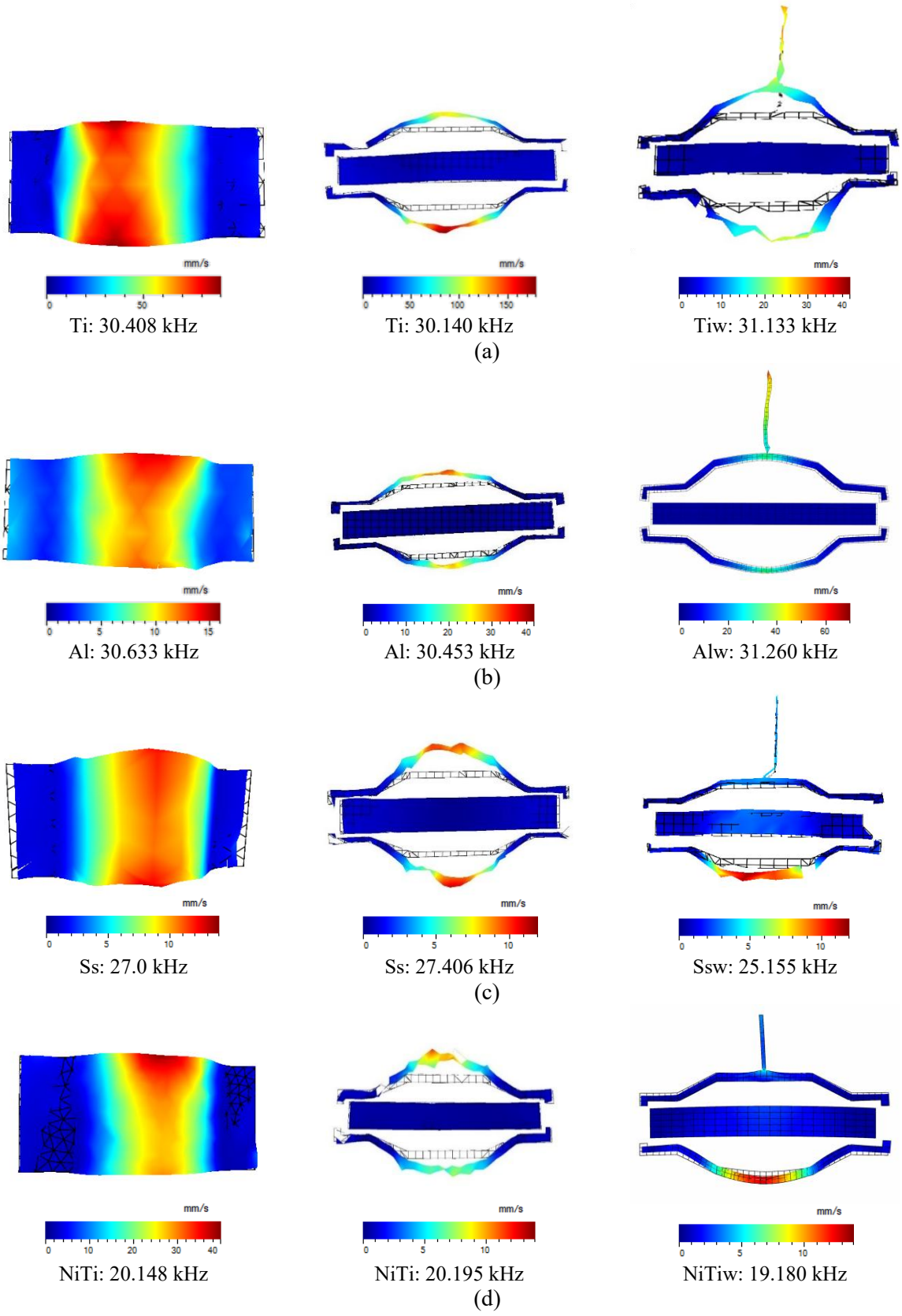


Figure 5.4 – Symmetric mode from LDV scans of transducers with and without wires.

The resonance frequencies obtained from EMA exhibited excellent agreement with the resonance frequencies measured using EIA for all wire-integrated transducers. The percentage difference between the two techniques ranged from 0.20% for the titanium transducer to 2.24% for the Nitinol transducer. This close correlation confirms that the resonances identified electrically through impedance measurements correspond directly to the mechanical vibration modes observed experimentally. The EMA mode shapes verified that the measured resonances were associated with the intended longitudinal operating mode, providing additional validation of the electromechanical characterisation results. The minor deviations in the resonance frequencies obtained from EMA and EIA measurements are likely attributable to differences in the excitation voltages.

In the titanium and aluminium prototypes (Figure 5.4a–b), the incorporation of the wire appeared to compensate for the asymmetry observed in the vibration response, resulting in a more balanced distribution of vibration across the end-caps. This behaviour was not observed for the stainless steel and Nitinol prototypes (Figure 5.4c–d), where wire integration resulted in a reduced vibration response at the wire-attached end-cap and a corresponding increase in vibration response at the free end-cap.

Across all configurations, the maximum vibration response occurred at the end-cap apex, consistent with the finite element predictions and confirming that the optimal location for end-effector integration had been identified. Although wire integration influenced the local vibration distribution, it did not alter the fundamental symmetric longitudinal mode shape. Instead, a reduction in vibration amplitude was observed near the wire-attached end-cap, particularly for the stainless steel and Nitinol configurations (Figure 5.4c–d).

A limitation of the present study is that each transducer configuration, both with and without wire integration, was fabricated as a single prototype. While this approach enables the identification of material-dependent trends, future work should investigate multiple nominally identical devices to quantify manufacturing variability and improve the statistical robustness of the findings.

5.4. Results from harmonic response analysis

The displacement amplitudes of the transducers with wires were measured at the tip of the Nitinol wire by harmonic analysis as described in the setup shown in Figure 4.10. All tests were conducted at ambient room temperature, as shown in Figure 5.5.

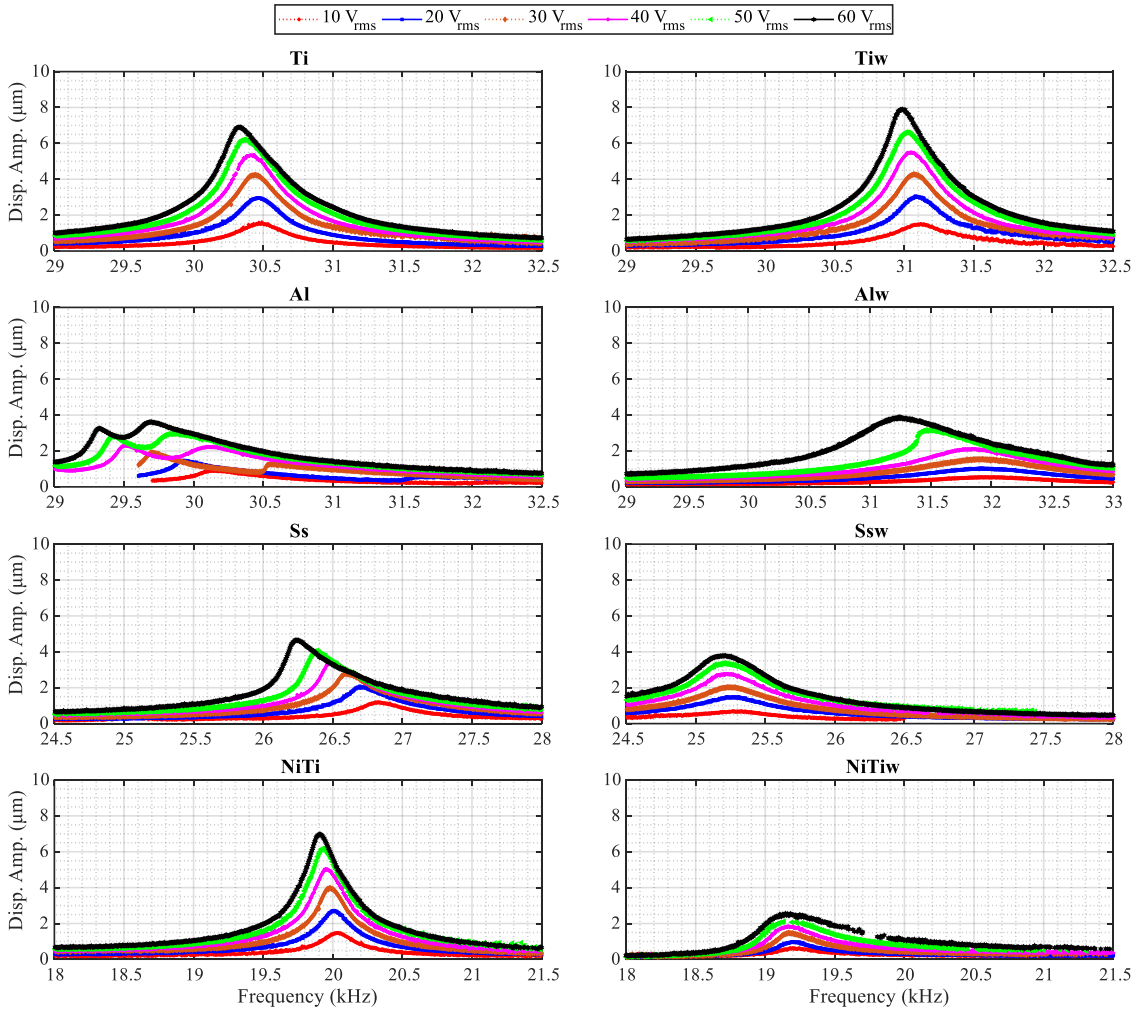


Figure 5.5 - Harmonic response analysis plots from 10 to 60 $V_{(rms)}$ for all transducers without/with attached wire.

The harmonic response measurements were taken specifically at the wire tip as this location represents the functional output point for wire-based surgical applications. Measurements taken at the end-cap and at the wire tip are not directly comparable, as they represent different physical points in the structure with different boundary conditions. Therefore, interpretation focuses on relative trends within the wire tip measurements rather than direct comparison with end-cap data.

Figure 5.6 presents the displacement amplitudes measured at the wire tip for each end-cap material as a function of excitation voltage. These measurements characterise how the wire itself responds when mechanically coupled to different transducer assemblies. The objective is to assess how the end-cap material influences the vibration transmitted along the wire and to determine whether wire-borne motion scales consistently with driving voltage.

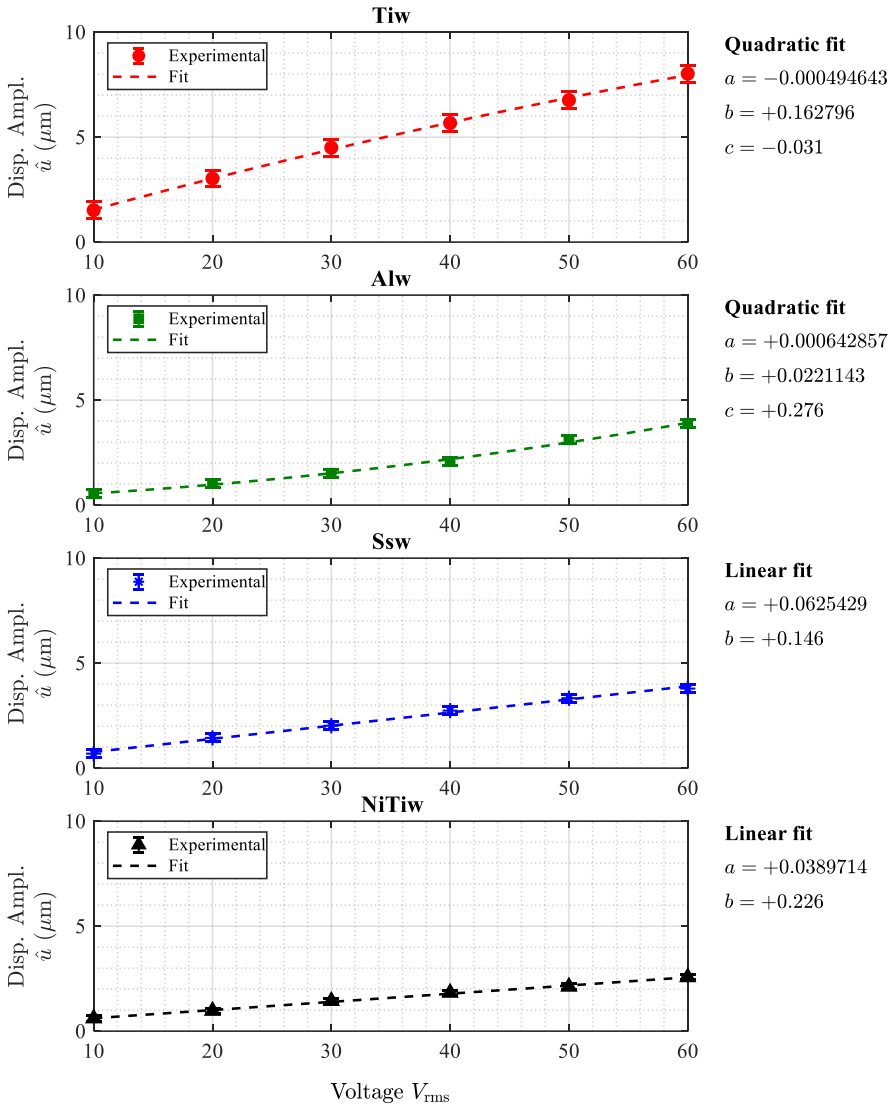


Figure 5.6 – Displacement amplitude as a function of voltage for transducers with wires.

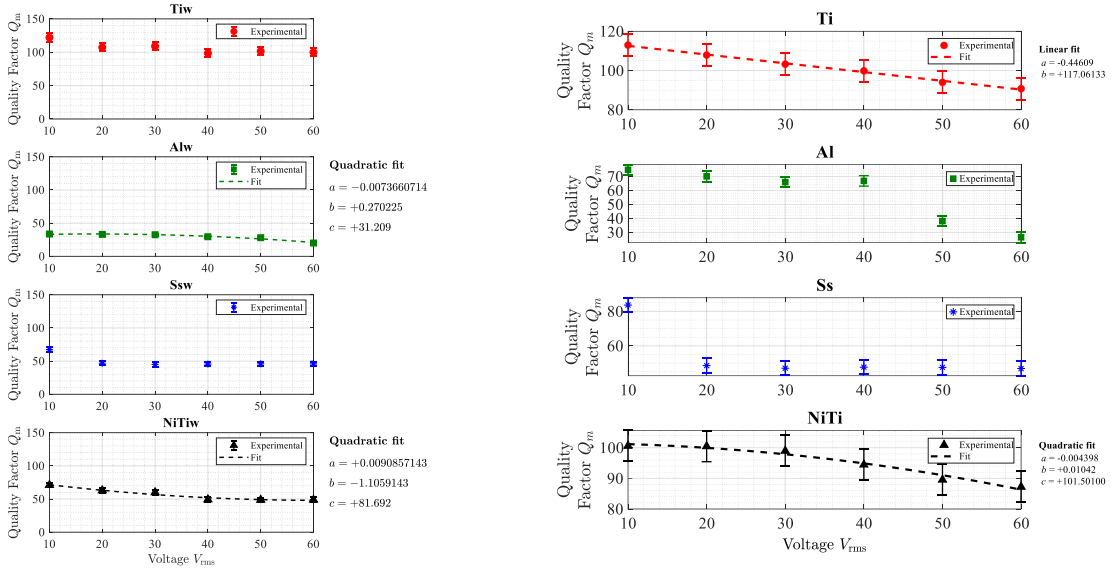
The titanium transducer with a wire generated the largest displacement amplitudes at higher excitation voltages, reaching 8.02 µm at 60 $V_{(\text{rms})}$, while the Nitinol transducer with a wire generated the lowest displacement amplitude of 2.57 µm at 60 $V_{(\text{rms})}$. The aluminium and stainless steel configurations exhibited intermediate displacement amplitudes of 3.88 and 3.79 µm, respectively, at 60 $V_{(\text{rms})}$. The voltage-dependent responses of the titanium and aluminium configurations exhibited slight curvature and were represented by second-order empirical relationships, with R^2 values of 0.9991 and 0.9958 and RMSE values of 0.066 and 0.075 µm, respectively. These relationships were selected to describe the observed deviations from a constant displacement–voltage gradient, rather than to imply a specific nonlinear

mechanism. In contrast, the stainless steel and Nitinol configurations exhibited approximately proportional increases in displacement amplitude with excitation voltage and were adequately represented by linear relationships, with R^2 values of 0.9953 and 0.9969 and RMSE values of 0.073 and 0.037 μm, respectively. Residual analysis supported these model selections, with no substantial systematic deviations remaining from the selected relationships. The results demonstrate that displacement amplitude increased with excitation voltage for all four wire-integrated configurations, although the magnitude and form of this increase differed between the end-cap material configurations. These differences cannot be attributed to the individual mechanical properties of the end-caps alone without direct measurements of internal strain, stress, or local stiffness within the assembled transducers.

From Figure 5.5, smaller resonance-frequency shifts were generally observed for the transducers incorporating wires compared with their corresponding wire-free configurations. Between 10 and 60 $V_{(rms)}$, the wire-free aluminium configuration exhibited the largest overall resonance-frequency shift (805 Hz), followed by stainless steel (440 Hz), titanium (140 Hz), and Nitinol (100 Hz). Following wire integration, the titanium, aluminium, stainless steel, and Nitinol configurations exhibited overall shifts of 115, 705, 120, and 65 Hz, respectively. The resonance-frequency variation was therefore lower across the investigated excitation range for all four configurations, with the largest reduction occurring for the stainless steel transducer, from 440 to 120 Hz.

The Nitinol configuration exhibited the smallest overall resonance-frequency variation between 10 and 60 $V_{(rms)}$, both before and after wire integration. This indicates that, within the investigated excitation range, its resonance frequency underwent a smaller overall change than those of the titanium, aluminium, and stainless steel configurations. Conversely, the aluminium configuration exhibited the largest resonance-frequency variation both before and after wire integration. These results demonstrate that the voltage-dependent resonance response remained dependent on end-cap material, while integration of the Nitinol wire modified the magnitude of the response. The reduced resonance-frequency variation following wire integration may be advantageous in ultrasonic applications where maintaining a consistent resonance condition under changing excitation levels is desirable [34–35]. However, these differences represent the behaviour of the complete transducer assemblies and therefore cannot be attributed solely to the intrinsic properties of either the end-cap materials or the Nitinol wire.

The mechanical quality factors of the transducers with and without wires were also compared across excitation voltages (Figure 5.7).



(a) Transducers with wires. (b) Transducers without wires.

Figure 5.7 – Mechanical quality factor as a function of voltage.

The mechanical quality factor generally decreased with increasing drive voltage for the transducers with and without wire integration, although the magnitude and form of this response varied considerably between configurations. The analysis of the wire-free transducers in Chapter 4 demonstrated that a common linear relationship was not appropriate for all four end-cap materials. The same approach was therefore applied following wire integration, with fitting functions retained only where they provided an adequate empirical representation of the measured behaviour. Comparisons between the wire-free and wire-integrated configurations were consequently based on the measured Q_m values, response characteristics and selected fitting behaviour rather than on linear gradients alone.

For the titanium configuration, the wire-free transducer exhibited a well-defined approximately linear reduction in Q_m, decreasing from 112.96 at 10 $V_{(rms)}$ to 90.77 at 60 $V_{(rms)}$. The linear model produced an R^2 value of 0.9954 and a gradient of -0.446 $Q_m/V_{(rms)}$. Following wire integration, Q_m decreased from 122.11 to 99.95 over the same excitation range and remained higher than the corresponding wire-free values. However, the with-wire response exhibited greater point-to-point variation despite its overall decrease, and no global fitting function was

retained because the measured fluctuations were not adequately described by a simple empirical relationship. Following wire integration, the titanium configuration exhibited higher measured Q_m values and a modified voltage-dependent response.

The aluminium configuration exhibited a markedly different effect of wire integration. Without the wire, Q_m decreased gradually from 74.79 at 10 $V_{(rms)}$ to 66.81 at 40 $V_{(rms)}$, before decreasing sharply to 38.09 and 26.50 at 50 and 60 $V_{(rms)}$, respectively. No global fit was assigned because neither the linear nor second-order model adequately represented the distinct high-voltage change, which corresponded to increasing interaction with the neighbouring asymmetric flexural mode. Following wire integration, Q_m was substantially lower, decreasing from 33.63 to 20.05 between 10 and 60 $V_{(rms)}$. In contrast to the wire-free response, the with-wire behaviour was adequately represented by a second-order empirical relationship (R^2=0.9621, RMSE=0.91). Following wire integration, the aluminium configuration exhibited substantially lower absolute Q_m values and an altered voltage-dependent response.

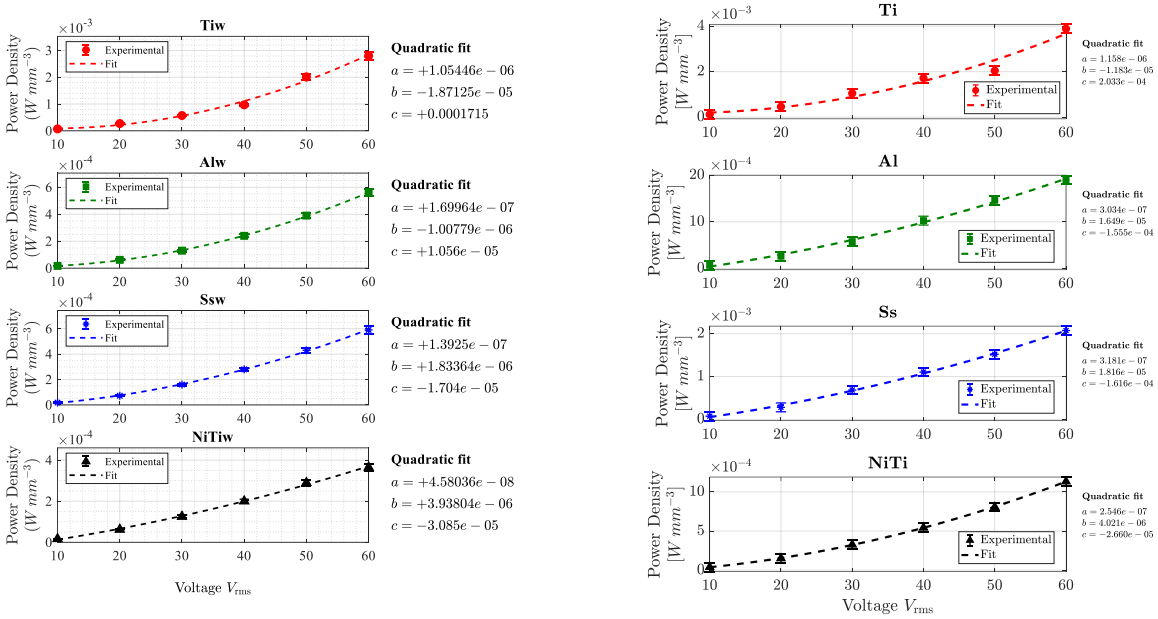
The stainless steel transducers exhibited similar characteristic behaviour before and after wire integration. Without the wire, Q_m decreased sharply from 83.69 at 10 $V_{(rms)}$ to 48.58 at 20 $V_{(rms)}$, before remaining comparatively stable between 47.06 and 46.86 over 30–60 $V_{(rms)}$. Following wire integration, Q_m similarly decreased sharply from 67.34 to 46.84 between 10 and 20 $V_{(rms)}$, before remaining within the narrow range of approximately 44.96–45.85 between 30 and 60 $V_{(rms)}$. No global fitting function was assigned to either response because the sharp initial reduction followed by a lower-Q_m plateau was not appropriately represented by a single linear or polynomial relationship. Following wire integration, Q_m was lower, particularly at the lowest excitation voltage, while the characteristic form of the stainless steel response remained broadly similar.

The Nitinol configuration exhibited a pronounced change in its mechanical quality factor following wire integration. Without the wire, Q_m decreased gradually from 100.58 at 10 $V_{(rms)}$ to 87.21 at 60 $V_{(rms)}$, with the mildly nonlinear response adequately represented by a second-order empirical model (R^2 = 0.9697, RMSE = 0.92). Following wire integration, Q_m was substantially lower, decreasing from 71.04 at 10 $V_{(rms)}$ to 48.82 at 60 $V_{(rms)}$. The response also changed in form, with a stronger reduction at lower excitation levels followed by a reduced rate of decrease at higher voltages. A second-order empirical relationship provided an R^2 of 0.9548 and an RMSE of 1.82, representing the observed curvature without introducing an additional breakpoint. The positive quadratic coefficient is consistent with the progressively

decreasing magnitude of the negative voltage-dependent gradient, although the fitted relationship should not be interpreted as evidence of a specific underlying nonlinear mechanism. Across the investigated excitation range, the wire-integrated Nitinol transducer exhibited a total measured reduction in Q_m of 22.22 compared with 13.37 for the corresponding wire-free transducer. Wire integration therefore reduced the absolute mechanical quality factor of the Nitinol configuration and altered the form of its voltage-dependent response.

Overall, the changes in mechanical quality factor following wire integration were strongly configuration dependent. The titanium transducer maintained the highest Q_m values following wire integration and exhibited higher values than its wire-free counterpart. In contrast, the aluminium, stainless steel and Nitinol configurations generally exhibited lower Q_m values following wire attachment. The stainless steel configuration retained a similar sharp initial reduction followed by a lower-Q_m plateau, whereas the response characteristics of the aluminium and Nitinol configurations were altered more substantially. These results demonstrate that the influence of wire integration cannot be characterised adequately using changes in linear gradient alone. Instead, the changes in absolute Q_m, response shape and selected empirical models indicate that the addition of the Nitinol wire and epoxy bonding layer modified the dynamic behaviour of the assembled transducers in a manner dependent on the end-cap configuration.

The power density of the flextensional transducers (with and without wire) is shown in Figure 5.8.



(a) Transducers with wires.

(b) Transducers without wires.

Figure 5.8 - Power density of flextensional transducers as a function of excitation voltage.

The titanium transducer exhibited the highest power density both with and without wire integration. Without the wire, the power density increased from 1.22 × 10^{-4} Wmm^{-3} at 10 $V_{(rms)}$ to 3.89 × 10^{-3} Wmm^{-3} at 60 $V_{(rms)}$, whereas the wire-integrated configuration increased from 7.00 × 10^{-5} Wmm^{-3} to 2.80 × 10^{-3} Wmm^{-3} over the same voltage range. The with-wire response was represented by a second-order empirical relationship with R^2 =0.9922 and an RMSE of 8.68 ×10^{-5} Wmm^{-3}. The lower absolute power density following wire integration indicates a difference in the electrical power-density response of the titanium configuration compared with its wire-free counterpart. However, power density alone does not provide a direct measure of electromechanical conversion efficiency and must be interpreted together with the measured displacement response.

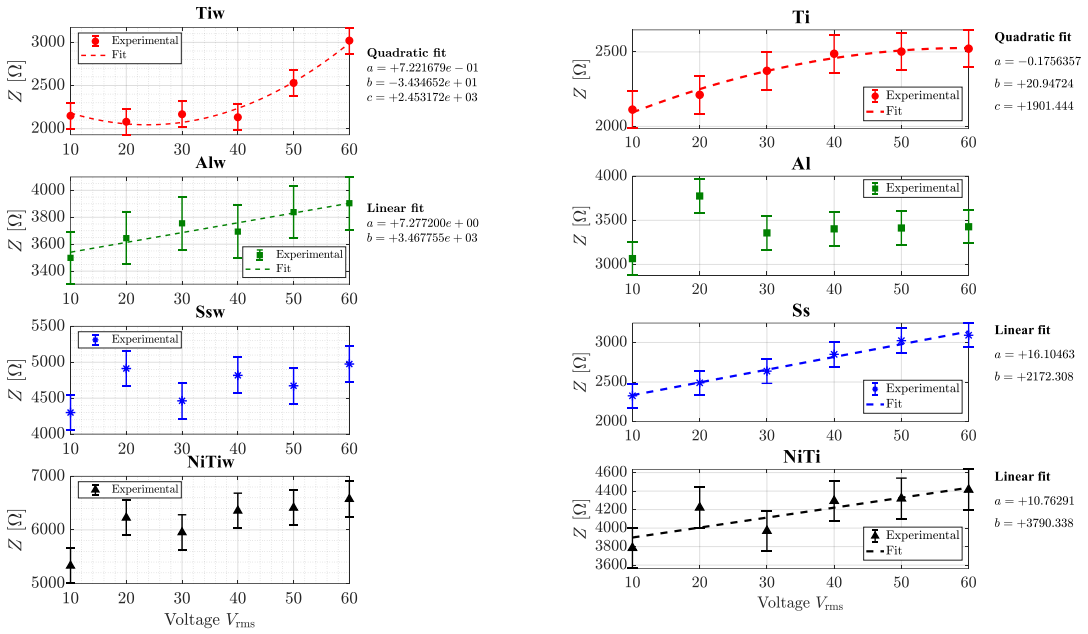
The stainless steel transducer exhibited the second-highest power density response in both configurations. Without wire integration, the power density increased from 7.33 × 10^{-5} Wmm^{-3} to 2.08× 10^{-3} Wmm^{-3}, while the wire-integrated configuration reached only 5.90 × 10^{-4} Wmm^{-3} at 60 $V_{(rms)}$. The with-wire response was described very strongly by a second-order empirical relationship, with R^2 =0.9996 and an RMSE of 4.18 × 10^{-6} Wmm^{-3}. The lower absolute power density following wire integration indicates a substantial change in the electrical power-density response of the stainless steel configuration.

The aluminium transducer exhibited a similar reduction following wire attachment. Without the wire, power density increased from 6.67×10^{-5} Wmm^{-3} to 1.90×10^{-3} Wmm^{-3} at 60 $V_{(rms)}$, whereas the corresponding wire-integrated transducer reached 5.60×10^{-4} Wmm^{-3} at 60 $V_{(rms)}$. A second-order empirical relationship represented the with-wire response closely, with R^2 =0.9997 and an RMSE of 3.04×10^{-6} W mm^{-3}. Following wire integration, the measured power density was substantially lower, indicating a marked difference in the electrical power-density response of the assembled transducer.

The Nitinol transducer exhibited the lowest power density both before and after wire integration. Without the wire, the measured power density increased from 4.0×10^{-5} Wmm^{-3} at 10 $V_{(\mathrm{rms})}$ to 1.13×10^{-3} Wmm^{-3} at 60 $V_{(rms)}$. Following wire integration, the corresponding values decreased to 1.67×10^{-5} and 3.65×10^{-4} Wmm^{-3}. Although the linear model already represented the with-wire response strongly, a second-order empirical relationship provided a better fit, with R^2 =0.9982 and an RMSE of 5.17×10^{-6} Wmm^{-3}. The lower absolute power density indicates a reduced electrical power-density response within the Nitinol configuration, but this should not be interpreted independently as poorer or superior energy-conversion efficiency.

At 60 $V_{(\mathrm{rms})}$, the power-density response followed the same ordering for the wire-free and wire-integrated configurations: Ti >Ss >Al >NiTi. Following wire integration, the absolute power density was lower for all four end-cap material configurations, while the end-cap material ordering was preserved. The reduction was particularly pronounced for the aluminium, stainless steel, and Nitinol configurations. These results indicate differences in electrical power density between the wire-integrated and wire-free configurations, with the magnitude of these differences dependent on the end-cap configuration. However, the contribution of changes in mechanical loading cannot be established from the power-density measurements alone.

The power-density results should therefore be interpreted together with the corresponding displacement-amplitude measurements rather than as a standalone measure of transducer efficiency. The titanium configuration with wire exhibited both the highest displacement amplitude and the highest power density at 60 $V_{(\mathrm{rms})}$, while the Nitinol configuration with wire exhibited both the lowest displacement amplitude and the lowest power density. The relative electromechanical performance of the transducers depends on the relationship between electrical power input and mechanical vibration output, rather than on power density alone. Figure 5.9 shows the relationship between the electrical impedance of transducers with and without wires against excitation voltage.



(a) Transducers with wires. (b) Transducers without wires.

Figure 5.9 – Electrical impedance as a function of excitation voltage.

For the transducers without wire integration (Figure 5.9b), distinct material-dependent changes in electrical impedance magnitude were observed with increasing excitation voltage. The titanium and stainless steel configurations exhibited overall increases in impedance, while the aluminium and Nitinol configurations displayed more pronounced point-to-point variation despite an overall increase across the investigated voltage range. These results established that the voltage-dependent electrical response differed between the end-cap material configurations even before the Nitinol wire was incorporated.

Following wire integration (Figure 5.9a), further material-dependent behaviour was observed. The titanium transducer with wire exhibited comparatively little change in impedance between 10 and 40 $V_{(rms)}$, followed by a pronounced increase at 50 and 60 $V_{(rms)}$. A linear model provided only a moderate representation of this response (R^2 =0.6795, RMSE = 190.09 Ω), whereas a second-order model substantially improved the agreement (R^2= 0.9673, RMSE = 60.69 Ω). Examination of the residuals also supported the presence of curvature rather than a constant voltage-dependent gradient. A second-order empirical fit was therefore used to describe the titanium response over the investigated voltage range.

The aluminium transducer with wire exhibited a more gradual increase in impedance, from 3,498.54 Ω at 10 $V_{(rms)}$ to 3,904.31 Ω at 60 $V_{(rms)}$. A linear fit produced R^2=0.8867 and an RMSE of 44.42 Ω, with a fitted gradient of 7.28 Ω/ $V_{(rms)}$. Introducing a second-order term provided only a negligible improvement (R^2=0.8946, RMSE = 42.84 Ω). The simpler linear relationship was retained as an adequate empirical description of the overall voltage-dependent response. Compared with the other wire-integrated configurations, the aluminium transducer therefore exhibited a relatively gradual and consistent change in electrical impedance with increasing excitation.

The stainless steel transducer with wire exhibited substantially greater point-to-point variation. The impedance increased overall from 4,300.26 Ω at 10 $V_{(rms)}$ to 4,975.25 Ω at 60 $V_{(rms)}$ but decreases occurred between 20–30 $V_{(rms)}$ and 40–50 $V_{(rms)}$. Neither the linear (R^2=0.3689, RMSE = 192.12 Ω) nor second-order (R^2=0.3726, RMSE = 191.55 Ω) model adequately represented this behaviour, and the second-order model provided essentially no improvement. Therefore, no fitting function was assigned to the stainless steel transducer data. The response was instead interpreted directly from the experimental measurements as a fluctuating impedance response superimposed upon an overall increase across the investigated voltage range.

The Nitinol transducer with wire exhibited the highest absolute impedance values of the four configurations, increasing overall from 5,330.34 Ω at 10 $V_{(rms)}$ to 6,574.43 Ω at 60 $V_{(rms)}$. However, this increase was not consistently linear, with a pronounced increase between 10 and 20 $V_{(rms)}$, followed by a reduction at 30 $V_{(rms)}$ and subsequent increases at higher excitation levels. The linear model produced R^2=0.7314 and an RMSE of 212.30 Ω, while the second-order model improved these values only moderately to R^2=0.7968 and an RMSE of 184.63 Ω. The residuals retained substantial deviations, particularly around the lower-voltage region. Consequently, no global fitting function was applied to the Nitinol transducer data, and the measured response was interpreted directly rather than imposing an empirical relationship that did not adequately represent the individual measurements.

Comparison with the corresponding wire-free configurations shows that the absolute impedance at 60 $V_{(rms)}$ was higher following wire integration for all four materials. The impedance of the titanium transducer increased from 2,521.71 Ω without wire to 3,020.58 Ω with wire, the aluminium transducer from 3,426.88 to 3,904.31 Ω, stainless steel transducer from 3,090.84 to 4,975.25 Ω, and the Nitinol transducer from 4,414.46 to 6,574.43 Ω. The difference was particularly pronounced for the stainless steel and Nitinol configurations. These differences indicate that wire integration was associated with an increase in electrical

impedance magnitude at 60 $V_{(rms)}$, with the magnitude of the increase dependent on the end-cap material.

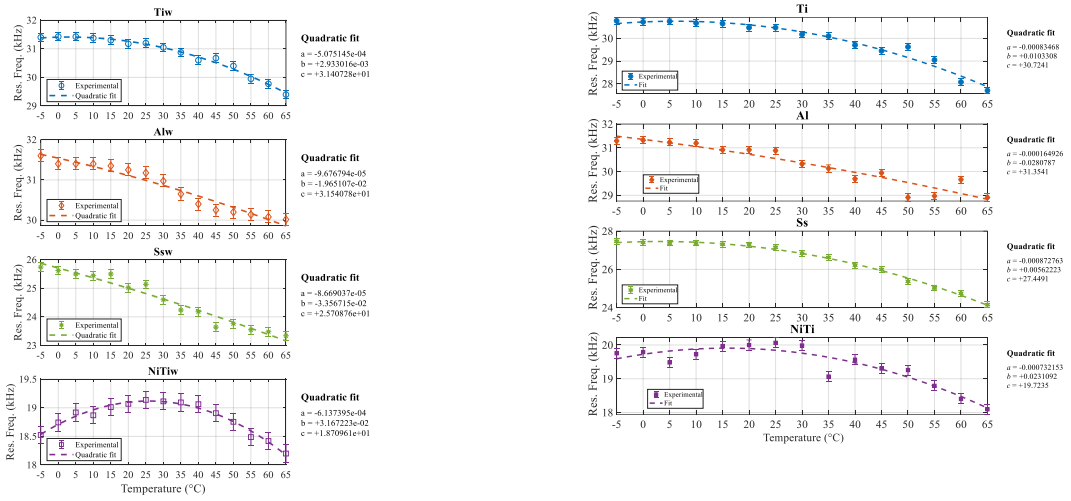
The impedance results should, however, not be interpreted independently as a direct measure of electromechanical conversion efficiency. Electrical impedance describes the opposition presented by the transducer at the measured operating condition, while the resulting mechanical response depends on the coupled electrical, piezoelectric and structural behaviour of the complete transducer. This is evident from comparison with the power-density and displacement-amplitude measurements. Although the Nitinol transducer with wire exhibited the highest absolute impedance and the lowest power density, the relationship between impedance, electrical power demand and mechanical displacement was not uniform across all four configurations. Similarly, the titanium transducer with wire exhibited the lowest impedance and the highest power density and displacement amplitude at 60 $V_{(rms)}$, but these observations alone do not establish a direct conversion-efficiency relationship.

Overall, the wire-integrated configurations exhibited differences in both the magnitude and voltage-dependent behaviour of electrical impedance compared with their wire-free counterparts, with the nature of these differences dependent on the end-cap material. The titanium configuration retained a smooth but nonlinear response, the aluminium configuration exhibited a comparatively gradual approximately linear increase, while the stainless steel and Nitinol configurations displayed sufficient point-to-point variation that global fitting functions were not justified. The wire-integrated configurations also exhibited higher absolute impedance values than their corresponding wire-free transducers at 60 $V_{(rms)}$, indicating a difference in the electrical loading of the assembled devices following wire integration. These impedance changes occurred alongside reductions in power density following wire integration; however, the relationship between impedance magnitude, electrical power demand and mechanical output was not uniform across the four configurations. The electrical impedance results should therefore be interpreted together with the displacement-amplitude, mechanical-quality-factor and power-density measurements rather than independently as a direct measure of electromechanical conversion efficiency. Collectively, the results indicate that the wire-integrated configurations exhibited different coupled electromechanical behaviour from their corresponding wire-free transducers, with the nature and magnitude of these differences dependent on the end-cap material.

5.5. Results from temperature studies

Temperature studies were conducted for the transducers with wires using the procedure in section 4.1.6. The resonance frequency, electrical impedance, and mechanical quality factor of the symmetric vibration mode were measured across a temperature range as specified in section 4.1.6 and are recorded in Figures 5.10-5.12 respectively.

A limitation of the present study is that temperature-dependent testing was not conducted on the wire-integrated Nitinol transducer containing the A_F 45 °C Nitinol end-cap. Due to time constraints, experimental investigations were restricted to the corresponding wire-integrated transducer containing the A_F 35 °C Nitinol end-cap. Future work should therefore examine the temperature-dependent behaviour of the A_F 45 °C configuration to determine whether similar trends in resonance frequency, impedance magnitude, phase angle and mechanical quality factor are observed following wire integration.



(a) Transducers with wires. (b) Transducers without wires.

Figure 5.10 – Resonance frequency as a function of temperature.

For the titanium configuration, the wire-free transducer exhibited a nonlinear decrease in resonance frequency from 30.775 kHz at −5 °C to 27.700 kHz at 65 °C, with a second-order model providing R^2 = 0.9653 and an RMSE of 0.1756 kHz. Following wire integration, the resonance frequency decreased from 31.400 to 29.400 kHz over the same temperature range. The linear model produced R^2 = 0.8777 and an RMSE of 0.2219 kHz, while the second-order model increased the coefficient of determination to R^2 = 0.9876 and reduced the RMSE to 0.0705 kHz. The linear residuals exhibited a systematic curvature pattern, whereas the second-order residuals were substantially smaller. The wire-integrated titanium configuration therefore

retained a nonlinear temperature-dependent response, but the total measured frequency reduction over the investigated range decreased from 3.075 kHz without the wire to 2.000 kHz following wire integration.

The aluminium configuration exhibited an approximately linear overall decrease in resonance frequency both before and after wire integration. Without the wire, resonance frequency decreased from 31.291 to 28.910 kHz, with a second-order model producing $R^2 = 0.8959$ and an RMSE of 0.2806 kHz. Following wire integration, the resonance frequency decreased from 31.600 to 30.015 kHz. A second-order model was applied consistently with the other configurations, producing $R^2 = 0.9489$ and an RMSE of 0.1279 kHz. The corresponding quadratic coefficients were -1.649×10^{-4} kHz/°C² without wire and -9.677×10^{-5} kHz/°C² following wire integration, indicating comparatively modest curvature within the overall decreasing temperature-dependent response. Although the second-order models provided only marginal improvements over the corresponding linear relationships, their use allowed a consistent empirical comparison across the transducer configurations. The measured frequency reduction decreased from 2.381 kHz without wire integration to 1.585 kHz with the wire.

The stainless steel configuration exhibited differences in its temperature-dependent response following wire integration. Without the wire, the transducer exhibited a strongly nonlinear reduction in resonance frequency from 27.469 to 24.156 kHz, with a second-order model providing $R^2 = 0.9947$ and an RMSE of 0.0786 kHz. Following wire integration, the resonance frequency decreased from 25.740 to 23.340 kHz. A second-order model was applied consistently, producing $R^2 = 0.9574$ and an RMSE of 0.1768 kHz, compared with $R^2 = 0.9556$ and an RMSE of 0.1804 kHz for the linear model. The fitted quadratic coefficient decreased in magnitude from -8.728×10^{-4} kHz/°C² without wire to -8.669×10^{-5} kHz/°C² following wire integration, indicating substantially less curvature in the fitted response. Therefore, although both configurations were represented using second-order empirical relationships, the wire-integrated stainless steel transducer exhibited an approximately linear decreasing trend over the investigated temperature range.

The Nitinol configuration exhibited the most distinctive comparison. Without wire integration, the resonance frequency remained comparatively stable at lower temperatures before decreasing more strongly at elevated temperatures, and a second-order empirical model represented the overall response with $R^2 = 0.8684$ and an RMSE of 0.2112 kHz. Following wire integration, the resonance frequency increased from 18.525 kHz at −5 °C to a measured

maximum of 19.138 kHz at 25 °C, before decreasing progressively to 18.200 kHz at 65 °C. A linear model was unsuitable for this response (R^2 = 0.1558, RMSE = 0.2590 kHz), whereas a second-order relationship produced R^2 = 0.9703 and an RMSE of 0.0486 kHz. The fitted relationship therefore captured the clear curvature of the response, with a broad maximum occurring in the lower-to-intermediate temperature range followed by increasingly negative temperature dependence at elevated temperatures.

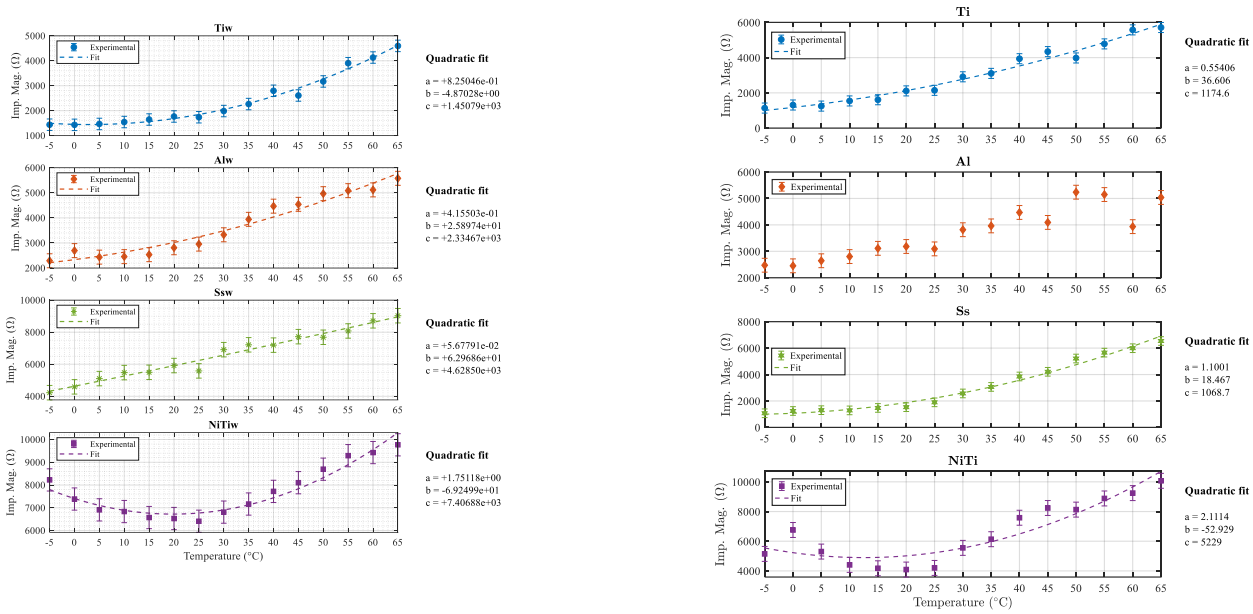
The nonlinear response of the wire-integrated Nitinol configuration should not, however, be interpreted as direct evidence of a discrete martensitic-to-austenitic transformation within the assembled transducer. The corresponding wire-free Nitinol end-cap exhibited an A_F of 35 °C, but neither the wire-free nor wire-integrated resonance measurements showed an abrupt resonance-frequency discontinuity at this temperature. In the wire-integrated configuration, the measured maximum occurred at 25 °C, below the nominal A_F, and the resonance frequency subsequently decreased smoothly rather than undergoing a discrete shift. The observed behaviour may therefore reflect the combined influence of the temperature-dependent mechanical properties of the Nitinol components, residual stresses introduced during manufacturing, the epoxy bonding layer, and the dynamic response of the complete transducer assembly rather than the phase transformation alone [27–30,34,35,47].

Comparison of the measured frequency changes further shows that the overall resonance-frequency variation was lower following wire integration between −5 and 65 °C for titanium, aluminium and stainless steel transducers. The measured reduction decreased from 3.075 to 2.000 kHz for titanium, from 2.381 to 1.585 kHz for aluminium, and from 3.313 to 2.400 kHz for stainless steel. The Nitinol comparison is less appropriately characterised by a simple endpoint difference because both the wire-free and wire-integrated responses were nonlinear and the wire-integrated configuration exhibited an intermediate maximum. The influence of wire integration is therefore better interpreted through the differences in response shape, fitted curvature and measured frequency variation rather than through a single frequency-temperature gradient.

These results demonstrate that wire integration influenced the resonance-frequency response of the flextensional transducers, with the nature and magnitude of the changes dependent on the end-cap material. The titanium transducer retained a nonlinear temperature-dependent response but exhibited a smaller overall frequency reduction following wire integration. Aluminium maintained an approximately linear overall response with reduced frequency

variation, while stainless steel exhibited substantially less curvature following wire attachment. The Nitinol configuration retained a distinctly nonlinear temperature dependence but exhibited a more clearly defined increase-to-maximum-and-decrease response following wire integration. Consequently, the observed changes cannot be characterised as a universal improvement in thermal stability or by a single common drift-rate comparison.

Figure 5.11 shows the effect on electrical impedance across a temperature range for all the transducers.



(a) Transducers with wires. (b) Transducers without wires.

Figure 5.11 – Electrical impedance as a function of temperature.

The titanium transducer with wire exhibited a nonlinear increase in electrical impedance magnitude with increasing temperature, from 1,436.88 Ω at −5 °C to 4,596.84 Ω at 65 °C. A linear relationship provided $R^2 = 0.8752$ and an RMSE of 364.2 Ω, whereas the second-order relationship improved R^2 to 0.9853 and reduced the RMSE to 124.9 Ω. The residuals were also considerably smaller for the second-order model and were generally distributed about the fitted response. The second-order relationship was therefore considered more appropriate. The positive curvature indicates that the impedance-temperature sensitivity increased progressively with temperature, with the electrical response of the wire-integrated titanium transducer becoming increasingly temperature dependent at elevated temperatures.

The aluminium transducer with wire exhibited an overall increase in impedance magnitude from 2,290.21 Ω at −5 °C to 5,577.00 Ω at 65 °C, accompanied by appreciable point-to-point variation. A linear relationship produced R^2 = 0.9323 and an RMSE of 295.8 Ω, whereas a second-order relationship increased R^2 to 0.9553 and reduced the RMSE to 240.4 Ω. The second-order relationship was adopted to maintain consistency with the fitting approach used for the other wire-integrated configurations. Although the quadratic model provided an improved representation of the experimental measurements, appreciable residual variation remained. The fitted curvature therefore describes the overall temperature-dependent trend empirically and should not be interpreted as evidence of a distinct underlying physical mechanism.

The stainless steel transducer with wire exhibited a strong overall increase in impedance magnitude, from 4,223.83 Ω at −5 °C to 9,029.82 Ω at 65 °C. A linear relationship represented the response well, producing R^2 = 0.9727 and an RMSE of 240.2 Ω. Introducing a second-order term produced essentially no improvement, with R^2 increasing only to 0.9730 and the RMSE decreasing marginally to 239.0 Ω. Nevertheless, the second-order relationship was retained to maintain consistency with the fitting approach adopted for the other wire-integrated configurations. The small quadratic coefficient indicates that the fitted response remained approximately linear, with a comparatively consistent increase in electrical impedance magnitude over the investigated temperature range. Although local deviations from the fitted relationship were observed, particularly around 25 °C, these did not alter the overall approximately linear temperature dependence.

The wire-integrated Nitinol transducer exhibited a distinctly nonlinear impedance-temperature response. The impedance magnitude was initially high at −5 °C, at 8,224.62 Ω, before decreasing to a minimum of 6,408.58 Ω at 25 °C and subsequently increasing to 9,768.19 Ω at 65 °C. A linear model provided a poor representation of the measured behaviour, with R^2 = 0.4968 and an RMSE of 778.8 Ω. A second-order relationship substantially improved the representation, producing R^2 = 0.9341 and reducing the RMSE to 281.8 Ω. The second-order model therefore provides a substantially more appropriate empirical description of the measured response. The fitted curvature captures the transition from decreasing impedance at lower temperatures to increasing impedance at elevated temperatures. Nevertheless, residual deviations remain, and the fitted relationship should be regarded as a representation of the overall nonlinear behaviour rather than a precise predictive model.

The behaviour of the wire-integrated Nitinol configuration is particularly relevant when considered alongside the independently measured transformation characteristics of the Nitinol end-cap. The end-cap material exhibited an A_F of 35 °C while the impedance response reached its lowest measured value at approximately 25 °C before increasing across the higher-temperature region. However, no discrete impedance change was observed at 35 °C that could be uniquely associated with completion of the martensitic-to-austenitic transformation. The present measurements therefore do not independently establish that the nonlinear impedance response was caused by the Nitinol phase transformation. Rather, the response may reflect the combined influence of the temperature-dependent mechanical state of the Nitinol end-cap and the dynamic behaviour of the complete wire-integrated transducer assembly. The persistence of a pronounced nonlinear response following wire integration nevertheless indicates that the Nitinol configuration retained a temperature dependence distinct from those of the titanium, aluminium and stainless steel configurations.

Comparison with the corresponding transducers without wire integration demonstrates that the addition of the wire modified both the magnitude and form of the temperature-dependent impedance responses. The titanium configuration retained a strongly nonlinear increase with temperature, although its second-order fit improved from R^2 = 0.9777 without the wire to R^2 = 0.9853 following wire integration, while the RMSE decreased from 230.6 Ω to 124.9 Ω. Aluminium changed from a response for which neither a linear nor second-order global model was considered sufficiently representative without the wire to a clearer overall increasing response following wire integration, for which a second-order relationship provided R^2 = 0.9553. Stainless steel changed from a strongly nonlinear response without the wire to an approximately linear response following wire integration, with the second-order relationship producing R^2 = 0.9730 and exhibiting only a small quadratic contribution.

These differences demonstrate that wire integration did not simply produce a uniform increase or decrease in impedance-temperature sensitivity but altered the electromechanical response differently for each end-cap configuration.

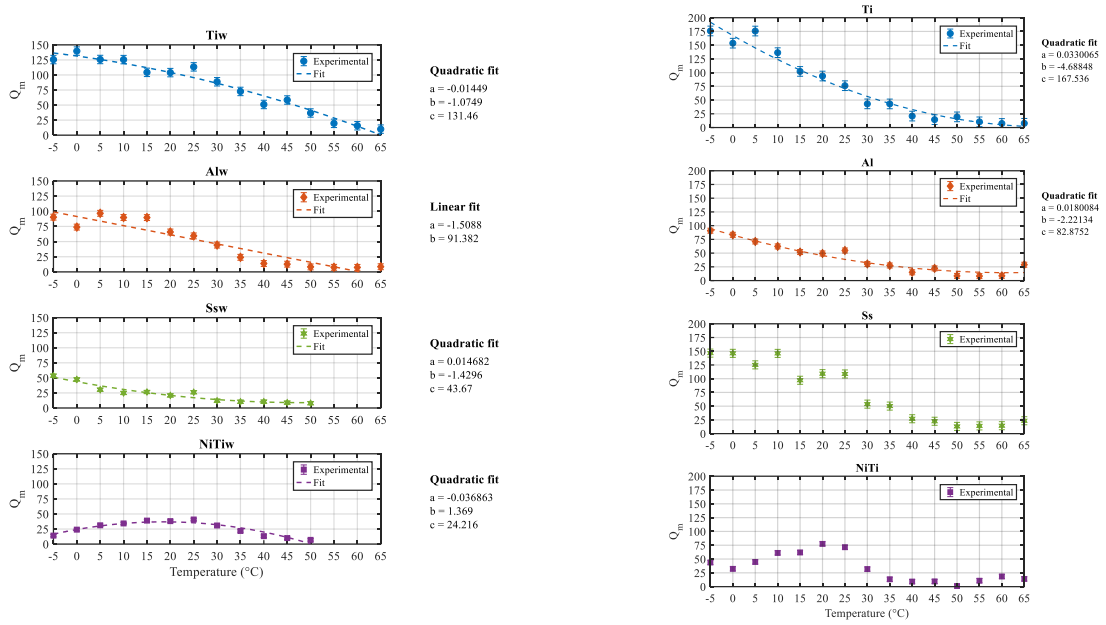
The Nitinol comparison is particularly notable. Both the non-wire and wire-integrated configurations exhibited a broad decrease in impedance over part of the lower-temperature range followed by a pronounced increase at elevated temperatures. The second-order fit produced R^2 = 0.8548 and an RMSE of 749.4 Ω without the wire to R^2 = 0.9341 and an RMSE of 281.8 Ω following wire integration. The persistence of this broad nonlinear form before and

after wire attachment suggests that the characteristic temperature-dependent behaviour was not eliminated by the additional wire and epoxy loading. However, because the impedance magnitude represents the response of the complete electromechanical system, this similarity alone cannot be used to attribute the behaviour specifically to the Nitinol phase transformation.

More generally, the temperature-dependent impedance magnitude of the wire-integrated transducers represents the behaviour of the complete assembled system, including the end caps, piezoceramic elements, adhesive interfaces and attached wire. Wire integration introduces additional mass, stiffness, damping and an additional bonded interface, each of which may alter the mechanical boundary conditions and consequently the electrical impedance measured through electromechanical coupling. Temperature-dependent changes in the dielectric, elastic and piezoelectric properties of the piezoceramic elements may additionally contribute to the measured response [188–190]. The influence of these mechanisms was not independently isolated in the present experiments; therefore, changes following wire integration should be interpreted as changes in the response of the assembled transducer rather than being attributed exclusively to the wire, epoxy layer or end-cap material.

Overall, material-dependent differences in impedance-temperature behaviour were observed between the wire-free and wire-integrated configurations. The titanium transducer retained a strongly nonlinear increase in impedance magnitude, the aluminium transducer exhibited an overall approximately linear increase accompanied by experimental variation, stainless steel exhibited a well-defined approximately linear increase, and the Nitinol transducer retained a distinctive nonlinear response characterised by an initial reduction followed by a pronounced increase at elevated temperatures. The results therefore indicate that the differences observed following wire integration depended on the dynamic characteristics of each transducer configuration rather than representing a common response across all four materials. In particular, the persistence of the nonlinear Nitinol response following wire integration provides evidence that its distinct temperature-dependent electromechanical behaviour remained observable in the complete wire-integrated assembly, while the present measurements do not independently isolate the contribution of the Nitinol phase transformation from the other temperature-dependent mechanisms within the transducer.

Figure 5.12 shows the effect on mechanical quality factor across a temperature range for all the transducers.



(a)Transducers with wires. (b)Transducers without wires.

Figure 5.12 - Mechanical quality factor as a function of temperature.

For the titanium transducer with wire integration, Q_m decreased overall from 125.60 at −5 °C to 10.05 at 65 °C. A linear relationship produced R^2 =0.9435 and an RMSE of 10.28, while a second-order relationship increased R^2 to 0.9628 and reduced the RMSE to 8.34. The second-order relationship was therefore retained as an empirical representation of the nonlinear temperature-dependent response. Compared with the titanium transducer without wire integration, which decreased from 175.86 to 7.69 and was also represented by a second-order relationship (R^2=0.9629, RMSE = 11.79), the wire-integrated configuration generally exhibited lower Q_m values at the lower temperatures. Both configurations nevertheless demonstrated a pronounced reduction in Q_m with increasing temperature. The persistence of this behaviour following wire integration indicates progressively reduced resonance sharpness with increasing temperature, consistent with increased effective mechanical losses within the assembled transducer. The wire-integrated configuration also exhibited different absolute mechanical quality factors from its wire-free counterpart.

The aluminium transducer with wire integration exhibited an overall reduction in Q_m from 90.29 at −5 °C to 8.51 at 65 °C. A linear relationship produced R^2 = 0.8800 and an RMSE of 12.04, while introducing a second-order term provided only a negligible improvement (R^2 = 0.8816, RMSE = 11.95), indicating that the additional curvature was not necessary to represent the overall decreasing trend. The simpler linear relationship was therefore retained as an empirical representation of the measured response.This differs from the aluminium transducer

without wire integration, for which the second-order relationship provided a substantially improved representation (R^2 =0.9323, RMSE = 6.94) compared with the linear model. The form of the temperature-dependent response therefore differed following wire integration rather than exhibiting a simple constant shift in Q_m. Nevertheless, both configurations exhibited substantial overall reductions in mechanical quality factor with increasing temperature, indicating progressively reduced resonance sharpness at elevated temperatures.

The stainless steel transducer with wire integration exhibited an overall decrease in Q_m from 53.63 at −5 °C to 7.97 at 50 °C. A linear relationship produced R^2=0.8519 and an RMSE of 5.53, whereas a second-order relationship increased R^2 to 0.9243 and reduced the RMSE to 3.96. The second-order relationship therefore provided a more appropriate empirical representation of the measured response, capturing the pronounced reduction in Q_m at lower and intermediate temperatures followed by comparatively smaller changes at elevated temperatures. Q_m could not be reliably determined using the 3 dB bandwidth method at 55, 60 and 65 °C and these temperatures were therefore excluded from the analysis. This behaviour differs from the stainless steel transducer without wire integration, for which substantial point-to-point variation prevented either a linear or second-order relationship from adequately representing the complete response. Following wire integration, the stainless steel configuration exhibited lower absolute Q_m values, particularly at the lower temperatures, while its measured temperature dependence was more readily represented by a second-order empirical relationship.

The wire-integrated Nitinol transducer retained the distinctive non-monotonic behaviour observed for the Nitinol transducer without wire integration. Q_m increased from 14.11 at −5 °C to a maximum measured value of 40.83 at 25 °C before decreasing to 6.99 at 50 °C. A linear relationship represented this response poorly (R^2=0.1882, RMSE = 10.39), whereas a second-order relationship provided a substantially improved representation, with R^2=0.8985 and an RMSE of 3.67. The second-order relationship was therefore retained as an empirical representation of the overall rise-and-fall behaviour. As with the stainless steel configuration, Q_m could not be reliably determined using the 3 dB bandwidth method at 55, 60 and 65 °C. The corresponding Nitinol transducer without wire integration also exhibited an initial increase in Q_m, reaching a maximum of 77.51 at 20 °C before decreasing substantially at higher temperatures; however, neither a linear nor second-order relationship adequately represented that dataset. Following wire integration, the absolute Q_m values were lower, and the maximum

measured value occurred at 25 °C, compared with 20 °C without wire integration, while the characteristic non-monotonic response remained evident.

The persistence of the non-monotonic Q_m response following wire integration is relevant when considered alongside the temperature-dependent thermomechanical characteristics of Nitinol reported in previous investigations [27–30,34,35]. The independently measured A_F of the Nitinol end-cap was 35 °C. However, the maximum Q_m occurred below A_F for both configurations, at approximately 20 °C without wire integration and 25 °C following wire integration, and neither configuration exhibited a discrete change in Q_m at 35 °C. The persistence of the rise-and-fall response after wire integration therefore indicates that this feature remained present in the dynamic behaviour of the assembled Nitinol configuration but does not independently establish that it resulted directly from the martensitic-to-austenitic transformation. Temperature-dependent Nitinol properties, together with changes in the piezoceramic elements, adhesive layers, structural interfaces and overall electromechanical behaviour, may all have contributed to the measured response [12,187].

5.6. Summary

This chapter investigated the integration of Nitinol wires into class IV flextensional ultrasonic transducers incorporating titanium, aluminium, stainless steel, and Nitinol end-caps. EIA, EMA, harmonic response analysis, and temperature-dependent characterisation were performed to evaluate the influence of wire integration on the electromechanical and dynamic performance of the transducers. The results demonstrated differences in resonance behaviour, mechanical quality factor, electromechanical coupling coefficient, displacement amplitude, power density and impedance response following wire integration, with the extent of these differences strongly dependent on the end-cap material.

EMA confirmed that wire integration did not alter the fundamental symmetric longitudinal operating mode of the transducers, although changes in vibration distribution were observed. In the titanium and aluminium configurations, the wire appeared to compensate for asymmetries in the vibration response. The stainless steel and Nitinol configurations exhibited reduced vibration amplitudes at the wire-attached end-cap and increased vibration amplitudes at the free end-cap. Good agreement was obtained between the resonance frequencies predicted by finite element analysis and those measured experimentally, supporting the suitability of the numerical modelling approach developed in this work.

Harmonic response analysis demonstrated that wire integration modified the voltage-dependent dynamic behaviour of all four transducer configurations. The magnitude of the resonance-frequency variation, displacement response and mechanical quality factor differed according to the end-cap material and could not in all cases be adequately represented using a common voltage-dependent relationship. The titanium transducer with wire integration exhibited the most favourable overall ultrasonic output, producing the highest displacement amplitudes and power densities among the wire-integrated configurations. In contrast, the Nitinol transducer produced lower displacement amplitudes and power densities. Mechanical quality factor generally decreased with increasing excitation, indicating increased mechanical losses and reduced resonance sharpness at higher drive levels, although the magnitude and form of this response differed between the four configurations.

Similarly, the temperature-dependent electrical impedance response differed substantially between the four wire-integrated configurations. The titanium transducer exhibited a pronounced nonlinear increase in impedance magnitude, which was strongly represented by a second-order relationship (R^2 = 0.9853, RMSE = 124.91 Ω). The aluminium transducer exhibited an overall increasing response accompanied by greater experimental variation, while the stainless steel transducer demonstrated a strong overall increase that was represented by a second-order empirical relationship (R^2 = 0.9730), with only a small quadratic contribution.

The wire-integrated Nitinol transducer again exhibited a distinct nonlinear response, characterised by an initial reduction in impedance followed by a pronounced increase at elevated temperatures. A second-order empirical relationship substantially improved the representation of this behaviour compared with a linear model (R^2 =0.9341 compared with 0.4968), although appreciable residual variation remained. These findings indicate that the changes observed following wire integration were not uniform across the four configurations but differed according to the end-cap material and complete transducer configuration.

The mechanical quality factor measurements further demonstrated material-dependent temperature responses. The titanium transducer with wire exhibited a pronounced nonlinear reduction in Q_m, while the aluminium configuration exhibited an overall decreasing response that was adequately represented by a linear relationship. Stainless steel also exhibited a substantial reduction in Q_m, with a second-order empirical relationship providing an improved representation of the measured response. The Nitinol configuration was again distinct, with Q_m increasing from 14.11 at −5 °C to a maximum measured value of 40.83 at 25 °C before

decreasing to 6.99 at 50 °C. A second-order relationship represented this rise-and-fall response considerably more effectively than a linear model (R^2 = 0.8985 compared with 0.1882). For the stainless steel and Nitinol configurations, Q_m could not be reliably determined using the 3 dB bandwidth method at the final three temperatures and these points were therefore excluded from the analysis.

The persistence of the distinct nonlinear temperature-dependent behaviour of the Nitinol configuration following wire integration is particularly relevant when considered alongside the thermomechanical characteristics of the Nitinol material [27–30,34,35]. The Nitinol end-cap exhibited an A_F of 35 °C, while the Nitinol wire exhibited an A_F of 30 °C. However, neither the resonance-frequency, impedance nor mechanical-quality-factor measurements demonstrated a discrete change at a single transformation temperature. The present measurements therefore do not independently establish that the observed nonlinear transducer responses resulted directly from the martensitic-to-austenitic transformation. Instead, they demonstrate that a distinct temperature-dependent electromechanical response remained present following wire integration and should be interpreted as the behaviour of the complete transducer assembly rather than that of the Nitinol components in isolation.

The temperature-dependent behaviour exhibited by the wire-integrated Nitinol transducer may be considered in relation to the material characteristics of the A_F 30 °C Nitinol wire. The DSC box-and-whisker plot (Figure 3.10a) demonstrated lower variability in the transformation temperatures of the wire compared with the A_F 35 °C Nitinol end-cap, indicating a more uniform transformation behaviour. The EDXS results additionally showed a consistently high nickel content of approximately 55 wt.% throughout the analysed wire locations (spectra 1, 2, 3, 4, 7, 8, 9 and 10 of Table 3.1), without the oxygen- and iron-rich regions identified within parts of the Nitinol end-cap. Together, the DSC and EDXS results therefore indicate greater uniformity in the measured transformation temperatures and local composition of the A_F 30 °C wire compared with the A_F 35 °C end-cap. This greater homogeneity may have contributed to the temperature-dependent dynamic behaviour observed following wire integration; however, the contribution of the wire cannot be isolated from the behaviour of the complete transducer assembly.

Overall, the results demonstrate that Nitinol wires can be successfully integrated into class IV flextensional ultrasonic transducers while retaining the fundamental operating mode of the devices. However, differences in electrical and mechanical loading were observed following

wire integration, with the nature and magnitude of these differences strongly dependent on the end-cap material. Of the wire-integrated configurations, titanium exhibited the highest displacement amplitudes and power densities, while maintaining comparatively high mechanical quality factors. The Nitinol configuration exhibited lower ultrasonic output but remained distinctive in its nonlinear temperature-dependent resonance-frequency, impedance and mechanical-quality-factor responses. These findings demonstrate that the performance of a wire-integrated flextensional transducer cannot be attributed solely to either the end-cap or wire material, but results from the combined electrical, mechanical, material and interfacial behaviour of the complete assembled system. Building upon the electromechanical characterisation presented in this chapter, Chapter 6 evaluates the cutting performance of the wire-integrated transducers using a bone-mimicking material, with particular attention given to the relationship between cutting behaviour and the resonance frequency, electrical impedance, phase and load-power responses observed during operation.

Chapter 6

Performance evaluation of transducers with wires

This chapter presents a systematic performance evaluation of flextensional transducers with wires, with a focus on their electrical, mechanical, and cutting behaviour under continuous excitation. The assessment examines impedance matching, displacement amplitude, resonance stability, electrical phase, and load power to understand how different end-cap materials influence energy transmission and operational robustness. This evaluation is essential for identifying material-dependent trade-offs relevant to the development of ultrasonic surgical devices operating under varying loading conditions.

6.1. Impedance matching

Ultrasonic surgical transducers are commonly driven using resonance tracking systems that continuously monitor the electrical response of the transducer and adjust the excitation frequency to maintain operation at or near resonance. Maintaining resonance is important because it maximises vibration amplitude, improves energy transfer efficiency, and minimises electrical power losses [96,199]. In this study, a PiezoDrive PDUS210-800 resonance tracking system was used to drive the ultrasonic transducers. The system provides automatic resonance tracking and is designed to operate most efficiently when connected to a load impedance close to its nominal output impedance of 400 Ω [199].

Since the electrical impedance of an ultrasonic transducer is strongly dependent on its geometry, materials, operating frequency, and boundary conditions, the impedance presented to the driving electronics may differ significantly from the optimal value required by the resonance tracking system. Impedance matching is often required to maximise power transfer between the driving electronics and the transducer while maintaining stable operation. To evaluate the electrical characteristics of the transducer near resonance, the electromechanical behaviour can be represented using an equivalent electrical circuit [96,169].

The Butterworth–Van Dyke (BVD) model, illustrated in Figure 6.1, is one of the most widely used equivalent circuit representations of piezoelectric transducers operating near resonance.

The model separates the electrical and mechanical contributions to the transducer response into lumped electrical elements.

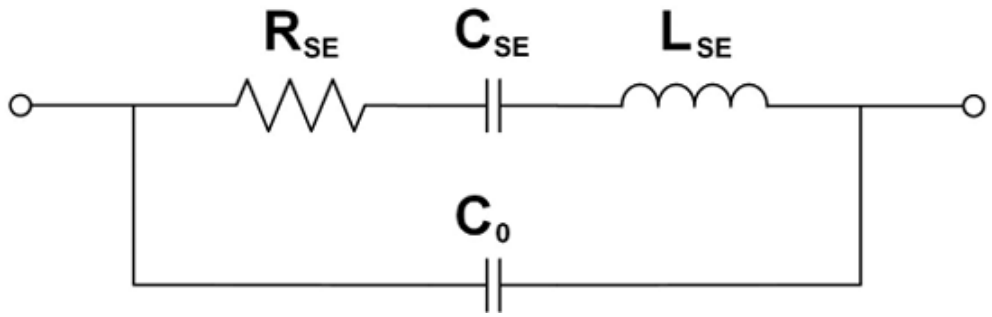


Figure 6.1 – BVD model at resonance.

The motional branch, comprising the equivalent resistance R_{SE}, capacitance C_{SE}, and inductance L_{SE}, represents the mechanical losses, compliance, and effective mass of the vibrating transducer, respectively. The parallel capacitance C_0 represents the static capacitance of the piezoelectric element when mechanical motion is neglected [199]. By fitting the measured impedance response to the BVD model, key transducer parameters can be extracted and subsequently used to assess impedance matching and optimise the interaction between the ultrasonic transducer and the resonance tracking system.

The impedance of the BVD model can be calculated from equation 6.1.

$$Z(\omega) = 1/\omega C_0[((\omega_s^2-\omega^2)+j\omega R_{SE}/L_{SE})/(-\omega R_{SE}/L_{SE}+j(\omega_p^2-\omega^2))] \quad (6.1)$$

The series (ω_s) and parallel (ω_p) angular frequencies can be calculated from equations 6.2 and 6.3 respectively;

$$\omega_s = (1/L_{SE}R_{SE})^{0.5} \quad (6.2)$$

$$\omega_p = [(C_{SE} + C_0)/(L_{SE} C_{SE} C_0)]^{0.5} \quad (6.3)$$

At the resonance frequency of the symmetric vibration mode of the Class IV transducer with wires, the inductive reactance associated with the motional inductance (L_{SE}) and the capacitive reactance associated with the motional capacitance (C_{SE}) become equal in magnitude and opposite in sign. The reactive components cancel, resulting in a net reactive impedance of zero. Under these conditions, the transducer exhibits a purely resistive electrical response with an overall phase angle of approximately 0º. The equivalent circuit therefore simplifies to a configuration in which the equivalent series resistance (R_{SE}) dominates the electrical behaviour, as shown in Figure 6.2 [96].

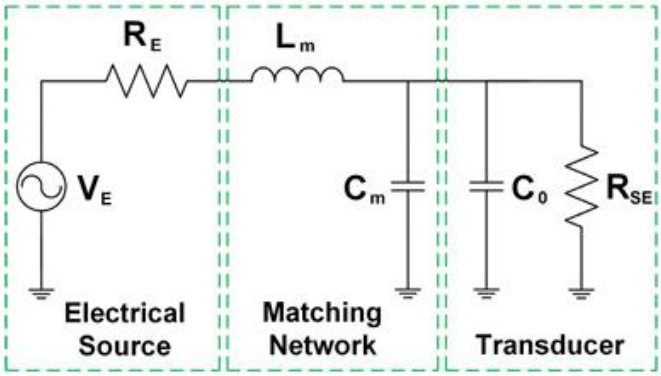


Figure 6.2 - Simplified equivalent circuit at resonance of a transducer matched to an electrical source.

Figure 6.2 presents an L-section impedance matching network consisting of a series inductance (L_M) and a shunt capacitance (C_M). The purpose of the matching network is to transform the electrical impedance of the transducer to more closely match the output impedance of the ultrasonic driver, thereby maximising power transfer and reducing reflected electrical power. In this study, V_E represents the electrical source, while R_E corresponds to the source resistance, which was 400 Ω. The component values of the matching network were calculated using standard L-section impedance matching network design equations [196].

For a source resistance R_E driving a load resistance R_{SE}, the quality factor of the matching network is given by:

$$Q = (R_{SE}/ R_E - 1)^{0.5} \qquad (6.4)$$

The required series inductive reactance is then

$$X_L = Q R_E \qquad (6.5)$$

and since $X_L = \omega L_M$, the matching inductance may be expressed as

$$L_M = R_E/\omega(R_{SE}/ R_E - 1)^{0.5} \qquad (6.6)$$

Similarly, the shunt capacitance is obtained from the corresponding L-section matching network relationship.

$$C_M = (1/ \omega R_{SE}) \times (R_{SE}/ R_E - 1)^{0.5} - C_0 \quad (6.7)$$

where C_0 is the static capacitance of the transducer. The calculated values of L_M and C_M provide the component values required to achieve impedance matching at the operating resonance frequency.

To implement the matching network experimentally, a 5-decade capacitance box (ELC Construction Électronique, Annecy, France) and a 7-decade inductance box (ELC Construction Électronique, Annecy, France) were used. A decade box is a variable passive component instrument that allows discrete inductance or capacitance values to be selected through a series

of switches, enabling rapid adjustment of circuit parameters without replacing individual components. The capacitance box was used to realise the required value of C_M, while the inductance box was used to realise L_M. The simplified equivalent circuit was assembled on a breadboard and connected between the ultrasonic driver (PiezoDrive, PDUS210-210 W Ultrasonic Driver and Analyser, Newcastle, Australia) and the transducer.

Before constructing the matching network, the resonance frequency of the symmetric vibration mode for each transducer was measured using an impedance analyser. These measurements were subsequently used to calculate the required matching network component values and to define the upper and lower resonance frequency limits within the PiezoDrive software during continuous excitation. The selected inductance and capacitance values, Table 6.1, were chosen to electrically match each transducer to the ultrasonic driver at the operating frequency, thereby minimising the reactive component of the impedance and reducing the phase difference between voltage and current. This impedance matching process enabled more efficient power transfer from the driver to the transducer, resulting in increased vibration displacement amplitude at the tip of the Nitinol wire.

Transducer end-cap materials	L_M/mH	C_M/pF
Nitinol	67	100
Titanium	18	100
Aluminium	25	100
Stainless Steel	30	100

Table 6.1 - Matching network parameters for flextensional transducers.

The inductance and capacitance values presented in Table 6.1 were determined experimentally using a 7-decade inductance box and a 5-decade capacitance box. The component values were adjusted iteratively while monitoring the transducer response to achieve satisfactory impedance matching, defined as minimising the reactive component of the electrical impedance and reducing the phase difference between voltage and current at the operating frequency. This enabled more efficient power transfer from the ultrasonic driver to the transducer and increased the vibration displacement amplitude at the tip of the Nitinol wire.

Although different inductance values were required for each transducer configuration owing to differences in their electrical characteristics, experimental tuning demonstrated that a

capacitance value of 100 pF provided suitable matching for all four transducers with Nitinol wires. Optimisation was primarily achieved through adjustment of the inductance, while the capacitance was maintained at a constant value. The values reported in Table 6.1 therefore represent experimentally optimised matching network parameters obtained through an iterative trial-and-error tuning procedure.

6.2. Displacement amplitude measurements

The displacement amplitude of the transducers with wires was measured using the harmonic analysis setup described in Sections 4.1.5, 4.2.3, and 5.4. The tests were conducted under a free boundary condition, as illustrated in Figure 4.12. The principal difference between the displacement measurements presented in this section and the harmonic response measurements discussed in Sections 4.1.5, 4.2.3, and 5.4 is the nature of the excitation signal employed. Harmonic response measurements were performed using burst sine excitation to characterise the frequency-dependent behaviour of the transducers and to identify their resonant characteristics over a frequency sweep. The present study was concerned with evaluating transducer performance at the operating resonance frequency over an excitation voltage range of 10 to 100 $V_{p\text{-}p}$.

For this reason, continuous sinusoidal excitation was employed during the displacement amplitude measurements. The transducers were driven continuously at their respective resonance frequencies while the excitation voltage was varied. This enabled the steady-state vibration response of each transducer configuration to be assessed under conditions representative of practical ultrasonic device operation. The measured displacement amplitudes provide a direct comparison of transducer performance as a function of drive voltage rather than frequency.

Figure 6.3-6.6 shows the measured displacement amplitude, electrical impedance, resonance frequency and load power respectively for the flextensional transducers with wires over the same excitation voltage range. The load power represents the real electrical power delivered by the ultrasonic driver to the transducer during operation and was obtained directly from the PiezoDrive ultrasonic driver and analyser. This parameter incorporates the combined effects of electrical impedance, electromechanical coupling and mechanical losses, making it a useful indicator of overall transducer performance. Comparison of load power alongside displacement amplitude provides insight into the electrical power required to achieve a given vibration response and is relevant when assessing the efficiency and operational performance of the different transducer configurations. These measurements were performed on electrically

matched transducers. The measured displacement amplitudes and electrical responses reflect the performance of the transducers under optimised driving conditions and provide a representative assessment of their behaviour during sustained operation.

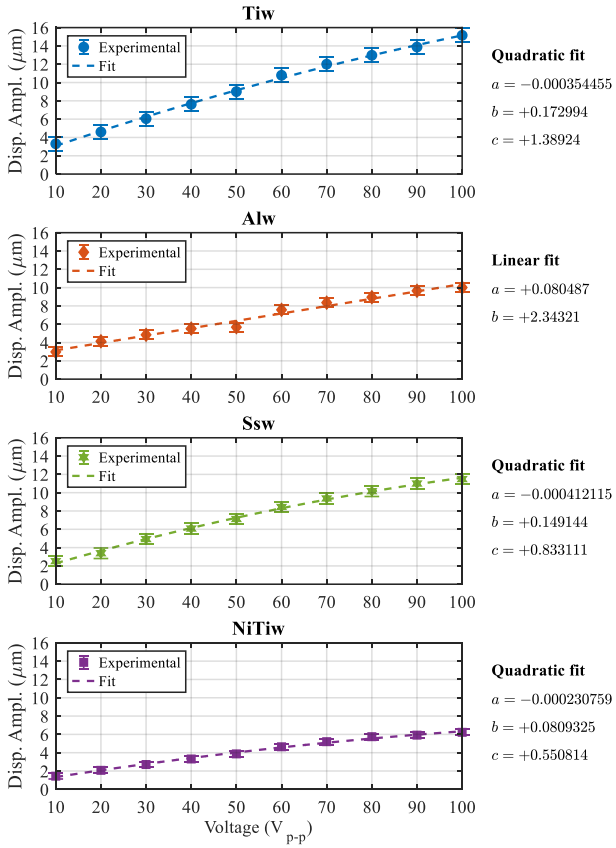


Figure 6.3 - Displacement amplitude as a function of excitation voltage for the wire-integrated transducers during continuous excitation.

Under approximately linear operating conditions, the displacement amplitude of a piezoelectric ultrasonic transducer is expected to increase proportionally with the applied excitation voltage [83], assuming that the electromechanical properties and operating conditions remain approximately constant. Departures from linearity may arise from amplitude-dependent changes in the effective mechanical and electromechanical response of the assembled transducer [83-84]. Consequently, linear relationships were considered as the initial representation of the experimental data, while second-order relationships were evaluated where the measured response exhibited systematic curvature. The selected relationships were assessed using the residual behaviour, R^2 and RMSE, without attributing the observed curvature to a specific physical mechanism.

The titanium transducer exhibited an increase in displacement amplitude from 3.31 µm at 10 $V_{p\text{-}p}$ to 15.16 µm at 100 $V_{p\text{-}p}$. Although a linear relationship provided a strong representation of the response (R^2 = 0.9933, RMSE = 0.3160 µm), a second-order relationship further increased R^2 to 0.9978 and reduced the RMSE to 0.1830 µm. The residuals were also reduced using the second-order relationship, supporting the presence of modest curvature within the measured response. The negative second-order coefficient indicates that the rate of increase in displacement amplitude decreased slightly as excitation voltage increased. Nevertheless, the titanium configuration maintained the greatest vibration output of the four transducers across the investigated voltage range.

The aluminium transducer exhibited an overall increase in displacement amplitude from 2.98 µm at 10 $V_{p\text{-}p}$ to 10.01 µm at 100 $V_{p\text{-}p}$. A linear relationship provided a strong representation of the measured response, producing R^2 = 0.9811 and an RMSE of 0.3211 µm. Introducing a second-order term produced only a small improvement, with R^2 = 0.9823 and an RMSE of 0.3108 µm. This improvement was insufficient to justify the additional model complexity, and the aluminium response was therefore considered approximately linear over the investigated excitation range. Some point-to-point variation remained, most notably around 50–60 $V_{p\text{-}p}$, but this did not alter the overall increasing response.

The stainless steel transducer exhibited an increase in displacement amplitude from 2.52 µm at 10 $V_{p\text{-}p}$ to 11.49 µm at 100 $V_{p\text{-}p}$. A linear relationship produced R^2 = 0.9877 and an RMSE of 0.3329 µm, whereas the second-order relationship increased R^2 to 0.9977 and reduced the RMSE substantially to 0.1454 µm. The second-order relationship therefore provided a stronger representation of the measured behaviour. As observed for the titanium transducer with wire, the negative second-order coefficient indicates a gradual reduction in the rate at which displacement amplitude increased with excitation voltage. The stainless steel transducer with wire produced the second-highest maximum displacement amplitude among the four configurations.

The Nitinol transducer with wire exhibited the lowest displacement amplitudes throughout the investigated voltage range, increasing from 1.44 µm at 10 $V_{p\text{-}p}$ to 6.23 µm at 100 $V_{p\text{-}p}$. A linear relationship produced R^2 = 0.9844 and an RMSE of 0.2006 µm, while a second-order relationship increased R^2 to 0.9953 and reduced the RMSE to 0.1101 µm. The second-order relationship therefore provided a stronger representation of the measured response and captured the progressively smaller increase in displacement amplitude at the highest excitation voltages. Although the Nitinol configuration produced substantially lower vibration amplitudes than the titanium, aluminium and stainless steel configurations, the present measurements do not

independently identify the material mechanism responsible for this difference. The response represents the behaviour of the complete wire-integrated transducer and may reflect differences in structural stiffness, mechanical losses, electromechanical coupling and the interaction between the end-cap, piezoceramic elements, adhesive interfaces and Nitinol wire.

Comparison with the harmonic response measurements presented previously requires consideration of the different voltage definitions and excitation arrangements used in the two experiments. The harmonic response measurements were expressed in $V_{(\mathrm{rms})}$, whereas the continuous-excitation measurements presented here were expressed in $V_{\mathrm{p\text{-}p}}$. For a sinusoidal waveform, $V_{p\text{-}p} = 2\sqrt{2}\, V_{(rms)}$ and consequently equal numerical voltage values in the two datasets do not represent equivalent excitation levels. For example, 100 $V_{\mathrm{p\text{-}p}}$ corresponds to approximately 35.4 $V_{(\mathrm{rms})}$. A direct comparison of displacement amplitudes at equal numerical voltage values would therefore be inappropriate. In addition, the continuous-excitation measurements incorporated the impedance-matching arrangement and differed from the burst harmonic-response measurements in their excitation conditions. The performance of the matched system is consequently evaluated using the combined displacement, electrical impedance and load-power measurements rather than attributing differences in displacement amplitude solely to the matching network.

During continuous excitation, the maximum measured displacement amplitudes remained below the approximately 30 μm peak-to-peak displacement reported as the lower end of the range associated with ultrasonic hard- and soft-tissue cutting [96]. At 100 $V_{\mathrm{p\text{-}p}}$, the titanium, stainless steel, aluminium and Nitinol configurations produced maximum measured displacement amplitudes of 15.16, 11.49, 10.01 and 6.23 μm, respectively. The titanium configuration therefore provided the greatest displacement output under the investigated continuous-excitation conditions. However, these measurements were obtained over the voltage range available within the present experimental arrangement, and the results should not be interpreted as defining the maximum achievable displacement of each transducer. Further optimisation of the transducer and electrical drive system would be required to investigate operation at displacement amplitudes more representative of those reported for ultrasonic surgical devices [96].

The electrical impedance magnitude exhibited markedly different voltage-dependent behaviour between the four wire-integrated transducers (Figure 6.4).

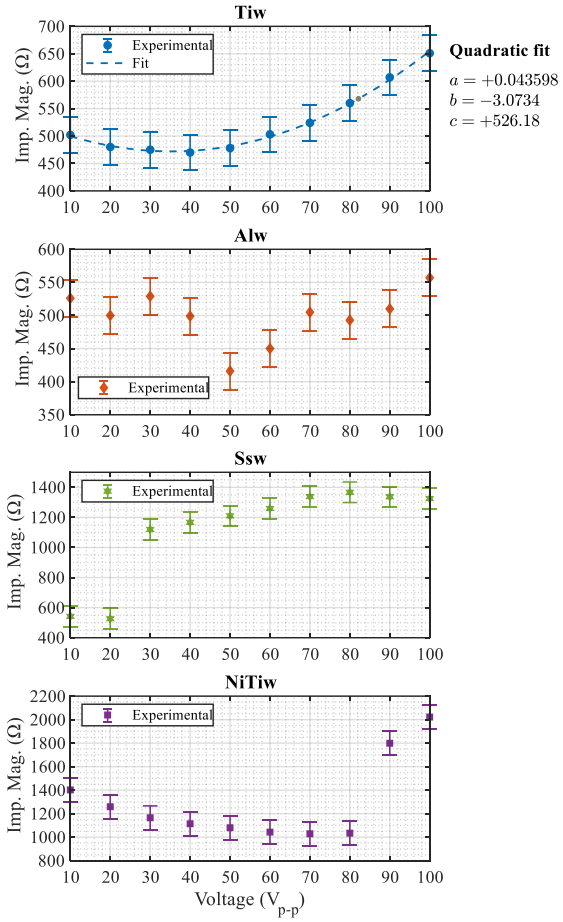


Figure 6.4 - Impedance magnitude as a function of excitation voltage for the wire-integrated transducers during continuous excitation.

For the titanium transducer with wire, the impedance decreased slightly from 502 Ω at 10 V_{p-p} to a minimum of 470 Ω at 40 V_{p-p} before increasing progressively to 651 Ω at 100 V_{p-p}. A linear relationship provided only a moderate representation of the response (R^2 = 0.7074, RMSE = 31.82 Ω), whereas a second-order relationship produced R^2 = 0.9975 and reduced the RMSE to 2.93 Ω. The second-order relationship was therefore considered more appropriate, as it captured the systematic curvature in the measured impedance response, including the transition from decreasing to increasing impedance with excitation voltage.

The change from decreasing to increasing impedance indicates that the electrical response of the assembled transducer changed with excitation level, potentially reflecting voltage-dependent changes in its electromechanical and mechanical resonance behaviour rather than a constant impedance response.

The aluminium transducer with wire exhibited comparatively limited overall variation in impedance magnitude, with values ranging between 416 and 557 Ω. Unlike the titanium

configuration, however, the measurements showed appreciable point-to-point variation and no clear global functional relationship with voltage. The linear model provided essentially no explanatory value (R^2 = 0.0102, RMSE = 37.85 Ω), while the second-order model improved the fit only to R^2 = 0.5548 with an RMSE of 25.39 Ω. Although a two-region linear model produced a further increase to R^2 = 0.6678, the remaining scatter and limited number of measurements did not provide sufficient justification for assigning distinct voltage-dependent regimes. No fitted relationship was retained for the aluminium transducer, and its behaviour is more appropriately described directly from the experimental measurements.

The stainless steel transducer with wire exhibited a pronounced increase in impedance between 20 and 30 $V_{p\text{-}p}$, from 526 to 1,120 Ω, followed by a more gradual increase to a maximum measured value of 1,367 Ω at 80 $V_{p\text{-}p}$ before decreasing slightly at higher voltages. A linear relationship produced R^2 = 0.6989 and an RMSE of 165.90 Ω, while a second-order relationship improved these values to R^2 = 0.9020 and 94.66 Ω, respectively. A two-region linear model produced only a modest further improvement (R^2 = 0.9158, RMSE = 87.76 Ω). However, the abrupt change between 20 and 30 $V_{p\text{-}p}$ and the subsequent plateau-like response were not considered adequately represented by a single global empirical relationship. No fitted curve was therefore retained. The measurements nevertheless indicate that the stainless steel configuration underwent a substantial change in electrical impedance with increasing excitation, indicating a strongly voltage-dependent electrical response of the assembled transducer.

The Nitinol transducer with wire exhibited the highest impedance magnitude over most of the investigated voltage range and a distinctly nonlinear response. Impedance decreased progressively from 1,402 Ω at 10 $V_{p\text{-}p}$ to 1,029–1,034 Ω between 70 and 80 $V_{p\text{-}p}$, before increasing sharply to 1,799 Ω at 90 $V_{p\text{-}p}$ and 2,022 Ω at 100 $V_{p\text{-}p}$. A linear relationship poorly represented this behaviour (R^2 = 0.1961, RMSE = 296.49 Ω). Although the second-order and two-region models increased R^2 to 0.8266 and 0.9006, respectively, substantial residuals remained, particularly around the high-voltage transition. No global fitting relationship was therefore retained. The sharp increase above 80 $V_{p\text{-}p}$ coincided with the high-excitation region in which the displacement amplitude exhibited a reduced rate of increase (Figure 6.3). This indicates that changes in the measured electrical and mechanical responses occurred over a similar excitation range, although the present measurements do not establish a causal relationship between them.However, the impedance measurements alone cannot establish whether this behaviour resulted specifically from stress-induced transformation of Nitinol,

resonance detuning, changes in mechanical loading, or another excitation-dependent effect within the complete transducer assembly.

The resonance-frequency response under continuous sinusoidal excitation (Figure 6.5) was dependent on the end-cap material.

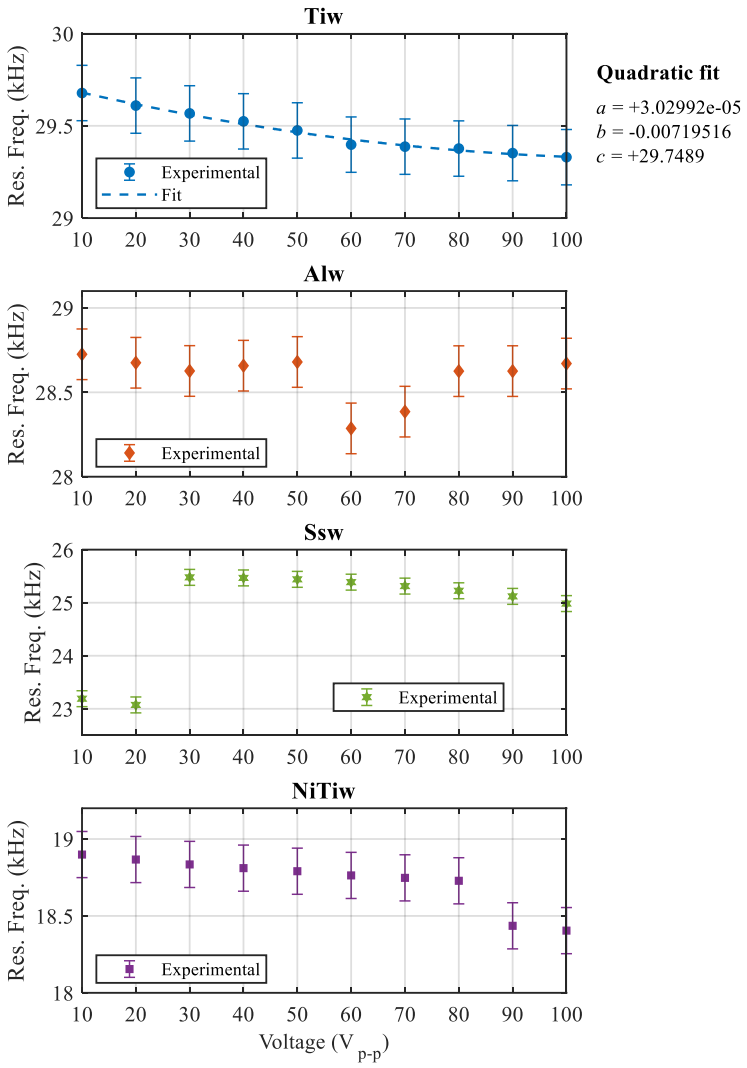


Figure 6.5 - Resonance frequency as a function of excitation voltage for the wire-integrated transducers during continuous excitation.

The titanium transducer with wire exhibited a gradual reduction in resonance frequency from 29.68 kHz at 10 $V_{p\text{-}p}$ to 29.33 kHz at 100 $V_{p\text{-}p}$. A linear relationship provided a good representation of the overall response (R^2 = 0.9518, RMSE = 24.98 Hz); however, the residuals indicated curvature in the measured response. A second-order relationship improved the coefficient of determination to R^2=0.9892 and reduced the RMSE to 11.79 Hz and was therefore

considered more appropriate. The fitted second-order relationship indicates a gradual reduction in the magnitude of the negative resonance-frequency gradient as excitation voltage increased, consistent with modest curvature in the overall measured response.

The aluminium transducer with wire exhibited comparatively small overall variation in resonance frequency but appreciable point-to-point fluctuations, particularly between 50 and 70 $V_{p\text{-}p}$. Neither the linear (R^2 =0.0703, RMSE = 130.20 Hz) nor second-order (R^2=0.3802, RMSE = 106.31 Hz) relationship adequately represented the measured response. Therefore, no global fitting function was applied. Although the resonance frequency remained within a relatively narrow overall range, the local variation indicates that its response to increasing excitation voltage was not described by a simple monotonic relationship.

The stainless steel transducer with wire exhibited the most pronounced voltage-dependent variation. The resonance frequency decreased slightly from 23.19 kHz at 10 $V_{p\text{-}p}$ to 23.07 kHz at 20 $V_{p\text{-}p}$, before increasing abruptly to 25.48 kHz at 30 $V_{p\text{-}p}$. Above this excitation level, the resonance frequency gradually decreased, reaching 24.98 kHz at 100 $V_{p\text{-}p}$. A linear relationship provided a poor representation of the complete response (R^2=0.3210, RMSE = 726.18 Hz), while the second-order relationship improved the fit (R^2 =0.7482, RMSE = 442.23 Hz) but did not adequately represent the abrupt transition between 20 and 30 $V_{p\text{-}p}$. No global fit was therefore retained. The 2.41 kHz increase between 20 and 30 $V_{p\text{-}p}$ represents a distinct change in the measured resonance response rather than a minor point-to-point fluctuation. The present measurements demonstrate the change clearly, although they do not independently establish its underlying mechanism.

The Nitinol transducer with wire exhibited a gradual reduction in resonance frequency from 18.90 kHz at 10 $V_{p\text{-}p}$ to 18.73 kHz at 80 $V_{p\text{-}p}$, followed by a decrease to 18.44 kHz at 90 $V_{p\text{-}p}$ and 18.40 kHz at 100 $V_{p\text{-}p}$. The linear relationship produced R^2=0.7796 and an RMSE of 76.05 Hz, while the second-order relationship improved these values to R^2= 0.8985 and 51.61 Hz, respectively. Nevertheless, neither global relationship adequately represented the distinct change observed at the highest excitation levels, and no global fit was therefore retained. The measured response instead indicates that the Nitinol transducer with wire maintained comparatively small resonance-frequency variation up to approximately 80 $V_{p\text{-}p}$, followed by increased frequency sensitivity at the highest excitation voltages.

Overall, the results demonstrate that resonance-frequency behaviour under continuous excitation cannot be characterised as uniformly stable across all four transducers. The titanium transducer with wire exhibited a smooth and comparatively predictable nonlinear reduction in resonance frequency, whereas the aluminium transducer with wire showed relatively small but

irregular fluctuations. The stainless steel transducer with wire exhibited a distinct transition between 20 and 30 $V_{p\text{-}p}$, while the Nitinol transducer with wire showed a more pronounced reduction above 80 $V_{p\text{-}p}$. These differences indicate that the voltage-dependent resonance response differed according to the complete transducer configuration and end-cap material. These results should therefore be interpreted alongside the corresponding displacement-amplitude and electrical-impedance measurements, particularly where changes occurred over similar excitation-voltage intervals. However, the present measurements do not independently establish the mechanisms responsible for these changes or their specific relationship to the impedance-matching arrangement.

The load power generally increased with excitation voltage for the four transducers with wires (Figure 6.6), although the form and magnitude of the response differed between configurations.

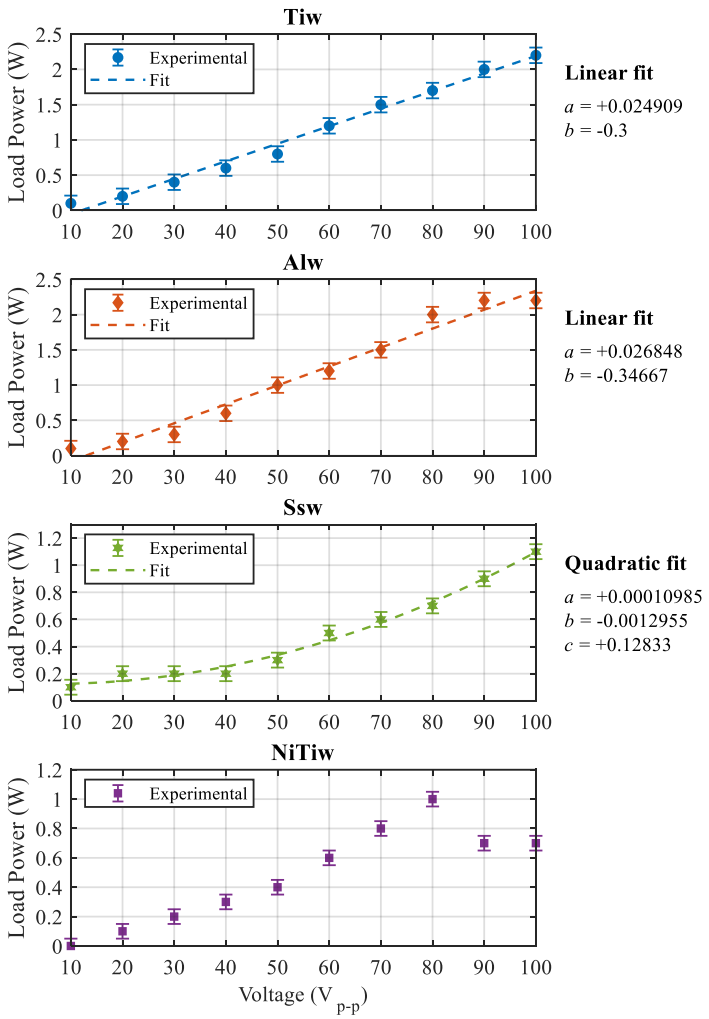


Figure 6.6 - Load power as a function of excitation voltage for the wire-integrated transducers during continuous excitation.

The titanium transducer with wire exhibited a progressive increase from 0.10 W at 10 $V_{p\text{-}p}$ to 2.20 W at 100 $V_{p\text{-}p}$. A linear relationship provided a strong representation of the measured response (R^2 = 0.9880, RMSE = 0.079 W), with a gradient of 0.0249 W/$V_{p\text{-}p}$. Although a second-order relationship produced a slightly higher R^2 of 0.9927 and lower RMSE of 0.061 W, the improvement was small and did not justify the additional model complexity. The linear relationship was therefore retained, indicating an approximately linear increase in the electrical power delivered to the load as excitation voltage increased.

The aluminium transducer with wire similarly exhibited an overall increase in load power, from 0.10 W at 10 $V_{p\text{-}p}$ to 2.20 W at 90–100 $V_{p\text{-}p}$. The linear relationship produced R^2 =0.9747 and an RMSE of 0.124 W, with a gradient of 0.0268 W/$V_{p\text{-}p}$. Application of a second-order relationship provided only a marginal improvement (R^2 = 0.9765, RMSE = 0.120 W), and the linear relationship was therefore considered sufficient to represent the overall response. The measured values nevertheless show that load power levelled at 2.20 W between 90 and 100 $V_{p\text{-}p}$, indicating that the approximately linear increase observed over most of the investigated range was not maintained at the highest excitation level.

The stainless steel transducer with wire exhibited lower load power than the titanium and aluminium configurations throughout the investigated voltage range, increasing from 0.10 W at 10 $V_{p\text{-}p}$ to 1.10 W at 100 $V_{p\text{-}p}$. Unlike the titanium and aluminium transducers with wire, the response exhibited appreciable positive curvature. A linear relationship produced R^2 =0.9268 and an RMSE of 0.087 W, whereas the second-order relationship increased the coefficient of determination to R^2 =0.9883 and reduced the RMSE to 0.035 W. The second-order relationship was therefore considered more appropriate for representing the measured response. The positive curvature of the fitted second-order relationship indicates that the rate of increase in measured load power became greater as excitation voltage increased, consistent with a nonlinear trend over the investigated voltage range.

The Nitinol transducer with wire exhibited the lowest and most distinctly non-monotonic load-power response. Load power increased from approximately 0 W at 10 $V_{p\text{-}p}$ to a maximum measured value of 1.00 W at 80 $V_{p\text{-}p}$, before decreasing to 0.70 W at both 90 and 100 $V_{p\text{-}p}$. A linear relationship provided R^2=0.8148 and an RMSE of 0.134 W, while a second-order relationship improved these values to R^2=0.8714 and 0.112 W, respectively. However, neither relationship adequately represented the increase to 80 $V_{p\text{-}p}$ followed by the subsequent reduction, and no global fitting function was therefore retained. The decrease in load power above 80 $V_{p\text{-}p}$ coincided with changes in the displacement-amplitude, electrical-impedance and resonance-frequency responses of the Nitinol transducer with wire at the highest excitation

levels. This correspondence indicates a change in the behaviour of the complete electromechanical system, although the present measurements do not independently establish whether this originated from the Nitinol material response, electrical matching, structural interactions, or a combination of these effects.

Overall, the titanium and aluminium transducers with wire exhibited the greatest load powers and approximately linear increases over most of the investigated excitation range, whereas the stainless steel transducer with wire exhibited a lower but increasingly nonlinear response. The Nitinol transducer with wire exhibited substantially lower load power and exhibited a distinct reduction above 80 $V_{p\text{-}p}$. When considered alongside the displacement-amplitude results, the higher load power of Tiw was accompanied by the highest measured displacement amplitude, reaching 15.16 μm at 100 $V_{p\text{-}p}$, whereas the Nitinol transducer with wire exhibited both lower load power and lower displacement amplitude. These results demonstrate that the measured load power and resulting vibration response varied with the complete transducer configuration, highlighting the importance of evaluating electrical power and displacement amplitude together when comparing transducer performance.

6.3. Cutting tests using the Nitinol wire

All cutting tests were conducted using the transducers incorporating Nitinol wires and operated in a handheld configuration intended to provide an initial assessment of cutting performance under representative operating conditions. The transducers were supported at the protruding flange regions of the end-caps to minimise interference with the vibrating wire and maintain a consistent cutting orientation. All wire-integrated transducers were tested on a bone-mimicking material (20 PCF solid foam blocks, Sawbones®, USA), which possesses bulk mechanical properties comparable to trabecular bone.

A single cutting trial was performed for each transducer configuration and each device was driven continuously for a duration of 350 seconds. This duration was selected to provide a sufficiently long and repeatable cutting interval for assessing sustained cutting behaviour, resonance tracking performance, and operational stability under continuous excitation. During testing, the wire penetrated the Sawbones specimen at a shallow oblique angle relative to the sample surface. This orientation was maintained visually throughout each experiment. Material removal occurred through repeated wire-material interaction driven by the longitudinal vibration of the transducer, resulting in progressive penetration of the specimen. Although minor variations in contact angle and applied force are unavoidable during practical operation, care was taken to maintain a consistent cutting approach across all tests.

During each cutting experiment, the electrical impedance, phase, resonance frequency, and load power were continuously monitored throughout the 350-second cutting period, as shown in Figure 6.7. These parameters were recorded to assess how sustained cutting influences the electromechanical behaviour of the transducer under representative operating conditions. The electrical impedance and phase provide insight into changes in electrical loading and electromechanical coupling during cutting, while the resonance frequency reflects changes in the dynamic response of the transducer arising from interaction with the specimen. Load power was monitored to quantify the electrical demand required to maintain cutting and to assess transducer stability during prolonged operation.

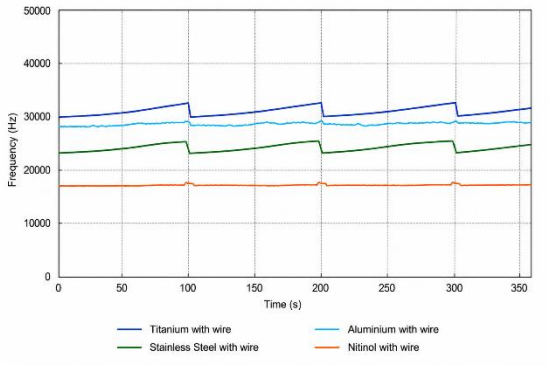
The cutting experiments presented here are subject to several limitations that should be considered when interpreting the results. The applied cutting force and cutting velocity were not independently measured or actively controlled, as no dedicated force-sensing or motion-tracking system was available and the experiments were performed using a manually guided cutting approach. The cutting depths presented in Figure 6.9 represent cumulative penetration achieved over a fixed cutting duration rather than a direct measure of instantaneous cutting efficiency. Future studies incorporating real-time force measurement, controlled feed rates, and depth monitoring would enable a more quantitative assessment of cutting mechanics and transducer performance.

A further limitation relates to the method used to support the transducer during cutting. Supporting the transducer at the flange regions may have influenced the boundary conditions of the system and introduced operator-dependent variability into the measured response. From both a repeatability and laboratory best-practice perspective, this method does not provide the well-defined support conditions that would be expected in a dedicated experimental setup. Future investigations should therefore employ a purpose-designed fixture or holder, such as a custom 3-D-printed support, to provide a safer, more repeatable, and better-defined boundary condition while minimising operator influence on the measured transducer behaviour.

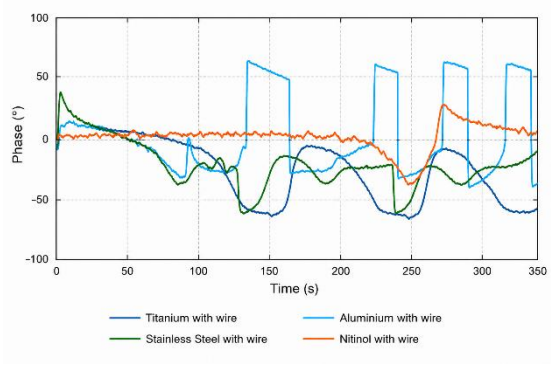
In addition, only a single cutting trial was performed for each transducer configuration and repeatability across multiple trials was not assessed. Owing to the time constraints associated with the scope and duration of the study, the cutting experiments were limited to one test per transducer configuration. The primary objective of these experiments was therefore to provide an initial comparative assessment of transducer behaviour during cutting rather than a statistically rigorous evaluation of cutting performance. During each experiment, the resonance

frequency, electrical impedance, phase, and load power were recorded simultaneously by the resonance tracking system, ensuring that all measured parameters corresponded to the same cutting event and operating conditions. The resonance frequency, impedance, phase, and load power responses presented in this chapter should be interpreted as representative comparative case studies rather than statistically validated performance trends. Repeated testing using multiple transducers and specimens would be required to quantify experimental variability, assess repeatability, and establish statistical confidence in the observed differences between transducer configurations.

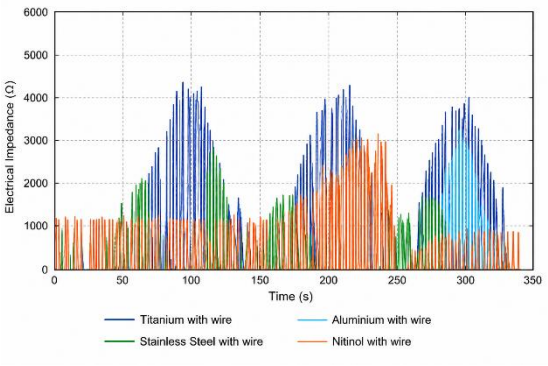
The present study also did not investigate the influence of wire geometry, wire diameter, wire length, irrigation conditions, transducer casing, or alternative end-effector designs. These factors may influence energy transmission, thermal behaviour, cutting efficiency, and device handling characteristics, and therefore warrant further investigation during future optimisation and device development studies. Despite these limitations, the experiments provide valuable comparative insight into the cutting behaviour and electrical response of wire-integrated flextensional transducers and establish a foundation for future investigations into Nitinol-based ultrasonic surgical devices.



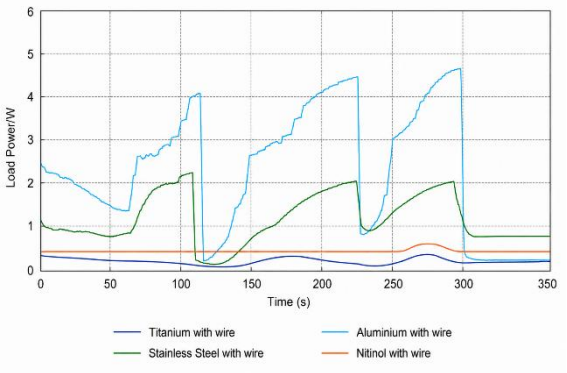
(a) Resonance frequency against time.



(b) Electrical phase against time.



(c) Electrical impedance against time.



(d) Load power against time.

Figure 6.7 - Parameters varying with time.

Figure 6.7a shows the resonance frequency measured continuously over 350 seconds for the four transducers with wire during cutting tests. The Nitinol and aluminium transducers with wires exhibit comparatively smooth frequency traces with only gradual variations over time, whereas the titanium and stainless steel transducers with wires show intermittent step-like changes in resonance frequency. These features occur at discrete time points rather than as continuous drift and are indicative of transient changes in the coupled electromechanical system during cutting.

For the titanium and stainless steel transducers with wires, the observed step changes in resonance frequency are attributed to brief changes in the effective mechanical and electrical loading at the wire–sample interface. As cutting progresses, intermittent changes in contact conditions, such as local engagement or release of material at the wire tip, alter the effective boundary conditions of the transducer–wire system. These changes are reflected as short-duration shifts in resonance frequency before the driver re-establishes operation close to the dominant vibration mode. This behaviour is more evident for titanium and stainless steel

transducers with wires, which both operate at higher resonance frequencies and higher vibration amplitudes, making them more sensitive to small changes in loading during cutting.

The Nitinol and aluminium transducers with wires show more stable resonance frequency traces with minimal abrupt changes. For the Nitinol transducer with wire, this behaviour is associated with its SMA characteristics, where deformation of the wire involves stress-induced microstructural mechanisms that allow the system to accommodate changes in loading without sharp changes in resonance frequency. The aluminium transducer with wire similarly exhibits a smoother frequency response, likely due to its reduced sensitivity to short-duration variations at the cutting interface under the same excitation conditions.

The Nitinol transducer with wire exhibits an electrical phase close to 0° for most of the cutting duration (Figure 6.7b), indicating that the system remains near resistive operation throughout the test. This behaviour suggests that the combined electromechanical system comprising the transducer, wire, and cutting interaction maintains a stable balance between stored and transferred energy, with minimal reactive dominance. The Nitinol transducer with wire undergoes stress-induced internal reconfiguration rather than abrupt elastic unloading, which results in a smooth and self-regulated electromechanical response under continuous excitation. The phase remains tightly clustered around zero, reflecting stable power transfer despite variations in mechanical interaction during cutting.

The titanium and stainless steel transducers with wires display repeatable phase minima characterised by sharp, narrow transitions in phase angle. These features correspond to periodic shifts in the electrical operating point caused by transient changes in the mechanical boundary conditions at the wire–material interface. As the wire intermittently engages, releases, or advances through the sample, the effective mechanical load reflected back to the transducer changes, temporarily altering the balance between reactive and resistive components of the electrical impedance. The repeatability of these phase excursions indicates a consistent cutting–engagement cycle rather than random instability, with titanium and stainless steel being more sensitive to these load variations due to their elastic response and stronger mechanical coupling to the wire.

The aluminium transducer with wire exhibits a distinctly different phase response, characterised by a small number of discrete plateau-like regions separated by abrupt transitions. These step-like phase segments indicate periods of quasi-steady electrical loading, punctuated by rapid changes when the cutting condition shifts. This behaviour suggests that the aluminium

transducer with wire alternates between a limited number of stable interaction states during cutting, likely due to its lower stiffness and higher compliance, which allow the wire–sample interaction to settle temporarily before transitioning to the next engagement condition.

The electrical impedance measurements (Figure 6.7c) further differentiate the transducers under cutting conditions. Titanium and stainless steel transducers with wires displays impedance maxima at repeatable time intervals. These maxima occur when the system operates closer to its effective electromechanical resonance under load, where mechanical energy transfer from the piezoelectric plate to the wire is most efficient. As the cutting interaction evolves, periodic changes in contact conditions cause the operating point to pass through these low-impedance states, producing the observed maxima.

The aluminium and Nitinol transducers with wires do not exhibit pronounced impedance maxima during cutting. For the aluminium transducer with wire, this suggests that the wire–material interaction does not drive the system sufficiently close to resonance during cutting to produce distinct impedance dips, leading to a more uniform electrical loading of the driver. The absence of sharp impedance features indicates a more gradual redistribution of electrical energy rather than discrete resonance-dominated events. For the Nitinol transducer with wire, the absence of distinct maxima is attributed to its mechanical response, where stress-induced phase accommodation alters the effective stiffness continuously during cutting. This results in a broader and more uniform impedance profile rather than discrete maxima.

The load power responses (Figure 6.7d) consolidate the trends observed in resonance frequency, phase, and impedance. Titanium, aluminium, and stainless steel transducers with wires exhibit step-like variations and local minima in load power, corresponding to the transient events seen in the other electrical parameters. These features indicate periods where the electrical power drawn from the driver changes abruptly due to short-duration shifts in impedance and phase as the wire interacts with the cutting medium. The Nitinol transducer with wire displays an almost constant load power throughout the cutting interval, with only a minor variation between approximately 255 to 292 seconds. This indicates that, despite ongoing cutting interaction, the electrical demand of the Nitinol transducer with wire remains largely unaffected by transient mechanical disturbances. The stable load power confirms that the Nitinol transducer with wire maintains a consistent electromechanical energy exchange with the driver during cutting, whereas the metallic end-cap systems exhibit stronger coupling between mechanical load fluctuations and electrical power consumption.

Taken together, the time-resolved measurements demonstrate that titanium and stainless-steel transducers with wires respond to cutting-induced load variations with repeatable, short-duration excursions in resonance frequency, phase, impedance, and load power. The aluminium transducer with wire shows intermediate behaviour characterised by discrete transitions rather than sharp excursions. The Nitinol transducer with wire, exhibits the most stable electrical and frequency response during cutting, with minimal transient features across all measured parameters. These results highlight the importance of material-dependent electromechanical interaction in wire-based ultrasonic cutting and show that stable cutting operation can be achieved either through effective driver tracking or through intrinsic material response to transient mechanical loading.

6.4. Assessment of cutting penetration in Sawbones material

This section evaluates the cutting penetration achieved by the flextensional transducers with wire during cutting tests. The primary objective of this analysis is to quantify the depth of penetration produced over a fixed cutting duration and to relate this outcome to the dynamic electrical and mechanical behaviour observed during the cutting tests. Cutting depth provides a physical metric of cutting effectiveness in ultrasonic surgical devices. For a fixed excitation condition and cutting duration, greater penetration depth indicates more efficient transfer of vibrational energy from the transducer–wire system into the bone-mimic. In the context of surgical applications, penetration depth is relevant because it reflects the device's ability to advance through material under sustained operation, rather than only achieving high vibration amplitudes in free boundary conditions.

Post-test analysis was conducted to visualise and compare the penetration depths produced by each transducer with wire. The Sawbones samples were sectioned (Figure 6.8) to expose the cut regions corresponding to each transducer, enabling a comparative assessment of cutting penetration.

The cutting depth in the Sawbones sample was measured using a scanning electron microscope (SEM), using the Zeiss Sigma VP field-emission scanning electron microscope (FE SEM). The secondary electron (SE) detector was used for imaging the Sawbones samples. The samples were coated with a conductive coating (Au-80 %; Pd- 20%) with a thickness of 10 nm. Aluminium tape was attached at the cut sites. SEM was conducted in high vacuum and high current conditions with an accelerating voltage of 5 kV. The SEM distance was 8.7 mm with

an aperture size of 30 µm. The tilt angle was set to 70 °. Figure 6.9 gives the SEM images of the four Sawbones samples.

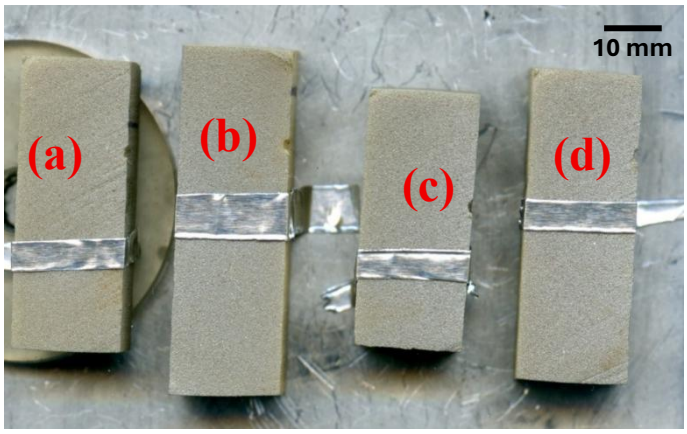
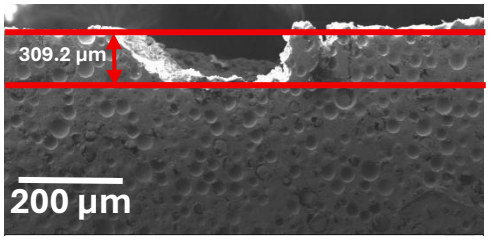
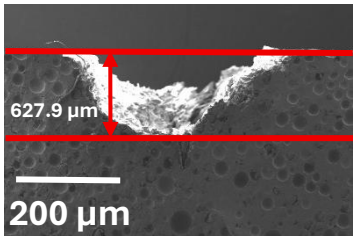


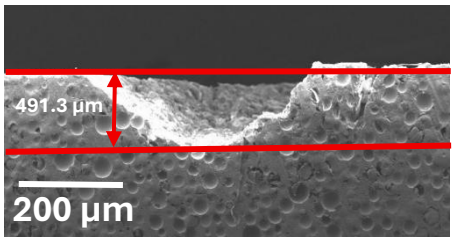
Figure 6.8 – Sawbones samples prepared for SEM. (a) Sawbones sample for aluminium transducer with wire. (b) Sawbones sample for Nitinol transducer with wire. (c) Sawbones sample for titanium transducer with wire. (d) Sawbones sample for stainless steel transducer with wire.



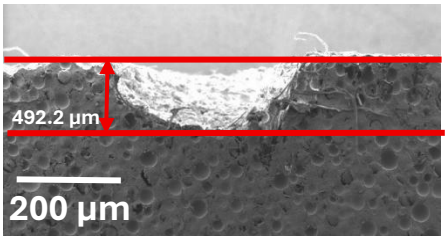
(a) SEM image of Sawbones sample following cutting with aluminium transducer with wire.



(b) SEM image of Sawbones sample following cutting with Nitinol transducer with wire.



(c) SEM image of Sawbones sample following cutting with Titanium transducer with wire.



(d) SEM image of Sawbones sample following cutting with Stainless steel transducer with wire.

Figure 6.9 - SEM images showing cut depths created by flextensional transducers with wires.

Post-test SEM analysis of the Sawbones specimens (Figure 6.9) revealed clear differences in cutting performance between the wire-integrated transducers. The Nitinol transducer with wire produced the greatest cutting depth (627.9 μm), followed by the stainless steel transducer with wire (492.2 μm) and the titanium transducer with wire (491.3 μm), while the aluminium transducer with wire produced the shallowest penetration (309.2 μm). These results demonstrate that the transducer configurations could produce material removal within the Sawbones samples and highlight the influence of end-cap material on cutting performance. Among the investigated configurations, the Nitinol transducer with wire exhibited the greatest penetration depth, indicating the most effective cumulative material removal over the 350-second cutting interval.

The cutting depth results were consistent with the electromechanical behaviour observed during continuous cutting. The Nitinol transducer with wire exhibited the most stable dynamic response throughout the cutting interval, maintaining comparatively stable resonance frequency, electrical impedance, load power, and near-zero phase conditions (Figure 6.7). Maintaining operation close to resonance promotes efficient energy transfer to the cutting interface and reduces losses associated with off-resonance operation. The titanium and stainless steel transducers with wires exhibited greater fluctuations in their electrical responses during cutting, while the aluminium transducer with wire demonstrated the lowest overall cutting performance. These observations suggest that sustained resonance stability and efficient energy transfer are important factors governing cumulative material removal during ultrasonic cutting.

Despite the relative differences observed between the transducers, the absolute cutting depths achieved after 350 seconds of continuous excitation were low, with all devices producing sub-millimetre penetration into the Sawbones material. The present study should be regarded as a proof-of-concept demonstration of cutting capability rather than a clinically representative assessment of surgical performance. The results highlight that there remains a substantial development pathway between demonstrating a functional laboratory concept and translating such technology into a practical surgical device. Future optimisation will likely require improvements in transducer design, wire geometry, end-effector configuration, irrigation systems, device packaging, and overall energy transfer efficiency to achieve clinically relevant cutting rates.

Several limitations should be considered when interpreting the cutting results. The experiments were performed using a manually guided cutting approach, with the applied cutting force and cutting velocity neither measured nor actively controlled. Only a single cutting trial was performed for each transducer configuration owing to the time constraints associated with the

scope and duration of the present study. As the Nitinol transducer with wire was tested later in the experimental programme, increasing operator familiarity with the cutting procedure may have influenced factors such as wire positioning, sample engagement, and applied force. A component of the observed differences in cutting depth may reflect operator-dependent effects in addition to intrinsic differences between the transducer configurations. Future investigations employing dedicated support fixtures, automated force control, and repeated cutting trials would therefore be beneficial for establishing repeatability and isolating the contribution of transducer performance from operator variability.

Nevertheless, the results demonstrate that Nitinol wire integration is feasible and can influence the cutting behaviour of flextensional ultrasonic transducers. The comparatively higher cutting depth and stable electromechanical response exhibited by the Nitinol transducer with wire suggest that shape memory alloy components may offer advantages for future ultrasonic surgical devices. The findings presented in this chapter provide an initial foundation for the continued development and optimisation of Nitinol-integrated ultrasonic cutting systems.

6.5. Summary

This chapter evaluated the performance of wire-integrated class IV flextensional transducers under continuous excitation and cutting conditions. Impedance matching enabled stable resonant operation, while the end-cap material influenced the displacement amplitude, electrical response and cutting behaviour of the transducers. Although all transducer configurations were capable of producing material removal in the Sawbones specimens, clear material-dependent differences in performance were observed. Among the investigated configurations, the Nitinol transducer with wire exhibited the most stable electromechanical response during cutting and achieved the greatest penetration depth.

The findings demonstrate that integrating a Nitinol wire into flextensional ultrasonic transducers is a feasible approach for ultrasonic cutting applications and highlight the importance of material selection in determining operational stability and cutting performance. While further optimisation is required before clinical implementation, the results provide a foundation for the continued development of Nitinol-integrated ultrasonic surgical devices.

Chapter 7

Conclusions and future work

7.1. Conclusions

The primary aim of this research was to investigate whether the Nitinol SMA could be integrated into the class IV flextensional ultrasonic transducers and whether the unique thermomechanical behaviour of Nitinol could be exploited to influence transducer performance. The work presented in this thesis demonstrates that Nitinol can be successfully incorporated into class IV flextensional ultrasonic transducers both as an end-cap material and as a wire attachment. Numerical modelling, electrical impedance analysis, harmonic response testing, temperature characterisation, material characterisation, and cutting experiments confirmed the technical feasibility of integrating Nitinol into flextensional ultrasonic transducer structures. The resulting devices exhibited stable operation over a range of electrical and thermal conditions, demonstrating that SMAs can be incorporated into the class IV flextensional architecture.

However, the principal motivation for incorporating Nitinol was not solely to demonstrate feasibility but to investigate whether the material's phase transformation behaviour could be utilised to influence resonance characteristics and potentially enable frequency-tuneable ultrasonic devices [27-30]. In this respect, the findings were more complex than originally anticipated. Although the Nitinol transducers exhibited distinctive temperature-dependent behaviour that differed from the titanium, aluminium, and stainless steel transducers, the thermally induced resonance frequency shift reported previously for Nitinol-based cymbal transducers was not observed [27-30]. Increasing the A_F temperature from 35 °C to 45 °C did not produce a fundamentally different qualitative response. These findings indicate that the relationship between Nitinol phase transformation behaviour and transducer resonance characteristics is more complex than originally hypothesised and cannot be explained solely by transformation temperature.

The findings indicate that transformation behaviour occurring within the Nitinol material does not necessarily translate directly into a measurable shift in transducer resonance frequency. Although DSC confirmed phase transformation behaviour within both the Nitinol end-caps and wires, the corresponding transducers did not exhibit the anticipated resonance tuning response. Several factors may have contributed to this behaviour, including residual stresses introduced

during wire-EDM manufacturing, geometric constraints associated with the flextensional transducer structure, and the unknown thermomechanical processing history of the Nitinol sheets before machining. Transformation temperature alone appears insufficient to provide controllable resonance tuning within the transducer architectures investigated in this study. Achieving practical frequency tuning is likely to require stronger coupling between the material transformation and the dominant vibration mode than was achieved through either the end-cap or wire-integration approaches investigated in this work.

Despite the absence of active frequency tuning, the research identified several characteristics of Nitinol that may be advantageous for future ultrasonic devices. Across the temperature studies, the Nitinol transducers generally exhibited greater resonance-frequency stability than the corresponding titanium, aluminium and stainless steel devices. The reduced sensitivity of resonance frequency to temperature variation suggests that Nitinol may provide benefits in applications where stable resonance behaviour is required over prolonged operating periods. In practical ultrasonic surgical systems, maintaining stable resonance behaviour may contribute to consistent vibration output and predictable cutting performance. The enhanced thermal stability observed in the Nitinol transducers may represent a significant advantage for future device development.

The wire-integrated transducers provided further insight into the practical application of Nitinol within ultrasonic systems. Although the anticipated transformation-driven resonance shift was again not observed, the Nitinol transducer with wire demonstrated the greatest cutting depth and one of the most stable electromechanical responses during sustained operation. The ability of the Nitinol transducer with wire to maintain comparatively stable resonance frequency, impedance, load power, and near-zero phase conditions during cutting suggests that resonance stability may play an important role in sustained material removal. However, the cutting depths achieved in the present study remained relatively small, with all transducers producing sub-millimetre penetration depths after 350 seconds of operation. These results indicate that substantial further optimisation would be required before such devices could be considered viable surgical instruments. The cutting studies should be regarded as proof-of-concept demonstrations of functionality rather than clinically representative assessments of cutting performance.

While the present work demonstrates that Nitinol can be integrated into class IV flextensional ultrasonic transducers, technical feasibility alone does not necessarily justify its adoption within practical ultrasonic surgical devices. Nitinol introduces increased material cost, more complex manufacturing and machining requirements [23,34], and additional variability arising

from thermomechanical processing and phase transformation behaviour [21,28]. Direct substitution of conventional metallic end-caps with Nitinol cannot presently be justified solely based on frequency tuneability.

The findings also provide important insight into the broader question of whether a single ultrasonic transducer capable of controlled frequency adjustment is a realistic objective. The absence of measurable transformation-driven resonance tuning does not necessarily imply that the concept itself is unachievable; rather, it suggests that the present implementation did not provide sufficient mechanical coupling between the Nitinol phase transformation and the dominant vibration mode of the transducer. In the designs investigated here, Nitinol functioned primarily as a structural component, with any local stiffness changes associated with the material transformation having insufficient influence to produce a clearly identifiable transformation-driven change in the global dynamic behaviour of the assembled device. Future frequency-tuneable transducers will require architectures specifically designed to amplify the influence of the phase transformation on resonance [200]. This may be achieved by positioning active SMA elements within regions of high modal strain, incorporating localised thermally activated tuning mechanisms, or developing hybrid structures in which Nitinol actively modifies the effective stiffness or boundary conditions of the vibrating system [200]. Such approaches would enable the material transformation to exert a significantly greater influence on the resonant response than was achieved in the present investigation.

7.2. Future work

Future investigations should explore alternative methods of integrating SMAs into ultrasonic transducers, including localised Nitinol actuation regions, actively heated inserts, hybrid structures, and geometries specifically designed to amplify transformation-induced stiffness changes. Such approaches may provide a more direct mechanism for controlling resonance behaviour than the end-cap and wire-integration strategies investigated in this thesis.

A key requirement for future studies will be the development of a dedicated thermal control system capable of rapidly and accurately controlling the temperature of the active Nitinol component during transducer operation. The present work relied on environmental temperature control, which provided valuable insight into temperature-dependent behaviour but did not permit real-time active tuning. A closed-loop thermal control system incorporating temperature feedback and resonance tracking could enable direct investigation of whether controlled phase transformation can be used to modify resonance characteristics during operation. Such a

platform would provide a more rigorous assessment of the feasibility of frequency-tuneable ultrasonic devices.

The findings of this thesis also highlight the importance of understanding material processing history when integrating Nitinol into ultrasonic devices. The thermomechanical history of the Nitinol sheets used in this study prior to wire-EDM machining was not fully known, and residual stresses introduced during manufacturing may have influenced the observed transducer behaviour. Future studies should incorporate comprehensive material traceability and characterisation before and after manufacturing processes. Attention should be given to the effects of machining, heat treatment, and cyclic loading on the transformation behaviour of the material and its subsequent influence on transducer performance.

Alternative SMAs may also warrant investigation. Materials such as Ni-Ti-Cu, Cu-Al-Ni, and Ni-Ti-Hf [7,12] possess different transformation characteristics, thermal hysteresis behaviour, and operating temperature ranges that may provide advantages for specific ultrasonic applications. Comparative studies would help establish whether alternative SMAs offer improved controllability, durability, or thermal responsiveness within flextensional transducer architectures.

Future work should also focus on improving the cutting performance of wire-integrated transducers. The cutting studies demonstrated proof-of-concept functionality; however, the cutting depths achieved remained very small and substantial optimisation is required before clinical translation could be considered. Future investigations should examine alternative wire geometries, wire diameters, end-effector configurations, irrigation systems, fixture-based support methods, and automated force control to improve cutting efficiency and establish repeatable performance metrics.

As development progresses towards clinical applications, future research should be conducted within a framework consistent with the principles of ISO 13485. ISO 13485 is the internationally recognised quality management standard for medical device development and emphasises risk management, process control, traceability, validation, and design verification [191]. The present study demonstrated that factors such as manufacturing history, machining processes, assembly methods, and testing procedures can significantly influence device behaviour. The implementation of ISO 13485 principles from the early stages of device development would improve reproducibility, support design verification, and strengthen the pathway towards regulatory approval and clinical translation of SMA-based ultrasonic surgical devices.

References

[1] F. Anyaegbunam, "Vibrations, waves and sounds", Solid Rock Press & Publishers, Sept. 2013. ISBN: 978-978-935-377-5.

[2] J. Gallego-Juaréz and K. Graff, "Power ultrasonics: applications of high-intensity ultrasound", Woodhead Publishing (Elsevier), 2015, doi:10.1016/C2014-0-01494-6.

[3] M. Lucas, A. Cardoni, E. McCulloch, G. Hunter and A. MacBeath, “Applications of power ultrasonics in engineering,” Proceedings of the Institution of Mechanical Engineers, Part C: Journal of Mechanical Engineering Science, vol. 219, no. 10, pp. 111–122, 2005, doi:10.1243/095440605X33021.

[4] X. Li, T. Stritch and M. Lucas, "Design of miniature ultrasonic surgical devices," 2019 IEEE International Ultrasonics Symposium (IUS), Glasgow, pp. 2641-2644,2019, doi: 10.1109/ULTSYM.2019.8926096.

[5] R. Cleary, X. Li, M. Lucas. “Incorporating direct metal laser sintered complex shaped Ti-6Al-4V components in ultrasonic surgical devices”. Journal of the Acoustical Society of America, 150(3),2163-2173,2021, doi:10.1121/10.0006379.

[6] D. Broughton, A. Welling, E. Monroe, K. Pirozzi, J. Schulte, and J. Clymer, “Tissue effects in vessel sealing and transection from an ultrasonic device with more intelligent control of energy delivery,” Med. Devices: Evidence Res., vol. 6, pp. 151–154, Sep. 2013.

[7] D. Kapoor. “Nitinol for medical applications: A brief introduction to the properties and processing of nickel-titanium shape memory alloys and their use in stents”. pp. 66–76,2017, doi: https://dx.doi.org/10.1595/205651317X694524.

[8] G.F. Andreasen and T.B. Hilleman “An evaluation of 55 substituted Nitinol wire for use in orthodontics.” The Journal of the American Dental Association, vol. 82, no. 6, pp. 1373-75, 1971.

[9] T.Duerig and K. Melton. “The history of our industry.” The International Conference on Shape Memory and Superelastic Technologies (SMST)., May 2015.

[10] C. Trepanier, T.K. Leung, M. Tabrizian, L.H. Yahia, J.G. Bienvenu, J.F.Tanguay, D.L. Piron and L. Bilodeau “Preliminary investigation of the effects of surface treatments on biological response to shape memory NiTi stents.” Journal of Biomedical Research, vol. 48, no. 2, pp. 165-71, 1999.

[11] S. A. Thompson," An overview of nickel-titanium alloys used in dentistry", International Endodontic Journal, vol. 33, no. 4, pp. 297-310, 2000.

[12] P.K. Kumar and D.C. Lagoudas. “Introduction to shape memory alloys.” Shape Alloys – Modelling and Engineering Applications, Springer, 2008.

[13] J.W. Mwangi, L.T. Nguyen, V.D. Bui, T. Berger, H.Zeidler and A.Schubert “Nitinol manufacturing and micromachining: a review of processes and their suitability in processing medical-grade nitinol”. Journal of Manufacturing Processes, no. 3, pp. 355-369, 2019.

[14] G. Welsch, “Ni-Ti shape memory alloys.” Materials Properties Handbook: Titanium Alloys, Materials Park, OH: ASM International, pp. 1035–48, 1994.

[15] A. S. Paula, J.P.H.G. Canejo, R.M.S. Martins and F.M. Braz Fernandez “Effect of thermal cycling on the transformation temperature ranges of a Ni-Ti memory alloy.” Journal of Materials Science and Engineering: A, vol. 378, pp. 92–96,2004.

[16] D. Stöckel, “Nitinol - a material with unusual properties,” Endovascular Update, no. 1, pp. 1–8, 1998.

[17] L.G. Machado and M.A. Savi. “Medical applications of shape memory alloys.” Brazilian Journal of Medical and Biological Research, vol. 36, pp. 683–91, 2003.

[18] A.Feeney and M.Lucas. “Smart cymbal transducers with Nitinol end caps tuneable to multiple operating frequencies.” IEEE Transactions on Ultrasonics, Ferroelectrics and Frequency Control, vol. 61, no. 10, pp. 1709–19,2014.

[19] O.E. Ozbulut, S. Hurlebaus and R. Descroches, “Seismic response control using shape memory alloys: A review,” Journal of Intelligent Material Systems and Structures, vol. 22, no. 14, pp. 1531–1549, 2011, doi: https://10.1177/1045389X11411220.

[20] S.Parvizi, S.M. Hashemi and S. Moein, “NiTi shape memory alloys: properties in nickel-titanium smart hybrid materials”, Elsevier, pp. 399–426, 2022. doi: https://10.1016/B978-0-323-91173-3.00021-3.

[21] C.H. Fu, M.P. Sealy, Y.B. Guo and X.T. Wei, “Austenite–martensite phase transformation of biomedical Nitinol by ball burnishing,” Journal of Materials Processing Technologies, vol. 214, no. 12, pp. 3122–3130, 2014, doi: https://10.1016/j.jmatprotec.2014.07.019

[22] M.A. Schmerling, M.A. Wilkov, A.E. Sanders and J.E. Woosley “A proposed medical application of the shape memory effect: an Ni-Ti Harrington rod for the treatment of scoliosis” Journal of Biomedical Materials Research, vol. 10, pp. 879–902, 1976.

[23] S. Abkowitz, J.M. Siergiej and R.R. Regan. “Titanium-nickel manufacturing methods*”,* 3,700,434, 1969.

[24] S.Tyagi, S.Singh and S. Mukhopadhyay, “Self and balloon-expandable stent implantation for severe native of aorta in adults.” American Heart Journal, vol. 146, no. 5, pp. 920–28, 2003.

[25] J. P. Carpenter, V.Riambau, D.Riethel and P.Peeters “Successful solutions to challenging EVAR indications.” Supplement to Endovascular Today, 2003.

[26] S.A. Thompson, “An overview of nickel-titanium alloys used in dentistry.” International Endodontic Journal, vol. 33, no. 4, pp. 297-310, 2000.

[27] A. Feeney and M.Lucas “A comparison of two configurations for a dual-resonance cymbal transducer*”.* 2018, doi:10.1109/TUFFC.2018.2793310.

[28] A. Feeney, “Nitinol cymbal transducers for tuneable ultrasonic devices”. University of Glasgow, Dec. 2014, http://theses.gla.ac.uk/5805/.

[29] R.J. Meyer Jr and R.E. Newnham, “Flextensional transducers with shape memory caps for tunable devices”. Journal of Intelligent Material Systems and Structures, no. 11(3), pp. 199–205,2000.

[30] S. Smith, X.Li, M. Hafezi, A.Feeney and M.Lucas “Enhanced resolution phase transformations in a Nitinol cymbal ultrasonic device”. pp. 1–4, University of Glasgow, 2022, https://doi.org/10.1109/IUS54386.2022.9957560.

[31] A.E.Clark, "Ferromagnetic materials for transducers". IEEE Transactions on Sonics and Ultrasonics, no.18(2), pp. 94-100,1971.

[32] E.J. Park, J. Werner and N.B. Smith “Ultrasound mediated transdermal insulin delivery in pigs using a lightweight transducer.” Pharmaceutical Research., vol. 24, no. 7, pp. 1396–1401, 2007.

[33] C.Mo, D.Arnold, W.C.Kinsel and W.W. Clark. “Modeling and experimental validation of unimorph piezoelectric cymbal design in energy harvesting.” Journal of Intelligent Material Systems and Structures., vol. 24, no. 7, pp. 828–36,2012.

[34] Y. Liu, M.Hafezi and A.Feeney “A cascaded Nitinol langevin transducer for resonance stability at elevated temperatures.” Ultrasonics 137, pp. 1–14, 2024, https://doi.org/https://doi.org/10.1016/j.ultras.2023.107201.

[35] Y.Liu, M.Hafezi and A.Feeney, “Dynamic stability of a Nitinol langevin ultrasonic transducer under power and current tracking condition.” Applied Acoustics vol. 225, pp. 1-9, 2024, https://doi.org/10.1016/j.apacoust.2024.110188.

[36] F. Bejarano, A. Feeney, R. Wallace, H. Simpson and M. Lucas. “Ultrasonic cutting device for bone surgery based on a cymbal transducer”. Physics Procedia, vol. 63, pp. 120–26, 2015, doi:https://doi.org/10.1016/j.ultras.2016.07.004

[37] A.Feeney, A. Tweedie, A. Mathieson and M.Lucas. “A miniaturized class IV flextensional ultrasonic transducer.” 44th Annual Symposium of the Ultrasonic Industry Association, Washington, DC, USA no. 87, pp. 10–15, Apr. 2016, https://doi.org/10.1016/j.phpro.2016.12.003.

[38] S.Chen and L. Yu, “Finite element analysis of flextensional transducer with slotted shell.” 2012 International Conference on Graphic and Image Processing. International Society for Optics and Photonics., 2013.

[39] K.D. Rolt, “History of the flextensional electroacoustic transducer,” The Journal of the Acoustical Society of America, vol. 87, no. 3, pp. 1340–1349, 1990.

[40] M.Y. Kaya and S. Alkoy, “Design, modelling and fabrication of a novel class V flextensional transducer: The sea-shell.” IEEE Transactions on Ultrasonics, Ferroelectrics, and Frequency Control, vol. 70, no.1 pp. 64-71, Jan. 2023.

[41] A. Mathieson, A. Feeney, A. Tweedie and M. Lucas. “Ultrasonic biopsy needle based on the class IV flextensional configuration.” 2015 IEEE International Ultrasonics Symposium Proceedings, pp. 1–4. 2015.

[42] M.C. Kong, D. Axinte, W. Voice, “Challenges in using waterjet machining of NiTi shape memory alloys: An analysis of controlled-depth milling”, Journal of Materials Processing Technology, vol. 211, no. 6, pp. 957-71, 2011, https://doi.org/10.1016/j.jmatprotec.2010.12.015.

[43] C. Öjmertz. “Nitinol cutting with micro abrasive waterjet for high precision & quality.”, 3 Oct. 2024, https://www.finepart.com/how-to-cut/nitinol-cutting-waterjet/.

[44] A. Baron, “Nitinol manufacturing and metal working”, 3 Oct. 2024, https://www.kelloggsresearchlabs.com/2019/01/04/nitinol-manufacturing-and-metalworking/.

[45] T. Todoroki, and H. Tamura, “Effect of heat treatment after cold working on the phase Transformation in NiTi Alloy.” Transactions of the Japan Institute of Metals, no. 28, pp. 83–94,1987.

[46] M. Bram, A. Ahmad-Khanlou, A. Heckmann, B. Fuchs, H.P. Buchkremer, D. Stöver, “Powder metallurgical fabrication processes for NiTi shape memory alloy parts”, Materials Science and Engineering: A, Vol. 337, no. 1–2, pp. 254-263, https://doi.org/10.1016/S0921-5093(02)00028-X.

[47] G.J. Puthenvila, M. Hafezi, A. Feeney and M. Lucas, “Resonance frequency stability of a Nitinol class IV flextensional transducer”. 18th International Conference on Advances in Experimental Mechanics, University of Liverpool, 3-5 September 2024.

[48] M. Hafezi and A.Feeney.” The thermomechanical behaviour of Nitinol for adaptive ultrasonic devices”. 18th International Conference on Advances in Experimental Mechanics, University of Liverpool, 3-5 September 2024.

[49] J. Fauvel, R. Flood, and R. J. Wilson, “Music and mathematics: from Pythagoras to fractals”. Oxford University Press, 2006.

[50] I. S. Caleon and R. Subramaniam, “From Pythagoras to Sauveur: tracing the history of ideas about the nature of sound”, Physics Education, vol. 42, pp. 173-179, March 2007.

[51] S. Dostrovsky, “Early vibration theory: physics and music in the seventeenth century, archive for the history of exact sciences”, vol. 14, pp. 169-218, 1975.

[52] R.B.Lindsay, “The story of acoustics”, Journal of the Acoustic Society of America, vol .39,pp. 629–644,1966.

[53] W. P. Mason, “Sonics and ultrasonics: early history and applications”, IEEE Transactions on Sonics and Ultrasonics, vol. SU-23, no. 4, pp. 224-232, July 1976.

[54] K.Graff, “Ultrasonics: Historical aspects”, Ultrasonics Symposium, pp. 1-10, 1977.

[55] K. Graff. “Historical highlights in ultrasonics- 2”, Proceedings of the IEEE International Frequency Control Symposium and Exposition, pp. 5-10, 2004.

[56] V. Mckusick, “Cardiovascular sound in health and disease”. Tindall and Cox, Ltd, 1958.

[57] T. Greenslade Jr, “The acoustical apparatus of Rudolph Koenig”, The Physics Teacher, vol. 30, pp. 518-524, 1992.

[58] R. G. Goldman, “Ultrasonic technology: Basic theory and modern practices”. Reinhold Publishing Corporation, 1962.

[59] D.Ensminger, L.J. Bond, "Ultrasonics: Fundamentals, Technologies, and Applications", CRC press, 2024.

[60] F. Galton, “Inquiries into human faculty and its development”. MacMillan and Co., 1883.

[61] J. Blitz, “Fundamentals of ultrasonics”. Butterworth & Co. (Publishers) Ltd., 1963.

[62] M. Gibbs, “Magnetostriction: 150 years from the discovery”, Physica Scripta, vol. T45, pp. 115-119, 1992.

[63] A. P. Cracknell, “Ultrasonics”. Wykeham Publications, 1980.

[64] C. Chilowsky and P. Langevin, “Production of submarine signals and the location of submarine objects”, 1917. US Patent 171547A.

[65] R. Wood and A. Loomis, “The physical and biological effects of high-frequency sound waves of great intensity”, The London, Edinburgh, and Dublin Philosophical Magazine and Journal of Science, vol. 4, no. 22, pp. 417-436, 1927.

[66] M.C. Catuna, “Sonic energy: a possible dental application.” Annals of Dentistry, vol. 12, pp. 100–01,1953.

[67] L. Balamuth, “Ultrasonics and dentistry”, Sound: Its uses and control, pp.15-19,1963.

[68] C. Cheery, M. Gibbons and J. Ronayne, “The origins of the air-turbine dental handpiece”. Journal of the American Dental Association, vol. 136, pp. 469–72,1974.

[69] L. Balamuth, Ultrasonics and dentistry. Sound 2 (2), 1963. https://dx.doi.org/10.1121/12369595.

[70] R. Meyers, W. Fry, F. Fry, L. Dreyer, D. Schultz, and R. Noyes, “Early experiences with ultrasonic irradiation of the pallidofugal and nigral complexes in hyperkinetic and hypertonic disorders”, Journal of Neurosurgery, vol. 16, no. 1, pp. 32-54, 1959.

[71] W. Fry, J. Barnard, F. Fry, and J. Brennan, “Ultrasonically produced localized selective lesions in the central nervous system”, American Journal of Physical Medicine & Rehabilitation, vol. 34, no. 3, pp. 413-423, 1955.

[72] C.Kelman. “Phaco-emulsification and aspiration: 500 cases”. American Journal of Ophthalmology vol. 75, 764–768, 1973.

[73] H. Mararow, “Bone repair after experimentally produced defects”. Journal of Oral Surgery, Anesthesia and Hospital Dental Services, pp. 107–14,1960.

[74] T.A. McFall, G.M. Yamane and G.W. Burnett, “Comparison of the cutting effect on bone of an ultrasonic cutting device and rotary burs”. Journal of Oral Surgery, Anesthesia and Hospital Dental Services, 19, 200-209,1961.

[75] J.E. Horton, T. M. Tarpley and L. D. Wood, “The healing of surgical defects in alveolar bone produced with ultrasonic instrumentation, chisel, and rotary bur”, Journal of Oral Surgery,

Oral Medicine, Oral Pathology, vol. 39, Issue 4,pp. 536-546, 1975, https://doi.org/10.1016/0030-4220(75)90192-9.

[76] J.E. Horton, T.M. Tarpley Jr. and J.R. Jacoway. “Clinical applications of ultrasonic instrumentation in the surgical removal of the bone.”, Journal of Oral Surgery, Oral Medicine, Oral Pathology, vol. 51, pp. 236–42,1981.

[77] H. Aro, H. Kallioniemi, A. Aho and P. Kellokumpu-Lehtinen, “Ultrasonic device in bone cutting: A histological and scanning electron microscopical study”. Acta Orthopaedica Scandinavica. Vol.52(1): pp. 5–10. doi: 10.3109/17453678108991750,1981.

[78] M.Volkov, I.S. Shepeleva. “The use of ultrasonic instrumentation for the transection and uniting of bone tissue in orthopaedic surgery.” Reconstructive Surgery and Traumatology, pp. 147–152,1974.

[79] F. Epstein, “The Cavitron ultrasonic aspirator in tumor surgery”. Clinical Neurosurgery. Vol. 31, pp. 497–505,1983.

[80] N.Horowitz and J.Rader, “Role of the ultrasonic surgical aspirator in gynecology”. Obstetrics and Gynecology Clinics of North America. Vol. 28 (4), pp.775–790,2001.

[81] J.L. Beziat, J. C. Bera, B. Lavandier and A.Gleizal, “Ultrasonic osteotomy as a new technique in craniomaxillofacial surgery.” International Journal of Oral Maxillofacial Surgery vol. 36, pp. 493–500, 2007.

[82] S.Schaeren, C.Jaquiery, M.Heberer, M.Tolnay, T. Vercellotti and I. Martin “Assessment of nerves using a novel ultrasonic device for bone cutting.” Journal of Oral and Maxillofacial Suregery, vol. 66, pp. 593–596, 2007.

[83] A.Mathieson, A. Cardoni, N. Cerisola and M. Lucas, "Understanding nonlinear vibration behaviours in high-power ultrasonic surgical devices", Proceedings of the Royal Society A: Mathematical, Physical and Engineering Sciences, 471, 2176, pp. 1364-5021, 2015.

[84] M.E. Schafer, “Ultrasonic surgical devices and procedures”. Sonic Tech, Inc., Ambler, PA, USA, 2015, http://dx.doi.org/10.1016/B978-1-78242-028-6.00021-1.

[85] K. Stähr, A. Eckstein, L. Holtmann, A. Schlüter, M. Dendy, S. Lang and S. Mattheis, “A comparative analysis of piezosurgery and oscillating saw for balanced orbital decompression,” Orbit, 2018. doi:10.1080/01676830.2018.1552709.

[86] T. Vercellotti, “Technological characteristics and clinical indications of piezoelectric bone surgery,” Minerva Stomatologica, vol. 53, no. 5, pp. 207–214, 2004. PMID: 15263875.

[87] M. Thomas, U. Akula, K. K. R. Ealla and N. Gajjada, “Piezosurgery: A boon for modern periodontics,” Journal of International Society of Preventive and Community Dentistry, vol. 7, no. 1, pp. 1–7, Jan-Feb 2017. DOI: 10.4103/2231-0762.200709.

[88] B. Zebian, L. Greuter, A.-M. Vasilica, F. Vitulli, D. Wang, I. Abdelfattah, P. Seetahal-Maraj, M. Dacdac, D. Rowland and C. Bleil, “A simple modification of the endoscopic ultrasonic aspirator (Söring ENP handpiece),” Operative Neurosurgery, vol. 29, no. 3, pp. 374-380, September 2025. DOI: 10.1227/ons.0000000000001500.

[89] C. Di Rienzo, A. Colasanti, G. Esposito, F. Ricciuti, and R. Anile, “Use of ultrasonic aspirator (Söring) in resection of brain metastases located in eloquent areas: technical note,” Acta Neurochirurgica, vol. 156, pp. 1575–1581, 2014. doi:10.1007/s00701-014-2123-7.

[90] P. F. Vetrano, L. Signorelli, A. Visocchi, “Ultrasonic aspiration in skull base surgery: comparison of Cavitron, Sonopet and Söring systems,” World Neurosurgery, vol. 114, pp. 389–395, 2018. doi:10.1016/j.wneu.2018.02.142.

[91] G. E. Daly, R. A. Luh, D. Balumuka, L. K. Howell and E. M. Wolfswinkel, “The Sonopet iQ® ultrasonic bone aspirator in craniofacial surgery: A scoping review and qualitative analysis,” Face, vol. 5, no. 2, pp. 261-271, June 2024. DOI: 10.1177/27325016241230672.

[92] J. F. Ha and R. S. Sieunarine, “Sonopet ultrasonic aspirator for bone removal in orbital surgery: a useful adjunct,” Orbit, vol. 31, no. 6, pp. 423–426, 2012. doi:10.3109/01676830.2012.717247.

[93] K. R. Renjith, “Ultrasonic bone scalpel (UBS) has a high safety index owing to its characteristics of tissue selectivity and elimination of rotary cutting risks,” Spine Surgery and Related Research, vol. 7, no. 3, pp. 250-258, 2023. DOI: 10.1016/j.spinee.2023.09.004.

[94] S. Henzi and J. Tarazi, “Sonopet ultrasonic aspirator versus Misonix BoneScalpel in terms of thermal injury risk,” Journal of Neurosurgery, 2018. doi:10.3171/2018.2.JNS172939.

[95] S. H. L. Tsai, C.-W. Chang, T.-Y. Lin, Y.-C. Wang, C.-B. Wong, A. K. Ghaith, M. A. Alvi, T.-S. Fu and M. Bydon, “The use of ultrasonic bone scalpel (UBS) in unilateral biportal endoscopic spine surgery (UBESS): Technical Notes and Outcomes,” Journal of Clinical Medicine, vol. 12, no. 3, p. 1180, 2023. doi:10.3390/jcm12031180.

[96] X. Li, T. Stritch, K.Manley and M.Lucas, “Limits and opportunities for miniaturizing surgical devices based on a Langevin transducer”. IEEE Transactions On Ultrasonics, Ferroelectrics, and Frequency Control, pp.2543–53, 2021, doi:10.1109/TUFFC.2021.3065207.

[97] A.D. Brickman, “Preloading of acoustic transducers for high-pressure operation.” The Journal of the acoustical society of America, vol. 34, no. 3, pp. 305–11, Mar. 1962.

[98] M. Lucas and A. Cardoni., “Strategies for reducing stress in ultrasonic systems*”.* vol. 41, pp.11-18,2005.

[99] J. Tsujino, T.Ueoka, K.Otoda and A.Fujimi, “One-dimensional longitudinal–torsional vibration converter with multiple diagonally slitted parts.” Faculty of Engineering, Kanagawa University, Yokohama 221-8686, Japan, vol. 38, pp. 72–76,2000.

[100] L. H. Royster, “The flextensional concept: a new approach to the design of underwater acoustic transducers”, Applied Acoustics, vol. 3, pp. 117-126, 1970.

[101] B. P. Naidu, A. B. Rao, N. S. Prasad, and K. Trinath, “Modal analysis of class V flextensional transducer”, Proceedings of the 2009 IEEE International Symposium on Ocean Electronics (SYMPOL), pp. 122-127, 2009.

[102] J. Zhang, “Miniaturized flextensional transducers and arrays”. PhD thesis, The Pennsylvania State University, 2000.

[103] J. F. Lindberg, “Material challenges for transducer designers in the 21st century”, Proceedings of SPIE, vol. 4699, pp. 485-498, 2002.

[104] A. Dogan, K. Uchino, and R. E. Newnham, “Composite piezoelectric transducer with truncated conical endcaps cymbal”, IEEE Transactions on Ultrasonics, F, vol. 44, pp. 597-605, May 1997.

[105] R. J. Meyer, Jr., W. J. Hughes, T. C. Montgomery, D. C. Markley, and R. E. Newnham, “Design of and fabrication improvements to the cymbal transducer aided by finite element analysis”, Journal of Electroceramics, vol. 8, no. 2, pp. 163-174, 2002.

[106] K.Uchino, "Manufacturing technologies for piezoelectric transducers", Actuators and Ultrasonic Motors, Springer, chapter 16, pp. 615-643,2017.

[107] J. F. Tressler and R. E. Newnham, “Doubly resonant cymbal-type transducers, IEEE Transactions on Ultrasonics”, Ferroelectrics and Frequency Control, vol. 44, pp. 1175-1177, September 1997.

[108] J. Zhang, W. J. Hughes, A.-C. Hladky-Hennion, and R. E. Newnham, “Concave cymbal transducers”, Material Research Innovations, vol. 2, no. 5, pp. 252-255, 1999.

[109] F. Bejarano, *“*Miniature ultrasonic bone cutting device based on a cymbal transducer.*”* University of Glasgow, 2014, http://theses.gla.ac.uk/5568.

[110] F., Bejarano, and M. Lucas. “Finite element modeling and design of cymbal transducers for power ultrasonics applications”. IEEE International Ultrasonics Symposium, pp. 1567–70, 2011.

[111] S. Lin, “An improved cymbal transducer with combined piezoelectric ceramic ring and metal ring”, Sensors and Actuators A 163, pp. 266- 276, 2010.

[112] S. Lin, “Analysis of the equivalent circuit of piezoelectric ceramic disk resonators in coupled vibration” Journal of Sound and Vibration, 231(2), pp. 277-290,2000.

[113] S. Lin, “Radial vibration of the combination of a piezoelectric ceramic disk and a circular metal ring”, Journal of Smart Material Structures, 16 (2), pp. 469- 476, 2007.

[114] R. J. Meyer, Jr. and R. E. Newnham,” Flextensional transducers with shape memory caps for tuneable devices”, Journal of Intelligent Material Systems and Structures, vol. 11, no. 3, pp. 199-205, March 2000.

[115] R.Devassy, S. Hanif, H.Krentel, H.C. Verhoeven, L.A.Torres-de la Roche and R. L. De Wilde. “Laparoscopic ultrasonic dissectors: Technology update by a review of literature.”. Dovepress, Medical Devices: Evidence and Research, 2019.

[116] G. V. Kurdjumov and L. G. Khandros, “First reports of the thermoelastic behaviour of the martensitic phase of Au-Cd alloys”, Doklady Akademii Nauk SSSR 66, pp. 211–213,1949.

[117] M. Wayman and J. Harrison, “The origins of the shape memory effect”, Journal of Minerals, Metals, and Materials 41 (99), 26–28, 1989.

[118] T. Saburi, T. Takagi, S. Nenno, K. Koshino, in: M. Doyama, S. Somlya and R. P. H. Chang (Eds.), “Shape memory materials”, MRS International Meeting on Advanced Materials, Vol. 9, pp. 147–152, 1989.

[119] Y. Liu, “Mechanical and thermomechanical properties of a Ti0.50Ni0.25Cu0.25 melt spun ribbon”, Materials Science and Engineering A 354, pp.286–291,2003.

[120] Z. L. Xie, J. Van Humbeeck, Y. Liu and L. Delaey, “TEM study of Ti50Ni25Cu25 melt spun ribbons”, Scripta Materialia 37 (3), pp.363–371,1997.

[121] R. Kainuma, M. Ise, C. Jia, H. Ohtani and K. Ishida, “Phase equilibria and microstructural control in the Ni-Co-Al system”, Intermetallics 4, 151,1996.

[122] D. Schryvers, P. Boullay, P. Potapov, R. Kohn and J. Ball, “Microstructures and interfaces in Ni-Al martensite: comparing HRTEM observations with continuum theories”, International Journal of Solids Structures 39 (3543).

[123] H. E. Karaca, I. Karaman, D. C. Lagoudas, H. J. Maier and Y. I. Chumlyakov, “Recoverable stress-induced martensitic transformation in a ferromagnetic CoNiAl alloy”, Scripta Materialia 49, pp. 831–836, 2003.

[124] P. J. Webster, K. R. A. Ziebeck, S. L. Town, and M. S. Peak, “Magnetic order and phase transformation in Ni2MnGa”, Philosophical Magazine B 49 (3), pp. 295–310, 1984.

[125] S. J. Murray, M. Marioni, S. M. Allen and R. C. O’Handley, “6% magnetic f ield-induced strain by twin-boundary motion in ferromagnetic Ni-Mn Ga”, Applied Physics Letters 77 (6), pp. 886–888,2000.

[126] D. Pitt, J. Dunne, E. White and E. Garcia, “SAMPSON smart inlet SMA powered adaptive lip design and static test”, Proceedings of the 42nd AIAAStructures, Structrual Dynamics, and Materials Conference, Seattle, WA, pp.1–11, 16-20 April 2001.

[127] B. Sanders, R. Crowe and E. Garcia, “Defense advanced research projects agency– Smart materials and structures demonstration program overview”, Journal of Intelligent Material Systems and Structures 15, pp. 227–233, 2004.

[128] J. Mabe, R. Cabell and G. Butler, “Design and control of a morphing chevron for take-off and cruise noise reduction”, in: Proceedings of the 26th Annual AIAA Aeroacoustics Conference, Monterey, CA, pp. 1–15, 2005.

[129] C. Willey, B. Huettl and S. Hill, “Design and development of a miniature mechanisms tool-kit for micro spacecraft”, in: Proceedings of the 35th Aerospace Mechanisms Symposium, Ames Research Center, pp. 1–14, 9-11 May 2001.

[130] A. Peffer, K. Denoyer, E. Fossness and D. Sciulli, “Development and transition of low-shock spacecraft release devices”, in: Proceedings of IEEE Aerospace Conference, Vol. 4, pp. 277–284, 2000.

[131] V. Birman, “Review of mechanics of shape memory alloy structures”, Applied Mechanics Reviews 50 (11), pp. 629–645,1997.

[132] B. Carpenter and J. Lyons, “EO-1 technology validation report: Lightweight flexible solar array experiment”, Tech. rep., NASA Godard Space Flight Center, Greenbelt, MD (8 August 2001).

[133] O. Godard, M. Lagoudas and D. Lagoudas, “Design of space systems using shape memory alloys”, in: Proceedings of SPIE, Smart Structures and Materials, Vol. 5056, San Diego, CA, pp. 545–558,2003.

[134] C. Meier and S. Seelecke, “Recent developments in shape memory alloy actuator technology for soft robotics,” Actuators, vol. 8, no. 1, p. 20, Feb. 2019.

[135] M. Karamoozian, T. Barati and A. Sadegh, “Additive manufacturing of Nitinol: process optimisation and evaluation of shape memory performance,” Materials & Design, vol. 191, 108610, Mar. 2020.

[136] A. J. Fleming, “Precision ultrasonic actuators and vibration control systems for microscale applications,” IEEE/ASME Transactions on Mechatronics, vol. 24, no. 2, pp. 612–623, Apr. 2019.

[137] R.I. Stephens, A.Fatemi, R.R. Stephens, H.O. Fuchs, “Metal fatigue in engineering, 2nd edition”, November 2000, ISBN: 978-0-471-51059-8.

[138] M.J. Mahtabi, N. Shamsaei and M.R. Mitchell, “Fatigue of Nitinol: The state-of-the-art and ongoing challenges”, Journal of the Mechanical Behavior of Biomedical Materials,vol. 50,

pp. 228-254, 2015, ISSN 1751-6161, https://doi.org/10.1016/j.jmbbm.2015.06.010.

[139] J. Van Humbeeck, “Cycling effects, fatigue and degradation of shape memory alloys” Journal of Physics IV. France 01, European Symposium of Martensitic Transformation and Shape Memory Properties, pp. 189-197, ttps://doi.org/10.1051/jp4:1991429.

[140] C.-L. Sun, S.S. Guo, W.P. Li, Z.B. Xing, G.C. Liu and X.-Z. Zhao, “Displacement amplification and resonance characteristics of the cymbal transducers”, Sensors and Actuators A: Physical, vol. 121, Issue 1, pp. 213-220, 2005, https://doi.org/10.1016/j.sna.2005.01.023.

[141] Y. Gao, L. Casalena, M.L. Bowers, R.D. Noebe, M.J. Mills and Y.Wang, “An origin of functional fatigue of shape memory alloys”, Acta Materialia 126, pp.389-400, January 2017.

[142] G. Eggeler, E. Hornbogen, A. Yawny, A. Heckmann and M. Wagner, “Structural and functional fatigue of NiTi shape memory alloys”, Materials Science and Engineering: A, vol. 378, Issues 1–2, pp. 24-33, 25 July 2004, ISSN 0921-5093, https://doi.org/10.1016/j.msea.2003.10.327.

[143] S. Miyazaki, T.Imai, Y. Igo and K. Otsuka, “Effect of cyclic deformation on the pseudoelasticity characteristics of Ti-Ni alloys”. Metallurgical Transactions A, pp .115–120 1986. https://doi.org/10.1007/BF02644447.

[144] S. Miyazaki, Y. Igo and K. Otsuka, “Effect of thermal cycling on the transformation temperatures of Ti-Ni alloys”,Acta Metallurgica, vol. 34(10), pp. 2045-2051, 1986, ISSN 0001-6160, https://doi.org/10.1016/0001-6160(86)90263-4.

[145] A. Chau, D. C. Hofmann, and J. A. Shaw, “Phase-tuned Nitinol via precision processing: enhanced cyclic performance for adaptive medical devices,” Acta Materialia, vol. 216, pp. 117-267, 2021.

[146] H. Huang, H.Y. Zheng and G.C. Lim,“Femtosecond laser machining characteristics of Nitinol”. Journal of Applied Surface Science 228(1–4), pp:201–206, 2004. https://doi.org/10.1016/j.apsusc.2004.01.018.

[147] K.C.Yung, H.H. Zhu and T.M. Yue,“Theoretical and experimental study on the kerf profile of the laser micro-cutting NiTi shape memory alloy using 355 nm Nd:YAG”. Journal of Smart Materials Structures 14(2), pp:337–342,2005. https://doi.org/10.1088/0964-1726/14/2/006.

[148] C.Li, S.Nikumb and F.Wong, “An optimal process of femtosecond laser cutting of NiTi shape memory alloy for fabrication of miniature devices”. Optics and Lasers in Engineering 44(10), pp:1078–1087,2006. https://doi.org/10.1016/j.optlaseng.2005.08.003.

[149] B.Muralidharan, K. Prabu and G. Rajamurugan, “Pulsed Nd:YAG laser machining of Nitinol: an experimental investigation”. Journal of Micromanufacturing 5(2), pp:144–148,2022. https://doi.org/10.1177/25165984211015482 .

[150] M. Frotscher, F. Kahleyss, T.Simon, D.Biermann and G. Eggeler,“Achieving small structures in thin NiTi sheets for medical applications with water jet and micro machining: a comparison”. Journal of Materials Engineering and Performance 20(4–5), pp:776–782,2011. https://doi.org/10.1007/s11665-010-9789-8.

[151] W.B. Jefrin Harris, A.V. Dehaleesan, S. Sampath and A.V. Krishnan,“A state-of-the-art review on electric discharge machining of shape memory alloys”. Materials Today Proceedings 72, pp:2518–2527,2023. https://doi.org/10.1016/j.matpr.2022.09.538

[152] T. Leppert, “A review on ecological and health impacts of electro discharge machining (EDM).In: AIP conference proceedings”, vol 2018. https://doi.org/10.1063/1.5056277.

[153] M.H. Wu, “Fabrication of Nitinol materials and components”, Proceedings of the International Conference on Shape Memory and Superelastic Technologies, pp.285-292, 2001.

[154] A. Tuissi, G. Rondelli, P. Bassani,“Plasma arc melting (PAM) and corrosion resistance of pure NiTi shape memory alloys ”, Shape Memory Superelasticity, vol.1, pp.50-57, 2015, DOI: 10.1007/s40830-015-0011-6.

[155] S.W. Robertson, A.R. Pelton and R.O. Ritchie, “Mechanical fatigue and fracture of Nitinol”, Institute of Materials, Minerals and Mining and ASM International, vol. 57(1), 1-37, 2012, DOI: 10.1179/1743280411Y.0000000009.

[156] J.P. Oliveira, R.M. Miranda and F.M. Braz Fernandes, “Welding and joining of NiTi shape memory alloys: A review”, Progress in Materials Science, vol. 88, pp. 412-466, 2017, https://doi.org/10.1016/j.pmatsci.2017.04.008.

[157] S. Wen, J. Gan, F. Li, Y. Zhou, C. Yan and Y. Shi. “Research status and prospect of additive manufactured nickel-titanium shape memory alloys”. Materials 2021, vol. 14, pp. 44-96, 2021, https://doi.org/10.3390/ma14164496.

[158] J. Van Humbeeck, “Additive manufacturing of shape memory alloys”. Shape Memory Superelasticity, pp. 309–312, 2018. https://doi.org/10.1007/s40830-018-0174-z.

[159] J. Walker, M.T. Andani, C. Haberland, & M. Elahinia, "Additive manufacturing of Nitinol shape memory alloys to overcome challenges in conventional Nitinol fabrication." Proceedings of the ASME 2014 International Mechanical Engineering Congress and Exposition. Volume 2A: Advanced Manufacturing. Montreal, Quebec, Canada. November 14–20, 2014. https://doi.org/10.1115/IMECE2014-40432

[160] D.J.S. Ruth, J.W. Sohn, K. Dhanalakshmi, S.B. Choi. “Control aspects of shape memory alloys in robotics applications: A Review over the Last Decade”. Sensors (Basel). vol. 22(13) June 27, 2022, doi: 10.3390/s22134860.

[161] C. Haberland, M. Elahinia, J.M. Walker, H. Meier and J.Frenzel, “On the development of high quality NiTi shape memory and pseudoelastic parts by additive manufacturing” Journal of Smart Materials and Structures 23, 2014, doi: 10.1088/0964-1726/23/10/104002.

[162] M. Elahinia “Shape memory alloy actuators: design, fabrication, and experimental evaluation” 2016, doi: 10.1002/9781118426913.

[163] M. H. Elahinia, M. Hashemi, M. Tabesh and S. B. Bhaduri, “Manufacturing and processing of NiTi implants: A review”, Progress in Materials Science, vol. 57, Issue 5, pp. 911-946, 2012, https://doi.org/10.1016/j.pmatsci.2011.11.001.

[164] C. Zhao, N.D. Parab, X. Li, K. Fezzaa, W. Tan, A.D. Rollett and T.Sun.”Critical instability at moving keyhole tip generates porosity in laser melting”. Science 370, pp.1080-1086, 2020. doi :10.1126/science.abd1587.

[165] Z.X. Khoo, J.E.M. Teoh, Y. Liu, C.K. Chua and S. Yang.“3D printing of smart materials: A review on recent progresses in 4D printing”. Virtual and Physical Prototyping, 10(3), vol.103–122. 2015. https://doi.org/10.1080/17452759.2015.1097054.

[166] J. Sam, B. Franco, J. Ma, I. Karaman, A. Elwany and J.H. Mabe, “Tensile actuation response of additively manufactured nickel-titanium shape memory alloys”, Scripta Materialia, vol. 146, pp. 164-168, 2018, https://doi.org/10.1016/j.scriptamat.2017.11.013.

[167] T. Bormann, R. Schumacher, B.Müller, “Tailoring selective laser melting process parameters for NiTi implants. Journal of Materials Engineering and Performance 21, pp. 2519–2524,2012. https://doi.org/10.1007/s11665-012-0318-9.

[168] T. Habijan, C. Haberland, H. Meier, J. Frenzel, J. Wittsiepe, C. Wuwer, C. Greulich, T.A. Schildhauer and M. Köller, “The biocompatibility of dense and porous Nickel–Titanium produced by selective laser melting”, Materials Science and Engineering: C,vol. 33, Issue 1, pp. 419-426, 2013, https://doi.org/10.1016/j.msec.2012.09.008.

[169] X. Li, Y. Wang, Y. Zeng, D. Shi, Z. Huang and K.H. Lam, “Optimisation of adhesive-free high-frequency miniature class IV transducers incorporating single-element piezoelectric plates”, Sensors and Actuators A: Physical, Volume 399, 2026, 117489, ISSN 0924-4247, https://doi.org/10.1016/j.sna.2026.117489.

[170] K. P. Menard, "Dynamic mechanical analysis: a practical introduction". 2nd ed. Boca Raton, FL: CRC Press, 2008.

[171] J. D. Ferry, "Viscoelastic Properties of Polymers". 3rd ed. New York: John Wiley & Sons, 1980.

[172] ASTM International, "ASTM D4065-17: Standard Practice for Plastics: Dynamic Mechanical Properties: Determination and Report of Procedures". West Conshohocken, PA: ASTM International, 2017.

[173] C. T. Chantler, L. F. Smale, J. A. Kimpton, D. N. Crosby, M. N. Kinnane, and A. J. Illig, "Characterization of the titanium Kβ spectral profile," Journal of Physics B Atomic Molecular and Optical Physics, vol. 46, no. 14, p. 145601, Jun. 2013, doi: 10.1088/0953-4075/46/14/145601.

[174] S. Nagaraja, G. Sena, P. Stafford, C. Braeuner, P. Hempel, A.R. Pelton and V.Ravi , "Effect of Nitinol microstructural on localized and uniform corrosion susceptibility", Shape Memory Superelasticity, vol.8, pp.118-128, 2022, https://doi.org/10.1007/s40830-022-00366-1.

[175] A.R. Pelton, S.M. Russell and J.DiCello , "The physical metallurgy of Nitinol for medical applications", Overview: Physical Metallurgy, pp. 33-37, 2003.

[176] H.Cui, H.Wu and D.Mantovani. "Effects of oxygen on the mechanical properties and phase transformations in NiTi alloys", Materials Science and Engineering A,2009, doi:10.1016/j.msea.2009.03.005.

[177] http://uk.rs-online.com/web/p/steel-rods-bars-tubes-hexagonals/4377168/. Accessed on 16th November 2024.

[178] https://www.smithmetal.com/ti-6al-4v-grade-5.htm. Accessed on 16th November 2024.

[179]https://uk.rs-online.com/web/p/metal-bars-metal-rods/0559189. Accessed on 16th November 2024.

[180] M.K. Gupta, V.Panwar and R. Prasad Mahapatra, "Temperature and strain rate dependent stress-strain behaviour of Nitinol", Materials Today: Proceedings, 43, 2021, pp. 395–399.

[181]https://www.henkel-adhesives.com/cl/en/product/electrically-conductive-adhesives/loctite_eccobonde32000.html. Accessed on 16th November 2024.

[182]https://www.ctscorp.com/ProductSeries/Pz26.htm#:~:text=Pz26%20is%20an%20all%2Dround,factor%20and%20low%20dielectric%20losses. Accessed on 8th November 2024.

[183] M. Hofmann, A. Haeberlin, S. de Brot, A. Stahel, H. Keppner and J Burger, "Development and evaluation of a titanium-based planar ultrasonic scalpel for precision surgery", Ultrasonics, Volume 130, 2023, 106927, ISSN 0041-624X, https://doi.org/10.1016/j.ultras.2023.106927.

[184] N. M. M. Maia and J. M. M. Silva, "Modal analysis identification techniques", Philosophical Transactions of the Royal Society A: Mathematical, Physical and Engineering Sciences, vol. 359, no. 1778, pp. 29-40, 2001.

[185] https://www.polytec.com/uk/vibrometry/technology/laser-doppler-vibrometry. Accessed on 8th November 2024.

[186] IEEE Standards Committee. IEEE Standard on Piezoelectricity (IEEE Std 176-2023). IEEE, New York, USA,2023.

[187] K. Otsuka, and C. M. Wayman, “Shape Memory Materials”. Cambridge University Press. 1998.

[188] L.Tang and W.Cao, “Temperature dependence of self-consistent full matrix material constants of lead zirconate titanate ceramics” Applied Physics Letters, vol. 106 (5), pp. 106-111,2015. https://doi.org/10.1063/1.4921128.

[189] L.Tang and W.Cao, “Characterization of full set material constants and their temperature dependence for piezoelectric materials using resonant ultrasound spectroscopy”, Journal of Visualized Experiments, 110, pp. 1-11, 2016. : http://www.jove.com/video/53461.

[190] A. Wellendorf, L.V. Damnitz, A.W. Nuri, D. Anders and S.Trampnau, “Determination of the temperature-dependent resonance behaviour of ultrasonic transducers using the finite-element method”, Journal of Vibration Engineering and Technologies (2024), 12:pp. 1277–1290,2023. https://doi.org/10.1007/s42417-023-00906-8.

[191] https://www.bureauveritas.ch/en/our-services/iso-13485-certification. Accessed on 26th May 2026.

[192] R. J. Siegel, J. Gunn, A. Ahsan, M. C. Fishbein, R. J. Bowes, D. Oakley, C. Wales, W. Steffen, S. Campbell, and H. Nita, “Use of therapeutic ultrasound in percutaneous coronary angioplasty. Experimental in vitro studies and initial clinical experience,” Circulation, vol. 89, no. 4, pp. 1587–1592, Apr. 1, 1994.

[193] G. B. McGuinness, M. P. Wylie, and G. P. Gavin, “Ablation of chronic total occlusions using kilohertz-frequency mechanical vibrations in minimally invasive angioplasty procedures,” Critical Review of Biomedical Engineering, vol. 38, no. 6, pp. 511–531, 2010.

[194] N. G. William, W. Chen, P. Lee, and C. Lau, “Initial experience and safety in the treatment of chronic total coronary occlusions with a new optical coherent reflectometry-guided radiofrequency ablation guidewire,” American Journal of Cardiology, vol. 92, no. 6, pp. 732–734, 2003.

[195] Z. Xu, “Controlled ultrasound tissue erosion: The role of dynamic interaction between insonation and microbubble activity,” Journal of Acoustic Society of America, vol. 117, no. 1, pp. 424, 2005.

[196] M.P. Wylie, G.B.McGuinness and G.P. Gavin, “Increased susceptibility of arterial tissue to wire perforation with the application of high-frequency mechanical vibrations”, IEEE Transactions on Biomedical Engineering, vol.59 (4), pp.1101-1109, 2012. https://ieeexplore.ieee.org/stamp/stamp.jsp?tp=&arnumber=6130594.

[197] J. G. Lin, and T. F. Chu, “Vibration characteristics and energy dissipation in ultrasonic horn design,” Ultrasonics, vol. 50, pp. 309–320, 2010.

[198] R. J. Siegel, J. Gunn, M. Ahsan, M. C. Fishbein, R. J. Bowes, D. Oakley, C. Wales, S. Steffen, S. Campbell, and H. Nita, “Use of therapeutic ultrasound in percutaneous coronary angioplasty: Experimental in vitro studies and initial clinical experience,” Circulation, vol. 89, no. 4, pp. 1587–1592, 1994.

[199] R.S. Cleary, “Resonant ultrasonic bone penetrating needles”. University of Glasgow, Feb. 2020, http://theses.gla.ac.uk/79041/.

[200] M. Hafezi, Y. Liu, and A. Feeney, “A Nitinol Langevin transducer with resonance tuneability for adaptive ultrasonic applications,” *Ultrasonics*, vol. 160, p. 107916, Dec. 2025, doi: 10.1016/j.ultras.2025.107916.

Appendix A

Posters and Conferences

G.J.Puthenvila, P. Barron, A.Feeney and M.Lucas, "Nitinol Characterisation for Incorporation into Ultrasonic Surgical Devices." Ultrasonics Industry Association (UIA) 50, Warwick, 25-27 April 2022. (Poster).

G.J. Puthenvila, M. Hafezi, A. Feeney and M. Lucas, “Resonance Frequency Stability of a Nitinol Class IV Flextensional Transducer”. The IEEE UK & Ireland Ultrasonics, Ferroelectrics and Frequency Control (UFFC) Chapter, University of Strathclyde, 4 April 2024. (Poster).

G.J. Puthenvila, M. Hafezi, A. Feeney and M. Lucas, “Resonance Frequency Stability of a Nitinol Class IV Flextensional Transducer”. 18th International Conference on Advances in Experimental Mechanics, University of Liverpool, 3-5 September 2024.